Simulation numérique de l'interaction de sels de platine avec des membranes lipidiques asymétriques

Timothée Rivel

To cite this version:

Timothée Rivel. Simulation numérique de l'interaction de sels de platine avec des membranes lipidiques asymétriques. Biophysique. Université Bourgogne Franche-Comté, 2020. Français. NNT : 2020UBFCD017 . tel-03128929

HAL Id: tel-03128929
https://theses.hal.science/tel-03128929
Submitted on 2 Feb 2021

THESE DE DOCTORAT DE L'ETABLISSEMENT UNIVERSITE BOURGOGNE FRANCHE-COMTE
PREPAREE A L'UNIVERSITE DE FRANCHE-COMTE

Ecole doctorale n°554
Environnements-Santé

Doctorat de physique

Par
Monsieur Timothée Rivel

Simulation numérique de l'interaction de sels de platine avec des membranes lipidiques asymétriques

Thèse présentée et soutenue à Besançon, le 06/02/2020

Composition du Jury :

Madame Bassereau, Patricia	Directrice de recherche, Institut Curie	Présidente
Madame Etchebest, Catherine	Professeur, Université Paris-Diderot	Rapporteur
Monsieur Vanni, Stefano	Professeur, Université de Fribourg	Rapporteur
Monsieur Khandelia, Himanshu	Professeur associé, University of Southern Denmark	Examinateur
Monsieur Monticelli, Luca	Chargé de recherche, Université de Lyon Professeur,	Examinateur
Monsieur Ramseyer, Christophe	Université de Franche-Comté	Directeur de thèse
Monsieur Yesylevskyy, Semen	Leading researcher, Académie des sciences de Kyiv	Co-directeur de thèse

ACKNOWLEDGEMENTS

I would like first to acknowledge the members of my PhD committee who gave their time and attention to get involved in my work. I'm very glad that I had the opportunity to start discussing the complex and exciting topic of membrane modelling and the study of their interactions with anticancer drugs and other molecules. Even if the conditions for organizing the PhD defence where difficult, all of you have shown me support and implication in the topic.

It is difficult to me to find strong enough words to thank Christophe Ramseyer for accepting me as a student and guiding me these several past years. Christophe, thank you for these so numerous discussions about our researches, your kind and constant support: you guided the five most inspiring years in my life and confirmed my affinity to sciences. I can only hope we will share some more Itaipava, Stargorod and research work in the very next years!

I cannot forget to thank Semen Yesylevskyy. Thank you for the time and energy you spent on teaching me Molecular Dynamics, sciences and its methodology. I am grateful that you kept driving me to overcome the technical challenges and disappointments every PhD student will face.

I would like to thank my colleagues of the K3-K4 who keep such an enjoyable atmosphere in the lab. Thank you Bruno, Christophe, Freddy, Jean, Michel, Sarah and (salut!) Manu. I want to express my acknowledgment to all the colleagues from Chrono-Environnement who are making the lab to be alive and dynamic. I'd like also to thank the PhD students I met there: Geoffrey, Deborah, Thibault, Nicolas, Jo and Norhan.

I know that in this exercise I will forget many of my friends from the present and from the past. So many of you helped me in my life. Thank you Johal, Auré, Mel, Rémi, Saad, Quentin, Antoine, Chapal, and everyone who knows the role they played for me!

Je ne pourrais pas manquer d'écrire ces mots pour les membres de ma famille qui ont toujours été là pour moi. À mes parents qui m'ont tant apporté, à mes grands-parents dont je saurais être plus fier : chaleureusement et sincèrement, merci !

Finally, I want to write to the person with whom I share my life, my sorrows and my joys. To you, Mariia, who share so much with me; you, Mariia, who stand me in my doubts and still laugh at my jokes, thank you!

LIST OF THE FIGURES

LIST OF THE TABLES

Chapter I - **Résumé de thèse**

Les membranes cellulaires sont généralement considérées comme des barrières physiques permettant la compartimentation et la spécialisation du milieu intracellulaire. Ce sont des systèmes dynamiques, dont la forme, la composition et les propriétés changent sur une large gamme des échelles de temps et d'espace. Ce remodelage des membranes a lieu au sein de différents processus cellulaires comme leur déplacement, leur différenciation ou encore le transport de vésicules. Les membranes doivent être suffisamment robustes et rigides pour maintenir l'intégrité de la cellule et dans le même temps, suffisamment flexibles pour permettre un continuel changement de forme. Plusieurs de leurs propriétés, telles que leurs propriétés thermodynamiques ou mécaniques ont été étudiées et associées à l'auto-organisation des lipides. Cependant, plusieurs questions restent ouvertes, en particulier en ce qui concerne le lien entre la composition des membranes et leur perméabilité face à des médicaments. La détermination de leur perméabilité est d'une grande importance pour des raisons toxicologiques, pour mieux comprendre la problématique de résistance aux médicaments de chimiothérapie exprimée par certaines lignées cancéreuses, mais aussi dans le but de développer de nouvelles stratégies pour le ciblage cellulaire.

1. Modéliser la matrice lipidique des membranes plasmiques : quelles propriétés sont liées à la perméation ?

Au cours de ce travail de thèse, nous avons recherché les propriétés chimiques et physiques connectées à la matrice lipidique des membranes plasmiques qui pourraient permettre de différencier les cellules cancéreuses des cellules saines et qui pourraient ainsi devenir de potentiels marqueurs pour un ciblage sélectif. Il est connu que les membranes plasmiques des cellules eucaryotes saines présentent une asymétrie dans la distribution des différents types de lipides entre les deux monocouches qui la composent. Cette asymétrie [1-3] est activement maintenue par certaines protéines; les flippases et les floppases. Ainsi, la monocouche extracellulaire est principalement composée de phosphatidylcholines (PC) et de sphingomyélines (SM) alors que la couche cytoplasmique est riche en phosphatidylsérines (PS) et en phosphatidyléthanolamines (PE).

Dans le cas des cellules apoptotiques, il est reconnu que cette asymétrie n'est plus préservée. En 1989, il a été montré que certaines lignées cancéreuses présentaient des signes similaires de *symétrisation*. La principale conséquence de ce phénomène est une surexposition en PS sur la monocouche extracellulaire des membranes plasmiques alors que ce lipide anionique est majoritairement présent au sein de la couche cytoplasmique dans les cellules saines [4, 5]. Des études ultérieures [6-8] utilisant de la cytométrie en flux après un marquage avec de l'annexin V ont confirmé ces premiers résultats. En particulier, il a été montré que cette surexposition en PS n'est pas un artefact dû à la présence de cellules apoptotiques dans l'échantillon [9]. L'exposition en PS a aussi été détectée dans le système vasculaire relié aux tumeurs [10, 11]. Une analyse de la littérature [4-9, 12, 13] nous permet de conclure que la proportion en PS sur la monocouche extracellulaire est ~7 fois supérieure dans des lignées cancéreuses que dans des cellules saines correspondantes. Ces observations sont d'une grande importance et pourraient résulter en une nouvelle approche dans le ciblage des cellules tumorales par le biais d'une reconnaissance sélective des phosphatidylsérines [8, 14-17] ou de la redistribution associée en PE [18]. Malgré l'importance de ce sujet, très peu d'études numériques ont été menées dans le but de modéliser des membranes de cellules cancéreuses de sorte à comparer leurs propriétés avec des modèles de membranes de cellules saines [19].

L'un des domaines de recherche les plus actifs quant à l'étude de la structure des membranes plasmiques concerne la présence de cholestérol. Cependant, bien que le cholestérol soit la molécule la plus abondante dans les membranes plasmiques après les lipides, sa distribution transversale au sein de la membrane est toujours sujet à débat [20-22]. Il a été observé expérimentalement que le cholestérol est principalement situé dans la monocouche cytoplasmique [23-25]. Pourtant, une forte affinité entre le cholestérol et les sphingomyélines a été établie expérimentalement [26] et des simulations numériques montrent une distribution accrue en cholestérol dans la monocouche extracellulaire [27-29]. L'existence de raft lipidiques ou de micro/nano-domaines dans les membranes est un autre domaine débattu à l'heure actuelle. Il a été montré *in vitro* que la présence de cholestérol et de sphingomyélines forme des régions plus rigides en phase liquide ordonnée (Lo) dans des liposomes unilamellaires géants (GUVs) ou dans des structures lipidiques déposées [1, 30, 31]. L'étude des rafts lipidiques présente aussi un large pendant *in silico* [30, 32-34]. Cependant, aucune observation de ces rafts lipidiques dans des cellules réelles n'a été publiée à ce jour. Cette difficulté d'observation des rafts sur des membranes cellulaires est attribuée à leur temps de vie ou à leur taille qui pourraient être inférieurs dans des cellules réelles que dans les systèmes étudiés [26, 32, 35]. Bien que ces rafts n'aient pas été observés, l'influence du cholestérol et des microdomaines riches en cholestérol sur la rigidité de la membrane, sur sa perméabilité et sur le fonctionnement des protéines membranaires est d'un grand intérêt [36-39].

En dehors des aspects liés à la composition des membranes plasmiques, un aspect mécanique a retenu notre attention. La courbure des membranes joue un rôle important au sein d'une grande variété de processus cellulaires [24, 40]. La formation de la courbure à la surface des membranes plasmiques résulte d'une compétition entre la courbure intrinsèque due à la géométrie des lipides et les influences conjointes des protéines membranaires et du cytosquelette. Dans les cellules eucaryotes, les domaines Bin/Amphiphysin/Rvs (BAR) [41] sont connus pour leur capacité à former des assemblages en trois dimensions qui altèrent les propriétés mécaniques de la membranes et induisent des courbures très importantes. Sous l'effet de la courbure induite par des protéines ou par le cytosquelette, la matrice lipidique doit se réorganiser lorsque sa courbure se voit modifiée. Peu d'études sur la réorganisation et la redistribution des lipides dans ces conditions ont été menées alors que ces effets induisant des changements locaux de la composition de la membrane sont connus pour avoir des conséquences importantes pour un grand nombre de pathologies telles que le cancer [42], la maladie d'Alzheimer [43] ou l'obésité [44]. La courbure est susceptible d'influencer ainsi la distribution en cholestérol dans la membrane, l'épaisseur de ses monocouches, le paramètre d'ordre des chaînes aliphatiques des acides gras des lipides et ainsi d'exercer un rôle important sur la diffusion de petites molécules ou de médicaments. Enfin, de récentes études ont corrélé la rugosité de la membrane plasmique au caractère cancéreux des cellules [45]. L'imagerie par force atomique montre de réelles différences entre l'état de surface de lignées cancéreuses et celle de cellules saines associées comme c'est le cas entre la lignée MCF7A de cellules tumorales mammaires en comparaison aux cellules non tumorales MCF10A [46, 47]. On peut ainsi supposer que les membranes de certaines lignées cancéreuses présentent une fonction de distribution des courbures locales bien plus large que ce l'on trouverait sur des membranes de cellules saines correspondantes. Cette distribution est aussi potentiellement décalée vers des courbures plus importantes. Ces hypothèses doivent être explorées pour déterminer si la courbure membranaire joue un rôle dans la cinétique du transport de médicaments vers le cytoplasme.

2. Vers des modèles numériques de la membrane plasmique

L'augmentation des ressources informatiques a permis un développement rapide des méthodes numériques de modélisation de membranes aussi bien en dynamique moléculaire tout-atome que gros grains [19, 48-53]. En particulier, de récentes études s'intéressent à l'hétérogénéité latérale des membranes (rafts et micro-domaines lipidiques) [48, 49] ou à la composition asymétrique en lipides et en cholestérol des monocouches lipidiques [29]. Bien que de plus en plus d'études numériques proposent des modèles membranaires prenant en compte la distribution asymétrique des lipides [50-52, 54], peu de travaux sont dédiés à l'étude de la perméation de molécules d'intérêt biologique au sein de modèles réalistes de la matrice lipidique des membranes plasmiques.

Les échelles de temps et de longueur liés au processus de diffusion passive font des simulations numériques une des meilleurs techniques, complémentaires aux expériences *in vitro,* permettant d'accéder à une échelle atomique. Avec le développement de simulations de dynamique moléculaire gros grains, utilisant en particulier le champ de force MARTINI [55-58], la tendance a été de s'éloigner des simulations tout-atome dans le domaine de la modélisation des membranes. Les modèles gros grains permettent un accroissement de plusieurs ordres de grandeurs de la taille et des temps caractéristiques accessibles. Ce type de simulations de dynamique moléculaire consiste à regrouper plusieurs atomes adjacents sous la forme de *grains* qui interagissent les uns avec les autres par le biais de potentiels empiriques. Comme le nombre de grains est nettement inférieur au nombre réel d'atomes contenus dans le système, cette simplification permet d'intégrer plus rapidement la trajectoire classique des molécules [55-58]. En particulier, les méthodes gros grains ont permis la création de modèles membranaires réalistes incluant une grande complexité dans la composition des systèmes [51]. Cependant, cette dernière étude était focalisée sur une membrane plane. Malgré les progrès importants dans le domaine de la dynamique gros grain, il est toujours nécessaire de recourir à des simulations tout-atome pour assurer une précision suffisante lors de l'étude de certains phénomènes tels que l'études des interactions entre des petites molécules ou des médicaments et des membranes lipidiques. La précision atomique permet de prendre en compte finement les effets de courbure et d'asymétrie à la fois sur la membrane lipidique elle-même et sur de potentielles molécules diffusant passivement.

Dans les paragraphes suivant, nous présentons des modèles de membranes lipidiques de cellules saines et cancéreuses et le protocole utilisé pour contrôler leur courbure. Ces modèles ont été réalisés avec l'aide de S. Yesylevskyy et reprennent les différentes propriétés des membranes détaillées précédemment.

2.1. De la composition des membranes plasmiques aux modèles

Au cours de ce travail, nous avons réalisé deux modèles distincts utilisant le même protocole et destinés à modéliser, d'une part, la matrice lipidique d'une membrane saine et d'autre part celle d'une membrane cancéreuse surexposant PS et PE sur sa monocouche extracellulaire. Le premier modèle que l'on qualifiera de *normal* est basé sur la lipidomique bien connue d'un érythrocyte de mammifère [59]. Le phosphatidylinositol, en concentration minoritaire, n'a pas été inclus dans notre système modèle. Le second modèle, qualifié de *cancéreux* fait intervenir des proportions de PS et de PE accrues dans la monocouche extracellulaire. La Figure I-1 donne une représentation schématique des deux modèles lipidiques et inclue les compositions lipidiques de ces modèles en les comparant avec les ressources présentes dans la littérature.

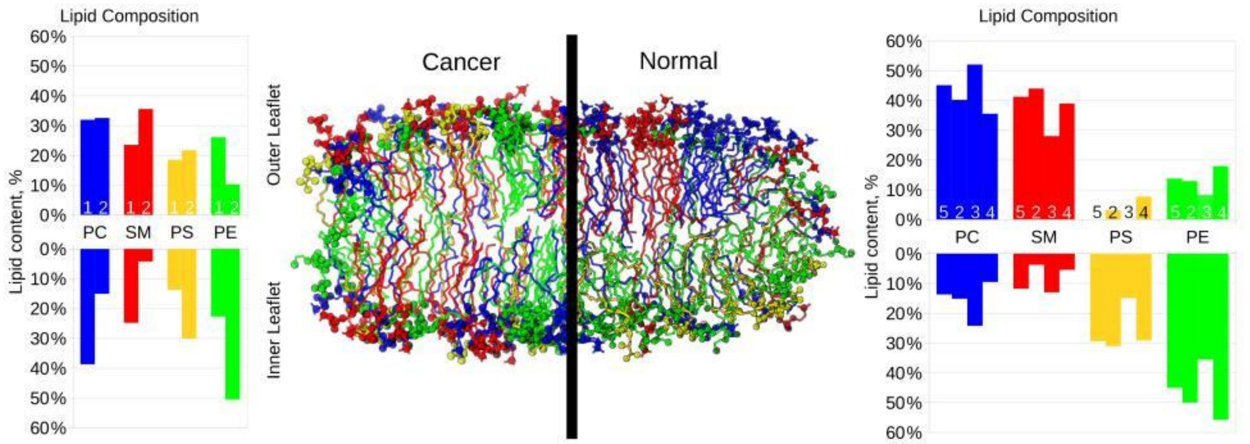

Figure I-1. Image des systèmes modélisés représentant la matrice lipidique de membranes saine et cancéreuse. Le PC est représenté en bleu, SM en rouge, PS en jaune et PE en vert. Pour plus de clareté, le cholestérol n'a pas été représenté sur l'image. Les têtes lipidiques sont représentées sous forme de sphères. Les histogrammes montrent l'abondance (normalisée pour chaque monocouche) relative des différentes espèces de lipides. Les chiffres 1 et 5 correspondent aux modèles présentés dans ce travail, le modèle 2 reprend le travail de Klähn et Zacharias [19], le modèle 3 celui de Ingólfsson *et al.* [50], le modèle 4 rapporte les données présentées par Marquardt *et al.* [24].

La bicouche lipidique initiale possède 33% mol de cholestérol. Nous avons aussi construit deux autres systèmes ; l'un étant complètement déplété du cholestérol et le second possédant 15% de cholestérol. Le système initial possède 102 lipides et 51 molécules de cholestérol dans chaque monocouche. Un système de référence composé uniquement de DOPC et utilisant le même protocole a aussi été créé. Il s'agit d'une membrane contenant 288 lipides.

2.2. Aspects techniques

La première étape dans la construction des modèles de membranes a été la construction d'un modèle plan et asymétrique pouvant être courbé à souhait par la suite. Le modèle a été préparé sous la forme d'une bicelle ; *i.e.* une bicouche lipidique dont au moins l'un des deux axes longitudinaux n'est pas infini, limitée par des coiffes cylindrinques dans le plan xz et formant une bicouche infinie (par effet de périodicité) le long de l'axe y (voir la Figure I-2 et la Figure I-3). Cette topologie permet aux monocouches lipidiques de s'équilibrer correctement en vue d'obtenir une aire par lipide réaliste par le biais d'échanges de lipides entre les monocouches et les coiffes qui jouent le rôle de réservoirs. Ces coiffes jouent un rôle extrêmement important, en particulier quand une courbure non nulle de la membrane sera imposée. En effet, la courbure impose un changement différentiel de l'aire des monocouches, imposant ainsi une redistribution des lipides en réaction à cette contrainte mécanique.

De sorte à conserver la structure potentiellement asymétrique de la membrane, il est fait l'usage d'un potentiel répulsif sélectif au niveau des coiffes lipidiques de sorte à ne pas autoriser d'échanges de lipides entre les deux monocouches [60-62]. Ainsi, tous les atomes des lipides à l'exception des atomes d'hydrogène et de l'extrémité des chaînes d'acides gras se sont vus attribuer un potentiel répulsif de type van der Waals (σ=0.8 nm, $\varepsilon=1\cdot10^{-7}$ J·mol^{-1}) agissant entre les atomes des lipides de la monocouche externe et ceux de la monocouche interne. Cela permet aux chaînes d'acides gras de conserver une interaction réaliste au sein de la bicouche tout en rendant le contact entre les lipides de différentes couches énergétiquement défavorable au niveau de la coiffe lipidique.

À contrario des lipides, le cholestérol est autorisé à se redistribuer librement au sein de la bicelle, y compris par le biais des coiffes lipidiques. Cet élément est important car la distribution du cholestérol au sein des deux monocouches n'est à priori pas connue. Le fait d'autoriser une redistribution du cholestérol par flip-flop ainsi que par le biais des coiffes permet de favoriser l'échanges de ces molécules et ainsi l'accès rapide à un état d'équilibre.

Ce protocole implique que seul le centre de la bicouche, suffisamment éloigné des coiffes lipidiques, puisse être analysé pour déterminer les propriétés de la membrane ou son interaction avec d'autres molécules (zone encadrée sur la Figure I-2).

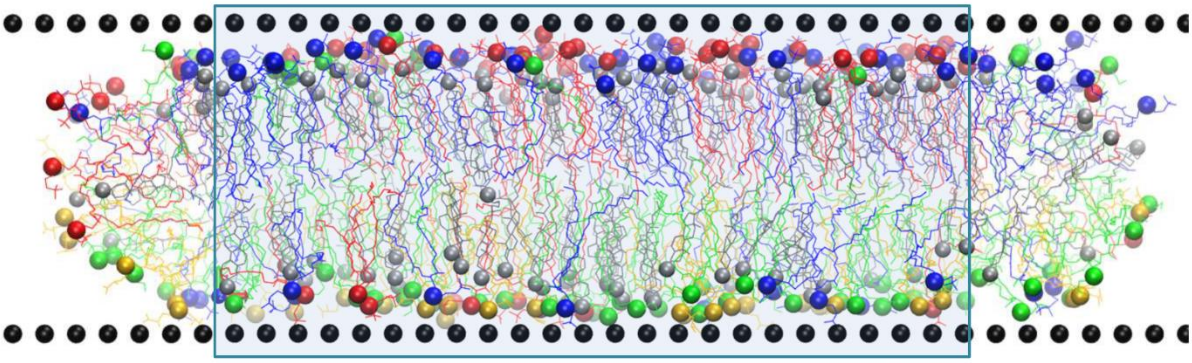

Figure I-2. Image du modèle de membrane “normale”. Les particules virtuelles du *mur* sont représentées sous la forme de sphères noires, le PC en bleu, SM en rouge, PE en vert et PS en jaune. Les molécules de cholestérol sont en gris. Les têtes lipidiques sont représentées sous la forme de sphères. La région centrale de la bicelle, utilisée lors des analyses des simulations, est encadrée.

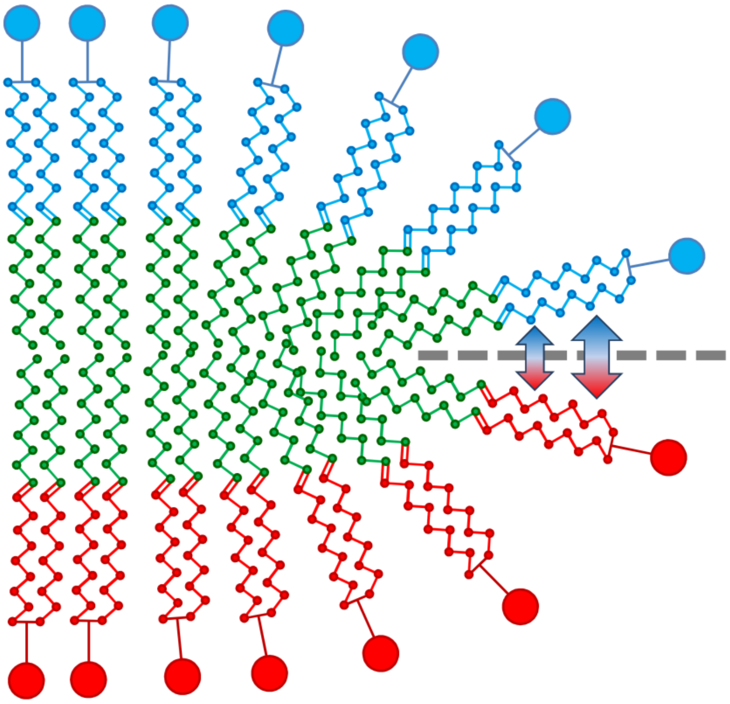

Figure I-3. Schéma d’une coiffe de la bicelle permettant de prévenir la symétrisation de la membrane. Les parties inférieures à la double liaison de l’acide oléique et qui interagissent normalement sont montrées en vert. Les têtes lipidiques et les parties supérieure à l’insaturation des acides oléiques sont montrés en bleu et en rouge selon la monocouche considérée. Une interaction fictive entre ces parties des lipides a été ajouté dans notre modèle, entre les lipides des différentes monocouches. Elle prend la forme d’un potentiel de Lennard-Jones et permet de prévenir la diffusion de lipides au niveau de la coiffe, qui induirait une symétrisation de la membrane.

Lors de ce travail, nous avons restreint l’étude de la courbure à un cas simplifié où notre système ne peut-être courbé que selon le plan xz. Pour contraindre la courbure du modèle membranaire, nous avons introduit un maillage de particules virtuelles qui se présente sous la forme de deux murs de particules formant chacun un réseau parallèle aux surfaces des monocouches de la membrane. Chaque particule virtuelle est composée d'une ancre fixe liée par le biais d'un potentiel harmonique (interaction de type liée) de longueur nulle et de constante de force valant 10 kJ·mol·nm^{-2} à une seconde particule virtuelle interagissant sélectivement avec la membrane. Cette dernière interaction prend la forme d'un potentiel de Lennard-Jones (σ=0.85 nm et $\varepsilon=1\cdot10^{-5}$ J·mol^{-1}) présent entre ces particules virtuelles et les atomes de carbone des chaînes aliphatiques des lipides. Le choix d'une distance maximale de prise en compte des interactions (*cutoff*) de 0.8 nm implique que ce potentiel n'induira que des interactions répulsives avec les lipides. Ce protocole permet d'éviter un lien direct avec les ancres fixées dans la boîte de simulation. De plus, l'interaction sélective avec une partie seulement des lipides de la membrane laisse la possibilité aux têtes lipidiques de s'organiser de manière réaliste.

Les murs de particules virtuelles sont distants de 5 nm l'un de l'autre et le maillage de particules virtuelles est initialement créé sous la forme d'une grille de ~0,51 nm de côté. Ce maillage de particules virtuelles, s'il contraint le cœur de la membrane, n'empêche en rien les lipides de diffuser latéralement et il ne perturbe pas non plus le mouvement des ions, du solvant ou des molécules de cholestérol.

La procédure visant à courber la membrane utilise au départ une bicelle plane et équilibrée, en présence des murs de particules virtuelles. Dans la version actuelle du protocole, la membrane est progressivement courbée en ajustant la position des particules virtuelles graduellement jusqu'à l'obtention de la courbure souhaitée. À titre d'exemple, de sorte à obtenir les modèles de membranes courbes utilisés lors de ce travail, présentant une courbure moyenne c=±0,2 nm^{-1}, trois courbures intermédiaires ont été obtenues (c=±0,05 nm^{-1}, c=±0,1 nm^{-1}, c=±0,15 nm^{-1}) et chacun de ces systèmes a été équilibré au moins pendant 200 ns. Pour les modèles de membranes asymétrique, comme le modèle dit *normal*, le sens selon lequel la membrane est courbée importe. Dans ce cas, deux membranes courbes ont été produites, l'une courbée positivement et l'autre négativement. Par convention, nos modèles de membranes présentent la monocouche externe pour des valeurs de z supérieures à la monocouche interne. Ainsi, une courbure positive implique que la monocouche interne soit convexe.

2.3. Estimation du biais dû au protocole utilisé

La première étape, avant d'utiliser le protocole décrit précédemment est de caractériser le biais induit, en particulier par la présence des particules virtuelles. Pour ce faire, nous avons comparé le profil de densité du modèle de bicelle normale avec un modèle de composition similaire sous forme de bicouche infinie. Nous avons aussi réalisé cette comparaison avec des systèmes composés de PC uniquement. Après équilibration des différents systèmes, nous avons analysé les dernières 50 ns de la trajectoire de nos simulations (Figure I-4).

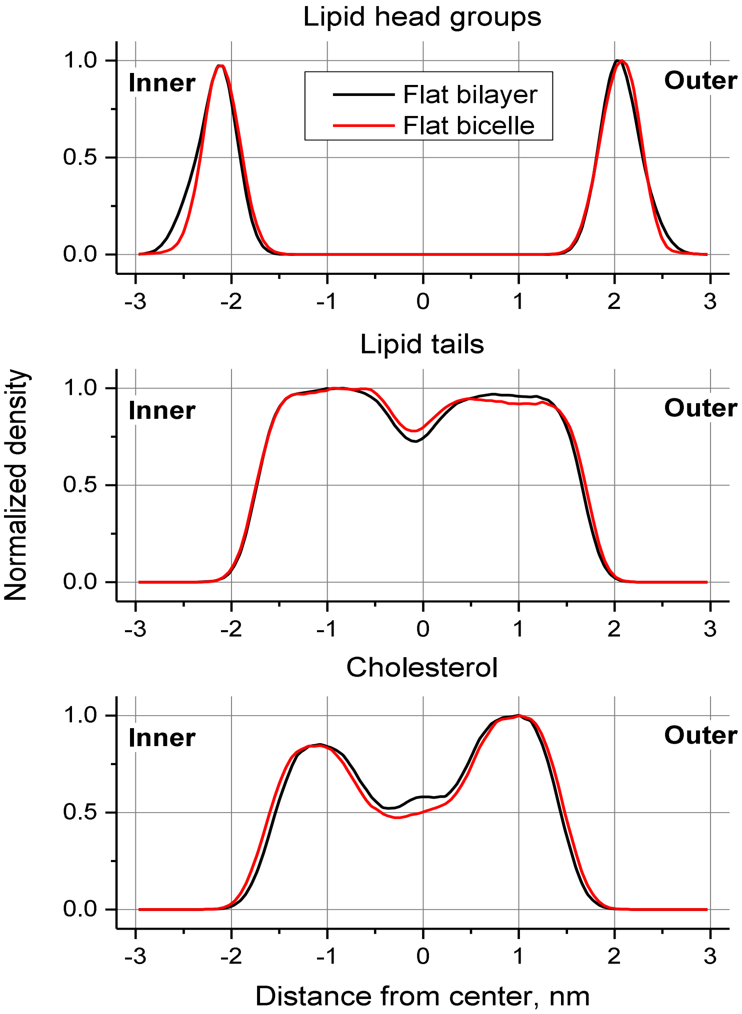

Figure I-4. Profil de densité normalisé des têtes lipidiques, des queues lipidiques et du cholestérol dans le modèle normal sous forme de bicelle utilisant le protocole de courbure et sous forme de bicouche non contrainte.

Il est clairement visible que l'influence des murs sur la distribution des lipides est mineure. Les murs ont une légère tendance à éliminer les têtes lipidiques les plus éloignées du centre de la bicelle mais ils ne modifient pas le centre de leur distribution (position des pics extrêmes) pour l'une ou l'autre des monocouches. La distribution des chaînes d'acides gras est très similaire dans les cas de la bicelle et de la bicouche à l'exception d'une différence mineure au niveau du cœur même des membranes. La distribution en cholestérol n'est elle aussi affectée que marginalement induisant un très léger élargissement de sa distribution. Ainsi, nous pouvons supposer que l'influence du protocole sur l'organisation du modèle de membrane reste très faible dans le cas de membranes planes. Nous ne pouvons que supposer que ces effets ne sont pas plus importants pour des membranes courbes du fait de l'absence de modèles de références courbes utilisables à titre de comparaison.

2.4. Effets de la courbure sur les propriétés des membranes

De sorte à analyser les effets de la courbure sur les propriétés des membranes, nous avons réalisé trois systèmes modèles basés sur la membrane *normale*. L'un est plan et les deux autres sont courbés positivement et négativement avec une courbure moyenne c=±0,2 nm^{-1}.

2.4.1.Influence de la courbure sur l'aire par lipide

L'aire par lipide est l'une des propriétés les plus étudiées concernant l'organisation des membranes lipidiques. Il est connu que l'aire par lipide dépend de la composition de la membrane à la fois en terme de lipidomique mais aussi en ce qui concerne la proportion de cholestérol ainsi que la présence contraintes mécaniques appliquées à la membranes (par le biais de protéines par exemple). L'aire par lipide a été calculée par le biais d'un diagramme de Voronoï [63]. La position de chaque tête de lipide a été estimée sur un plan tangent à la membrane. L'aire de chaque polygone de Voronoï a ainsi été déterminé sur ce plan. Cette technique permet d'obtenir une estimation précise de l'aire de chaque type de lipide, respectivement dans la monocouche extracellulaire et dans la monocouche intracellulaire. La Figure I-5 présente les résultats ainsi calculés. Tous les types de lipides suivent une même tendance selon laquelle leur aire par lipide est 25-35% plus faible lorsqu'ils sont présents dans la membrane convexe. Ces variations importantes peuvent être expliquées par de simples considérations géométriques. Même après une réorganisation et une rééquilibration de la membrane courbée (impliquant une diminution du nombre de lipides présents dans la membrane convexe), le stress mécanique dû à la courbure est encore bien présent et l'aire totale de la monocouche convexe ayant diminué, l'aire par lipide de chaque type de lipides présents dans cette couche diminue elle aussi. Bien entendu, l'effet est réciproque dans la monocouche concave, dont l'aire a augmenté.

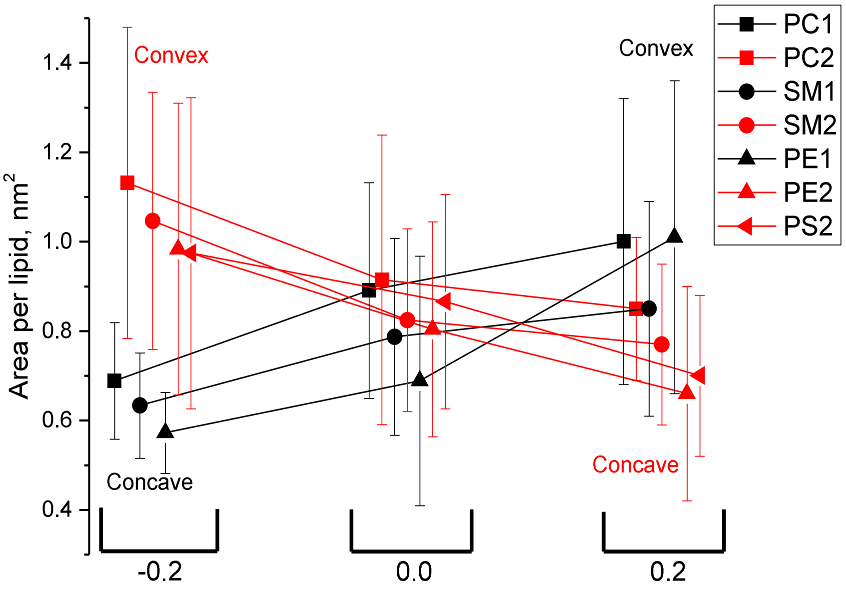

Figure I-5. Aire par lipide moyenne pour chaque type de lipides présents dans les monocouches externes et internes en fonction de la courbure de la membrane.

2.4.2.Effet de la courbure sur la distribution du cholestérol

Le cholestérol est connu pour ses propriétés dynamiques au sein de la membrane, lui permettant de diffuser latéralement, ou encore d'effectuer un flip-flop dans des temps caractéristiques de l'ordre de la centaine de nanosecondes. L'orientation du cholestérol est susceptible d'être influencée par la composition lipidique locale – en particulier par les chaînes d'acides gras qui sont en contact direct avec les molécules de cholestérol.

Nous avons étudié l'orientation des molécules de cholestérol en fonction de la courbure. La Figure I-6 montre la distribution des inclinaisons du cholestérol pour chaque monocouche lipidique pour trois valeurs de courbure dans le cas du modèle de membrane normal. Tout d'abord, ces distributions montrent deux orientations majeures du cholestérol dans la membrane : la majorité du cholestérol est intercalé entre des chaînes aliphatiques des acides gras et se trouve être presque parallèle à la normale de la membrane, une plus faible proportion du cholestérol est située au niveau du cœur de la membrane et est orientée perpendiculairement à la normale de la membrane. Il est intéressant de voir que l'orientation du cholestérol dépend fortement de la courbure de la membrane. L'inclinaison du cholestérol est systématiquement plus importante pour une couche concave que pour une couche plane, pour laquelle elle est de même plus importante que pour une couche convexe. Cette effet est toutefois asymétrique, puisque l'inclinaison est plus prononcée dans le cas de la monocouche interne. Cette asymétrie pourrait être attribué à la présence de SM dont l'affinité avec le cholestérol pourrait contribuer à le maintenir davantage aligné avec la normale à la membrane.

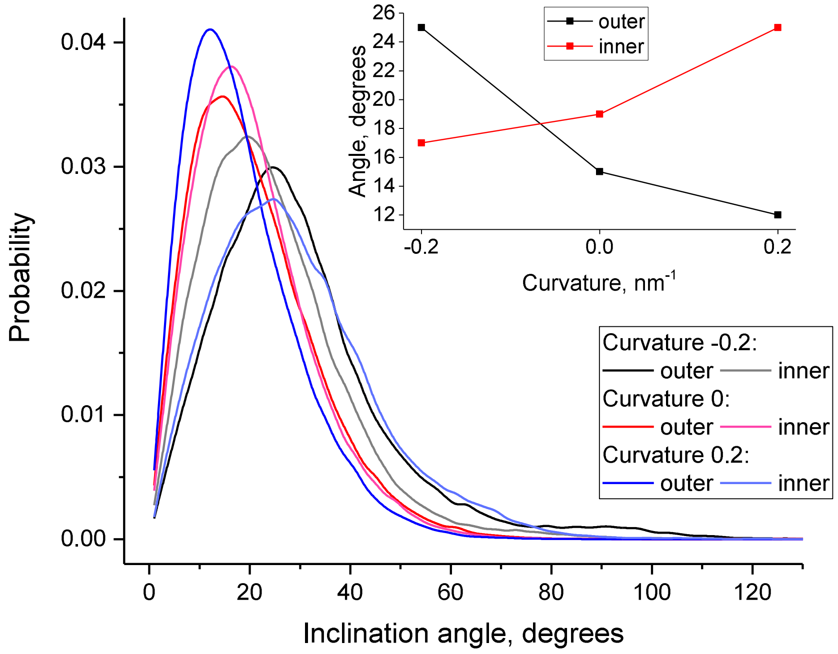

Figure I-6. Distribution des angles moyens du cholestérol avec la normale à la membrane pour chaque monocouches (interne et externe) et pour différentes courbures de la membrane. L'angle est calculé entre la normale locale à la membrane définie par rapport à la position du groupement OH du cholestérol et un vecteur calculé entre un atome de carbone en queue du cholestérol et le même groupement OH. L'encart montre l'angle le plus probable du cholestérol pour les monocouches interne et externe en fonction de la courbure.

2.4.3.Influence de la courbure sur le profil en densité

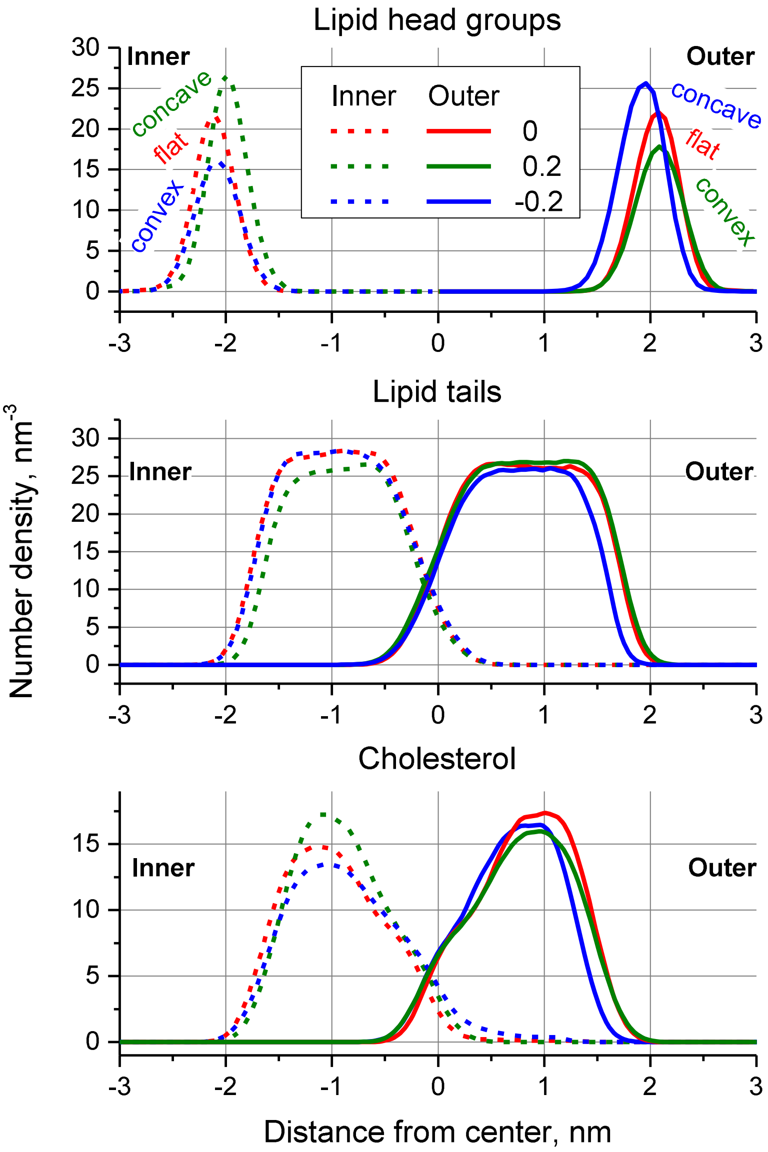

Figure I-7. Profil de densité des têtes lipidiques, des acides gras et du cholestérol pour les monocouches interne et externe, pour différentes courbures de la bicelle.

Le profil de densité pour les différents groupes lipidiques a été calculé pour les trois courbures étudiées. La Figure I-7 montre ces résultats pour les têtes lipidiques, les acides gras et le cholestérol. L'un des principaux effets de la courbure est une diminution de la densité des têtes lipidiques de la monocouche convexe et une augmentation correspondante de celle de la monocouche concave. Le second effet systématique, signe d'une empreinte importante de la courbure sur la structuration de la membrane, est une diminution de l'épaisseur de la monocouche concave de ~1,3 Å alors que l'épaisseur de la monocouche convexe ne voit pas son épaisseur varier.

2.4.4.Effet de la courbure sur l'arrangement dynamique des chaînes d'acide gras

Le paramètre d'ordre des lipides est un critère important caractérisant l'organisation des lipides dans la membrane. Il montre l'orientation et l'ordre global des chaînes aliphatiques des queues lipidiques en fonction de leur profondeur dans la membrane. Le paramètre d'ordre de membranes planes peut être déterminé expérimentalement ce qui permet une comparaison directe avec les résultats issus de simulations. Toutefois, à l'heure actuelle, la simulation numérique reste le seul moyen d'obtenir une estimation du paramètre d'ordre pour une courbure donnée.

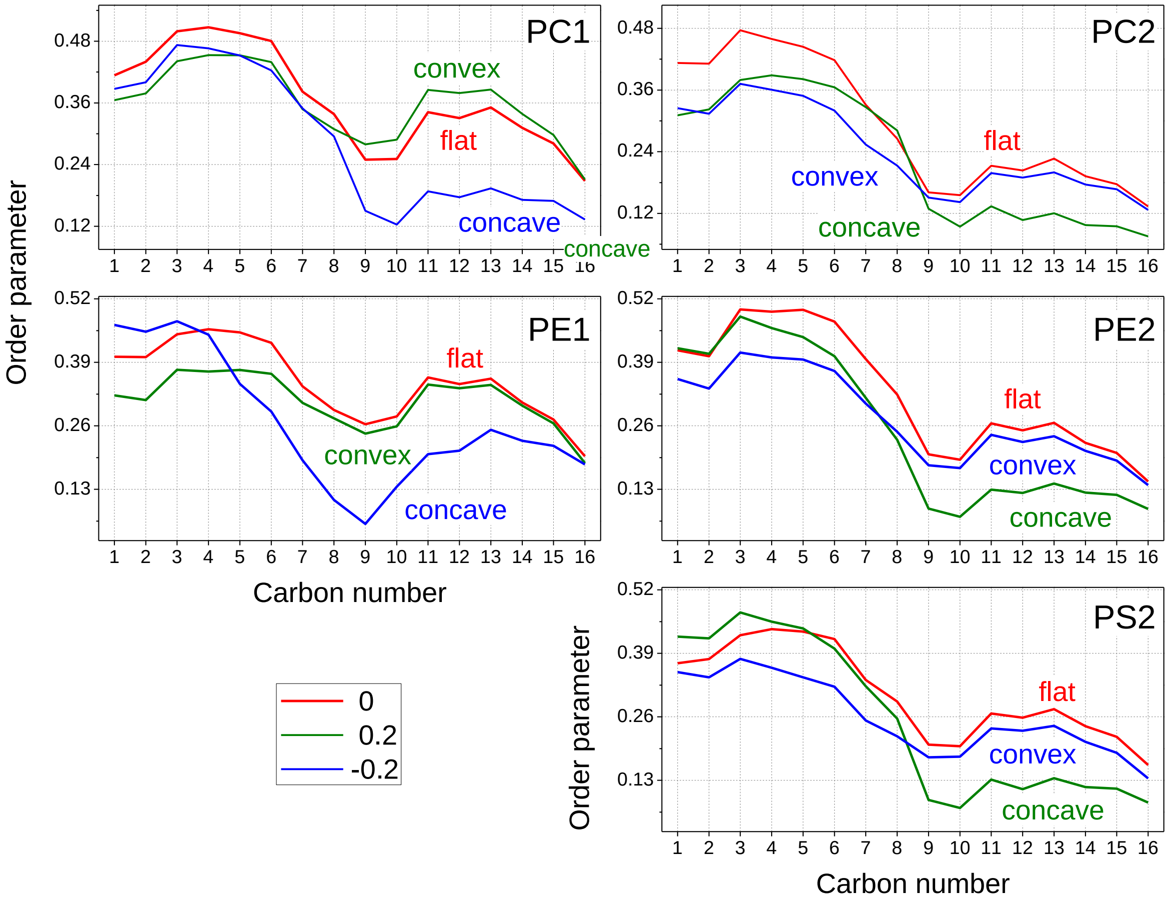

Figure I-8. Paramètre d'ordre des chaînes d'acide gras pour chaque type de phospholipide étudié pour les monocouches interne et externe et pour différentes courbures. Les sous-figures indiquent le type de phospholipide (PC, PE ou PS) suivi de l'identification de la monocouche considérée : 1. monocouche internet et 2. monocouche externe.

La Figure I-8 montre les valeurs du paramètre d'ordre pour les différents types de phospholipides, pour chaque monocouche et pour différentes courbures du modèle de membrane normal. Dans le cas des monocouches concaves, il est clair que le paramètre d'ordre est drastiquement diminué à partir de la double liaison présente sur les acides oléiques des lipides. Cet effet pourrait être relié à l'augmentation de la densité de lipides sur les monocouches concaves du fait de la diminution du volume accessible : le volume accessible diminuant, les chaînes d'acides gras se réorganisent pour occuper l'espace présent, cette réorganisation diminuant leur ordre.

2.5. Effets du cholestérol sur les propriétés des membranes

De sorte à analyser les effets du cholestérol sur les propriétés des membranes, nous avons utilisé les systèmes modèles plans pour lesquels nous voulions analyser les propriétés de perméation des sels de platine par la suite. Ces modèles incluent une bicelle de DOPC pur, le modèle normal avec 33% mol de cholestérol, deux variantes déplétées respectivement à 15 % et à 0 % de cholestérol et le modèle cancéreux.

2.5.1.Profil de densité

Nous avons calculé les profils de densité des différents modèles membranaires simulés. La Figure I-9 montre essentiellement que la quantité de cholestérol est directement et positivement reliée à l'épaisseur de la membrane. Pour chacun de nos systèmes, la distribution en cholestérol est assez symétrique à l'exception du modèle incluant 15 % de cholestérol. Le fait que le cholestérol est libre de se redistribuer dans la membrane et la faible quantité absolue de cholestérol dans ce dernier modèle pourrait expliquer ce phénomène.

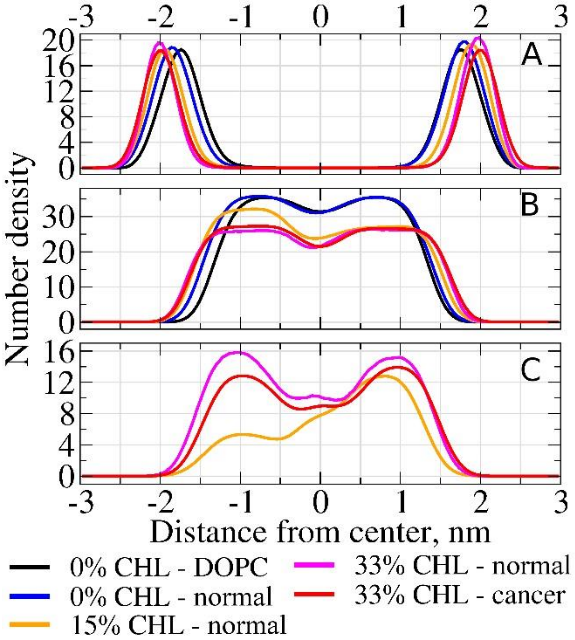

Figure I-9. Profil de densité des têtes lipidiques (A), des acides gras (B) et du cholestérol (C) pour différents modèles de membranes. La monocouche externe correspond aux distances positives depuis le centre de la membrane.

2.5.2.Paramètre d’ordre

Le paramètre d’ordre dépend nettement de la teneur en cholestérol des membranes (Figure I-10). Ce dernier augmente pour des teneurs importantes. Cela s’explique par la nature du cholestérol à se positionner entre les chaînes d’acide gras des lipides, rigidifiant ainsi la membrane.

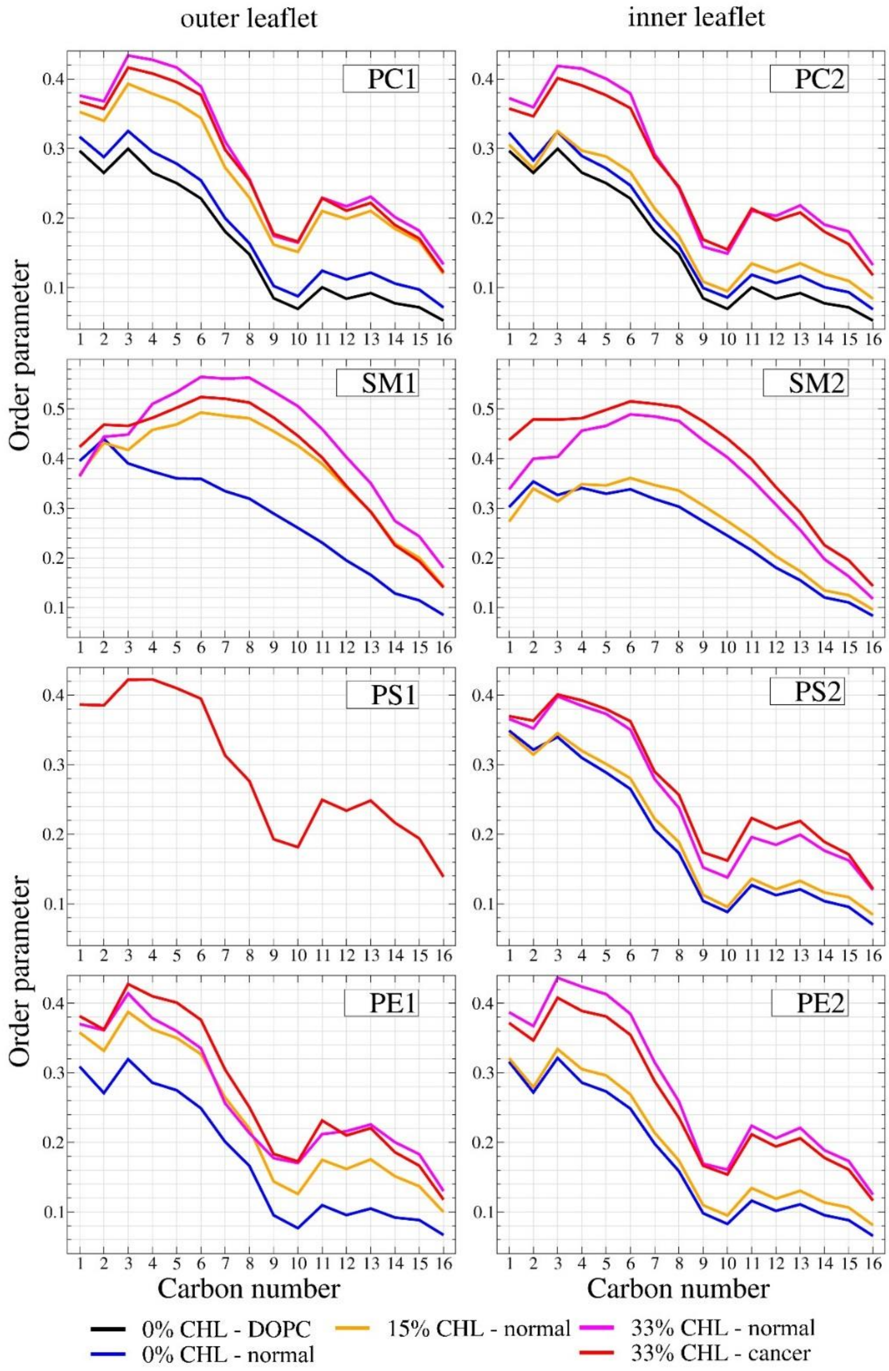

Figure I-10. Paramètre d’ordre des queues lipidiques pour les monocouches internes et externes des modèles de membranes étudiés.

En outre, le paramètre d’ordre de la membrane de DOPC pur est inférieur à celui du modèle normal sans cholestérol. Cela s’explique en particulier par la présence de SM dont les chaînes d’acides gras saturées sont plus ordonnées. Le paramètre d'ordre des sphingomyélines suit une évolution intéressante pour les différents systèmes modélisés. En effet, en dessous d'un certain seuil en cholestérol dans la monocouche, il est possible d'observer une rupture remarquable de la forme du paramètre d'ordre (SM1 à 0% et SM2 à 0% et 15%). Cette observation montre une nouvelle fois l'affinité forte entre SM et cholestérol.

2.6. Limitations et conclusions

Le présent protocole permet d'étudier à la fois les effets de différentes propriétés des membranes et, dans un second temps, l'influence de ces propriétés sur la perméation de petites molécules. Toutefois, le protocole proposé comporte diverse limitations. En premier lieu, s'il est possible de caractériser le biais induit par les murs de particules virtuelles sur les modèles de membranes planes, cela reste impossible pour les modèles courbées. Ainsi, les différentes observations sur les modèles de membranes courbes doivent être interprétées avec prudence. Une autre limitation est directement liée à la complexité induite par la présence de différents types de lipides dans la membrane et de cholestérol. Un système d'une telle complexité a peu de chance d'être réellement équilibré pour des simulations d'une durée inférieure à la microseconde. Un échantillonnage idéal devrait laisser à la possibilité aux lipides de diffuser latéralement sur toute l'extension de la bicelle ce qui prendrait plusieurs dizaines ou centaines de microsecondes de simulations. Bien entendu, en particulier dans le cadre de simulations de dynamique moléculaire tout-atome, ces temps d'intégration sont largement inaccessibles.

Néanmoins, les simulations effectuées mettent en exergue de manière explicite des propriétés différentes dues à la courbure ou à la teneur en cholestérol :

- L'épaisseur du cœur des couches concaves diminue d'environ 1,3 Å en comparaison à celle d'une couche plane.
- L'aire par lipide des couches convexes augmente alors que celle des couches concaves diminue.
- Le paramètre d'ordre des lipides diminue drastiquement dans le cœur des couches convexes.
- L'orientation du cholestérol par rapport à la normale à la membrane est plus faible pour une couche convexe que concave.
- Le cholestérol a tendance à se retrouver plus proche du cœur de la membrane lorsque celle-ci est courbée.
- La teneur en cholestérol augmente l'épaisseur de la membrane.
- Le paramètre d'ordre est plus important pour une membrane riche en cholestérol.
- L'affinité entre le cholestérol et SM se traduit par un changement de conformation des chaînes d'acides gras de SM. Ce changement est visible par une variation de son paramètre d'ordre à partir d'une certaine teneur en cholestérol.

3. Perméation dans des modèles réalistes de la matrice lipidique des membranes plasmiques

Le cisplatine, c*is*-diamminedichloroplatine(II), est l'un des agents anticancéreux les plus anciens et les plus répandus, adopté dans le traitement d'un large spectre de néoplasies solides, en particulier pour les affections cancéreuses des ovaires, des testicules, du colon, de la vessie, du cou et de la tête, des poumons et pour d'autres carcinomes, sarcomes, lymphomes ou encore des affections cancéreuses de cellules germinales [64, 65]. Dans le cas particulier des cancers des testicules, les chimiothérapies basées sur l'usage du cisplatine montrent des résultats positifs supérieurs à 90% [66]. Malgré son succès, l'action du cisplatine à l'échelle moléculaire n'est pas encore totalement comprise et de nombreuses études sont menées en vue de pallier les effets secondaires importants limitant la dose utilisée [66-68]. Une autre problématique fondamentale dans l'utilisation du cisplatine est l'existence de phénomènes innés ou acquis de résistance [67, 69] conduisant seulement 1% du cisplatine présent dans une cellule cancéreuse à interagir avec l'ADN nucléaire qui est supposé être sa principale cible [70]. Ainsi, une étude à l'échelle atomique du transport du cisplatine au niveau de la cellule est d'une importance capitale dans l'optique de développer des solutions alternatives qui n'hériteront pas des effets secondaires ou des problèmes de résistance connus du cisplatine.

Au cours de ce travail, une étude précise de la bibliographie concernant le cisplatine et ses modes d'action et de transport a été réalisée. Il est souligné que les modes d'action du cisplatine au sein de la cellule sont plus complexes que la simple chélation d'atomes d'azote au niveau de guanines de l'ADN nucléaire. En particulier, au moins deux autres chemins sont susceptibles de conduire à la mort cellulaire, incluant un stress du réticulum endoplasmique ou des dommages au niveau de l'ADN mitochondrial. La seconde complexité, rarement abordée, est celle de la chimie du cisplatine en solution. Le cisplatine natif dans un milieu biologique va se retrouver en équilibre, selon le pH du milieu et la concentration en ions chlorure, avec ses espèces filles dont l'un ou les deux groupements chloro ont été substitués par des groupements aqua ou hydroxo. Enfin, le transport du cisplatine a été un sujet à débat au sein de la communauté scientifique depuis sa mise sur le marché américain en 1978. Deux principales hypothèses ont été étudiées quant au mode de franchissement prédominant de la membrane plasmique par le cisplatine : la diffusion passive au sein de la matrice lipidique de la membrane plasmique et la diffusion active assistée, en particulier, par les canaux à cuivre hctr1. Ce travail bibliographique permet de montrer, d'une part, la prévalence du processus de diffusion passive dans le transport du cisplatine au sein de la cellule et, d'autre part, l'importance d'une description fine du milieu biologique et des différentes espèces platinées présentes en solutions.

Ainsi, plusieurs études ont été mises en œuvre pour mettre à jour une image actualisée de la diffusion passive du cisplatine au sein de la membrane. Tout d'abord, il a été montré que l'utilisation d'une composition proche de la lipidomique réelle de la membrane plasmique induit des résultats drastiquement différents que l'étude dans un modèle mono-composant simpliste (*cf.* section 3.2). Ensuite, l'influence de l'état de la membrane a été étudiée, de sorte à savoir si le transport du cisplatine était affecté par la distribution asymétrique des lipides dans la membrane plasmique (*cf.* section 3.2). Dans le même temps, l'influence de la teneur en cholestérol sur le processus de diffusion a aussi été questionnée (*cf.* section 3.2). Après ces études réalisées sur des modèles de membranes planes, une étude de l'influence de la courbure sur la diffusion du cisplatine a été menée (*cf.* section 3.3). Cette étude tend à avoir une portée plus générale que la simple analyse de la perméation du cisplatine dans des modèles de membranes courbes, et l'analyse d'autres petites molécules comme l'eau ou les ions chlorure et sodium ou celle d'un autre médicament anticancéreux (la gemcitabine) a été menée dans l'optique d'apporter plus de généralité aux résultats obtenus. Ces travaux réalisés pendant cette thèse ouvrent d'autres perspectives qui sont présentées en fin de paragraphe (*cf.* section 3.4).

De sorte à étudier la perméation de différentes espèces au sein de la matrice lipidique de la membrane plasmique, différentes observables ont été choisies. Le profil d'énergie libre est une observable de choix permettant de caractériser la barrière d'énergie nécessaire pour observer une transformation. Cette caractéristique thermodynamique est le pendant direct d'une observable mesurable expérimentalement : le coefficient de partition. Dans le cas de systèmes lipidiques, cette mesure est en quelque sorte une estimation de la lipophilicité du système. Pour donner un sens relié plus encore à la propension d'un ligand à perméer une membrane, le calcul du coefficient de perméabilité est d'un grand intérêt. Celui-ci est aussi accessible expérimentalement et se base numériquement sur la détermination combinée du coefficient de partition et du coefficient de diffusion du ligand étudié. Une rapide description du mode de calcul de ces observables est donné en section 3.1.

3.1. Le modèle de solubilité-diffusion inhomogène (ISD)

3.1.1.Le potentiel de force moyenne

De sorte à caractériser les interactions d'une molécule impliquée dans un processus physico-chimique, il est fréquent d'avoir recours à l'estimation du profil d'énergie libre le long de coordonnées de réaction **ξ**. Les coordonnées de réaction **ξ** sont une restriction pertinente des coordonnées accessibles par le système qui donnent une description satisfaisante du processus en cours.

Dans ce travail, il est essentiellement question de la perméation d'un ligand – généralement un médicament anticancéreux – au travers d'un modèle de la matrice lipidique de la membrane plasmique. Selon l'ensemble thermodynamique utilisé, deux définitions de l'énergie libre sont directement accessibles : l'énergie libre de Helmotz, F, associée à une mesure dans l'ensemble canonique et l'énergie libre de Gibbs, G, associée à une mesure dans l'ensemble isotherme-isobare. Dans les discussions suivantes, nous nous permettrons de parler abusivement d'énergie libre sans préciser s'il est question de F ou de G. La différence entre ces deux observables provient d'un terme de forme $P{\cdot}V$ où P est la pression et V le volume du système, terme qui est généralement considéré comme faible pour les systèmes à l'état liquide.

La meilleure estimation du profil d'énergie libre en fonction des coordonnées de réaction, en simulations de dynamique moléculaire, est dénommée potentielle de force moyenne (PMF). La principale difficulté dans le calcul du PMF est la faible probabilité du sous-système considéré à échantillonner correctement l'espace des phases sur toutes les coordonnées de réaction en un temps d'intégration limité. En effet, certaines des conformations le long des coordonnées de réaction sont notoirement défavorables (*i.e.* le cœur d'une membrane lipidique pour un composé lipophobe). L'une des méthodes les plus utilisées à l'heure actuelle pour outrepasser cette difficulté est celle de « l'*umbrella sampling* » (échantillonnage parapluie).

Pour simplifier la description de cette méthode, considérons un système type que nous allons étudier : il s'agit d'une membrane lipidique au travers de laquelle le ligand va perméer, suivant généralement la direction normale au plan de la membrane, notée z. La méthode consiste ainsi à diviser l'unique coordonnée de réaction, c'est-à-dire l'axe z, en plusieurs intervalles et d'explorer séparément chaque intervalle. Pour ce faire, un potentiel dit de biais w(z) est appliqué et s'ajoute à l'énergie potentielle totale du système. Celui-ci prend généralement la forme d'un potentiel harmonique centré au milieu de l'intervalle considéré (généralement ces intervalles sont nommés *fenêtres*) et contraignant le ligand dans la zone souhaitée. Formellement, l'énergie libre du ligand est reliée à la probabilité $P^l(z)$ de trouver ce ligand dans un état correspondant à une valeur de z :

$$P^l(z) = \lim_{t\to\infty} \frac{1}{t} \int_0^t \delta\big(z - z(t)\big)dt = \rho(z) = \frac{\int e^{-\frac{V(\mathbf{r})}{k_B T}} \delta\big(z - z(\mathbf{r})\big)d\mathbf{r}}{\int e^{-\frac{V(\mathbf{r})}{k_B T}} d\mathbf{r}}. \quad \text{(I-1)}$$

Dans le cas de la technique d'*umbrella sampling*, le potentiel de biais rentre dans l'expression (I-1) tel que :

$$P_b^l(z) = \frac{\int e^{-\frac{V(\mathbf{r})+w(z)}{k_B T}} \delta\big(z - z(\mathbf{r})\big)d\mathbf{r}}{\int e^{-\frac{V(\mathbf{r})+w(z)}{k_B T}} d\mathbf{r}}. \quad \text{(I-2)}$$

Finalement, l'expression de l'énergie libre peut être établie comme étant :

$$F(z) = -k_B \ln\big(P_b(z)\big) - w(z) - k_B \ln\left(\left\langle e^{-\frac{w(z)}{k_B T}} \right\rangle_0\right), \quad \text{(I-3)}$$

où $\langle \dots \rangle_0$ est la moyenne d'ensemble dans l'ensemble canonique pour le système non biaisé.

La méthode la plus utilisée afin d'obtenir un profil d'énergie libre précis consiste à ne pas utiliser une seule fenêtre de simulation pour une valeur particulière de la coordonnée de réaction, mais plusieurs d'entre elles. Cela permet d'améliorer l'échantillonnage obtenu pour une fenêtre donnée. Pour ce faire, la méthode d'analyse pondérée de l'histogramme (WHAM) est l'une des plus utilisées. L'idée est de reconstruire la distribution de probabilité sur tout l'intervalle considéré le long de la coordonnée de réaction sous la forme d'une somme pondérée des distributions de probabilité obtenues pour chaque fenêtre P_i^l :

$$P^l(z) \propto \sum_{i=1}^{N_w} \alpha_i(z) \cdot P_i^l(z). \tag{I-4}$$

Les poids $\alpha_i(z)$ sont déterminés de sorte à minimiser la variance de la distribution de probabilité par le biais d'une méthode auto-consistante utilisant généralement les multiplicateurs de Lagrange [71].

3.1.2.Le modèle ISD

Le modèle de solubilité-diffusion inhomogène (ISD) permet d'obtenir une estimation du coefficient de perméabilité d'une membrane envers un ligand en prenant en compte l'hétérogénéité transversale de la membrane. Ce modèle se base sur la règle de Meyer-Overton qui lie la perméabilité P au coefficient de partition membrane/solvant K, au coefficient de diffusion D et à l'épaisseur de la membrane d :

$$P = \frac{K \cdot D}{d}. \tag{I-5}$$

Cette règle considère le milieu membranaire comme étant homogène dans toute son épaisseur. Il est connu que cette approximation est bien trop importante pour donner une estimation réaliste du coefficient de perméabilité. Ainsi, une forme intégrale dépendant de la position z a été proposée permettant d'avoir accès à la perméabilité P(z) et à la résistance R(z) locales:

$$P(z) = \frac{1}{R(z)} = \left[e^{\frac{W(z)}{kT}} / D(z)\right]^{-1}. \tag{I-6}$$

C'est cette définition du coefficient de perméabilité qui a été utilisée lors de nos calculs. Il est discuté plus en détail, dans le corps du manuscrit des limites de cette méthode de calcul associées en particulier à la détermination précise du coefficient de diffusion local D(z).

3.2. La perméation du cisplatine dans des membranes planes

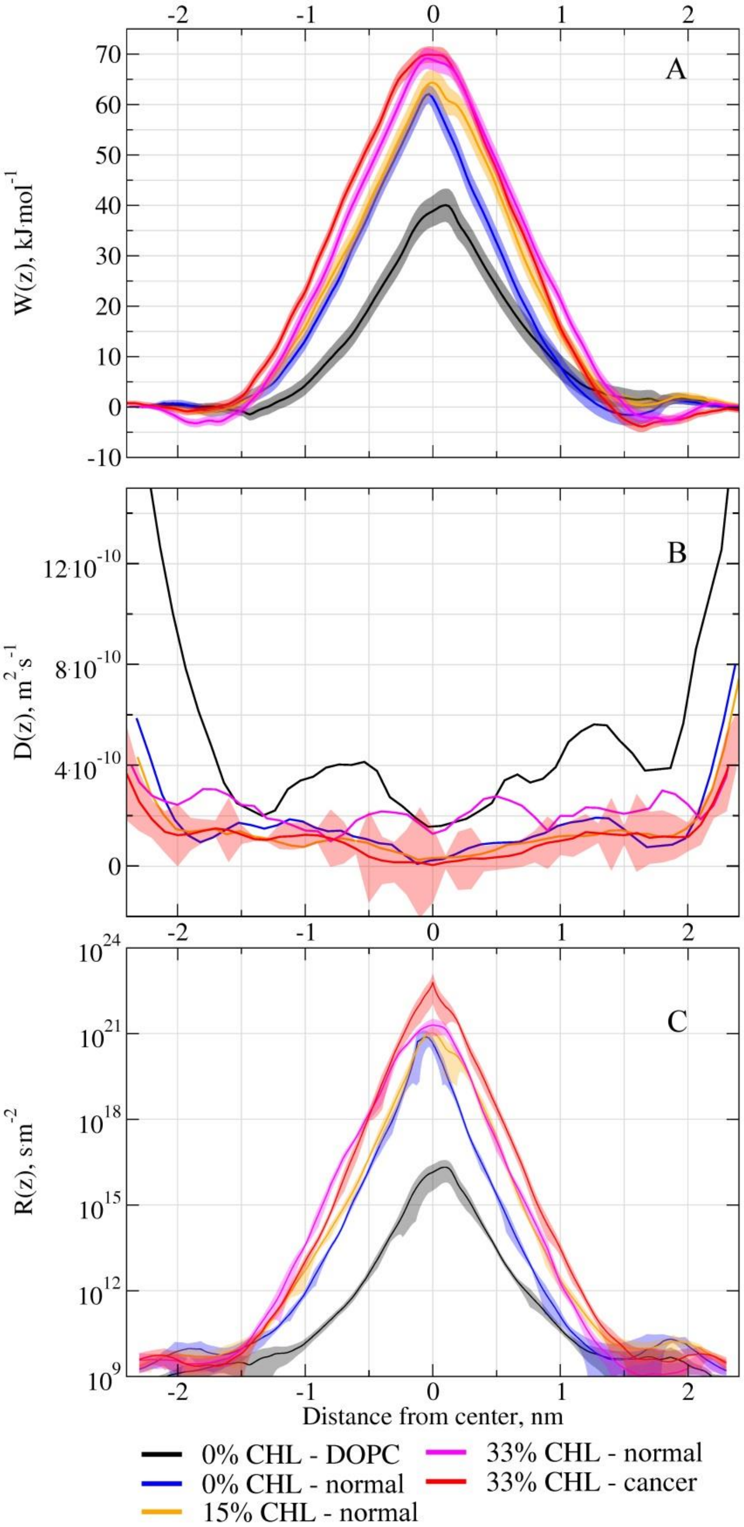

Figure I-11. (A) PMFs du cisplatine, W(z) ; (B) coefficient de diffusion local, D(z) ; et (C) résistance locale R(z) pour différents systèmes.

La Figure I-11 montre les résultats des calculs du PMF et des coefficients de diffusion et de résistance pour les modèles de membranes étudiés. Le cisplatine étant connu pour être une espèce lipophobe, il est normal d'observer une barrière de potentiel importante centrée au centre de la membrane. La principale différence que l'on peut constater est le grande écart entre les modèles pluri- et le modèle mono-composant pour lequel la perméation est bien plus favorable. L'effet de la teneur en cholestérol est lui aussi très marqué, et l'on constate que la rigidification de la membrane sous l'effet d'une quantité de cholestérol accrue va de paire avec une augmentation de la résistance à la perméation. Enfin, et de manière surprenante, la surexposition de PE et PS dans la couche extracellulaire a pour effet de diminuer la perméabilité du cisplatine. Les calculs des coefficients de perméabilité intégrés sur toute l'extension de la membrane ont été réalisés et reporté dans la Table I-1 où ils sont comparés avec les résultats issus de la littérature.

Table I-1. Valeurs du coefficient de perméabilité global pour les systèmes étudiés comparés à des valeurs extraites de la littérature.

Author	System	Permeability
---	---	$P, m \cdot s^{-1}$
Présent travail	DOPC (0% CHL)	$2.2 \pm 0.05 \cdot 10^{-7}$
	Normal (0% CHL)	$8.7 \pm 0.3 \cdot 10^{-12}$
	Normal (15% CHL)	$4.8 \pm 0.1 \cdot 10^{-12}$
	Normal (33% CHL)	$1.74 \pm 0.03 \cdot 10^{-12}$
	Cancer (33% CHL)	$1.59 \pm 0.06 \cdot 10^{-13}$
Nierwzicki *et al.*[72]	DMPC bilayer (simulations)	$6.67\ 10^{-7}$
Eljack *et al.[73]*	Vésicules de DOPC ($[Cl^{-}] = 150$ mM)	$1.06\ 10^{-8}$
	Vésicules de DOPC ($[Cl^{-}] = 10$ mM)	$8.93\ 10^{-10}$
El-Kareh *et al.[74]*	Cellules ovariennes résistantes A2780/CP3	$1.87\ 10^{-9}$
	Carcinome du colon COLO 205	$1.24\ 10^{-9}$
	Cellules ovariennes de type sauvage A2780	$1.21\ 10^{-9}$
	Cancer de la tête et du cou CAL 27	$1.19\ 10^{-10}$
	Cancer gastrique MKN45	$1.01\ 10^{-10}$
	Cancer gastrique MKN74	$4.90\ 10^{-11}$
	Mélanome C32	$4.79\ 10^{-11}$
	Mélanome G361	$2.21\ 10^{-11}$
Ghezzi *et al.[75]*	Cancer mammaire MCF-7	$6.57\ 10^{-11}$

3.3. Perméation au travers de membranes courbes

Dans le cas des membranes courbes, des calculs similaires ont été menés. Nous présentons ici les résultats pour les deux médicaments anticancéreux que sont le cisplatine et la gemcitabine (Figure I-12). Les calculs ont aussi été réalisés pour l'eau et les ions chlorure et sodium. Bien que les effets décrits ci-après présentent une intensité dépendant de l'espèce considérée, leur aspect systématique pour chacune des espèces étudiées est à prendre en considération. La Figure I-12 permet d'observer que la courbure de la membrane joue un rôle important dans la perméation des petites molécules. Dans le cas des membranes courbes, la hauteur des profils d'énergie libre et du coefficient local de résistance diminuent de manières notables et les profils sont rétrécis. Il en résulte une augmentation du coefficient de perméabilité d'un ou de deux ordres de grandeurs. Qui plus est, un décalage de la position du maximum d'énergie ou de résistance est visible et dépend de l'orientation de la courbure. Ce décalage, toujours dans le sens de la couche concave, est la signature du changement d'aire par lipide observé à la section 2.4.1.

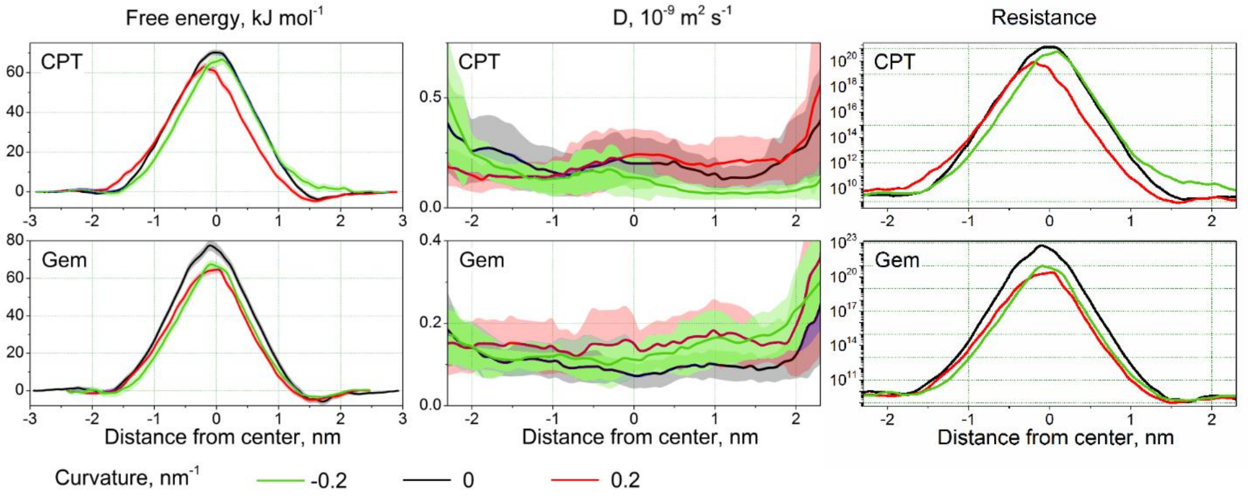

Figure I-12. PMFs, coefficient de diffusion local et résistance locale de la gemcitabine (Gem) et du cisplatine (CPT) pour différents systèmes plans et courbes.

3.4. Perspectives

3.4.1. Une image globale du cisplatine dans la cellule

Il a été mentionné précédemment que la chimie du cisplatine en solution est complexe, générant différentes espèces filles dont l'un ou les deux groupements chloro ont été substitués. Les études précédentes ont été menées principalement avec un modèle de cisplatine natif, qui est l'espèce majoritaire dans le milieu extracellulaire, où la concentration en ions chlorure est importante (~110 mM). Pour autant, de sorte à établir une image précise du processus de perméation, la prise en compte de cette chimie en solution est d'une grande importance. L'un des projets actuellement en cours consiste en la modélisation de ces espèces filles et en l'étude de leur perméation en vue de la création d'un modèle pharmacocinétique du cisplatine. Ce modèle prend en compte les conditions physiologiques de pH et de concentration en ions chlorure dans deux compartiments que sont les milieux intra- et extra-cellulaires. Les réactions de substitution sont décrites sous la forme de simples réactions de premier ordre dont les constantes cinétiques proviennent de la littérature [76]. Les processus de diffusion sont eux aussi représentés par des réactions du premier ordre et la constante cinétique est déduite à partir du coefficient de perméabilité. Enfin, certaines des réactions à l'origine de certains des phénomènes de résistance au cisplatine, en particulier avec les glutathions et les métallothionéines, sont envisagées. Les paramètres de ces dernières réactions proviennent de travaux antérieurs réalisés au sein de notre groupe [77]. Ce travail est susceptible d'offrir une meilleure image des espèces en présence à l'intérieur de la cellule et de leurs proportions en fonction de différentes conditions de pH et de concentration en ions chlorure. Cela pourra permettre, d'une part, de vérifier si la diffusion passive est bien le processus majoritaire lors de son influx et de son efflux, et, d'autre part, de mieux cerner les mécanismes de résistances reliés aux conditions physiologiques locales. La Figure I-13 donne un aperçu du modèle en cours de création. Le calcul du profil d'énergie libre des espèces de cisplatine monosubstituées a déjà été mené et montre bien un impact important à la fois de la concentration différentielle en ions chlorure entre les milieux intra- et extra-cellulaires et de la topologie précise de la molécule – en particulier de sa charge.

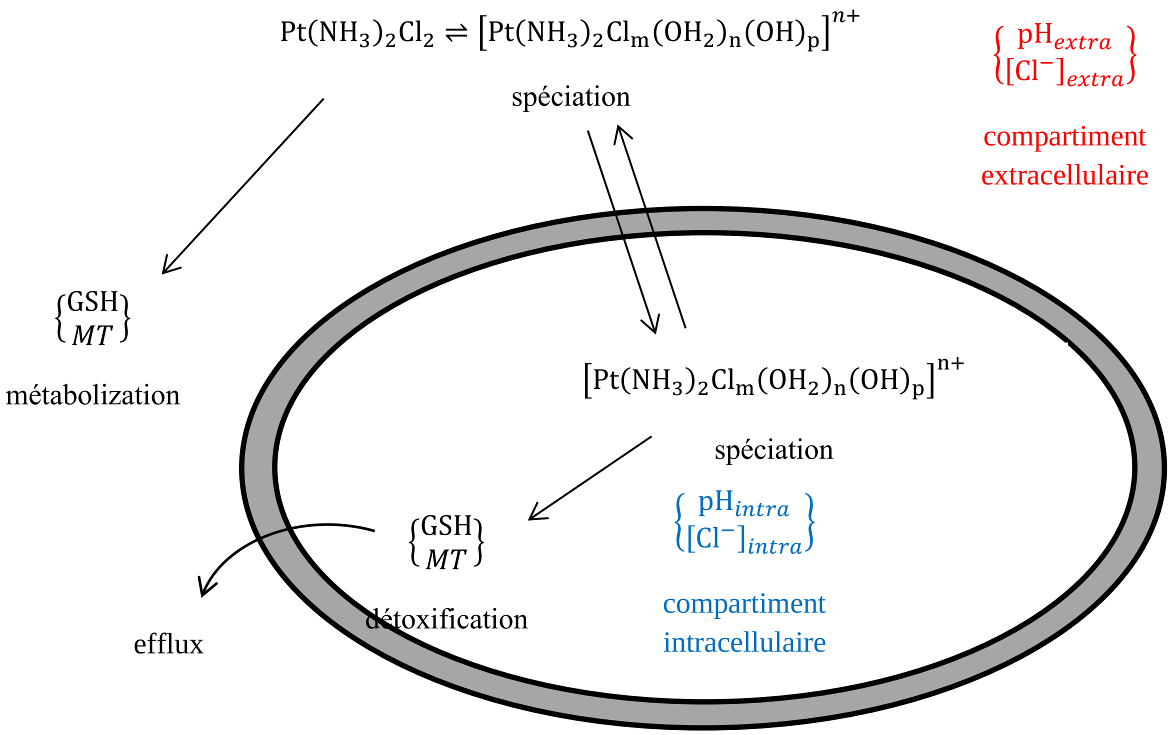

Figure I-13. Représentation du modèle pharmacocinétique considéré pour le cisplatine. Deux compartiments sont présents : le milieu intracellulaire et le milieu extracellulaire. Ces compartiments présentent chacun des valeurs réalistes de concentration en ions chlorure et de pH. La spéciation du cisplatine, i.e. les réactions de formations d'espèces apparentées en solution,est prise en compte sous la forme de réactions du premier ordre. Les processus de détoxification sont simplifiés sous la forme de l'interactions avec des glutathions et des métallothionéines. Les processus de diffusion sont encodés sous la forme de réactions de premier ordre basées sur le calcul de la perméabilité pour les différentes espèces au travers de modèles membranaires.

3.4.2. Vers la sélectivité

Ce travail a bien montré les limites du cisplatine comme candidat vers un traitement sélectif des cellules cancéreuses. Seul, le cisplatine présente une plus grande propension à perméer une membrane de cellule saine qu'une membrane de cellule cancéreuse. Les différentes propriétés de la matrice lipidique des membranes saines et cancéreuses nous permettent néanmoins de nous demander s'il existe d'autres candidats qui seraient en mesure de faire la distinction. Dans cette optique, nous avons commencé une collaboration avec l'équipe de P. Couvreur (Institut Galien, France). Cette équipe utilise le squalène, un précurseur naturel du cholestérol, en vue de fonctionnaliser des médicaments. Le squalène interagit fortement avec les cellules du fait de sa forte lipophilicité. Le procédé de squalénisation [78] a été utilisé avec succès avec différents médicaments (gemcitabine [79] et doxorubicine [80] par exemple). Dans le cadre de cette collaboration, nous avons commencé à étudier la perméation de la squalène-gemcitabine (SQGem) au sein des modèles de membrane cancéreuse et saine. Les premiers résultats obtenus nous permettent de supposer que la forte asymétrie des membranes saines pourrait jouer le rôle de réservoir envers la SQGem, effet qui n'est pas visible dans le cas du modèle de membranes cancéreuses. Ainsi, ces premiers résultats pourraient être le signe d'une forme de sélectivité de la SQGem envers les membranes surexposant PS/PE.

4. Conclusions

Au cours de ce travail, nous avons montré qu'une modélisation réaliste de la matrice lipidique de la membrane plasmique est d'une grande importance dans la compréhension des processus de transport passifs au travers la membrane plasmique. Les simulations réalisées montrent que les modèles de membranes mono-composants ne représentent pas une bonne image de la structure lipidique de la membrane plasmique. L'étude de la perméation du cisplatine dans le modèle de membrane saine et dans la bicelle de DOPC pur montre une différence de 5 à 6 ordres de grandeurs sur les coefficients de perméabilité. Cela provient principalement de deux facteurs : l'**hétérogénéité des lipides** et la **teneur en cholestérol**. Le cholestérol est connu pour jouer un rôle important sur la rigidité de la membrane et pour être l'une des pierres angulaires dans le processus de formation de rafts lipidiques. Dans le présent travail, nous avons montré que la variation de sa proportion de 0 à 33% abaisse la perméabilité de la membrane au cisplatine d'un ordre de grandeur. La différence restante étant ainsi attribuée à la différence de composition lipidique entre les modèles de membrane. Cette hétérogénéité, dans le cas de la perméation du cisplatine conduit à une membrane moins perméable.

La **courbure locale** de la membrane induit d'importantes modifications sur la structure même de la membrane ainsi que sur les processus de perméation. Le stress mécanique résultant de la courbure de la membrane conduit à une modification de l'épaisseur de la couche convexe et de l'aire par lipide des deux monocouches. Le cœur de la membrane – *i.e.* la fin des chaînes d'acide gras – se réorganisent et leur paramètre d'ordre décroît dans cette région. La courbure joue aussi un rôle sur la distribution et l'orientation du cholestérol qui se retrouve plus proche du cœur de la membrane quand celle-ci est courbe, ce qui explique en partie les variations susmentionnées du paramètre d'ordre. Ces propriétés structurelles ont un impact visible sur la perméation de différents ligands. Les coefficients de perméabilité de l'eau, des ions chlorure et sodium, de la gemcitabine et du cisplatine augmentent avec la courbure quel que soit le type de membrane étudié. Toutefois, si cet effet est d'une grande importance dans la compréhension des processus de diffusion, cet effet semble systématique et donc ne pas pouvoir être utilisé dans le but d'améliorer directement la sélectivité de médicaments.

Enfin, l'**asymétrie** transversale de la membrane plasmique joue un rôle important dans les processus de perméation. Il est connu que cette asymétrie est maintenue activement lors du fonctionnement normal de la cellule. Dans le même temps, il a été montré dans la littérature, que des cellules apoptotiques ainsi que des cellules non-apoptotiques issues de lignées cancéreuses montre une *symétrisation* de la répartition des lipides visible sous la forme d'une surexposition en PS, et possiblement en PE, dans la monocouche extracellulaire. Nous avons montré que le cisplatine est assez peu affecté par cet effet, et d'une manière négative : la perméabilité du modèle de membrane cancéreuse est un ordre de grandeur plus faible que celle du modèle de membrane saine dans le cas du cisplatine. Suite à ces résultats, nous avons voulu savoir si cet effet de surexposition de lipides dans la monocouche extracellulaire pouvait être utilisé dans le but d'obtenir un effet de sélectivité des médicaments envers les membranes cancéreuses. Nous avons donc débuté une étude sur la SQGem dont les premiers résultats indiquent une différence dans la perméabilité au travers des modèles de membranes saines par rapport aux modèles de membranes cancéreuses. Ces résultats pourraient indiquer que la SQGem présente une plus grande facilité à perméer au travers de membranes de cellules cancéreuses pour lesquelles PS/PE seraient surexposés sur la monocouche extracellulaire.

Pour conclure, nous avons mis en exergue quatre paramètres intercorrélés qui influencent tous le processus de diffusion passive : 1. l'hétérogénéité des lipides, 2. la teneur en cholestérol, 3. la courbure de la membrane et 4. l'asymétrie de la membrane. Bien sûr, les modèles de membrane développés ne dessinent pas une image parfaite de la matrice lipidique des membranes plasmiques réelles. Tout d'abord, leur complexité est limitée à quatre types de têtes lipidiques excluant les acides phosphatidiques (PA), les phosphatidylglycérols (PG) ou d'autres types plus *exotiques*. L'une des raisons principales de cette simplification est la volonté d'obtenir des systèmes dont la taille ne devienne pas prohibitive en terme de ressources de calcul. En effet, si l'on augmente la diversité des lipides représentés, leur présence dans la membrane doit rester statistiquement pertinente ou les temps de simulations doivent augmenter pour échantillonner correctement cette complexité. C'est pour la même raison que nous nous sommes limités à l'utilisation d'un seul type de chaînes d'acide gras dans nos modèles. Les modèles de membranes qui sont aujourd'hui la vitrine des possibilités numériques [50, 51, 81, 82] et qui embarquent une très grandes variétés de lipides, incluant une représentation réaliste de la distribution des chaînes d'acide gras sont actuellement étudiés par le biais de dynamique moléculaire gros grains. Malheureusement, ces simulations ne permettent pas d'obtenir une analyse fine des processus de perméation, laissant ainsi une place de choix à la modélisation tout-atome.

Chapter II - **Introduction**

A large part of the research in the development of anticancer drugs is devoted to the improvement of the ADME-T profile, *i.e.* administration, delivery, metabolism, excretion and toxicity profile. In this optics, many studies are focusing on the delivery/metabolism issue. The most common agents used in chemotherapy are administrated intravenously. One of the major issues in this case is the low efficiency of the transport from the blood vessels to the tumor due to the metabolization of a large amount of the drug and because the tumor tissues are generally not specifically targeted by the medicine.

To tackle these important problems many studies were devoted to the use of nanocarriers [83-85]. Different techniques are in-development and consist either in the encapsulation or in the functionalization of the drugs in order to reduce their chemical availability during their transport to the cancer tissues. One of the trends from the mid-2000's is the use of carbon nanostructures. However, these materials are known to exhibit a low biological compatibility as well as problems with their excretion, making them not widely accepted by the medical community. Many other candidates in the search of an improved ADME-T profile were proposed, including encapsulated drugs in polymeric micelles or dendrimers or in liposomes [85].

Many of the anticancer drugs aim at intracellular targets which require them to diffuse though the plasma membrane of the diseased cells. Another major problem of the existent drugs related to their delivery is the poor efficiency of these drugs on site to selectively permeate the cancer cells. Many drugs will exert their cytotoxicity to normal cells and possibly face intrinsic or acquired mechanisms of resistance on the way to their targets. The central topic of this work resides in giving a better understanding of the passive permeation process of different classes of anticancer agents. One of which is one of the most used families of anticancer drugs: the platinum salts. These salts are known to induce severe side effects. It is known that various cancer cell lines exhibit resistance phenomena towards them, lowering their efficiency. The study of their permeation could give a better understanding of their modes of transport to the cell and possibly give insights into more efficient drug designs which could selectively diffuse in cancer cells, lowering the required dose and thus the associated side effects.

One of the key aspects of these issues is the scale, both in space and time, involved in the processes of diffusion. The plasma membranes of eukaryotes are ~4nm thick, the most of the drugs are in between several ångströms and 1 nm long and the whole diffusion process takes several tens or hundreds of nanoseconds. In order to access relevant observables, these characteristic times and lengths should be sampled sufficiently – meaning that the resolution of the probe should be at least one order of magnitude higher than these quantities[1]. These scales are on the edge of the nowadays best equipment, but they enter plainly the ranges of computer simulations which could help having an atomistic description of the problematic and of the phenomena at play. Especially, in this work, we have been using all-atoms molecular dynamics simulations to estimate the interactions of different drugs with model membranes.

The main problem to model passive diffusion of ligands in the plasma membrane is to create a relevant model of the membrane. Yet, it is known that the plasma membrane of eukaryotes is a complex and organized mixture of thousands of types of lipids, of hundreds of proteins and carbohydrates which can exhibit a variety of compositions depending on the precise cell origin. Thus, one of the parts of the present work was to select the relevant properties of the membrane which should be embedded in the model in order to give a realistic picture of the diffusion process. Since the present study deals with the passive diffusion of drugs; it can be assumed that treating only the lipid matrix of the plasma membrane is relevant. The lipids are the main component in number of the plasma membrane. However, the goal of the work was to enhance the general model membranes which are often considering one only component.

Chapter III -presents the all-atoms molecular dynamics – the main tool used in the thesis. The description of the quantum mechanical origins of molecular dynamics simulation is detailed. A discussion of the choice of the force fields for our systems is presented. Chapter IV -presents lipid model membranes developed during this work and discusses their properties. Especially, the setup for a bicelle model with controllable curvature is discussed and the influence of the curvature on the membrane properties is analyzed. Additionally, a simple model for the lipid matrix of cancer cells is discussed. Chapter V -gives first an insight in the knowledge of the modes of actions and of transport of cisplatin as well as about its chemistry in biological media and then gives an analysis of the permeation of cisplatin in different model membranes, studying the effect of the lipid transversal asymmetry and the cholesterol content. Chapter VI -presents a study of the permeation of different small compounds and anticancer drugs in order to quantify the effects of curvature on the permeation. Chapter VII -gives general conclusions on the present work and opens towards the important issue of the design of a membrane selective anticancer drug.

---

[1] To be more precise, one could make a link with the sampling theory to which C. Shannon and many others contributed.

Chapter III - **About all-atoms molecular dynamics**

The core of my thesis was done using all-atoms (AA) molecular dynamics (MD) simulations. It is though essential to justify why we choose this technique among others and to describe the theoretical backgrounds and technical details implemented in the corresponding softwares. Many books, reviews and manuals are available and detail thoroughly the basics of this method [86, 87]. However, the complexity of our systems and the setups that have been developed in the present work required to understand better and deeper what is “behind” the AAMD technique and its numerical implementation. Up to now, AAMD methods are still under very active development and restricted to a small research community. Indeed, their development requires a strong knowledge in quantum mechanics and statistical physics. In this chapter, I try to give an overview of my current understanding in such simulations on the basis of my physics backgrounds.

The choice was made not to present every method of analysis used in this thesis in the present chapter, but to link them with the discussions in the following chapters. Hence, the methods devoted to the study of the permeability of ligands through the model membranes, including the computation of the potential of mean force (PMF), the diffusion coefficient, the permeability coefficient, *etc.* and the methods devoted to the study of the properties of the membranes, namely, the computation of the area per lipid, the order parameter, *etc.* are presented in the following chapters.

1. The road to classical atomic simulations

AAMD provides the motions of an ensemble of atoms. However, it would be wrong to believe that molecular dynamics is essentially based on the foundations of classical mechanics and that it relies on the motions of the atomic nuclei governed by “string-like” interactions. Both the classical description of the interatomic interactions (which are mainly governed by electron-nuclei and electron-electron interactions) encoded in any MD force field and the equations of time evolution of the atoms in the system are originally described by quantum mechanics. There is thus a “jump” to do from pure quantum dynamics (QD) to classical AAMD that requires necessarily some approximations. The most common road to extract classical molecular dynamics goes generally through the Born-Oppenheimer approximation [88] which separates slow (nuclei) from fast (electrons) motions and describes the motions of atoms as a classical ensemble of point particles whose energy is defined by their nuclear

Hamiltonian only. There are other methods which derive from this “electron-nuclei” separation treatment such as, for instance, *ab initio* molecular dynamics (AIMD) methods. An elegant, but not so widespread, demonstration [87] of the emergence of MD simulations as a classical limit of the time-dependent Schrödinger equation goes through the time-dependent self-consistent field (TDSCF) method. The advantage of this latter demonstration is that it keeps a more general and powerful form at the beginning of the reasoning when one separates the total wave function in two terms (electrons and nuclei) as well as it conserves the time-dependency in the electronic Schrödinger equation up to an advanced stage. TDSCF theory is also remarkable in the sense that it really helps to understand at which steps and degree of approximation which methods (AAMD, AIMD, *etc.*) could originate.

In a general way, the time evolution of atoms and molecules in the non-relativistic limit is given by the time-dependent Schrödinger equation such that:

$$i\hbar\frac{\mathrm{d}}{\mathrm{dt}}|\Psi(\mathrm{t})\rangle = \widehat{\mathrm{H}}|\Psi(\mathrm{t})\rangle, \tag{III-1}$$

where $|\Psi(\mathrm{t})\rangle$ is the state vector of the quantum system at the time t such that the wave function in space representation is written as $\Psi(\mathbf{r},\mathrm{t}) = \langle\mathbf{r}|\Psi\rangle$ with $|\mathbf{r}\rangle$ being the position eigenvector, $\widehat{\mathrm{H}}$ is the Hamiltonian operator representing the system energy and such that $\widehat{\mathrm{H}} = \widehat{\mathrm{T}} + \widehat{\mathrm{U}}$ where $\widehat{\mathrm{T}}$ and $\widehat{\mathrm{U}}$ are the operators corresponding respectively to the kinetic energy and to the potential energy and $\hbar = \frac{\mathrm{h}}{2\pi}$ is the reduced Planck constant.

For a system with N_n atoms and N_e electrons, the Hamiltonian operator can be approximated as the sum of the nuclear and electronic contributions to the kinetic and potential energies:

$$\widehat{\mathrm{H}}(\{\mathbf{r_i}\},\{\mathbf{R_I}\}) = \widehat{\mathrm{T}}_{\mathrm{n}}(\{\mathbf{R_I}\}) + \widehat{\mathrm{T}}_{\mathrm{e}}(\{\mathbf{r_i}\}) + \widehat{\mathrm{U}}_{\mathrm{nn}}(\{\mathbf{R_I}\}) + \widehat{\mathrm{U}}_{\mathrm{ee}}(\{\mathbf{r_i}\}) + \widehat{\mathrm{U}}_{\mathrm{en}}(\{\mathbf{r_i}\},\{\mathbf{R_I}\}), \tag{III-2}$$

where $\{\mathbf{r_i}\} = \mathbf{r_1} \dots \mathbf{r_i} \dots \mathbf{r_{N_e}}$ designates the ensemble of coordinates of the N_e electrons and $\{\mathbf{R_I}\} = \mathbf{R_1} \dots \mathbf{R_I} \dots \mathbf{R_{N_n}}$ refers to the ensemble of coordinates of the N_n nuclei. Hence the Hamiltonian operator can be written in the following form referred to as the Coulomb Hamiltonian:

$$\begin{aligned}\widehat{\mathrm{H}}(\{\mathbf{r_i}\},\{\mathbf{R_I}\}) = &-\left(\sum_{I=1}^{N_n}\frac{\hbar^2}{2M_I}\Delta_{\mathbf{R_I}}\right) - \left(\sum_{i=1}^{N_e}\frac{\hbar^2}{2m_e}\Delta_{\mathbf{r_i}}\right) + \left(\sum_{I=1}^{N_n}\sum_{J>I}\frac{Z_I Z_J e^2}{4\pi\varepsilon_0|\mathbf{R_I}-\mathbf{R_J}|}\right)\\ &+\left(\sum_{i=1}^{N_e}\sum_{j>i}\frac{e^2}{4\pi\varepsilon_0|\mathbf{r_i}-\mathbf{r_j}|}\right) - \left(\sum_{I=1}^{N_n}\sum_{j=1}^{N_e}\frac{Z_I e^2}{4\pi\varepsilon_0|\mathbf{R_I}-\mathbf{r_j}|}\right),\end{aligned} \tag{III-3}$$

where Z_I is the atomic number of the I-th atom, M_I is the mass of its nucleus, m_e is the mass of an electron, ε_0 is the vacuum permittivity, $\mathbf{R_I}$ is the position of the I-th atom and $\mathbf{r_i}$ is the position of the i-th electron. For the sake of clarity, these different terms can be rewritten in a more compact way, introducing $\widehat{\mathrm{U}}$ and $\widehat{\mathrm{H}}_{\mathrm{e}}$ which are respectively the sum of the potential energy contributions and the so-called electronic Hamiltoninan:

$$\begin{aligned}\widehat{\mathrm{H}}(\{\mathbf{r_i}\},\{\mathbf{R_I}\}) &= -\left(\sum_{\mathrm{I}=1}^{\mathrm{N_n}}\frac{\hbar^2}{2\mathrm{M_I}}\Delta_{\mathbf{R_I}}\right)-\left(\sum_{\mathrm{i}=1}^{\mathrm{N_e}}\frac{\hbar^2}{2\mathrm{m_e}}\Delta_{\mathbf{r_i}}\right)+\widehat{\mathrm{U}}(\{\mathbf{r_i}\},\{\mathbf{R_I}\})\\ &= -\left(\sum_{\mathrm{I}=1}^{\mathrm{N_n}}\frac{\hbar^2}{2\mathrm{M_I}}\Delta_{\mathbf{R_I}}\right)+\widehat{\mathrm{H}}_{\mathrm{e}}(\{\mathbf{r_i}\},\{\mathbf{R_I}\})\,.\end{aligned}\tag{III-4}$$

1.1. Separation of the total wave function

Solving the time-dependent Schrödinger equation in this pure QD approach reaches obvious technical limits for any system more complex than a few atoms. The key point used to solve such a system is to separate the total wave function Ψ into an electronic and a nuclear contributions. In the frame of the so-called single-determinant *ansatz*, it is supposed that Ψ can be written as the product of an electronic wave function and a nuclear wave function, respectively ϕ and χ so that:

$$\Psi(\{\mathbf{r_i}\},\{\mathbf{R_I}\};\mathrm{t}) \approx \phi(\{\mathbf{r_i}\};\{\mathbf{R_I}\},\mathrm{t})\chi(\{\mathbf{R_I}\};\{\mathbf{r_i}\},\mathrm{t})e^{\frac{i}{\hbar}\int_{\mathrm{t_0}}^{\mathrm{t}}\mathrm{dt}'\left\langle\phi\chi\middle|\widehat{\mathrm{H}}_{\mathrm{e}}(\{\mathbf{r_i}\},\{\mathbf{R_I}\})\middle|\chi\phi\right\rangle},\tag{III-5}$$

where the semicolons separate the variables written on the left from the parametric dependences written on the right. The exponential term in the total wave function expression is a phase factor introduced in order to obtain a simpler and more meaningful set of equations later on [89]. The parametric dependences inside the bra and ket vectors are omitted for the sake of clarity and $|\chi\phi\rangle = |\chi\rangle\otimes|\phi\rangle$. Both wave functions are taken so that they are individually normalized:

$$\langle\phi(\{\mathbf{R_I}\},\mathrm{t})|\phi(\{\mathbf{R_I}\},\mathrm{t})\rangle = 1\ \forall\{\mathbf{R_I}\},\mathrm{t};\ \langle\chi(\{\mathbf{r_i}\},\mathrm{t})|\chi(\{\mathbf{r_i}\},\mathrm{t})\rangle = 1\ \forall\{\mathbf{r_i}\},\mathrm{t}.\tag{III-6}$$

One can then insert this last expression (III-5) in the time-dependent Schrödinger equation and multiply by $\langle\phi|$ or $\langle\chi|$ which would yield the following system of time-dependent Schrödinger equations:

$$\begin{cases} i\hbar\dfrac{\partial}{\partial\mathrm{t}}|\phi(\{\mathbf{R_I}\},\mathrm{t})\rangle = -\left(\displaystyle\sum_{\mathrm{i}=1}^{\mathrm{N_e}}\frac{\hbar^2}{2\mathrm{m_e}}\Delta_{\mathbf{r_i}}\right)|\phi(\{\mathbf{R_I}\},\mathrm{t})\rangle \\ \qquad +\left\langle\chi(\{\mathbf{r_i}\},\mathrm{t})\middle|\widehat{\mathrm{U}}(\{\mathbf{r_i}\},\{\mathbf{R_I}\})\middle|\chi(\{\mathbf{r_i}\},\mathrm{t})\right\rangle\otimes|\phi(\{\mathbf{R_I}\},\mathrm{t})\rangle \\ i\hbar\dfrac{\partial}{\partial\mathrm{t}}|\chi(\{\mathbf{r_i}\},\mathrm{t})\rangle = -\left(\displaystyle\sum_{\mathrm{I}=1}^{\mathrm{N_n}}\frac{\hbar^2}{2\mathrm{M_I}}\Delta_{\mathbf{R_I}}\right)|\chi(\{\mathbf{r_i}\},\mathrm{t})\rangle \\ \qquad +\left\langle\phi(\{\mathbf{R_I}\},\mathrm{t})\middle|\widehat{\mathrm{H}}_{\mathrm{e}}(\{\mathbf{r_i}\},\{\mathbf{R_I}\})\middle|\phi(\{\mathbf{R_I}\},\mathrm{t})\right\rangle\otimes|\chi(\{\mathbf{r_i}\},\mathrm{t})\rangle \end{cases}\tag{III-7}$$

This set of equations shows that each type of particle now evolves in the mean field of the other, through the average values $\left\langle\chi\middle|\widehat{\mathrm{U}}\middle|\chi\right\rangle$ for the electrons and $\left\langle\phi\middle|\widehat{\mathrm{H}}_{\mathrm{e}}\middle|\phi\right\rangle$ for the nuclei. This dynamics for nuclei and electrons ruled by parametrically time-dependent effective potentials was introduced as early as in 1930 by Dirac [90] and forms the basis of the time-dependent self-consistent field (TDSCF) method.

1.2. Nuclei as classical particles

The second main approximation is to assume that nuclei can be treated as particles instead as of wave functions. Indeed, since the nuclear de Broglie wavelength is at least one order of magnitude lower than the interatomic distances in liquids, the nuclear wave packets can be taken as a non-coherent sum of the individual nuclear wave functions. Also, the nuclei masses are such that the nuclear wave functions are well localized. Thus, the nuclei are systems for which the classical mechanics could draw a satisfying description. This approximation is the basis of many *ab initio* and classical dynamics methods and the first step towards the numerical implementation of simulation techniques with a lower complexity and a better scalability. In this frame, the nuclear wave function χ is expressed as a simple wave of amplitude $\mathrm{A}(\{\mathbf{R_I}\};\{\mathbf{r_i}\},\mathrm{t})$ and phase $\mathrm{S}(\{\mathbf{R_I}\},\{\mathbf{r_i}\},\mathrm{t})$, both being real values:

$$\chi(\{\mathbf{R_I}\};\{\mathbf{r_i}\},\mathrm{t}) = \mathrm{A}(\{\mathbf{R_I}\},\{\mathbf{r_i}\},\mathrm{t})\mathrm{e}^{\frac{i}{\hbar}\mathrm{S}(\{\mathbf{R_I}\},\{\mathbf{r_i}\},\mathrm{t})}. \tag{III-8}$$

Using this last expression of the wave function in the nucleus time-dependent Schrödinger equation leads to the final form of the TDSCF equations for the nucleus:

$$\begin{cases} \dfrac{\partial \mathrm{S}}{\partial \mathrm{t}} + \displaystyle\sum_{\mathrm{I}=1}^{\mathrm{N_n}} \frac{1}{\mathrm{M_I}} \left(\nabla_{\mathbf{R_I}}\mathrm{S}\right)^2 + \int \mathrm{d}\mathbf{r}\phi^*\widehat{\mathrm{H}}_\mathrm{e}\phi = \hbar^2 \sum_{\mathrm{I}=1}^{\mathrm{N_n}} \frac{1}{\mathrm{M_I}} \frac{\Delta_{\mathbf{R_I}}\mathrm{A}}{\mathrm{A}} \\ \dfrac{\partial \mathrm{A}^2}{\partial \mathrm{t}} + \nabla_{\{\mathbf{R_I}\}} \cdot \left[\displaystyle\sum_{\mathrm{I}=1}^{\mathrm{N_n}} \frac{\mathrm{A}^2}{\mathrm{M_I}} \nabla_{\mathbf{R_I}}\mathrm{S}\right] = 0 \end{cases} \tag{III-9}$$

This system is intrinsically equivalent to the nuclear Schrödinger equation. The second equation is the continuity equation which ensures the conservation of the norm of the wave function $|\chi|$ and thus of the nuclear density of probability with time (see [91] for more details, especially chapters IV and VI). The road to derive this last system of equations is not straightforward. One should assume that the total nuclear wave function is a non-coherent sum of the individual nucleus wave functions. This assumption relies on the classical treatment of the interactions of the nuclei in between one another.

1.3. Classical limits of the TDSCF equations

The two TDSCF equations have different meaning. The second one does not depend on $\hbar$ and though represents already a classical feature. If one identifies the probability density to find the nuclei in the positions $\{\mathbf{R_I}\}$ as $\mathrm{P^n}(\{\mathbf{R_I}\}) = \mathrm{A}^2$ and the probability current as $\mathbf{J} = \left[\sum_{\mathrm{I}=1}^{\mathrm{N_n}} \frac{\mathrm{A}^2}{\mathrm{M_I}} \nabla_{\mathbf{R_I}}\mathrm{S}\right]$, one will find the expression of the continuity equation in quantum mechanics:

$$\frac{\partial \mathrm{P}}{\partial \mathrm{t}} + \nabla_{\{\mathbf{R_I}\}} \cdot \mathbf{J} = 0. \tag{III-10}$$

This equation has exactly the form of the continuity equation in hydrodynamics describing a fluid of probability density $\mathrm{P^n}$ and of flow **J**.

Interestingly, the first equation of the previous system (III-9) can be rewritten if one considers that the second term containing $\hbar$ vanishes at the classical limit[2]:

$$\frac{\partial \mathrm{S}}{\partial \mathrm{t}}+\sum_{\mathrm{I}=1}^{\mathrm{N_n}}\frac{1}{\mathrm{M_I}}\left(\nabla_{\mathbf{R_I}}\mathrm{S}\right)^2+\int \mathrm{d}\mathbf{r}\phi^*\widehat{\mathrm{H}}_{\mathrm{e}}\phi=0, \qquad \text{(III-11)}$$

which is an isomorphic expression to the Hamilton-Jacobi equation of motion. To make it be clearer, one can introduce the velocity field $\mathbf{v}=\frac{\mathbf{J}}{\mathrm{P}}=\sum_{\mathbf{I=1}}^{\mathbf{N_n}}\frac{\nabla_{\mathbf{R_I}}\mathrm{S}}{\mathrm{M_I}}$, and $\mathrm{V_e}$, the electronic potential such that:

$$\frac{\partial \mathrm{S}}{\partial t}+\sum_{\mathrm{I}=1}^{\mathrm{N_n}}\mathrm{M_I}\mathbf{v}_{\mathbf{I}}^{\mathbf{2}}+\mathrm{V_e}=0. \qquad \text{(III-12)}$$

This last system can be written in the same form as the Newton equation noting that it embeds the same term as in the fluid dynamics equations from Euler:

$$\begin{cases}\frac{\mathrm{d}}{dt}\mathrm{M_1}\mathbf{v_1}=-\nabla_{\mathbf{R_1}}\mathrm{V_e}\\ \vdots\\ \frac{\mathrm{d}}{dt}\mathrm{M_I}\mathbf{v_I}=-\nabla_{\mathbf{R_I}}\mathrm{V_e}\\ \vdots\\ \frac{\mathrm{d}}{dt}\mathrm{M}_{\mathbf{N}_n}\mathbf{v}_{\mathbf{N}_n}=-\nabla_{\mathbf{R}_{\mathbf{N}_n}}\mathrm{V_e}\end{cases}. \qquad \text{(III-13)}$$

In the light of these developments, one can see that Newton's second law for nuclei emerges from quantum mechanics with few approximations which are namely:

- The assumption that the total wave function can be separated in a nuclear and an electronic wave functions.
- The classical nature of the nuclei, which permits to assume that every nucleus state vector is orthogonal to one another.
- The classical hypothesis for the nuclear equation which tends to take $\hbar \rightarrow 0$ and leads to the Hamilton-Jacobi equation.

Thus, one obtains a simple system of $\mathrm{N_n}$+1 coupled equations which forms the basis of the so-called Erhenfest dynamics:

---

[2] For a rigorous demonstration which does not involve the classical approximation $\hbar \rightarrow 0$ which should not be applied directly in this case, one can read the work by Bornemann *et al.* [92].

$$\begin{cases} i\hbar \dfrac{\partial}{\partial \mathrm{t}} |\phi\rangle = \widehat{\mathrm{H}}_{\mathrm{e}} |\phi\rangle \\ \dfrac{\mathrm{d}}{\mathrm{dt}} \mathrm{M}_1 \mathbf{v_1} = -\nabla_{\mathbf{R_1}} \mathrm{V_e} \\ \qquad \vdots \\ \dfrac{\mathrm{d}}{\mathrm{dt}} \mathrm{M_I} \mathbf{v_I} = -\nabla_{\mathbf{R_I}} \mathrm{V_e} \\ \qquad \vdots \\ \dfrac{\mathrm{d}}{\mathrm{dt}} \mathrm{M}_{\mathbf{N_n}} \mathbf{v}_{\mathbf{N_n}} = -\nabla_{\mathbf{R}_{\mathbf{N_n}}} \mathrm{V_e} \end{cases} . \tag{III-14}$$

Hence, the Erhenfest dynamics embeds a fine description of the electronic structure which includes electronic transitions. This can be shown by developing the electronic wave function ϕ on the basis of the electronic states $\{\phi_k\}$:

$$|\phi\rangle = \sum_{\mathrm{k}=0}^{\infty} \mathrm{c_k} |\phi_k\rangle, \tag{III-15}$$

where $c_k(;t)$ are complex coefficients such that $\sum_{k=0}^{\infty} |c_k(;t)|^2 = 1$. It is possible to restrain the study to the adiabatic hypothesis which states that any transition from the state k is most unlikely to occur. This drives to lose the time-dependency in the electronic Schrödinger equation and to have only an eigenvalue problem of eigenvalue E_k. At this step, the present formalism is written in the very same way than the Born-Oppenheimer MD method for a chosen state k. If one chooses the state k to be the ground state denoted k=0, under the approximation that the transition energy in between the ground state and the first excited state is big compared to the thermal energy $k_b \cdot T$, then one obtains:

$$\begin{cases} \widehat{\mathrm{H}}_{\mathrm{e}} |\phi_0\rangle = \mathrm{E}_0 |\phi_0\rangle \\ \dfrac{\mathrm{d}}{\mathrm{dt}} \mathrm{M}_1 \mathbf{v_1} = -\nabla_{\mathbf{R_1}} \mathrm{V_e} \\ \qquad \vdots \\ \dfrac{\mathrm{d}}{\mathrm{dt}} \mathrm{M_I} \mathbf{v_I} = -\nabla_{\mathbf{R_I}} \mathrm{V_e} \\ \qquad \vdots \\ \dfrac{\mathrm{d}}{\mathrm{dt}} \mathrm{M}_{\mathbf{N_n}} \mathbf{v}_{\mathbf{N_n}} = -\nabla_{\mathbf{R}_{\mathbf{N_n}}} \mathrm{V_e} \end{cases} . \tag{III-16}$$

Technically, it is possible to decouple this previous system in order to solve the electronic eigenvalue problem separately than the classical mechanics equations of the nuclei. Thus, if one determines $\mathrm{E}_0(\{\mathbf{R_I}\})$ for all configurations $\{\mathbf{R_I}\}$, one will determine the full potential energy surface (PES), *i.e.* the electronic energy for all the accessible configurations of the nuclei. Classical MD relies on this scheme; the PES is determined for different configurations. The critical step is to fit these quantum mechanically obtained data with analytical functions for pair, 3-bodies or 4-bodies interactions[3], creating an analytical form of the PES from which the forces can be deduced. The set of parameters of the different atomic

---

[3] This assumption that the interactions can be developed as an expansion of many-body interactions allows to reducing the complexity of the task. Generally, no more than 4-bodies interactions (dihedrals) are taken into account.

properties including especially the partial charges and the parameters of the interactions is referred to as the **force field** (FF). Only the Newton's equations remain to be solved which will drive the system of atoms to explore the PES. On the other hand, one may prefer to solve on-the-fly the electronic eigenvalue problem and enters the realm of a wide range of *ab initio* (AI) MD techniques. Obviously, classical MD and AIMD techniques are complementary and three criteria are to be considered to define the type of techniques to use to treat a system: 1. its size, 2. the scale of the relaxation time involved in the phenomena of interest and 3. its "chemical" complexity. AIMD techniques are necessarily having a much higher cost than classical MD, limiting this technique in the frame of the present work. The membranes which are studied here are embedding several hundreds of thousands of atoms and the longest characteristic times of the main processes of interest – *i.e.* passive permeation processes – are on the order of tens to hundreds of nanoseconds. These constraints drive us to stick to highly efficient classical MD methods which are the only ones, at the date, to permit to explore such complexity. At the same time, the needs for a precise description of the molecular interactions binds us to the use of an atomic scale precision and forbids us to consider coarse grained techniques.

2. Classical force field and interactions in MD simulations

AAMD relies on a set of parameters building the so-called force field. A classical force field is the set of all the atomic parameters, including the atomic masses and partial charges of every atoms of the system as well as a simplified representation of the PES which encodes all the interatomic interactions in the form of additive many-body terms. These interactions strongly depend on the precise neighborhood of the given atoms. In this sense, the set of parameters describing the interactions of one atom with its neighbors is not related only to its atomic number but also to the precise nature of the molecule in which this atom is present as well as to the environment surrounding the atom (*e.g.* a precise solvent, a surface, a lipid membrane, *etc.*), meaning that there exist potentially more than one unique set of parameters for one precise atomic type. This is driving to the development of numerous specialized force fields. It is worth mentioning that these different force fields are *a priori* incompatible and that building an atomic system strongly relies on both the choice of the parameters and on their coherence. One way to achieve such a coherent description is to use one only method to determine the whole set of parameters forming the force field. This could be done by the use of experimental methods – mainly scattering and spectroscopy measurements – by means of *ab initio* computations, or by a mix of the both approaches.

2.1. An appropriate force field for lipid membranes

Importantly, in the frame of simulations of biological systems where different environments are in presence (e.g. water based solvent and lipid membrane), the choice of accurate parameters is of first importance. In this work, since the angular stone resides in a realistic description of the lipid matrix of the plasma membrane and of its properties, the precise choice of the lipid parameters is an essential question. The so-called Stockholm lipids (Slipids) force field [93-96] was used to describe all the lipids as well as cholesterol. This force field was created in the aim to reproduce the experimental behavior of self-assembled lipid structures made of one precise lipid type. Mainly, the agreement with scattering form factors from X-ray or neutron scattering, deuterium order parameters from NMR studies, area and volume per lipid and lipid bilayer thickness have been checked. Since the systems we are interested in are bringing much complexity – especially by involving a mix of several lipid types along with cholesterol and since the studies of the membrane properties are of first interest – an all-atomistic description is needed. Indeed, coarse grained force fields as well as united-atoms ones might induce more variations of the order parameters than AA FF. However, it is known that the transition temperature in between gel phase (L_α) and the liquid-crystalline phase (L_β) might be artificially increased if one uses explicit hydrogen atoms which may result in a too low area per lipid (A_L). Jämbeck and Lyurbatsev [93] tackled these limitations with the Slipids FF which has the advantage to be used in the natural isobaric-isothermal conditions which permits to have a direct link in between the MD observables and the experiments. To build the FF, an iterative process was used. The initial set of parameters was first based on the CHARMM36 FF [97]. The partial atomic charges were then computed with ab initio methods at the same level of theory. Then, the Lennard-Jones parameters were altered in order to agree with experimental values of heat of vaporization. At the end, the torsional terms were recomputed with ab initio methods. At the same time, in order to take into account the natural environment of the lipid head groups, computations of the partial charges were done for them in a dielectric continuum with $\varepsilon = 78.4$.

2.2. Force fields of the ligands

In order to study the interactions of various ligands – especially cancer drugs of different kinds – with the lipid matrix of the plasma membrane, different force fields were developed in our group. More discussions on these force fields can be found on the relevant sections were the interactions with the membrane of cisplatin (*cf.* Chapter V -4.1), its speciated species (*cf.* Chapter V -5.1), carboplatin (*cf.* Chapter V -5.2), oxaliplatin (*cf.* Chapter V -5.2) are discussed.

2.3. General form of the PES functional

In order to build complex biological systems in interaction with numerous compounds, including potentially proteins and small molecules, the Slipids FF was made using the very same formalism than the general AMBER force field [98] (GAFF) for amino acids. The implementation of the AMBER force fields in the Gromacs package embeds parameters for a wide range of ions as well as for water. In the frame of our studies, the parameters of the AMBER99SB force field were used for different molecules, including the AMBER TIP3p parameters for the water model which is also known to be compatible with the Slipids FF [95]. Both the Slipids FF and the GAFF use the same potential energy functional form, denoted as $\mathrm{V}(\{\mathbf{R_i}\})$, which can be written as follows:

$$\begin{aligned}
\mathrm{V}(\{\mathbf{R_i}\}) = {} & \sum_{i<j} 4\varepsilon_{ij}\left(\left(\frac{\sigma_{ij}}{R_{ij}}\right)^{12} - \left(\frac{\sigma_{ij}}{R_{ij}}\right)^{6}\right) + \sum_{i<j}\frac{q_i q_j}{4\pi\varepsilon_0 R_{ij}} + \sum_{i<j} k_{ij}^{b}\left(R_{ij} - R_{ij}^{0}\right)^2 \\
& + \sum_{i<j<k} k_{ijk}^{a}\left(\theta_{ijk} - \theta_{ijk}^{0}\right)^2 + k_{ijk}^{UB}\left(R_{ik} - B_{ik}^{0}\right)^2 \\
& + \sum_{i<j<k<l} k_{ijkl}^{\phi}\left(1 + \cos\left(n\phi_{ijkl} - \phi_{ijkl}^{0}\right)\right)^2 \\
& = \sum_{i<j} V_{LJ}^{ij}\left(\mathbf{R_i}, \mathbf{R_j}; \varepsilon_{ij}, \sigma_{ij}\right) + \sum_{i<j} V_{C}^{ij}\left(\mathbf{R_i}, \mathbf{R_j}; q_i, q_j\right) \qquad \text{(III-17)} \\
& + \sum_{i<j} V_{b}^{ij}\left(\mathbf{R_i}, \mathbf{R_j}; k_{ij}^{b}, R_{ij}^{0}\right) \\
& + \sum_{i<j<k} V_{UB}^{ijk}\left(\mathbf{R_i}, \mathbf{R_j}, \mathbf{R_k}; k_{ijk}^{a}, k_{ijk}^{UB}, \theta_{ijk}^{0}, B_{ik}^{0}\right) \\
& + \sum_{i<j<k<l} V_{d}^{ijkl}\left(\mathbf{R_i}, \mathbf{R_j}, \mathbf{R_k}, \mathbf{R_l}; k_{ijkl}^{\phi}, n, \phi_{ijkl}^{0}\right).
\end{aligned}$$

In this last expression, $R_{ij} = \left|\mathbf{R_i} - \mathbf{R_j}\right|$ is the distance in between two punctual atoms, and $\left\{\varepsilon_{ij}, \sigma_{ij}, q_i, q_j, k_{ij}^{b}, R_{ij}^{0}, k_{ijk}^{a}, k_{ijk}^{UB}, \theta_{ijk}^{0}, B_{ik}^{0}, k_{ijkl}^{\phi}, \phi_{ijkl}^{0}\right\}$ is the set of parameters for every i-th, j-th, k-th and l-th atom, respectively. The terms of this functional can be split in two categories:

- *The non-bonded terms*, $V_{LJ}^{ij}\left(\mathbf{R_i}, \mathbf{R_j}; \varepsilon_{ij}, \sigma_{ij}\right)$ and $V_{C}^{ij}\left(\mathbf{R_i}, \mathbf{R_j}; q_i, q_j\right)$.

Two terms describe the interactions which do not involve a chemical bond. The first term which is on the form of a Lennard-Jones 12-6 potential represents the attractive van der Waals interactions and the atomic repulsion originating from the Pauli exclusion principle. This potential is characterized by a well of depth ε_{ij} and by the closest distance from the i-th atom to the j-th, denoted σ_{ij}, at which the potential is null. The second term concerns the Coulomb electrostatic interactions and depends on the charges q_i and q_j of the atoms i and j.

- *The bonded terms*, $V_{b}^{ij}\left(\mathbf{R_i}, \mathbf{R_j}; k_{ij}^{b}, R_{ij}^{0}\right)$, $V_{UB}^{ijk}\left(\mathbf{R_i}, \mathbf{R_j}, \mathbf{R_k}; k_{ijk}^{a}, k_{ijk}^{UB}, \theta_{ijk}^{0}, B_{ik}^{0}\right)$ and $V_{d}^{ijkl}\left(\mathbf{R_i}, \mathbf{R_j}, \mathbf{R_k}, \mathbf{R_l}; k_{ijkl}^{\phi}, n, \phi_{ijkl}^{0}\right)$.

These terms include the pair interactions in the form of a simple harmonic potential $V_{b}^{ij}\left(\mathbf{R_i}, \mathbf{R_j}; k_{ij}^{b}, c\right)$ where k_{ij}^{b} is the bond force constant and R_{ij}^{0} is the equilibrium distance. The so-called Urey-Bradley potential, $V_{UB}^{ijk}\left(\mathbf{R_i}, \mathbf{R_j}, \mathbf{R_k}; k_{ijk}^{a}, k_{ijk}^{UB}, \theta_{ijk}^{0}, B_{ik}^{0}\right)$, describes the bond-angle vibrations between a triplet of atoms and consists in a harmonic potential depending on the angle $\theta_{ijk}\left(\mathbf{R_i}, \mathbf{R_j}, \mathbf{R_k}\right)$ as well as a harmonic correction term. The angle force constant is denoted k_{ijk}^{a} and θ_{ijk}^{0} is the equilibrium angle. The Urey Bradley constants, written k_{ijk}^{UB} and B_{ik}^{0} are the ones embedded in the expression of the harmonic correction. Finally, a dihedral potential $V_d^{ijkl}\left(\mathbf{R_i}, \mathbf{R_j}, \mathbf{R_k}, \mathbf{R_l}; k_{ijkl}^{\phi}, n, \phi_{ijkl}^{0}\right)$ is parametrically depending on k_{ijkl}^{ϕ}, the dihedral constant, n is the multiplicity and ϕ_{ijkl}^{0} the dihedral angle equilibrium. This last potential is a description of the interactions resulting from the torsional degrees of freedom of any chain of four covalently bonded atoms.

2.4. Non-bonded interactions

The computation of all the terms of the energy potential functional described in eq. (III-17) would lead – in the frame of simulations of biological systems embedding hundreds of thousands of atoms – to a computational cost exceeding the present computational possibilities. In order to run simulations on pretty big systems for hundreds of nanoseconds, some more approximations are in need. Especially in the case of non-bonded interactions, several strategies are used.

2.4.1.LJ potential

- *Dealing with the number of terms in the PES functional*

One should note that not all the LJ parameters are computed at the *ab initio* level but generally only the interactions on the form $V_{LJ}^{ii}(\mathbf{R_i}, \mathbf{R_i}; \varepsilon_{ii}, \sigma_{ii})$ and that, for cross terms, a specific combination rule is applied. In the case of the present FF, the Lorentz-Berthelot rules were used such that:

$$\begin{cases} \varepsilon_{ij} = \left(\varepsilon_{ii}\varepsilon_{jj}\right)^{1/2} \\ \sigma_{ij} = \dfrac{\sigma_{ii} + \sigma_{jj}}{2} \end{cases}. \tag{III-18}$$

These rules save a lot of preliminary computations at the cost of a certain increase in the error; for instance, it is known that the Berthelot rule consisting in a geometric mean of the well depth mainly gives overestimated values of the van der Waals interactions.

- *Dealing with the complexity for computing the LJ terms*

The LJ terms have an infinite range and the number of pairs to be taken into account for, say, the i-th atom, increases as the squared of the distance to this atom. This drives rapidly to a bottleneck problem where the computational cost for computing the long range LJ interactions will become prohibitive. To tackle this technical limitation, it is customary to apply a cut-off distance after which the potential is considered to be null. Thus, the pair interactions are computed only if the distance in between the two atoms does not exceed the cut-off radius. In the frame of LJ interactions where the repulsive term rapidly drops down and the vdW term reaches zero in the limit of long range interactions, this approximation does not lead to dramatic errors. One should note that MD simulations are using periodic boundary conditions (PBC) which are applied – generally – to every surfaces of the simulation box. In this case, the application of a cut-off becomes necessary to avoid some interactions, *i.e.* the cut-off radius should be smaller than half of the smallest edge of the simulation box.

Technically, the computation of the pair interactions relies on the efficiency of algorithms dedicated to neighbor searching. In a nutshell, most of the MD packages use algorithms for the generation of pair interaction lists. The update of such list is generally less often than the integration of the Newton equations. This is another reason of the inaccuracy in the computations of non-bonded terms which leads to an energy drift.

- *Dispersion corrections*

The cut-off applied to the LJ term is used because of its believed small influence on the repulsive term of the LJ 12-6 potential. Nonetheless, it is known that the use of a cutoff biases substantially the potential energy contribution as well as the computed pressure. It is stated that for simulations computed in isobaric conditions, the observables computed from these simulations, especially the estimation of the free energy profile which is of first importance to characterize the permeation of molecules through membranes, might significantly lose accuracy if no corrections are applied [99]. Hence, energy and pressure corrections on the dispersion term of the non-bonded interactions were used in the present simulations as it is advised by the creators of Slipids FF. These corrections are not optimal yet, especially for inhomogeneous systems such as the membranes in water solvent we simulated. Indeed, this corrections assumes that the values of $\langle C^{(6)}_{\mathrm{water}} \rangle = \langle 4\varepsilon_{\mathrm{water}}\sigma^{6}_{\mathrm{water}} \rangle \sim \langle C^{(6)}_{\mathrm{lipid}} \rangle$, where the average dispersion $\langle C^{(6)}_{\mathrm{water}} \rangle = \frac{2}{N(N-1)} \sum_{i=1}^{N} \sum_{j>i}^{N} 4\varepsilon_{ij}\sigma^{6}_{ij}$. New developments for the computations of the LJ interactions are starting to use the so called particle-mesh Ewald method primarily dedicated to electrostatic interactions and mentioned in the next paragraph.

2.4.2.The electrostatic potential

In the case of electrostatic interactions, applying a simple cut-off for long-range interactions might lead to important errors since the potential decreases as r^{-1} which leads to non-negligible values even at a distance of several nanometers. The use of periodic boundary conditions (PBC) gives, here, the opportunity to apply the so-called Ewald summation method or its extensions such as the particle mesh Ewald (PME) method; both of which being developed for periodic structures (crystals). The PME method keeps at the same time a good accuracy and a computational cost not much greater than that of cut-off methods. The total Coulomb energy of an infinitely periodic system of N particles is given by:

$$V_C(\mathbf{R_i}, \mathbf{R_j}, \mathbf{n}; q_i, q_j) = \frac{1}{8\pi\varepsilon_0} \sum_{n_x=-\infty}^{\infty} \sum_{n_y=-\infty}^{\infty} \sum_{n_z=-\infty}^{\infty} \sum_{j=1}^{N} \sum_{i=1}^{N'} \frac{q_i q_j}{R_{ij\mathbf{n}}}, \qquad \text{(III-19)}$$

where $\mathbf{n} = \begin{pmatrix} n_x L_x \\ n_y L_y \\ n_z L_z \end{pmatrix}$, with $\{L_x, L_y, L_z\}$ the lengths of the edges on the axes of the simulation box. $R_{ij\mathbf{n}} = |\mathbf{R_i} - \mathbf{R_{jn}}| = |\mathbf{R_i} - (\mathbf{R_j} + \mathbf{n})|$. The double-counting of the interactions drives to a factor ½ in the first term of this expression. The « ' » stands for the exclusion of the self-interaction, *i.e.* for j=i and $n_x=n_y=n_z=0$. The convergence of this last expression is not only slow but also dependent on the order to sum up the terms. The conditional convergence of this sum was addressed by Ewald in 1921 [100]. The N punctual charges in the simulation have each a charge density distribution ρ given by the Dirac distribution such that:

$$\rho_i(\mathbf{R}) = q_i \delta(\mathbf{R} - \mathbf{R_i}). \qquad \text{(III-20)}$$

The first step in the Ewald summation is to split the charge density distribution in two contributions; a *short-range* one, denoted ρ_i^S and a long-range one denoted ρ_i^L. In this aim, one may use an arbitrary Gaussian distribution:

$$\begin{gathered} \rho_i(\mathbf{R}) = \rho_i^S(\mathbf{R}) + \rho_i^L(\mathbf{R}) \\ \rho_i^S(\mathbf{R}) = q_i \delta(\mathbf{R} - \mathbf{R_i}) - q_i G(\mathbf{R} - \mathbf{R_i}), \\ \rho_i^L(\mathbf{R}) = q_i G(\mathbf{R} - \mathbf{R_i}) \end{gathered} \qquad \text{(III-21)}$$

with $G(\mathbf{R}) = \frac{1}{(2\pi\sigma^2)^{\frac{3}{2}}} e^{-\frac{|\mathbf{R}|^2}{2\sigma^2}}$, the Gaussian distribution where σ is the standard deviation of the Gaussian distribution. Thus, the Coulomb interactions can be written again taking this transformation into account so that:

$$\begin{aligned} & V_C(\mathbf{R}, \mathbf{R}', \mathbf{n}; q_i, q_j) \\ & = \frac{1}{8\pi\varepsilon_0} \sum_{n_x=-\infty}^{\infty} \sum_{n_y=-\infty}^{\infty} \sum_{n_z=-\infty}^{\infty} \sum_{j=1}^{N} q_j \sum_{i=1}^{N'} q_i \left[\iiint_{-\infty}^{\infty} \frac{\delta(\mathbf{R} - \mathbf{R}') - G(\mathbf{R} - \mathbf{R}')}{|\mathbf{R} - \mathbf{R}'|} d\mathbf{R}' \right. \\ & \left. + \iiint_{-\infty}^{\infty} \frac{G(\mathbf{R} - \mathbf{R}')}{|\mathbf{R} - \mathbf{R}'|} d\mathbf{R}' \right]. \end{aligned} \qquad \text{(III-22)}$$

From a physical point of view one should remember that the punctual charge hypothesis can be taken as a limit case of the Gaussian distribution for a null standard deviation. Thus, in the first term, V_C^S, subtracting a Gaussian charge distribution to the Dirac charge distribution creates in some way a screening of the long distance interactions, making this sum converging rapidly for short-range ("S") interactions. In order to obtain the expression of the Coulomb potential energy, one may solve the Poisson's equation of the potential field $\phi(\mathbf{R})$. Since both the short and the long ranges terms involve a Gaussian distribution, let's solve the Poisson's equation for this distribution:

$$\Delta\phi_G(\mathbf{R}) = -\frac{G(\mathbf{R})}{\varepsilon_0}. \qquad \text{(III-23)}$$

The Gaussian distribution being invariant by rotation, one can write the previous vector equation as a scalar equation depending only on r, the distance from the center of the Gaussian distribution, using spherical coordinates:

$$\frac{1}{\mathrm{r}}\frac{\partial^2}{\partial \mathrm{r}^2}[\mathrm{r}\phi_{\mathrm{G}}(\mathrm{r})] = -\frac{\mathrm{G}(\mathrm{r})}{\varepsilon_0}. \tag{III-24}$$

Integrating two times over r yields:

$$\mathrm{r}\phi_{\mathrm{G}}(\mathrm{r}) = \int_0^{\mathrm{r}} \frac{\sigma^2}{\varepsilon_0}\phi_{\mathrm{G}}(\mathrm{r})\mathrm{dr}'. \tag{III-25}$$

It is then possible to introduce the error function $\mathrm{erf}(\mathrm{r}) = \frac{2}{\sqrt{\pi}}\int_0^{\mathrm{r}} e^{-\mathrm{r}'^2}\mathrm{dr}'$ which is intrinsically related to the Gaussian distribution, noting that:

$$\mathrm{erf}\left(\frac{\mathrm{r}}{\sigma\sqrt{2}}\right) = \frac{2}{\sqrt{\pi}}\frac{1}{\sigma\sqrt{2}}\int_0^{\mathrm{r}} e^{-\frac{\mathrm{r}'^2}{2\sigma^2}}\mathrm{dr}', \tag{III-26}$$

which finally gives:

$$\phi_{\mathrm{G}}(\mathrm{r};\sigma) = \frac{1}{4\pi\varepsilon_0 \mathrm{r}}\mathrm{erf}\left(\frac{\mathrm{r}}{\sigma\sqrt{2}}\right). \tag{III-27}$$

This allows writing the expressions of the potential fields for short and long ranges:

$$\begin{cases} \phi_{\mathrm{i}}^{\mathrm{S}}(\mathbf{R_i};\sigma) = \dfrac{1}{4\pi\varepsilon_0}\dfrac{\mathrm{q_i}}{\mathrm{R_i}}\mathrm{erfc}\left(\dfrac{\mathrm{R_i}}{\sigma\sqrt{2}}\right) \\ \phi_{\mathrm{i}}^{\mathrm{L}}(\mathbf{R_i};\sigma) = \dfrac{1}{4\pi\varepsilon_0}\dfrac{\mathrm{q_i}}{\mathrm{R_i}}\mathrm{erf}\left(\dfrac{\mathrm{R_i}}{\sigma\sqrt{2}}\right) \end{cases}, \tag{III-28}$$

with $\mathrm{erfc}(\mathrm{r}) = 1 - \mathrm{erf}\,(\mathrm{r})$, being the complementary error function and $\mathrm{R_i} = |\mathbf{R} - \mathbf{R_i}|$. We thus can write the potential energy of the different contributions:

$$\begin{cases} \mathrm{V_C^S}\big(\mathbf{R_i},\mathbf{R_j},\mathbf{n};\mathrm{q_i},\mathrm{q_j};\sigma\big) = \dfrac{1}{8\pi\varepsilon_0}\displaystyle\sum_{\mathrm{n_x}=-\infty}^{\infty}\sum_{\mathrm{n_y}=-\infty}^{\infty}\sum_{\mathrm{n_z}=-\infty}^{\infty}\sum_{\mathrm{j}=1}^{\mathrm{N}}\mathrm{q_j}\sum_{\mathrm{i}=1}^{\mathrm{N}'}\dfrac{\mathrm{q_i}}{\mathrm{R}_{\mathrm{ij}\mathbf{n}}}\mathrm{erfc}\left(\dfrac{\mathrm{R}_{\mathrm{ij}\mathbf{n}}}{\sigma\sqrt{2}}\right) \\ \mathrm{V_C^L}\big(\mathbf{R_i},\mathbf{R_j},\mathbf{n};\mathrm{q_i},\mathrm{q_j};\sigma\big) = \dfrac{1}{8\pi\varepsilon_0}\displaystyle\sum_{\mathrm{n_x}=-\infty}^{\infty}\sum_{\mathrm{n_y}=-\infty}^{\infty}\sum_{\mathrm{n_z}=-\infty}^{\infty}\sum_{\mathrm{j}=1}^{\mathrm{N}}\mathrm{q_j}\sum_{\mathrm{i}=1}^{\mathrm{N}'}\dfrac{\mathrm{q_i}}{\mathrm{R}_{\mathrm{ij}\mathbf{n}}}\mathrm{erf}\left(\dfrac{\mathrm{R}_{\mathrm{ij}\mathbf{n}}}{\sigma\sqrt{2}}\right) \end{cases}. \tag{III-29}$$

With these last expressions, one can really see the physical meaning of this separation: the short-range term vanishes for r → ∞ leading to the common sense attributed to these both terms denoted as "short range" and "long range" interactions. A further separation of the long-range term is usually done to make the computations simpler. The self-interaction term is computed separately and thus subtracted from $\mathrm{V_C^L}$ so that $\widetilde{\mathrm{V}}_{\mathrm{C}}^{\mathrm{L}} = \mathrm{V_C^L} - \mathrm{V_C^{self}}$. One can estimate the self-interaction contribution for long-range interactions by considering the limit:

$$\lim_{R_{ij\mathbf{n}}\to 0} \mathrm{erf}\left(\frac{R_{ij\mathbf{n}}}{\sigma\sqrt{2}}\right) = \frac{2}{\sqrt{\pi}}\frac{1}{\sigma}R_{ij\mathbf{n}}, \tag{III-30}$$

therefore:

$$V_C^{\mathrm{self}}(q_i;\sigma) = \frac{1}{2^{5/2}\pi^{3/2}\varepsilon_0\sigma}\sum_{i=1}^{N} q_i^2. \tag{III-31}$$

If the short-range sum can be directly computed thanks to the erfc function which ensures a fast convergence, the long-range term has to be computed differently. The idea beneath this separation introduced by Ewald [100] is to obtain a converging sum in the reciprocal space. The total charge density field can be expressed as a periodic function which will allow applying the Bloch's theorem further on:

$$\rho^L(\mathbf{R}) = \sum_{n_x=-\infty}^{\infty}\sum_{n_y=-\infty}^{\infty}\sum_{n_z=-\infty}^{\infty}\sum_{i=1}^{N}\rho_i^L(\mathbf{R}+\mathbf{n}), \tag{III-32}$$

thus one may take the Fourier transform of the total charge density $\hat{\rho}^L(\mathbf{k})$ and of the long-range potential field $\hat{\phi}^L(\mathbf{k})$ which is also periodic:

$$\begin{cases} \hat{\rho}^L(\mathbf{k}) = \iiint\limits_V \rho^L(\mathbf{R})e^{-i\mathbf{k}\cdot\mathbf{R}}d\mathbf{R} = \iiint\limits_V \sum_{i=1}^{N} q_i G(\mathbf{R}+\mathbf{n})\, e^{-i\mathbf{k}\cdot\mathbf{R}}d^3\mathbf{R} \\ \hat{\phi}^L(\mathbf{k}) = \iiint\limits_V \phi^L(\mathbf{R})e^{-i\mathbf{k}\cdot\mathbf{R}}d^3\mathbf{R} \end{cases}, \tag{III-33}$$

where V is the volume of the supercell, *i.e.* the volume of the simulation box. Therefore, the expression of the charge density field can be written as:

$$\hat{\rho}^L(\mathbf{k};\sigma) = \sum_{i=1}^{N} q_i e^{-i\mathbf{k}\cdot\mathbf{R}_i} e^{-\frac{\sigma^2|\mathbf{k}|^2}{2}} \tag{III-34}$$

Once again, to find the expression of the potential energy, one has to solve the Poisson's equation which links the charge density field to the potential field:

$$\Delta\phi^L(\mathbf{R}) = -\frac{\rho^L(\mathbf{R})}{\varepsilon_0}. \tag{III-35}$$

Noting that, given a function f($\mathbf{x}$) absolutely continuous, the Fourier transform of its derivative is $\widehat{f'}(\mathbf{k}) = i\mathbf{k}\hat{f}(\mathbf{k})$ which yields:

$$\mathbf{k}^2\hat{\phi}^L(\mathbf{k}) = \frac{\hat{\rho}^L(\mathbf{k})}{\varepsilon_0}. \tag{III-36}$$

Hence, the Fourier transform of the potential field takes the following expression:

$$\hat{\phi}^{\mathrm{L}}(\mathbf{k};\sigma) = \sum_{i=1}^{N} \frac{q_i}{k^2\varepsilon_0} e^{-i\mathbf{k}\cdot\mathbf{R}_i} e^{-\frac{\sigma^2|\mathbf{k}|^2}{2}}. \tag{III-37}$$

One has then to apply the inverse Fourier transform to find the potential field in the direct space:

$$\phi^{\mathrm{L}}(\mathbf{R},\mathbf{R_i};q_i,\sigma) = \frac{1}{V}\sum_{\mathbf{k}}\sum_{i=1}^{N} \frac{q_i}{k^2\varepsilon_0} e^{-i\mathbf{k}\cdot(\mathbf{R}-\mathbf{R}_i)} e^{-\frac{\sigma^2|\mathbf{k}|^2}{2}}. \tag{III-38}$$

This last expression can be further simplified if the total charge of the simulation box is neutral by noting that, in this case, $\sum_{i=1}^{N} q_i = 0$. This will give no contribution for **k**=0. In MD simulations, the systems should have a null global charge, since the use of PBC conditions would make a non-null value added *theoretically* an infinite number of times. Hence, one can write the long-range Coulomb potential energy such that:

$$V_C^{\mathrm{L}}\left(\mathbf{R_i},\mathbf{R_j},\mathbf{n};q_i,q_j,\sigma\right) = \frac{1}{V}\sum_{\mathbf{k}\neq 0}\sum_{j=1}^{N}\sum_{i=1}^{N} \frac{q_iq_j}{k^2\varepsilon_0} e^{-i\mathbf{k}\cdot\left(\mathbf{R}_j-\mathbf{R}_i\right)} e^{-\frac{\sigma^2|\mathbf{k}|^2}{2}} \tag{III-39}$$

It is customary to introduce a structure factor, analog to the one in crystallography, to simplify the previous expression:

$$S(\mathbf{R_i},\mathbf{k};q_i) = \sum_{i=1}^{N} q_i e^{i\mathbf{k}\cdot\mathbf{R}_i}, \tag{III-40}$$

therefore, the expression of the electrostatic interactions can be written as follows:

$$\begin{aligned}
&V_C\left(\mathbf{R_i},\mathbf{R_j},\mathbf{n},\mathbf{k};q_i,q_j,\sigma\right)\\
&\quad= V_C^{\mathrm{S}}\left(\mathbf{R_i},\mathbf{R_j},\mathbf{n},q_i,q_j,\sigma\right) + V_C^{\mathrm{L}}\left(\mathbf{R_i},\mathbf{R_j},\mathbf{k};q_i,q_j,\sigma\right) - V_C^{\mathrm{self}}(;q_i,\sigma)\\
&\quad= \frac{1}{8\pi\varepsilon_0}\sum_{n_x=-\infty}^{\infty}\sum_{n_y=-\infty}^{\infty}\sum_{n_z=-\infty}^{\infty}\sum_{j=1}^{N} q_j \sum_{i=1}^{N'} \frac{q_i}{R_{ij\mathbf{n}}}\operatorname{erfc}\left(\frac{R_{ij\mathbf{n}}}{\sigma\sqrt{2}}\right)\\
&\quad+ \frac{1}{2V\varepsilon_0}\sum_{\mathbf{k}\neq 0}\sum_{j=1}^{N}\sum_{i=1}^{N} \frac{e^{-\frac{\sigma^2|\mathbf{k}|^2}{2}}}{k^2}\left|S\left(\mathbf{R_i},\mathbf{R_j},\mathbf{k};q_i,q_j\right)\right|^2\\
&\quad- \frac{1}{2^{\frac{5}{2}}\pi^{\frac{3}{2}}\varepsilon_0\sigma}\sum_{i=1}^{N} q_i^2.
\end{aligned} \tag{III-41}$$

The idea beneath this separation in the previous expression is to obtain strictly converging terms. The short-range term converges rapidly for long distances thanks to the presence of the erfc function and the long-range term converges rapidly in the reciprocal space due to the $e^{-\frac{\sigma^2|\mathbf{k}|^2}{2}}$. Thus, one can truncate the direct space sum with a cut-off in the order of the nanometer and the reciprocal space sum by computing it for ± 10 wave vectors in each direction. Although the convergence of the electrostatic potential is ensured, the complexity inherent to this method is generally of $\mathcal{O}(N^2)$ which remains really pricy for big systems as it is customary to find in the frame of membrane simulations. The optimal choice of σ has been proven to improve the convergence of these sums driving to a complexity of $\mathcal{O}(\mathrm{N}^{3/2})$.

The choice of σ is directly related to the further evolutions of the Ewald summation method which, in its raw state, remains prohibitive for systems with $N>10^5$. For big values of σ it can be shown that the complexity of the direct sum can be bound to $\mathcal{O}(N)$. The initial idea in order to improve the Ewald summation method relies on the proposition of an efficient method to tackle the computation of the reciprocal sum. The basis of the nowadays most-used method was mainly provided by Darden *et al.* who based their developments on the so-called particle-mesh (PM) and particle-particle particle-mesh method (P^3M) developed by Hockney and Eastwood and released the particle-mesh Ewald (PME) method [101]. The main idea of this method is the use of the efficient fast Fourier transform (FFT) algorithm in the system by computing the Gaussian contributions of each particle on a grid that discretely meshes the simulation box. On each node of this grid, the electrostatic contributions are interpolated, resulting in a lattice of charges in the supercell, easy to treat with the highly efficient discrete Fourier transform algorithms such as FFT. PME methods are now the standard methods used in all the MD softwares and greatly improved the scalability of the simulations giving a complexity of $\mathcal{O}\big(\mathrm{N}\cdot\log(\mathrm{N})\big)$.

2.4.3.1-4 interactions

It has been shown that inside molecules, the use of the non-bonded terms in between close neighbors, potentially directly covalently bonded, is detrimental to the accuracy of the computations. Instead, in such close-distances, the bonded terms are used to define the stretch, angle or dihedral interactions in between atoms i and i+1, i and i+2, i and i+3 and i and i+4. The second and third atoms involved in the interactions with a first atom i, respectively denoted as i+1 and i+2, are considered to be too close to this first atom and are simply excluded from the non-bonded interactions. The fourth atom, i+3, is generally a limit case where the repulsive, dispersion and electrostatic interactions are generally weighted by a given coefficient to obtain a weaker interaction closer to reality. In the case of the implementation of AMBER99SB in the Gromacs package, the weight coefficient for the LJ interactions is of 0.5 and the one for the electrostatic interactions is of 0.8333. The second and third atoms around any i-th atom create the so-called exclusion list and the fourth ones form the so-called 1-4 interactions. Generally, from the fifth atom, no further weights or corrections are applied.

3. The statistical nature of MD simulations

The apparent determinist nature of MD simulations shown in the Newton’s equations is somewhat illusory. Since one wants to obtain macroscopic observables from any atomic system, one should do an ensemble average. This means that one should sample all the microstates, as it is the way in Monte Carlo simulations, by generating successively different configurations. A big enough number of these configurations will finally give a good estimate of the observables. MD simulations are first a tool to generate efficiently a set of these configurations in the aim of sampling the phase space. In that respect, one should not see MD as a purely determinist technique and should especially avoid to give any conclusions on the dynamics of a system without extreme caution. Indeed, the time progression only becomes a propagator of the system from one state to another and allows – in the case of an ergodic system – to make such ensemble average as if we generate as many systems with different initial conditions and the estimate of the macroscopic variable A will be its average $\langle \mathrm{A} \rangle$:

$$\begin{aligned} \langle \mathrm{A}(\mathbf{r},\mathbf{p})\rangle_{\mathrm{ensemble}} = \langle \mathrm{A}(\mathbf{r},\mathbf{p})\rangle_{\mathrm{time}} &= \iint\limits_{\forall\Gamma} \mathrm{A}(\mathbf{r},\mathbf{p})\rho(\mathbf{r},\mathbf{p})\mathrm{d}\mathbf{r}\mathrm{d}\mathbf{p} \\ &= \lim_{\mathrm{t}\to\infty}\frac{1}{\mathrm{t}}\int_0^{\mathrm{t}} \mathrm{A}(\mathbf{r},\mathbf{p};\mathrm{t})\mathrm{d}\mathrm{t}', \end{aligned} \tag{III-42}$$

with Γ representing a point in the phase space, *i.e.* a set of $\{\mathbf{r},\mathbf{p}\}$ and $\rho(\mathbf{r},\mathbf{p})$ the normalized probability density function of the given ensemble such that:

$$\rho(\mathbf{r},\mathbf{p}) = \frac{\tilde{\rho}(\mathbf{r},\mathbf{p})}{\int_{\forall\Gamma}\tilde{\rho}(\mathbf{r},\mathbf{p})\mathrm{d}\mathbf{r}\mathrm{d}\mathbf{p}} = \frac{\tilde{\rho}(\mathbf{r},\mathbf{p})}{\mathrm{Z}(\mathbf{r},\mathbf{p})}, \tag{III-43}$$

with $\tilde{\rho}(\mathbf{r},\mathbf{p})$ the plain density in the phase space and Z the partition function of the given statistical ensemble.

The dynamics resulting from the time integration of the equations of motion will give trajectories which – due to the inner nature of MD simulations – might be far from real trajectories. Indeed, the many approximations in MD simulations result in an imperfect description of the many-fold potential energy surface (PES) functional. Thus, while the system is making a path on the PES, the classical approximations leaving the system in its fundamental state only, the fixed time-step which might not sample accurately some fast atomic processes, the classical estimation of the parameters of the potential energy functional as well as its limited formal expression or the finite numerical precision of the computations make this path potentially far from the *real* path on the *real* PES. Thus, not only the idea of ensemble average is necessary to estimate macroscopic observables, but only macroscopic observables should be measured and ultimately, no “true” causal relations should be considered in between two successive frames of a trajectory. Nonetheless, macroscopic state transitions can be studied by means of MD simulations if one can sample accurately enough the phase space in the different macroscopic states. This allows MD to be a tool of choice for the study of docking, of protein unfolding, of lipid flip-flopping, *etc.* even if these phenomena are by nature time-dependent. This leads to another concern: the ergodic hypothesis is never proven for the systems one studies. Not only we do not know if this hypothesis can be applied but we know that the typical times (in the range of the tens to the hundreds of nanoseconds) used for sampling the phase space of a system with a dynamic equilibrium are usually extremely small towards the real time range that should be used if one wants to explore most of the phase space. However, MD simulations have proven to give a precise and useful insight in the studies of atomic and molecular processes, and have proven to lead to trustworthy estimations of thermodynamic observables. This is mainly because, working in the vicinity of some local minimum of the PES, the macroscopic observables are converging rapidly to some values close to the true values.

3.1. Integrating the equations of motion

Considering the classical equations of motions described earlier, one can assume that there exists a finite time-step Δt which will allow sampling the resulting trajectories well enough. To take into account the fast vibrational modes of C-H bonds, it is customary to take a time step of 1 fs. In the Gromacs package, the time step is defined system wide at the contrary of some other MD packages. However, the use of constraints to describe some of the bonds involving fast relaxation times might allow the user to increase this time step up to 2 fs in the frame of AAMD.

Formally, the discretization of the Newton's equations can be obtained by a simple Taylor expansion of the coordinates and the velocities of any atom i:

$$\begin{cases} \mathbf{r_i}(\mathrm{t}+\Delta\mathrm{t}) = \mathbf{r_i}(\mathrm{t}) + \mathbf{v_i}(\mathrm{t})\Delta\mathrm{t} + \mathbf{F_i}(\mathrm{t})\dfrac{\Delta\mathrm{t}^2}{2\mathrm{m}_i} + \dddot{\mathbf{r}}_\mathbf{i}(\mathrm{t})\dfrac{\Delta\mathrm{t}^3}{3!} + \mathcal{O}(\Delta\mathrm{t}^4) \\ \mathbf{v_i}(\mathrm{t}+\Delta\mathrm{t}) = \mathbf{v_i}(\mathrm{t}) + \mathbf{F_i}(\mathrm{t})\dfrac{\Delta\mathrm{t}}{\mathrm{m}_i} + \ddot{\mathbf{v}}_\mathbf{i}(\mathrm{t})\dfrac{\Delta\mathrm{t}^2}{2} + \dddot{\mathbf{v}}_\mathbf{i}(\mathrm{t})\dfrac{\Delta\mathrm{t}^3}{3!} + \mathcal{O}(\Delta\mathrm{t}^4) \end{cases}. \qquad \text{(III-44)}$$

One of the simplest numerical implementations of an integration algorithm is the Euler algorithm which truncates the Taylor expansion at the second order. However, this algorithm lacks different fundamental properties in need when one deals with Hamiltonian systems which are conserving different quantities. The main one is the direct consequence of the Liouville's theorem which states that a canonical transformation – such as the time-integration of the equations of motion – should conserve the volume of the phase space for any Hamiltonian system. The kinds of transformations which are conserving such quantity are called symplectic. If one wants to compute one *real* trajectory in the phase space of an ensemble of particles, the integrator should fulfill such property as symplecticity. Otherwise, the computed virtual trajectory will rapidly become far from the *real* one implying that the system will not follow the real dynamics and that its *a priori* conserved properties, such as its energy in the case of time-independent Hamiltonian systems, might not be conserved anymore. At the same time, conservation of energy, angular momentum or other conserved quantities directly depends on the property of time-reversibility of an integration algorithm. Indeed, in the case of time-reversible algorithm, any backwards transformation in time will lead ultimately to the set of initial conditions, *i.e.* to the initial values of the conserved quantities, meaning that the drift on these values should be null. The Euler algorithm is neither symplectic nor time-reversible leading to important energy drifts for long time integrations, which sum to the ineluctable round-off errors, resulting in trajectories far from the real trajectories.

This is on these bases that the Verlet family of integrators was developed. The original Verlet algorithm is based on the knowledge of both the current positions of the atoms $\mathbf{r}(\mathrm{t})$ and the positions of these atoms at the previous time step $\mathbf{r}(\mathrm{t}-\Delta\mathrm{t})$. On top, the forces at the time t, derived from the interatomic potential are also necessary. This algorithm does not couple positions and velocities as it is the case for the Euler algorithm:

$$\mathbf{r_i}(\mathrm{t}+\Delta\mathrm{t}) = 2\mathbf{r_i}(\mathrm{t}) - \mathbf{r_i}(\mathrm{t}-\Delta\mathrm{t}) + \mathbf{F_i}(\mathrm{t})\frac{\Delta\mathrm{t}^2}{2\mathrm{m}_i} + \mathcal{O}(\Delta\mathrm{t}^4). \tag{III-45}$$

The Verlet algorithm gives rise to numerical imprecisions because a small term of order $\Delta\mathrm{t}^2$ is added to a difference of $\mathcal{O}(\Delta\mathrm{t})$ terms. But the inner nest of the problem resides in the computations of the velocities. The first drawback of this formalism is that the computation of the velocities is subsequent to the update of the position by one step, the velocities being computed as follows:

$$\mathbf{v_i}(\mathrm{t}) = \frac{\mathbf{r_i}(\mathrm{t}+\Delta\mathrm{t}) - \mathbf{r_i}(\mathrm{t}-\Delta\mathrm{t})}{\mathbf{2}\Delta\mathrm{t}} + \mathcal{O}(\Delta\mathrm{t}^2). \tag{III-46}$$

Finally, if the error in positions is of the fourth order, it remains on the second order for the velocities.

Mainly two algorithms were proposed to address the issues of the Verlet integrator; namely leap-frog and velocity-Verlet. These two algorithms are implemented in the Gromacs package but the last one does not allow the use of every option and may be more time-consuming. On the other hand, the use of leap-frog algorithm might lead to bigger imprecisions than velocity-Verlet, especially when one does not work in the microcanonical ensemble. However, the size of our systems, the important number of simulations which had to be undertaken and the in-development status of the MD techniques and setups we used in this thesis drove us to stick to the leap-frog algorithm, especially in a demand of performance and stability.

Though better algorithms exist, the errors induced by the use of the leap-frog integrator in the frame of our work with mid-size systems (several 100 000 atoms) remains small[4]. The leap-frog algorithm requires the expression of the forces determined from the potential energy and permits to compute the new set of positions and velocities where these both sets of parameters are calculated with half a time-step of difference:

$$\begin{cases} \mathbf{r}(\mathrm{t}+\Delta\mathrm{t}) = \mathbf{r}(\mathrm{t}) + \mathbf{v}\left(\mathrm{t}+\frac{1}{2}\Delta\mathrm{t}\right)\Delta\mathrm{t} \\ \mathbf{v}\left(\mathrm{t}+\frac{1}{2}\Delta\mathrm{t}\right) = \mathbf{v}\left(\mathrm{t}-\frac{1}{2}\Delta\mathrm{t}\right) + \mathbf{F}(\mathrm{t})\frac{\Delta\mathrm{t}}{\mathrm{m}} \end{cases} \tag{III-47}$$

---

[4] Main errors involved, due to temperature/pressure coupling, are decreasing with 1/N.

3.2. MD simulations in other statistical ensembles

The notion of measure in statistical physics is linked to the statistical ensemble in which one works. The Hamiltonian ruling the atomic interactions is intrinsically time independent. Hence, the system naturally conserves its energy. Similarly, the Hamiltonian used in MD simulations describes traditionally a closed system where the number of atoms N is also conserved. Finally, the intrinsic definition of the simulation box conserves the volume of the system: by default, integration in time has no consequences on the box size. Thus, the natural ensemble in which MD simulations are applied is the microcanonical ensemble (NVE).

If the NVE ensemble is natural in MD simulations, NVT, NPT, NPH or other ensembles are more common in real-life experiments. Working in isobaric and/or in isothermal conditions is generally achieved by coupling the system to a barostat and/or to a thermostat. In other words, one generally couples the system to a big enough environment whose macroscopic properties are the ones to be reached by the system; the size of this environment will allow it not to be perturbed by the coupling so that one may consider that the environment is all the time at the equilibrium with the same macroscopic properties as in the initial conditions.

The use of a thermostat or of a barostat means that one should modify the Newton's/Hamilton's equations of motions. In such case the incompressibility of the phase-space assured by the Liouville's theorem does not apply since the system is not Hamiltonian anymore. This might drive the measures in the system not to be invariant upon canonical transformation and thus, the time average of an observable may not give an ensemble average of this observable. Thus, some methods that are used as thermostat, *e.g.* the Nosé-Hoover method, tackle this problem by conserving the measure for canonical transformations.

A more general problem when one wants to work in a statistical ensemble is that the coupling should give not only a coherent averaged value of any macroscopic observables but also of its fluctuations. The most widely used thermostat and barostat are based on the Berendsen method. Applied as a thermostat, the velocities are scaled during the integration process so that the variation of the temperature will be proportional to the difference in between the target temperature and the measured one:

$$\frac{\mathrm{dT(t)}}{\mathrm{dt}} = \frac{1}{\tau}\left(\mathrm{T}_0 - \mathrm{T(t)}\right), \tag{III-48}$$

with the time constant τ determining the strength of the coupling in between the system and the heat bath at the temperature T_0. This last parameter has a crucial importance: the coupling is null for $\tau \rightarrow \infty$ and instantaneous for $\tau = 0$. For too small values, the strong discontinuities in the particle velocities and the unrealistic fluctuations of the temperature will result in a dramatic bias. Generally, the values of τ are in the range of 1/10 ps. Importantly, applying this thermostat drives the system not to sample the canonical ensemble. The error on ensemble averages being inversely proportional to N, most of the computations using this thermostat for big enough system will still lead to quite correct estimates of the observables.

In this work, we have been using the velocity-rescaling method which is a variant of the Berendsen thermostat at the notable difference that a stochastic term is included in order to generate a correct kinetic energy K distribution [99]. The fluctuations given by the use of this thermostat would be statistically relevant in the frame of the canonical ensemble.

More complex approaches were developed and it worth mentioning the existence of the Nosé-Hoover dynamics. This thermostat implies a more complicated scheme where the Newton’s equations of motions are modified to include explicitly a friction term which plays the role of the coupling term to the thermal reservoir. This method shows some bad performances during the equilibration process and might generate – in some cases – non-ergodic systems. In the light of this information, we decided to keep to the simpler velocity-rescale algorithm whose performances and accuracy are proven.

The very same kinds of methods are applied once one needs to work with constant pressure. In the case of membrane simulations, it has been proven that the NPT ensemble is the most appropriate, with modern FF, to reproduce accurately physicochemical properties. In this thesis, we assumed that the efficiency of the Berendsen algorithm and the rather limited bias it implies were justifying its use over more sophisticated methods such as Parrinello-Rahman.

Chapter IV - **Realistic model plasma membranes of normal and cancer cells**

Membranes in cells are usually considered to act as physical barriers that allow compartmentalization and specialization of the intracellular medium. They are also highly dynamic assemblies, changing their shape, composition and properties on a variety of spatial and temporal scales. This dynamical reshaping of membranes occurs during different cell processes such as motion, division, differentiation and vesicle trafficking. Membranes must thus be sufficiently rigid and robust to maintain the integrity of the cell compartments and flexible enough to allow continuous changes of their shapes. Since the introduction of the fluid-mosaic model [102], many structural/property relationships like thermodynamic and mechanical properties have been elucidated on the basis of lipid self-organization arguments. However, many open questions remain concerning the links between membranes composition and their permeability to drugs. Determination of permeability membranes to drugs is indeed of great importance for toxicological reason, for addressing cell resistance issues to chemodrugs, but also for finding new strategies for targeting cells, especially cancer ones. In this thesis, we searched for chemical and physical features connected to membrane lipids that could help to differentiate cancer and normal cells and though be potential markers for selective targeting. We investigated three “main ingredients” that may play an important role on the membrane permeation to drugs, namely composition (lipids and cholesterol contents), curvature and asymmetry between leaflets of the lipid membranes. In the following section, a short review based on an analysis of a large set of results extracted from literature, is given. It helped us to build two realistic models of “cancer” and “normal” lipid matrices of the plasma membranes which could be subsequently used to study the permeation of small molecules – especially of cancer drugs. Of note, this literature search and the way these two models were built have been published recently in two articles [54, 103].

1. Plasma membrane properties at a glance: asymmetry, cholesterol distribution and curvature

The continuous increase of computer power has stimulated the rapid development of computational approaches for the modeling of realistic cell membranes using both atomistic and coarse-grained molecular dynamics techniques [19, 48-53]. In particular, recent works address such phenomena as lateral heterogeneity of the membranes (lipid rafts and micro-domains, lipid sorting) [48, 49] or the asymmetry of the lipid composition and the cholesterol content between the monolayers [29].

Although more and more computational studies are trying to mimic an actual asymmetric lipid content of the membrane monolayers [50-52, 54], a really few works are making these model membranes involved in a controlled setup aiming at studying the permeation properties of molecules of biological interest.

One of the main insights from the community in the structure of membranes concerns cholesterol (CHL). However, the transversal distribution of CHL – the most abundant molecule in eukaryotic membranes after the lipids, is subject to debates [20-22]. It has been observed experimentally [23-25] that CHL resides mostly in the cytoplasmic leaflet. On the other hand, the affinity of cholesterol to sphingomyelins (SM) has been shown experimentally [26] and *in silico* simulations also tend to show an increased distribution of CHL in the outer leaflet [27-29]. The existence of lipid rafts or micro/nano-domains in the membranes is another debated concept. It is shown that cholesterol and sphingomyelin lipids form regions of rigid liquid-ordered phase (Lo) *in vitro* in giant unilamellar vesicles (GUVs), in liposomes or in deposited lipid structures [1, 30, 31]. The rafts were also extensively studied *in silico* [30, 32-34]. However, there are difficulties in observing the rafts in real cells, which are usually attributed to their small life time or to their size, which appears to be much smaller in real cells in comparison to artificial membranes [26, 32, 35]. Despite the fact that the rafts are not yet observed directly in living cells, the influence of cholesterol and cholesterol-rich microdomains on the membrane rigidity, on permeability for small molecules and on the functioning of the membrane proteins is of great interest [36-39].

In normal eukaryotic cells, an asymmetry in the lipid composition between the monolayers of the plasma membrane is usually present. It is now recognized as an important factor of membrane functioning. In that case, the composition of the membrane leaflets is highly uneven [1-3] and is actively maintained by a group of proteins – the flippases and floppases. This results in an extracellular leaflet composed mostly of phosphatidylcholine (PC) and SM and a cytoplasmic leaflet enriched in phosphatidylserine (PS) and phosphatidylethanolamine (PE). In apoptotic cells, it is known that this asymmetry is not preserved. In 1989 it has been proposed that the plasma membrane of some cancer cells can also exhibit such a symmetrized structure. As a consequence, PS may be more exposed on the extracellular leaflet of their plasma membranes, while this anionic lipid is predominantly located in the intracellular leaflet in the normal cells [4, 5]. Subsequent studies using flow cytometry after labeling by annexin V confirmed these findings [6-8]. It was also shown that exposure of PS in cancer cells is not an artifact caused by the presence of apoptotic cells in the sample [9]. PS exposure was also detected in the vasculature of the tumors [10, 11]. Table IV-1 summarizes the existing literature about PS exposure in different cancers and cancer cell lines. It is now clear that the outer monolayer of cancer cells contains on average ~7 times more PS than the normal control cells. These findings are of importance since they could result in a new approach in targeting tumors by selective recognition of exposed PS [8, 14-17] or related redistribution of PE [18]. Despite the growing importance of this field we have found little research where *in silico* modeling of the membranes of cancer cells was performed [19].

Table IV-1. Overview of the relevant publications referring to a quantitative increase in PS exposure in the extracellular leaflet of the plasma membrane of tumorigenic cells. A group of publications addressing specially the overexpression of PS (and possibly the phosphatidylethanolamine) in the tumoral vasculature cells has been omitted. If this was possible, the relative increase in proportion of PS in the extracellular leaflet in a tumoral cell versus a reference one has been indicated. The cited papers are the work of Connor *et al.*[4], Utsugi *et al.*[5], Rao *et al.*[7], Sugimura *et al.*[12], Cichorek *et al.*[13], Schröder-Borm *et al.*[8], Kirszberg *et al.*[6] and Riedl *et al.*[9].

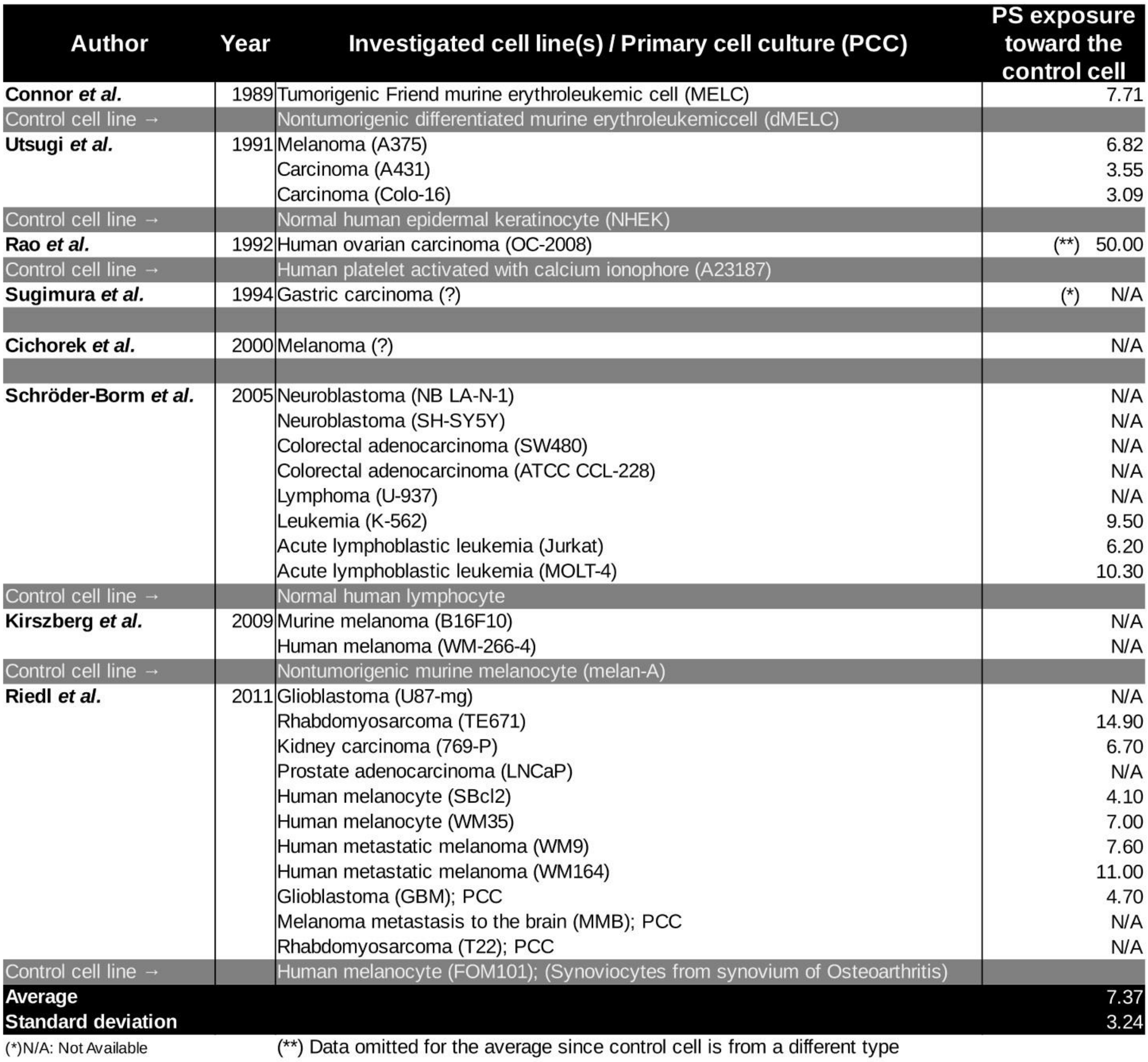

Author	Year	Investigated cell line(s) / Primary cell culture (PCC)	PS exposure toward the control cell
Connor *et al.*	1989	Tumorigenic Friend murine erythroleukemic cell (MELC)	7.71
Control cell line →		Nontumorigenic differentiated murine erythroleukemiccell (dMELC)	
Utsugi *et al.*	1991	Melanoma (A375)	6.82
		Carcinoma (A431)	3.55
		Carcinoma (Colo-16)	3.09
Control cell line →		Normal human epidermal keratinocyte (NHEK)	
Rao *et al.*	1992	Human ovarian carcinoma (OC-2008)	(**) 50.00
Control cell line →		Human platelet activated with calcium ionophore (A23187)	
Sugimura *et al.*	1994	Gastric carcinoma (?)	(*) N/A
Cichorek *et al.*	2000	Melanoma (?)	N/A
Schröder-Borm *et al.*	2005	Neuroblastoma (NB LA-N-1)	N/A
		Neuroblastoma (SH-SY5Y)	N/A
		Colorectal adenocarcinoma (SW480)	N/A
		Colorectal adenocarcinoma (ATCC CCL-228)	N/A
		Lymphoma (U-937)	N/A
		Leukemia (K-562)	9.50
		Acute lymphoblastic leukemia (Jurkat)	6.20
		Acute lymphoblastic leukemia (MOLT-4)	10.30
Control cell line →		Normal human lymphocyte	
Kirszberg *et al.*	2009	Murine melanoma (B16F10)	N/A
		Human melanoma (WM-266-4)	N/A
Control cell line →		Nontumorigenic murine melanocyte (melan-A)	
Riedl *et al.*	2011	Glioblastoma (U87-mg)	N/A
		Rhabdomyosarcoma (TE671)	14.90
		Kidney carcinoma (769-P)	6.70
		Prostate adenocarcinoma (LNCaP)	N/A
		Human melanocyte (SBcl2)	4.10
		Human melanocyte (WM35)	7.00
		Human metastatic melanoma (WM9)	7.60
		Human metastatic melanoma (WM164)	11.00
		Glioblastoma (GBM); PCC	4.70
		Melanoma metastasis to the brain (MMB); PCC	N/A
		Rhabdomyosarcoma (T22); PCC	N/A
Control cell line →		Human melanocyte (FOM101); (Synoviocytes from synovium of Osteoarthritis)	
Average			7.37
Standard deviation			3.24

(*)N/A: Not Available (**) Data omitted for the average since control cell is from a different type

Besides the asymmetry of the membrane, its curvature also plays an important role in many cellular processes [24, 40]. Recent studies have shown that membrane curvature is not a passive consequence of cellular architecture but an active driving force in many processes involving membrane remodeling and trafficking [104]. Local differences in membrane curvature form microenvironments in which specific molecular interactions are more likely to occur. Formation of the membrane curvature is achieved by the complex interplay between intrinsic curvatures of the lipids in the membrane leaflets, the influence of integral and peripheral proteins and the influence of the cytoskeleton. While the intrinsic spontaneous curvature of the membrane is mostly determined by its lipid composition, instantaneous local curvature is usually dynamically modulated by proteins which are either integrated into the lipid bilayer thus acting like wedges or attached to its periphery. In eukaryotes, the bin/amphiphysin/rvs (BAR)-domains containing proteins [41] are well-known for their ability to form 3D assemblies and act as molecular scaffolds that reshape the membrane and alter its mechanical properties. While the membrane proteins and the influence of the cytoskeleton could lead to dramatic changes in the membrane shape and curvature, the membrane lipids should redistribute and repack to adapt to these changes. Surprisingly, little attention is paid to lipid repacking and redistribution in curved membranes despite the fact that changes in the lipid composition are known to be important for a range of pathologies, such as cancer [42], Alzheimer’ s disease [43] and obesity [44]. The curvature influence in the distribution of cholesterol in the membrane, in the thickness of its leaflets and in the order parameter of the lipid tails as well as on the passive diffusion of drugs and small molecules through the membrane remains an opened question.

Some recent studies start to correlate the roughness of the plasma membrane to their potential cancerous character [45]. It is visible on Atomic Force Microscopy images of different cancer cell lines and sane cells, such as the breast cancer cell MCF7A and the sane breast cell MCF-10A [46, 47] that the surface shape of the cells is drastically different. One can expect that the curvature distribution function of malignant cells will be much larger than one of normal cells. This distribution function of the curvatures is possibly not only widened but also shifted to bigger curvatures. These hypotheses should be explored to understand if membrane curvature could result in different transport kinetics selectively towards the cell status.

Cellular phenomena such as the formation of synaptic vesicles [105] and apoptotic bodies [106, 107], the membrane fusion [108, 109], budding of enveloped viruses from the plasma membrane [110, 111], formation of the blebs during apoptosis [106, 107], blood cell maturing [112] and mitosis [113] are also likely to be influenced by phospholipid asymmetry, membrane curvature and cholesterol distribution [114]. That is why numerical simulations are nowadays considered as the best complementary techniques in membrane science since they are able to operate at an atomistic level. With the development of high-quality coarse-grained (CG) methods, such as the MARTINI force field [55-58], the global trend of membrane simulations shifted away from atomistic simulations. Coarse-grained models allow increasing time and length scales of simulations by several orders of magnitude. In the CG models the groups of adjacent atoms are combined into “beads” which interact with each other by means of empirical potentials. Since the number of beads is much smaller than the number of individual atoms, a significant increase in the speed of computations could be achieved [55-58]. In particular, CG methodology allows the simulation of very large membrane patches with a large number of lipid species, and which could be considered as accurate models for real cell membranes in terms of lipid content [51]. However, this study was focused on a flat membrane. Despite impressive progress in the field of CG simulations atomistic molecular dynamics studies of the membranes are still necessary to achieve an accurate atomistic description. Notably, atomistic simulations are necessary in the studies of detailed interactions of ligands and drugs with the membranes. An atomistic description also provides the most detailed view on the effects of curvature and asymmetry on the membrane properties including the translocation of ligands and drugs through the lipid bilayer. In the following sections, we present realistic lipid model membranes of normal and cancer cells with a tunable and controlled curvature. The properties of the membranes with different cholesterol content ranging from 0% to 33% molar ratio are compared. Also, a special focus has been put on the study of the effects of curvature, both on the CHL distribution and on the structural consequences on the membrane.

2. A realistic lipid model of plasma membrane with controllable curvature

Curvature, asymmetry, lateral heterogeneity and their non-trivial relationship make real cell membranes very complex objects, making them hard to study experimentally at a nanoscopic resolution. Discriminating membranes of cancer cells from normal ones is certainly beyond the possibilities offered by current experimental techniques. That is why numerical simulations at the molecular level are nowadays considered as the best complementary techniques in membrane science.

Building models with a given amount of different lipids and cholesterol is not a difficult task but controlling asymmetry and curvature of these systems remains a numerical challenge. To the best of our knowledge, there is no comprehensive and systematic study which addresses the influence of curvature on realistic membranes with asymmetric lipid content of monolayers. One of the possible reasons for this is the methodological difficulty of setting up, running and analyzing such simulations. Indeed, the membrane curvature is a transient property of the membrane which changes from one region to the other and evolves quickly over time [115]. In order to study the changes of various membrane properties as a function of curvature, one needs either to fix the curvature or to sample only those regions of the membrane which display the needed curvature at each simulation time step. The second option seems to be more attractive since it does not impose artificial constraints on the membrane and the methods for determining both local [61] and global [116] membrane curvatures as a function of atomic coordinates are available. However, sampling a sufficiently wide range of curvatures in free all atom MD simulations is problematic because of the required simulation times (up to hundreds of microseconds). Such times are accessible only in a few individual state-of-the-art simulations but they are still prohibitively large for routine use and especially for any systematic analysis. In contrast, restricting global membrane curvature to a particular predefined value is much more promising in this respect since it makes the problem much more computationally viable. However, no technique for restricting membrane curvature to some given value was available to date before this PhD work.

With the help of S. Yesylevskyy, we developed a new method for simulating membranes with a pre-defined curvature; the method is applicable at both the atomistic and coarse grained levels. It allows keeping free the lateral diffusion of the lipids without introducing major bias or artifacts. This technique does not change the basic properties of the membrane such as density, thickness or area per lipid and allows the influence of the membrane curvature to be studied.

2.1. Asymmetric flat membrane model of normal cells

At first, we designed a model for flat and asymmetric membranes which could also be subsequently used to force it to any designed curvature. The membrane was prepared as a bicelle which is limited by cylindrical caps in the xz plane and forms an infinite bilayer along the y direction (see Figure IV-1 and Figure IV-2). This allows the monolayers to relax to their optimal areas by exchanging lipids with the bicelle caps, which serve as "compensatory reservoirs". These caps are very important especially when the curvature on that membrane will be further imposed. Indeed, the areas of concave and convex monolayers become different in that case and the lipids have to redistribute in order to compensate for the resulting mechanical strain.

Another method using "inverted domains" was used in previous studies on the spontaneous bending of asymmetric membranes [62]. This method is not optimal for the current work because it doubles the size of the system and makes it less computationally friendly. To avoid these drawbacks we designed this present setup relying on this bicelle geometry of the membrane. The lipid content of inner and outer monolayers is different and their mixing in the regions of the bicelle caps should be prevented. In order to achieve this we used selective artificial repulsive potentials similar to the one used in previous works from our group [60-62]. All heavy atoms of the lipids (except the carbon atoms of the distal parts of the tails below the double bond) were assigned an additional weak Van der Waals repulsive potential (σ=0.8 nm, $\varepsilon=1\cdot10^{-7}$ J·mol^{-1}) which acts between the lipids of inner and outer monolayers only. This allows the ends of the lipid tails to interact normally in the bilayer region of the bicelle while the lateral contacts between the lipids from the different monolayers in the caps of the bicelle become energetically unfavorable. Such a setup prevents the mixing of the monolayers effectively without any detectable effect on the bilayer part of the system.

The cholesterol molecules could diffuse freely through the bicelle caps which allows their redistribution between the monolayers during equilibration of the system. This is important because the correct cholesterol content in each monolayer is not known in advance and such mechanisms of cholesterol exchange between the monolayers facilitates to achieve an optimal cholesterol content in the equilibrated system. Only the middle of the bicelle, where the bilayer structure is not perturbed by the caps (shaded region in Figure IV-1), is used for analysis.

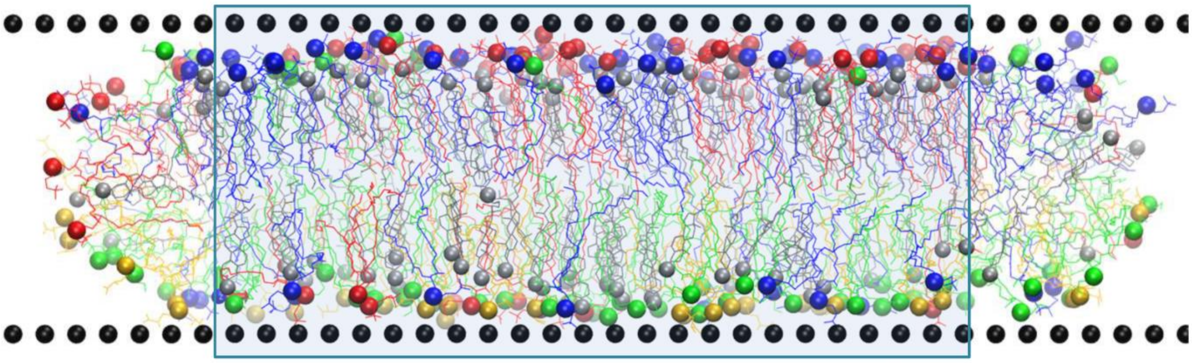

Figure IV-1. Snapshot of the simulated "normal membrane" system. The wall particles are shown as black spheres. PC lipids are blue, SM are red, PE are green and PS are yellow. Cholesterol molecules are gray. Head groups of lipids and cholesterol are shown as spheres. The central region of the bicelle which is used for analysis is shaded.

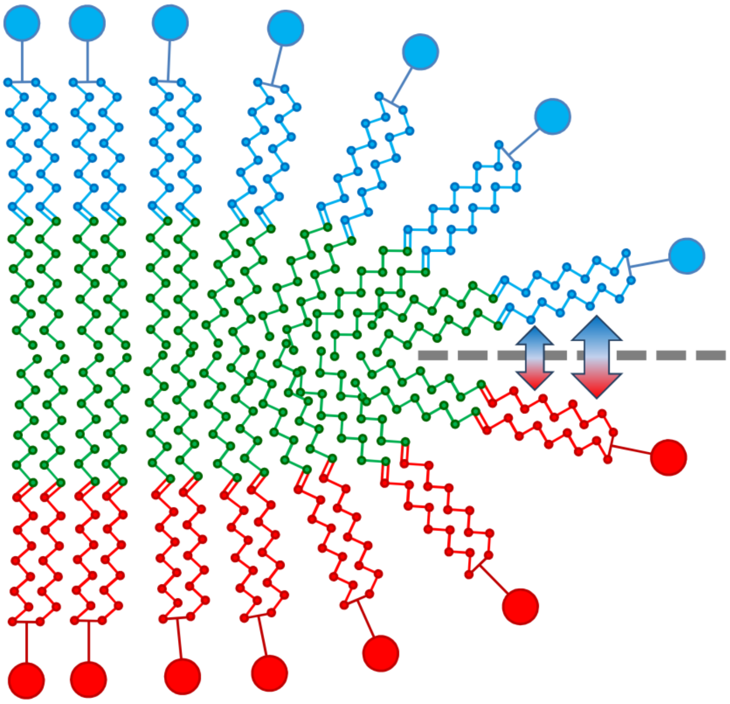

Figure IV-2. Scheme of the bicelle cap which prevents mixing of the lipids from different monolayers. Distal parts of the tails (below the double bond), which interact normally, are shown in green. Proximal parts of the tails and head groups of lipids from different monolayers are shown in blue and red respectively. There is an additional artificial van der Waals repulsion between blue and red atoms (shown by the arrows) which prevents the mixing of the lipids from different monolayers. Approximate boundary between the monolayers is shown by gray dashed line.

2.2. Asymmetric curved membrane model: the bending procedure

We used artificial dummy particles for bending the previous asymmetric flat membrane described in the previous section. The idea was to put the membrane between two repulsive surfaces of artificial particles – the walls – which restrict the global shape of membrane but which do not affect the lateral dynamics of individual membrane lipids (Figure IV-3). We decided to bend the membrane in a single xz plane for simplicity; however, our method is applicable to any desired shape in three dimensions.

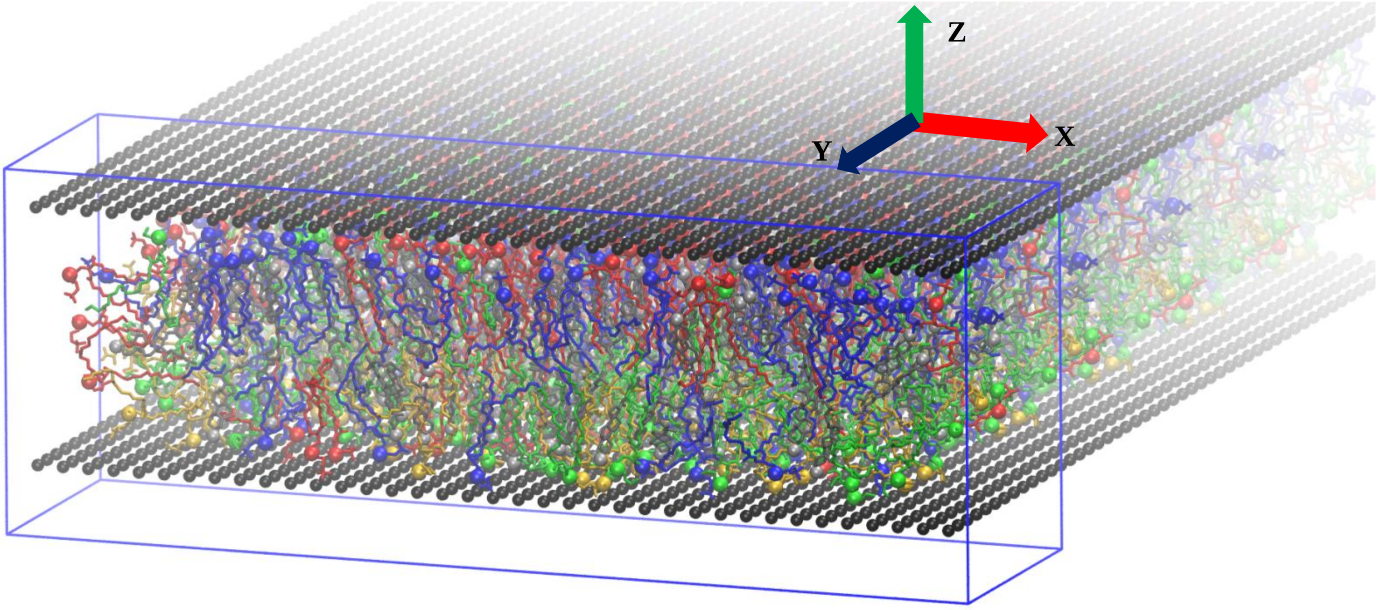

Figure IV-3. Perspective view of the simulated "normal membrane" system. The wall particles are shown as black spheres. PC lipids are blue, SM are red, PE are green and PS are yellow. Cholesterol molecules are gray. Head groups of the lipids the cholesterol are shown in as spheres. Four periodic images of the system are shown in the y direction. The blue frame shows the simulation box.

The walls are composed of independent non-interacting beads which consist of an anchor and a shell particle. The anchor is a dummy particle which is fixed in absolute coordinates and which does not interact with any other particles in the system. The shell particle is connected to an anchor by a harmonic bond of zero length with a force constant of 10 $kJ \cdot mol^{-1} \cdot nm^{-2}$. The shell particles selectively interact with the carbon atoms of the lipid acyl tails by van der Waals interactions only. The parameters of this Lennard-Jones interaction are σ=0.85 nm and $\varepsilon=1 \cdot 10^{-5}$ $J \cdot mol^{-1}$ which means that the potential is purely repulsive within the short-range cut-off r_c=0.8 nm widely adopted in Amber force field [117]. Such a setup eliminates unwanted direct interactions of the lipid atoms with fixed anchor particles and allows the walls to be positioned precisely at the same time by moving anchors to the desired position.

The walls are initially at the level of lipid head groups of each monolayer of the flat bilayer at a distance of 5 nm from each other. The dummy beads are arranged in a rectangular grid in the plane of the wall with a spacing of ~0.51 nm.

The shell particles of the walls are impermeable for the hydrophobic lipid tails but completely transparent for all other atoms. Thus, they restrict the general shape of the membrane hydrophobic core effectively without influencing the lateral diffusion of the lipids or the dynamics of lipid head groups, cholesterol, ions or water molecules. The distance between the walls and the parameters of repulsive

Van der Waals interactions are adjusted empirically in order to minimize the influence of the walls on the membrane structure and properties. The density profiles of various chemical groups of the lipids were compared for planar bilayers with and without the walls.

The procedure of bending the membrane starts from the planar bicelle equilibrated in the presence of the walls. The shape of the membrane is changed gradually by moving the anchor particles of the walls towards their new locations, which correspond to the membrane with the desired curvature. The shell particles push the hydrophobic core of the membrane and force it to bend accordingly.

Figure IV-4 shows three production systems used in this work: the initial planar system with zero curvature ($c = 0\ nm^{-1}$, middle panel in Figure IV-4), the system with positive curvature ($c = 0.2\ nm^{-1}$, top panel in Figure IV-4) and the system with negative curvature ($c = -0.2\ nm^{-1}$, bottom panel in Figure IV-4). All systems were subject to production runs which were 250 ns long.

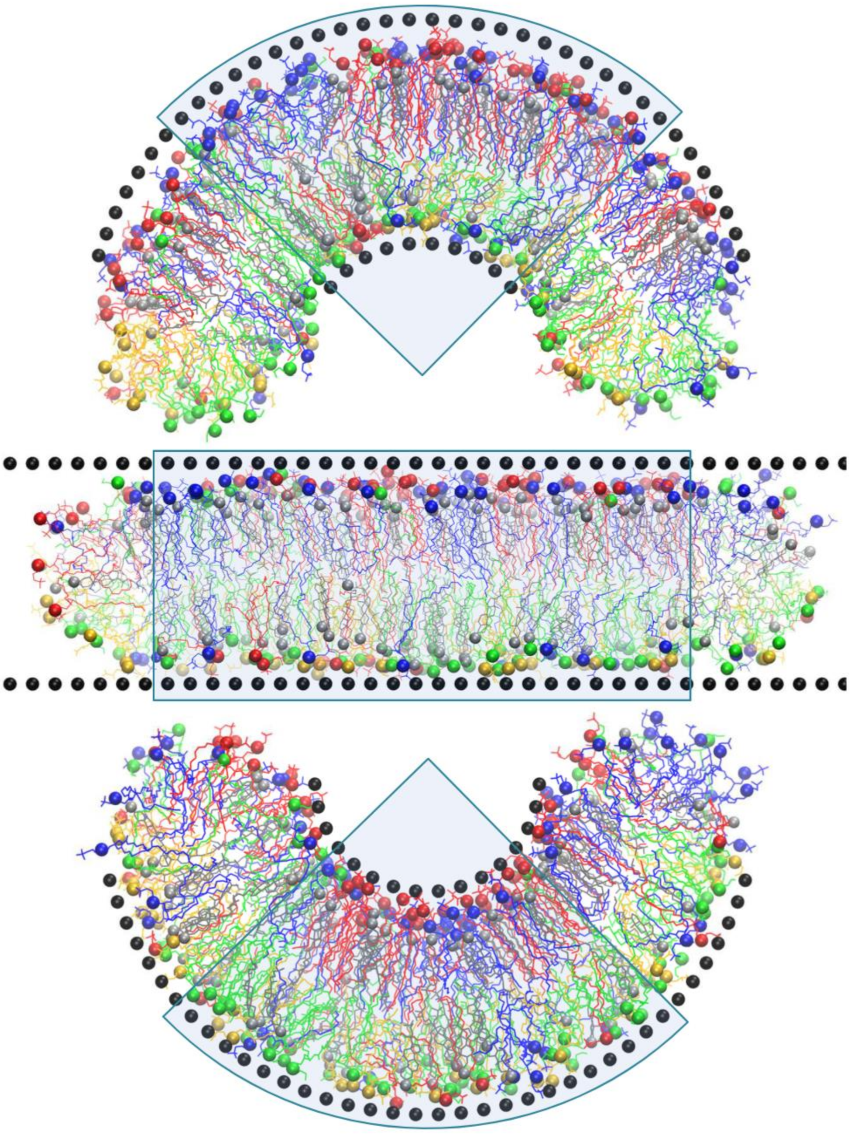

Figure IV-4. Snapshots of the simulated systems with the curvature c = 0.2 nm-1 (top), c = 0 nm-1 (middle) and c = -0.2 nm-1 (bottom). The wall particles are shown as black spheres. PC is blue, SM is red, PE is green and PS is yellow. Cholesterol molecules are gray. Head groups of lipids and cholesterol are shown as spheres. The sectors which are used for analysis are shaded.

In order to produce the curved membranes, the following procedure is used. The planar bilayer equilibrated in the presence of the walls is used as the initial system. The mean curvature c which we wanted to obtain is set and the center of the curvature is determined as shown in Figure IV-5. New positions of the anchor particles, which correspond to desired curvature, are also computed. The distances between the dummy beads within each wall are kept constant to ensure that the density of dummy particles per unit area of each monolayer is the same as in the planar bilayer. After that all anchor particles are moved with a constant rate towards their new positions during a time period of 5 ns. The dummy particles push the hydrophobic core of the membrane and force it to bend accordingly. Due to the different arc lengths of upper and lower walls some beads of the latter, which appear beyond the needed sector, are removed as shown in Figure IV-5. The system is then equilibrated for 200 ns with the anchor particles fixed in their new positions in order to relax any strain introduced by the forced bending. The bending is performed in several stages with a curvature step of 0.05 nm^{-1} (from 0 to 0.05 nm^{-1}, from 0.05 to 0.1 nm^{-1}, *etc.*) to reduce the mechanical stress imposed on the bicelle at each stage. For our asymmetric bicelle, the direction of the bending (upwards or downwards) is important due to the different lipid content of the monolayers. Nine systems were generated with curvatures of -0.2, -0.15, -0.1, -0.05, 0, 0.05, 0.1, 0.15 and 0.2 nm^{-1} where positive curvature means bending downwards (inner monolayer is concave as shown in Figure IV-5) while negative curvature means bending upwards (outer monolayer is concave). The two systems with the largest curvatures (c = 0.2 nm^{-1}, top panel in Figure IV-4, and c = -0.2 nm^{-1}, bottom panel in Figure IV-4) were used for the production runs which were 250 ns in duration.

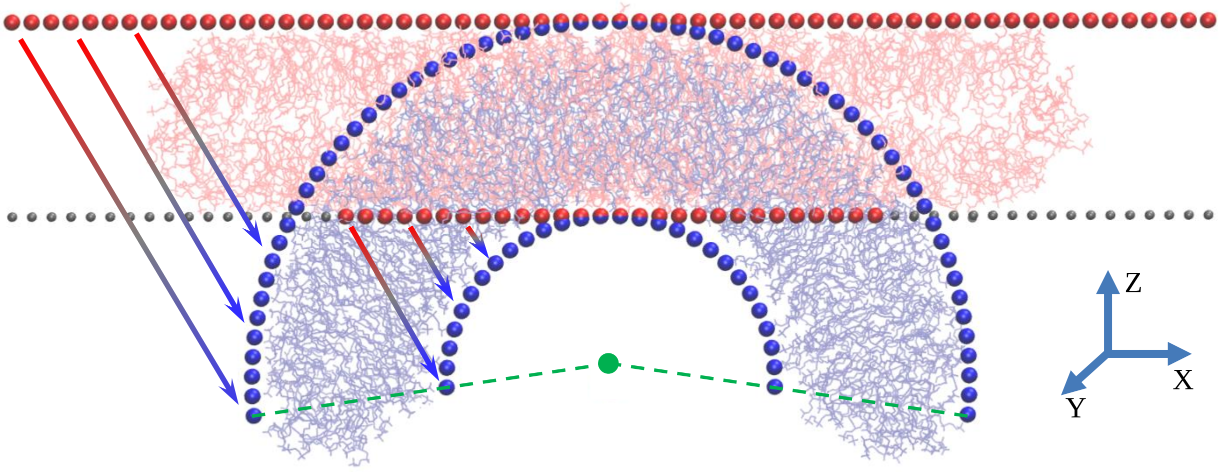

Figure IV-5. Scheme of membrane bending showing a model bicelle with a final curvature of 0.15 nm^{-1}. The initial planar bicelle is shown as pink lines. The final curved bicelle is light blue. Wall particles are shown as red (initial positions) and blue (final positions) spheres. The wall particles from lower wall, which are dropped after the bending, are gray. The arrows show the trajectories of pulling of the wall particles. Green point indicates the center of curvature and the dashed lines indicate the sector occupied by the walls.

2.3. The “normal” and “cancer” model membranes

With such bicelle-like systems and bending procedure, any type of membranes could be in principle generated with good accuracy. In the course of this PhD, we created a realistic model of the lipid matrix of the plasma membrane, referred to as “normal membrane” hereafter, which was designed according to well-established lipid content of mammalian erythrocyte membranes [59]. Phosphatidylinositol was not included into the present simulations due to its small concentration which results in about one molecule per system. In this model, the asymmetry of real mammalian plasma membranes is taken into account – the outer monolayer is enriched in sphingomyelin (SM) and 1,2-dioleoyl-sn-glycero-3-

phosphocholine (DOPC), while the inner monolayer is enriched in 1,2-dioleoyl-sn-glycero-3-phosphoethanolamine (DOPE) and 1,2-dioleoyl-sn-glycero-3-phospho-L-serine (DOPS).

The model of the lipid matrix of the plasma membrane of a cancer cell, referred to as “cancer membrane” hereafter, was built using the same protocol but with increased proportions in DOPS and DOPE in the extracellular leaflet. Figure IV-6 shows a schematic representation of the normal and cancer membranes along with their lipid compositions and a comparison to available experimental data. Table IV-2 shows the lipid content of the monolayers of normal and cancer membranes. In the case of the cancer membrane the distribution of the lipid species was symmetrized to emphasize the overexpression in PS/PE in the extracellular leaflet.

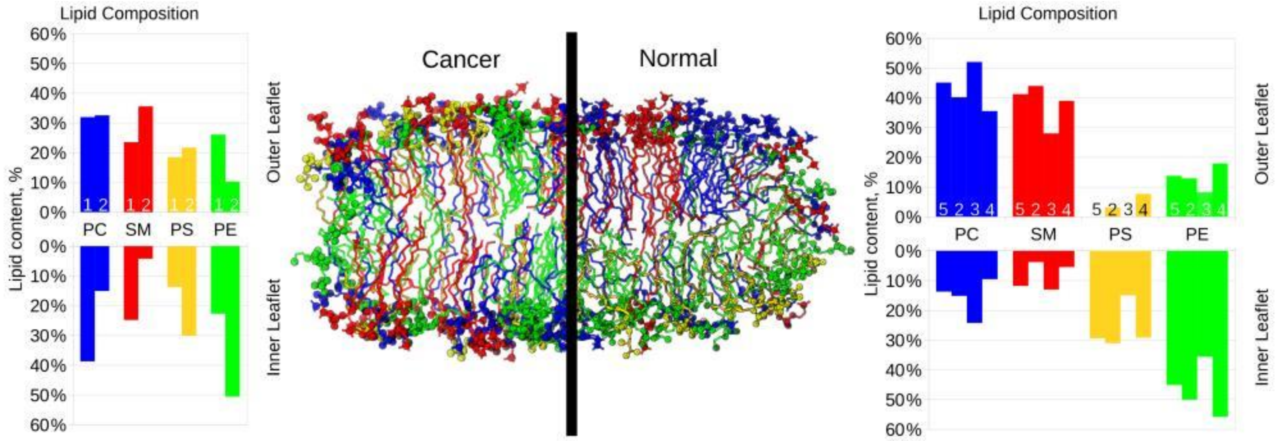

Figure IV-6. Snapshots of the simulated systems for cancer and normal membrane models. DOPC is shown in blue, SM in red, DOPS in yellow and DOPE in green. For the sake of clarity cholesterol is not shown. Head groups of lipids are shown as spheres. The histograms show the relative abundance of different lipid species for inner and outer monolayers for each membrane model (normalized for each monolayer). Numbers 1 and 5 correspond to the cancer and normal models presented in this work respectively, model 2 refers to the work by Klähn and Zacharias [19], model 3 to the work by Ingólfsson *et al.* [50], model 4 to the data reported by Marquardt *et al.* [24].

Table IV-2. Lipid content (absolute number of molecules) of the monolayers of simulated membrane models.

Component	Normal		Cancer	
	Outer	Inner	Outer	Inner
SM (sphingomyelin)	42	12	27	27
PC (1,2-dioleoyl-sn-glycero-3-phosphocholine)	46	14	30	30
PE (1,2-dioleoyl-sn-glycero-3-phosphoethanolamine)	14	46	30	30
PS (1,2-dioleoyl-sn-glycero-3-phospho-L-serine)	0	30	15	15
Cholesterol	51	51	51	51

The initial bicelle has a cholesterol molar content of 33% relative to the lipids. We also constructed the systems with cholesterol contents of 15% and 0% by randomly removing half of the cholesterol molecules in the former and all of them in the latter. An equal amount of cholesterol was removed from both monolayers in the case of 15% content.

Initially each monolayer contains 102 lipids and 51 cholesterol molecules (for the systems with 33% CHL). Cholesterol molecules are allowed to diffuse through the bicelle caps and redistribute themselves between the monolayers during the simulations. The lipids are arranged initially into a 17x6 grid in each monolayer with cholesterol molecules intercalated randomly between them. The system is pre-equilibrated as an infinite bilayer with periodic boundary conditions for 10 ns and then converted to a bicelle by adding extra layers of water from both sides in the x direction. After the addition of the restricting walls, the system is equilibrated as a planar bicelle for ~500 ns.

A reference single-component DOPC membrane was also simulated. This system was also arranged as a bicelle using the same setup except for the fact that no repulsive potential is applied in the caps since the mixing of the monolayers is allowed in this case. The flat bicelle with the walls was built separately using the procedure described before. It contained 288 lipids and ~46000 water molecules.

For comparison, a pure DOPC bilayer containing 128 lipids and 5120 water molecules was also built as an unconstrained normal bilayer.

3. Accuracy of the membranes models: the influence of the walls

In order to check whether the repulsive walls, which are used to maintain the membrane curvature, influence the structure of the membrane, we prepared a reference bilayer, which is free from any restraints and has the same lipid content as the flat part of the bicelle with restricting walls. We used the last 50 ns of the trajectory of equilibrated flat bicelle and counted the mean number of lipids and cholesterol in its bilayer region excluding the caps. We then constructed the flat infinite bilayer with the same composition and simulated it using the usual setup with semi-isotropic pressure coupling for 200 ns without any restraints. We computed the density profiles for the lipid heads, lipid tails and cholesterol molecules across the membranes in the cases of flat reference bilayer and the bi4.celle with zero curvature. The results are shown in Figure IV-7.

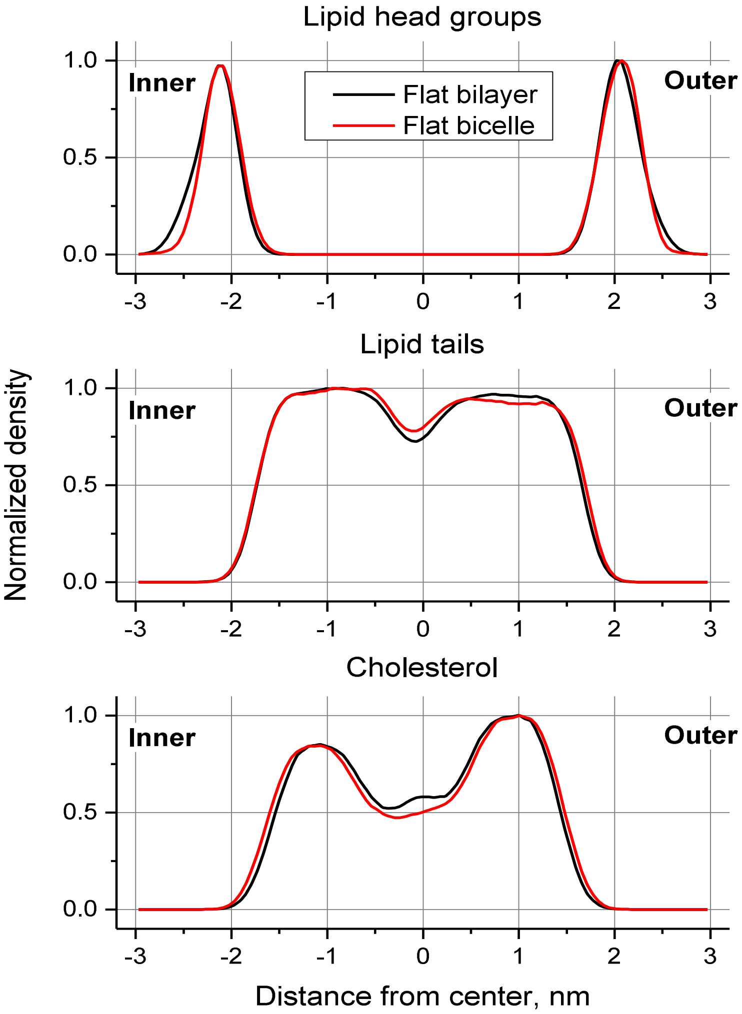

Figure IV-7. Normalized densities of lipid head groups, lipid tails and cholesterol in reference flat bilayer and flat bicelle of the same composition.

It can be clearly seen that the influence of the walls on the distribution of lipid head groups is minor. The walls slightly decrease the outer parts of the distribution for head groups in the region around 2.5 nm from the center. Thus the walls marginally decrease the number of headgroups protruding far into the bulk phase while keeping their average position and other parts of distribution unchanged. The distributions of the lipid tails with and without the walls are almost indistinguishable except for the central region where minor deviations are observed. The thickness of the hydrophobic membrane core is not affected by the walls. The distribution of cholesterol is marginally broader in the bicelle with the walls, but this effect is very small. Differences in the central region of the membrane are rather chaotic and are likely to be caused by an undersampling of cholesterol diffusive motions, which is inevitable in such a complex multi-component system.

In order to verify if the influence of repulsive walls depends on lipid composition we additionally studied simple monocomponent membrane composed from pure 1,2-dioleoyl-sn-glycero-3-phosphocholine (DOPC). For this membrane we prepared the reference bilayer without restrictive walls and the planar bicelle with the walls in the same way as for asymmetric membrane, described above. We then computed the density profiles for the lipid head groups and tails in both systems. The results are shown in Figure IV-8. They are very similar to Figure IV-7, which confirms that the influence of the walls remains minor regardless of the lipid composition of the membrane.

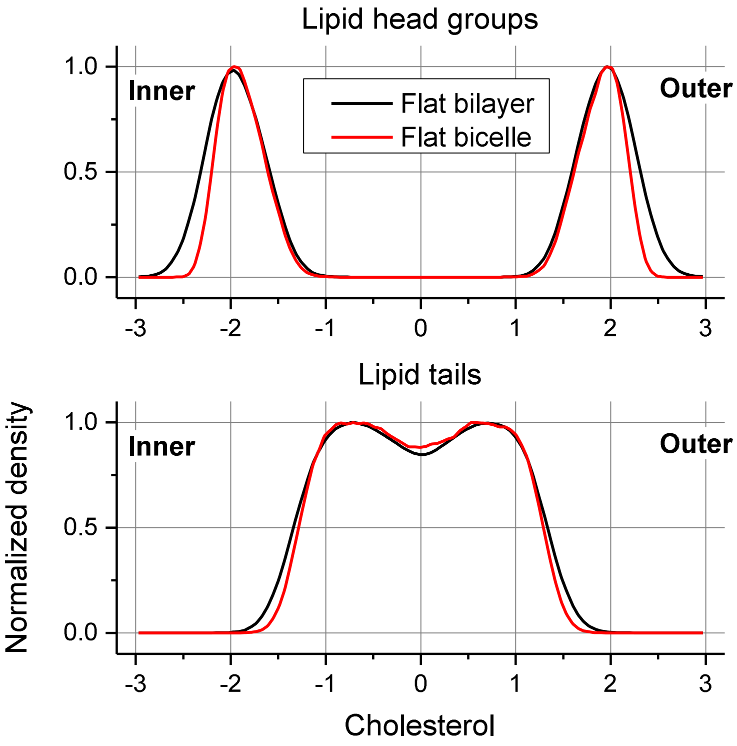

Figure IV-8. Normalized densities of lipid head groups and tails in reference flat bilayer and flat bicelle for symmetric pure DOPC membrane.

At that step, it is possible to conclude that the repulsive walls in our setup have almost no influence on the major structural properties of the flat membrane such as the thickness of the hydrophobic core, average location of the head groups and distribution of cholesterol. In the case of the curved bicelles it is not possible to separate the influence of the walls from the influence of the curvature itself because the walls are necessary to maintain the curvature. We assume that the effects observed in the curved bicelles are caused mostly by the membrane curvature itself while the influence of the walls remains as small as in the flat system. Such extrapolation may not be completely accurate but, given the absence of any reference system for curved membranes, it remains the best possible assumption.

5. The effects of curvature on the membrane properties

5.1. Area per lipid *versus* curvature

The area per lipid is one of the basic properties used to characterize lipid bilayers. It is known to depend on the mechanical strain of the membrane, lipid composition and cholesterol content. Thus, it is expected to depend strongly on the membrane curvature as well. The areas per lipid were determined using the

Voronoi tessellation [63]. In brief, the tangent membrane plane was determined in the vicinity of the head group of each lipid. Positions of adjacent lipid heads are projected onto this plane and the area of the Voronoi polyhedron centered at the target lipid is computed. This technique allows us to compute the areas per lipid and to obtain statistics per lipid type. This provides reliable estimates of the average area per lipid for all lipid species in inner and outer monolayers (Figure IV-9). All lipid species follow the same trend, namely a decrease of the area per lipid from convex to flat and from flat to concave monolayers. This decrease is remarkably large and reaches between 25-35% depending on the lipid type. The areas per lipid of the same lipid species in the inner and outer monolayers are different but large standard deviations make the significance of these differences less reliable.

The observed dramatic changes in the areas per lipid could be explained by geometrical considerations. Indeed, the head groups of the lipids become congested in the concave monolayers while much more space is available to them in the convex monolayers. As a result, the area per lipid is expected to be maximal in convex monolayers and minimal in the concave ones.

The contribution of the lateral mechanical strain to the changes of the areas per lipid is minimal in our setup. The inner and outer monolayers equilibrate their surface areas and volumes quickly due to the bicelle caps, which serve as adjustable reservoirs for extra lipids. We also calculated the mean number of lipids found in the inner and outer monolayers of the bicelle for different curvature. We observed that the number of lipids in both monolayers changes in accordance with the membrane curvature. The caps of the bicelle effectively accommodate excessive lipids from the concave monolayer and donate necessary amount of lipids to the convex monolayer which prevents development of mechanical strain effectively.

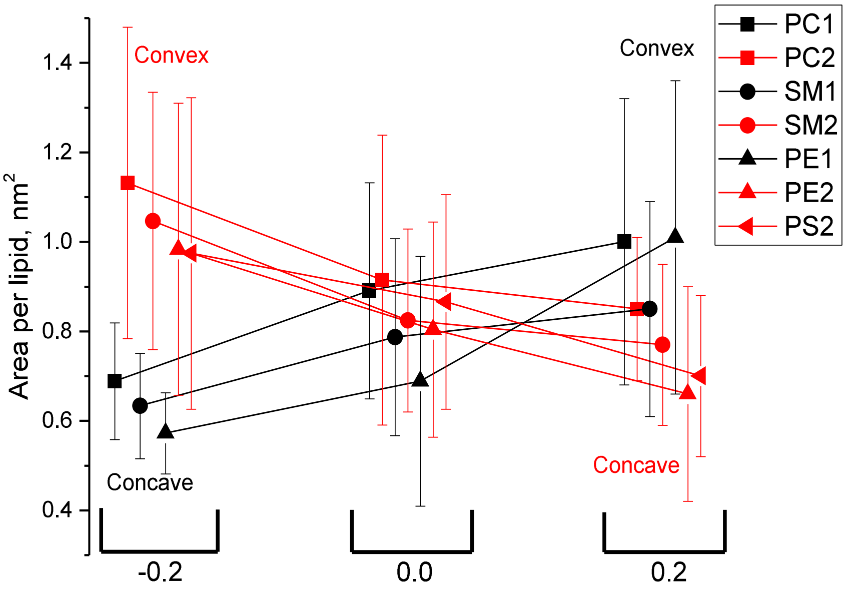

Figure IV-9. Average areas per lipid for all lipid species of inner and outer monolayers as a function of curvature.

5.2. Cholesterol distribution *versus* curvature

Cholesterol molecules are known to be highly dynamic in the lipid bilayer. They diffuse quickly in the lateral direction, change position vertically in the lipid monolayers and exhibit flip-flop transitions within the time scale of hundreds of nanoseconds. The orientation of cholesterol may also change following the topology of lipid tails, which usually surround rigid sterol rings.

Figure IV-10 shows the distribution of the cholesterol inclination angle depending on the curvature and the monolayer. Two distinct fractions of cholesterol molecules could be distinguished. The major fraction is intercalated between the lipid tails with a vertical orientation (roughly parallel to the membrane normal). The minor fraction is located in the center of the hydrophobic core of the membrane and is oriented horizontally (perpendicular to the membrane normal). The existence of these two fractions was also found shown before in coarse-grained [62] simulations, however, their dependence on the membrane curvature was never previously studied.

The main maximum corresponds to the major cholesterol fraction while the minor fraction is visible as a residual probability density around 90°. The position of the major peak shows a pronounced dependence on the curvature. The inset in Figure IV-10 shows that the inclination angle of the cholesterol decreases when the curvature of a particular monolayer changes from concave to flat or to convex. This decrease is equally pronounced for both monolayers. The absolute value of the inclination angle is systematically larger in the inner monolayer. This may be caused by the influence of high SM concentration in the outer monolayer which aligns cholesterol molecules to the membrane normal and decreases the inclination angle.

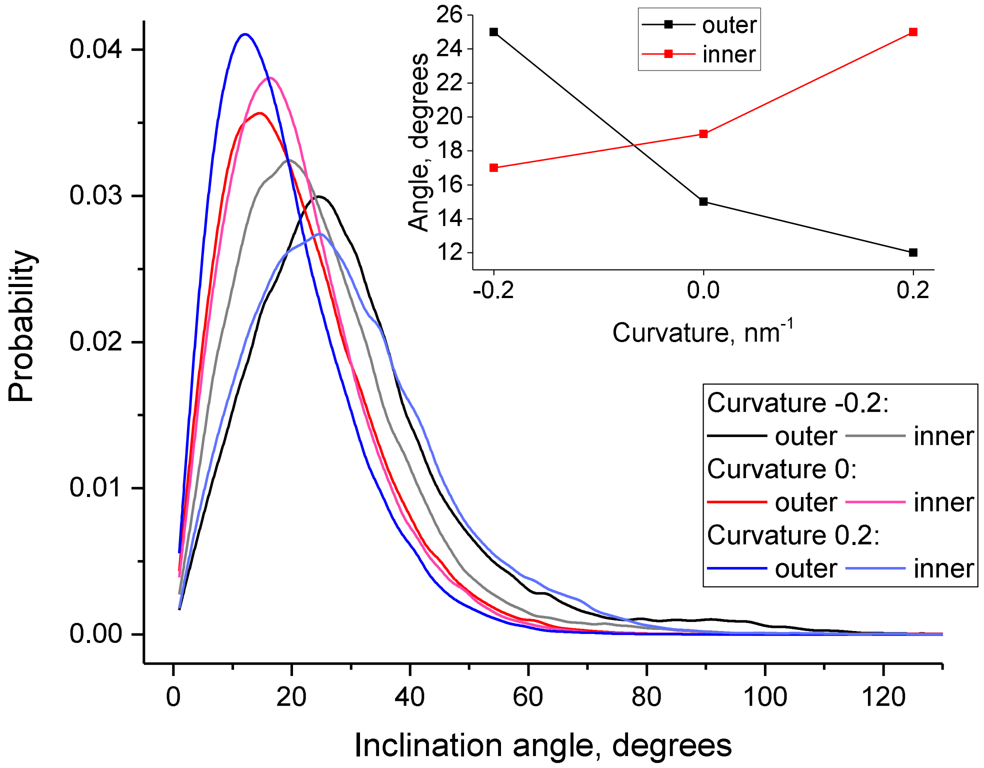

Figure IV-10. Distribution of inclination angles of cholesterol molecules in inner and outer monolayers as a function of the membrane curvature. The inset shows the position of the major maximum of cholesterol distribution as a function of curvature. The angle is computed relatively to the local membrane using the normal position of the cholesterol -OH group. The long axis of the cholesterol molecule is defined as a vector from the carbon atom at tail branching to -OH group *[63]*.

Figure IV-11 shows the distribution of the depth of cholesterol location in the membrane depending on curvature and the monolayer. The minor cholesterol fraction is clearly visible in this figure as a small peak near ~1.75 nm. The position of the peak which corresponds to the major cholesterol fraction changes significantly depending on the curvature. The distance of cholesterol head groups from the membrane surface is minimal in the flat membrane and increases upon bending (inset in Figure IV-11). This effect is less pronounced in the outer monolayer. Regardless of the curvature it is also evident that cholesterol molecules are located deeper in the inner monolayer than that of the outer monolayer. This effect is likely to be caused by the complexation of cholesterol with SM lipids in the outer monolayer which results in its lower vertical mobility.

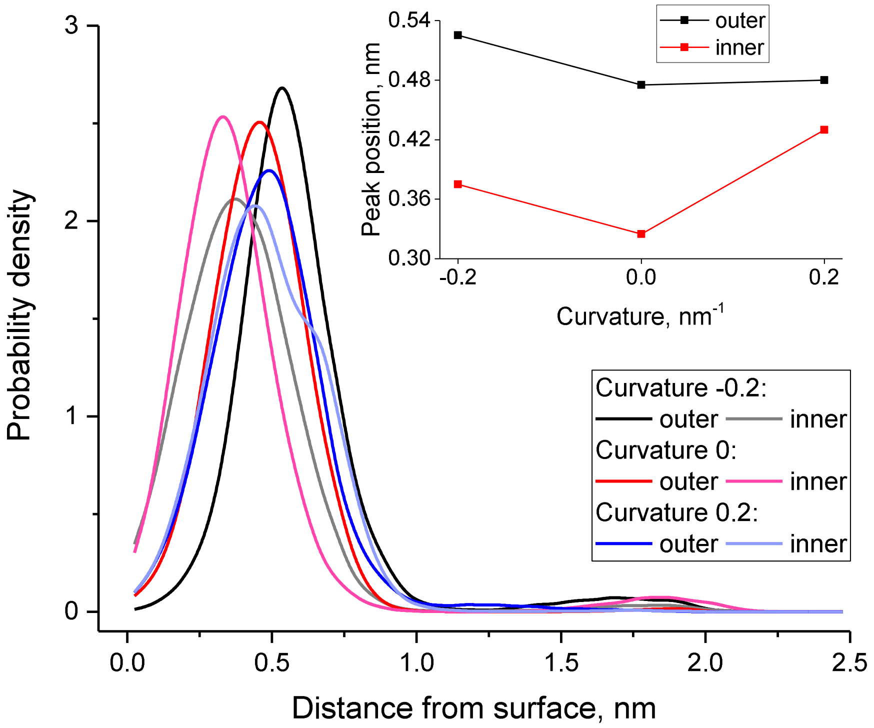

Figure IV-11. Distribution of the distances of cholesterol molecules from the membrane surface in inner and outer monolayers as a function of the membrane curvature. The distance is measured from approximated membrane surface to the OH group of cholesterol. The inset shows the position of the major maximum of cholesterol distribution as a function of curvature.

The minor cholesterol fraction resides in the central region of the membrane, thus it cannot be reliably attributed to either the inner or outer monolayer. It should be considered as a single pool of cholesterol molecules located between the membrane leaflets. The strong dependence of the relative abundance of the minor cholesterol fraction (relative to total number of cholesterol molecules in the system) on curvature in observed (see Figure IV-11). In the membrane with positive curvature (c = 0.2) there are no cholesterol molecules in the minor fraction between the leaflets. In the flat membrane (c = 0) about 1.7% of cholesterol is in the minor fraction. Finally, in the membrane with a negative curvature (c = -0.2) the minor fraction increases to 2.5%. This effect is again in good agreement with higher SM concentration in outer monolayer. Indeed, for c = -0.2 the outer concave monolayer is compressed at the level of head groups. Rigid complexes of cholesterol with SM are likely to become less energetically favorable in such conditions and some cholesterol molecules are expelled towards the center of the membrane, which helps to relax the conformational strain of SM lipids. In contrast for c = 0.2 the outer monolayer is convex. This creates some extra free volume for the cholesterol molecules between the rigid saturated tails of SM lipids, and the minor cholesterol fraction disappears.

Our results are in line with previous observations showing the high mobility of cholesterol and sensitivity of its position and orientation to the state of surrounding lipids. In addition to the well-known effects of the lipid content and mechanical strain, the depth and inclination of cholesterol molecules in the membrane appears to be highly sensitive to the curvature of individual monolayers.

5.3. Density profiles *versus* curvature

The density profiles of the different chemical groups of lipids are the most obvious indicator of the membrane structural changes upon bending. These profiles are very well-known for flat model membranes from both experiments and simulations. It is thus interesting to see if the density profiles change upon bending.

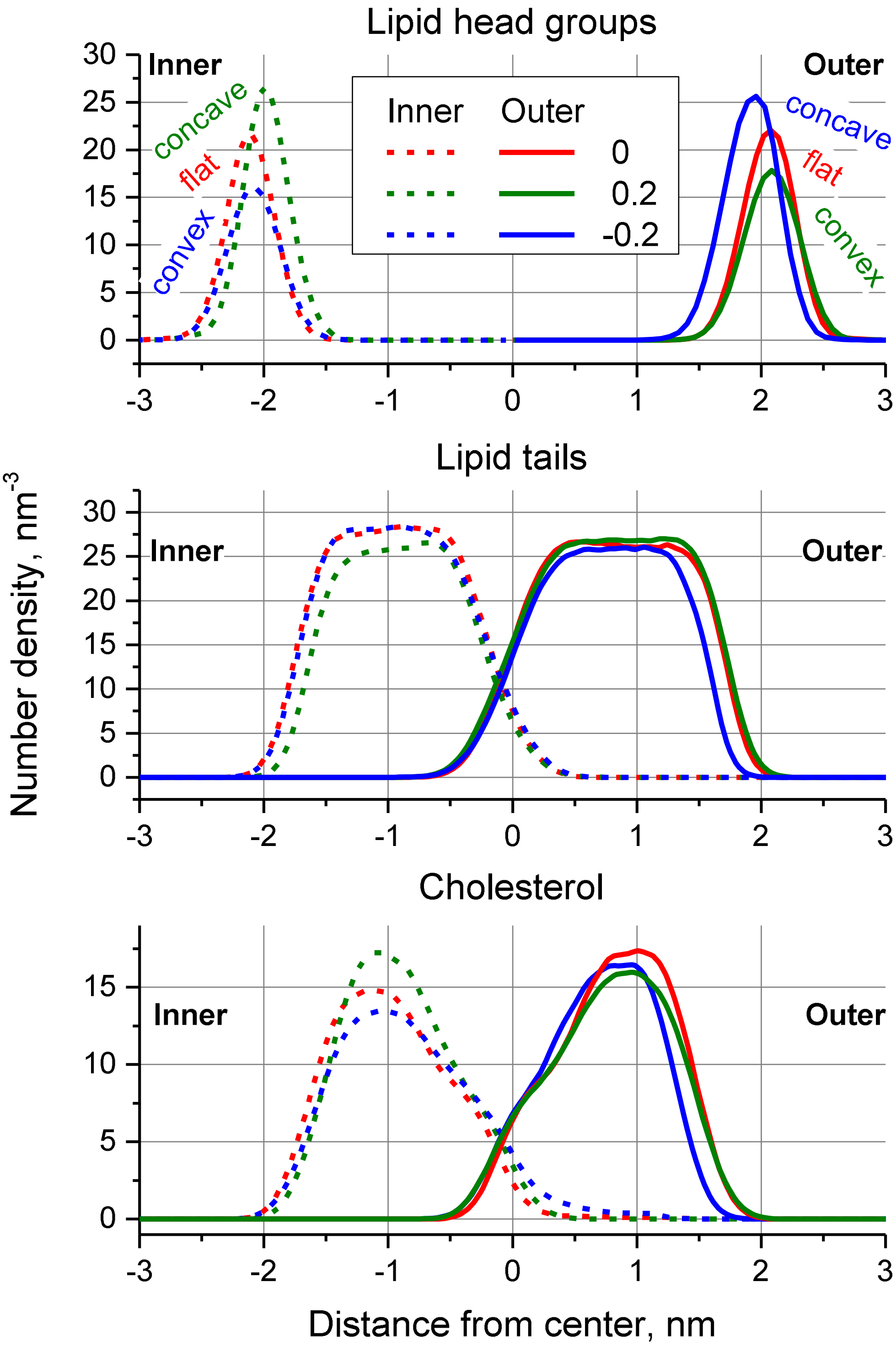

Figure IV-12. Density of lipid head groups, lipid tails and cholesterol of inner and outer monolayers of the bicelles with different curvatures.

For the sake of clarify, we provide the relation between the curvature of the bicelle and the topology (concave or convex) of its inner and outer monolayers in Table IV-3.

Table IV-3. Relation between the curvature of the bicelle and the topology (concave or convex) of its inner and outer monolayers.

Curvature, nm^{-1}	0.2	0	-0.2
Outer monolayer (PC1, SM1, PE1)	Convex	Flat	Concave
Inner monolayer (PC2, SM2, PE2, PS2)	Concave	Flat	Convex

Figure IV-12 shows that the curvature leads to visible changes in the density profiles. In particular it leads to a significant decrease in the density of lipid head groups on the convex membrane surface while it leads to an increase in their density on the concave surface (Figure IV-12 top panel). The peak, which corresponds to the concave surface shifts closer to the membrane centre by ~1.3Å. At the same time, the peak corresponding to the convex surface does not move.

The edge of the tail distribution (the boundary of the hydrophobic region) of the concave monolayer also shifts towards the center of the membrane by ~1.2-1.3Å while the tails of the convex monolayer are not affected. In the case of $c = 0.2$ there is also a visible depletion in the density of the tails in the inner concave monolayer (Figure IV-12 middle panel).

The general shape of cholesterol distribution is similar in both flat and curved membranes (Figure IV-12 bottom panel). The density of cholesterol in the inner monolayer exhibits the same behavior as that of the head groups: it increases for $c = 0.2$ and decreases for $c = -0.2$. The density in the outer monolayer changes in a less systematic way but clearly follows a decrease in the thickness of this monolayer for $c = -0.2$. The outer monolayer has a much higher content of SM which is known to form strong complexes with cholesterol. Due to this interaction, changes in the density of cholesterol in the outer monolayer could be less pronounced.

The results obtained show marked asymmetric behavior of the concave and convex monolayers. The density profiles of convex monolayers are barely affected by curvature while the concave monolayer becomes thinner by ~1.3Å due to decrease in the thickness of its hydrophobic region. This effect is unlikely to be easily detectable experimentally due to the lack of resolution of the experimental techniques and small magnitude of the effect (about the lengths of one C-C bond in lipid tails). However, it may lead to changes in the macroscopic properties of the curved membranes, such as the permeability for hydrophilic compounds.

5.4. Dynamical behavior of the tails *versus* curvature

The order parameter of the lipid tails is an important criterion that characterizes the lipid packing in the membrane. It shows the orientation and the general ordering of the hydrocarbon tails for particular depth in each membrane leaflet. The order parameter in flat bilayers could be determined experimentally and compared directly to simulation results. However, it is not clear how to determine this experimentally in curved membranes since the curvature is rapidly evolving as a local property. Thus, numerical simulations remain the only technique up to date to estimate the changes of lipid ordering in curved membranes. Our results suggest that the order parameter of lipid tails changes significantly and non-trivially upon membrane bending.

Figure IV-13 shows the order parameter of the tails of all phospholipid species in both the inner and outer monolayers for different values of curvature. It can be clearly seen that the distal parts of the tails (below the double bond for carbons 9-10) of all phospholipids become much less ordered in concave monolayers, while keeping approximately the same ordering as flat membranes in convex monolayers. This result is expectable from the purely geometrical point of view. Indeed, in the concave monolayers the lipid head groups are “congested” while the volume available to the distal parts of the tails is larger than in the flat membrane. As a result distal parts of the tails fill available space by becoming less ordered.

The proximal parts of the tails (atoms between the head and the double bond) show lipid-specific behavior. The proximal parts of PC tails are less ordered in curved membranes in comparison to the flat one but there is almost no difference between the convex and concave monolayers. The proximal parts of PE and PS tails in concave monolayers are ordered equally or even higher than in the flat membrane. In contrast, the proximal parts of PE and PS tails in convex monolayers are much less ordered than in the flat membrane. These results are not easily explainable by simple geometric considerations because the chemical nature of the lipid head groups becomes important for structuring proximal parts of the tails.

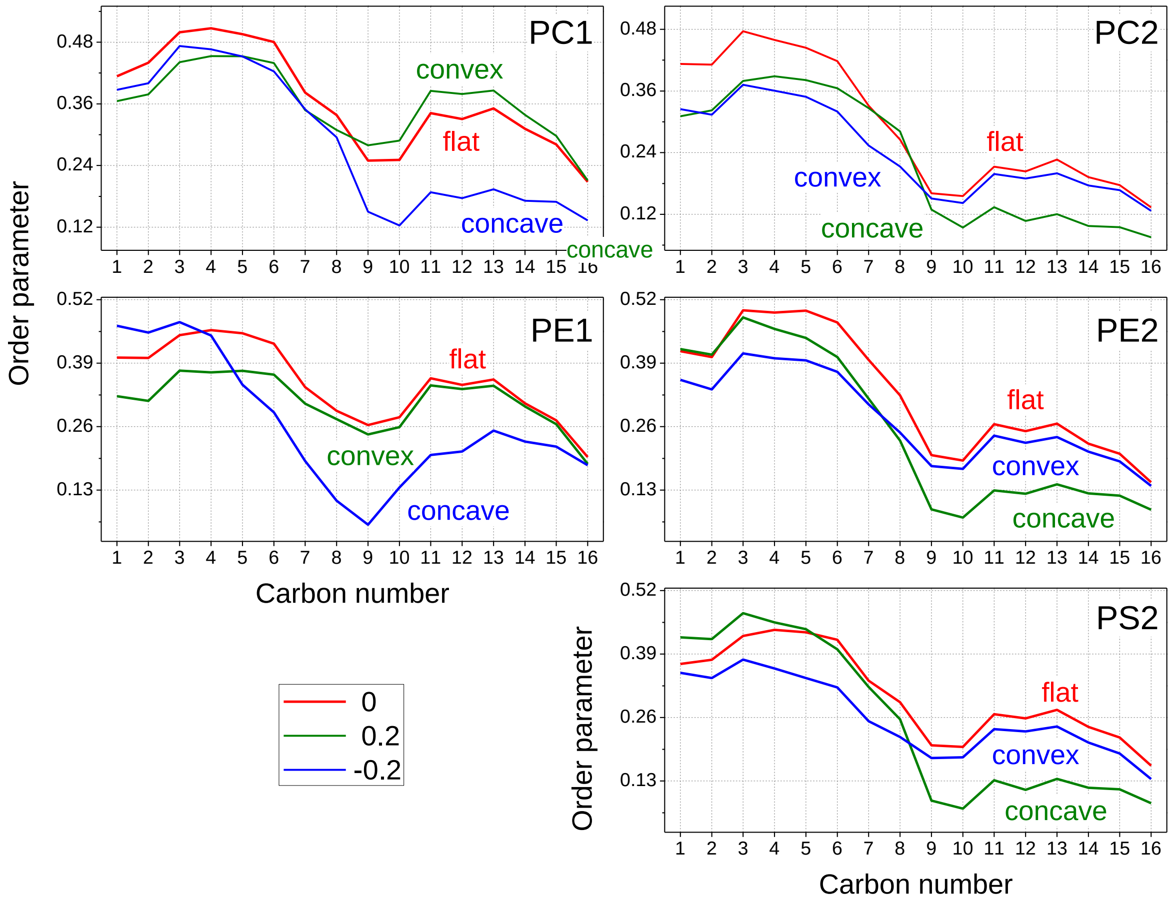

Figure IV-13. Order parameter of the lipid tails for all studied phospholipid species in inner and outer monolayer as a function of curvature. Each panel shows order parameter of indicated lipid in outer (1) or inner (2) monolayer. Topology of the monolayer, which corresponds to each curve (convex, concave or flat), is indicated.

Table IV-4. Summary of the influence of curvature on the order parameter of phospholipids. The symbols show the change of ordering of proximal and distal parts of lipid tails in comparison to flat membrane. "-" means moderate decrease of ordering, "--" strong decrease of ordering, "-=" slight decrease or no change, "+=" slight increase or no change.

Monolayer curvature	Convex		Concave	
Part of the tail	Proximal	Distal	Proximal	Distal
PC	-	+/=	-	--
PE	-	-/=	+/=	--
PS	-	-/=	+/=	--

Table IV-4 summarizes the observed effects of the curvature. Curvature never leads to a significant increase in the ordering while a dramatic decrease of ordering occurs in the distal parts of lipid tails in concave monolayers. A smaller but still significant decrease of ordering is observed in the proximal parts of the tails in a convex monolayer. The scheme in Figure IV-14 illustrates this effect. The areas of lipid tails where there is a significant decrease of ordering is observed and marked.

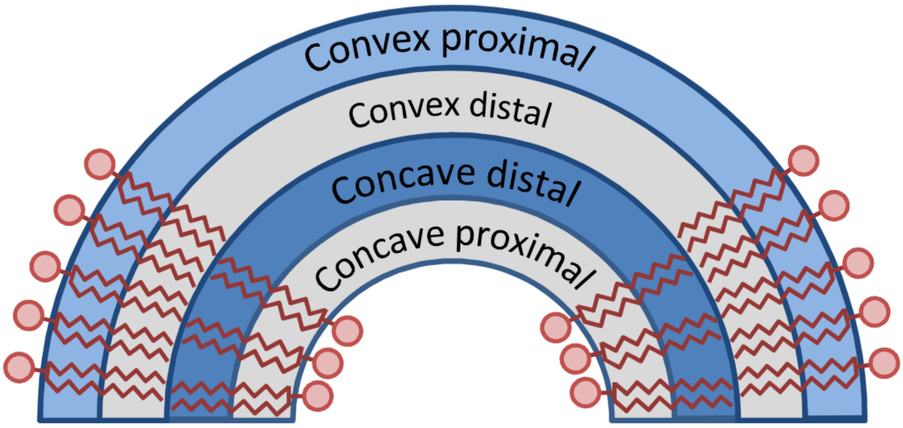

Figure IV-14. Scheme of the effect of curvature on the ordering of lipid tails. Proximal and distal parts of concave and convex monolayers are marked. The parts which show no significant change of ordering upon bending are shown in light gray. The part which shows a moderate decrease of ordering (convex proximal, "-" in Table IV-4) is shown in light blue. The part with show a significant decrease of ordering (concave distal, "--" in Table IV-4) is shown in blue.

The changes of ordering in saturated sphingomyelin tails are different and should be analyzed separately. The most ordered part of SM tails in the flat membrane is in the region of carbons 7-8, while the proximal and distal parts of the tails are much less ordered. This maximum shifts to carbons 6-7 in the convex monolayers and to carbons 8-9 in the concave monolayers. Surprisingly, in the case of c = -0.2 the ordering of SM tails in both monolayers decreases significantly for all carbon atoms. In the case of c = 0.2 such a decrease is observed in the proximal part of the concave inner monolayer and in the distal part of convex outer monolayer (Figure IV-15). The reason of such inconsistent behavior is not clear.

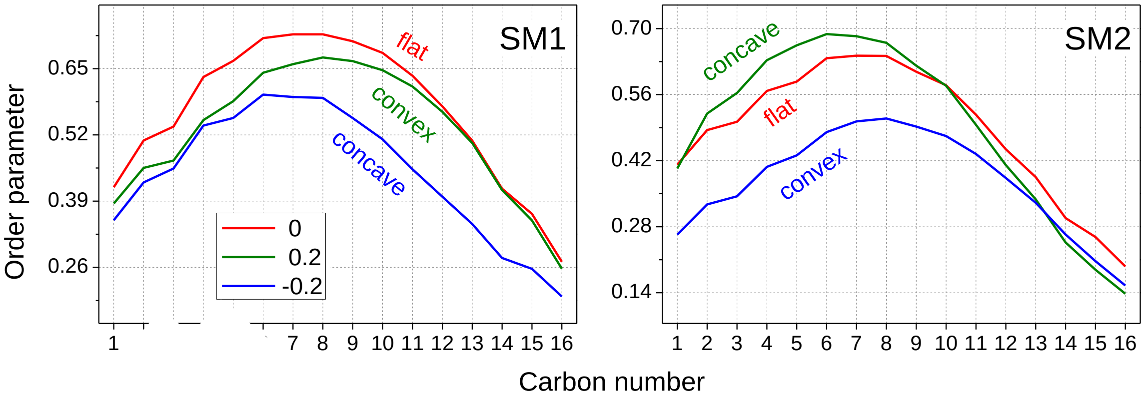

Figure IV-15. Order parameter of the sphingomyelin tails in inner (SM1) and outer (SM2) monolayers as a function of curvature. Topology of the monolayer, which corresponds to each curve (convex, concave or flat), is indicated.

An observed non-trivial decrease in the lipid order parameter in certain parts of the curved membrane could also be detected directly in specifically designed experiments. For example the ordering-sensitive fluorescent dyes with the chromophores located at a well-defined depth may allow us to observe the curvature-related decrease of ordering directly. This effect may also influence the permeability of the membrane to bulky compounds, which may allow the ordering of surrounding lipid tails.

6. The effects of cholesterol on the membrane properties

It is well known that cholesterol content changes the physical properties of the membrane significantly, in a way referred to in the literature as the “condensing effect|” [36]. In order to assess these changes in our systems we computed the density profiles of head groups and tails (Figure IV-16) and the order parameter of the lipid tails (Figure IV-17).

6.1. Density profiles vs cholesterol concentration

It is clearly visible from Figure IV-16 that the distance between the head groups (the thickness of the membrane) increases with cholesterol content. This trend is shown as a function of cholesterol content in Figure IV-18. The trends for the inner and the outer leaflets of the normal membrane exhibit slightly different slopes but both of them demonstrate perfect linear dependence (the correlation coefficients of linear regression are 0.998 and 0.988 respectively). The pure DOPC bilayer is the thinnest, which is expected taking into account a more compact conformation of its unsaturated lipid tails. The cancer membrane with 33% cholesterol has identical thicknesses of both monolayers which is comparable with the thickness of the outer leaflet of the normal membrane with the same cholesterol content.

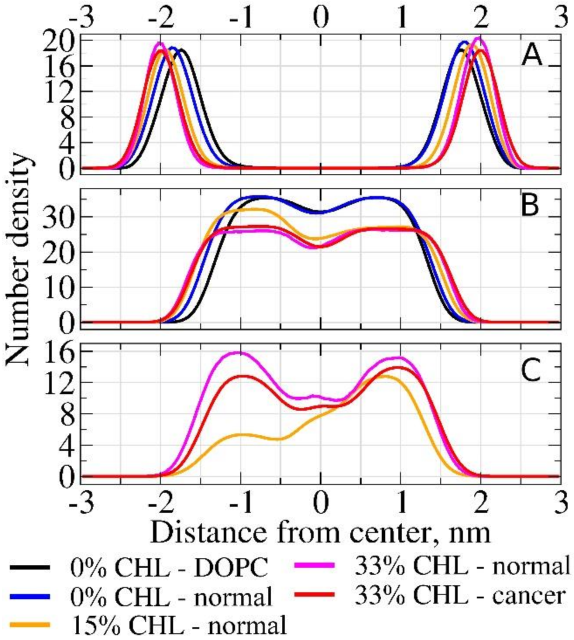

Figure IV-16. Number densities of the lipid head groups (A), lipid tails (B) and cholesterol (C) for different model membranes. Outer leaflet corresponds to positive distances from the membrane center.

The density profiles of cholesterol for normal and cancer membranes at 33% CHL content are comparable. For both normal and cancer membranes, the inner and outer monolayers contain approximately the same number of CHL molecules (the density profiles are symmetric). In our setup the CHL molecules could diffuse freely over the bicelle caps and redistribute between the monolayers. This may explain the visible asymmetry of the cholesterol distribution in the system with 15% of cholesterol.

6.2. Dynamical behavior of the tails vs cholesterol concentration

Such redistribution of cholesterol influences the density of the lipid tails. It is evident from Figure IV-17 that the density of the tails decreases substantially upon an increase in the cholesterol content. This is expected since CHL molecules intercalate between the tails and increase the total volume of the monolayer. The redistribution of CHL to the outer monolayer correlates with smaller tails density in this monolayer at a 15% cholesterol content.

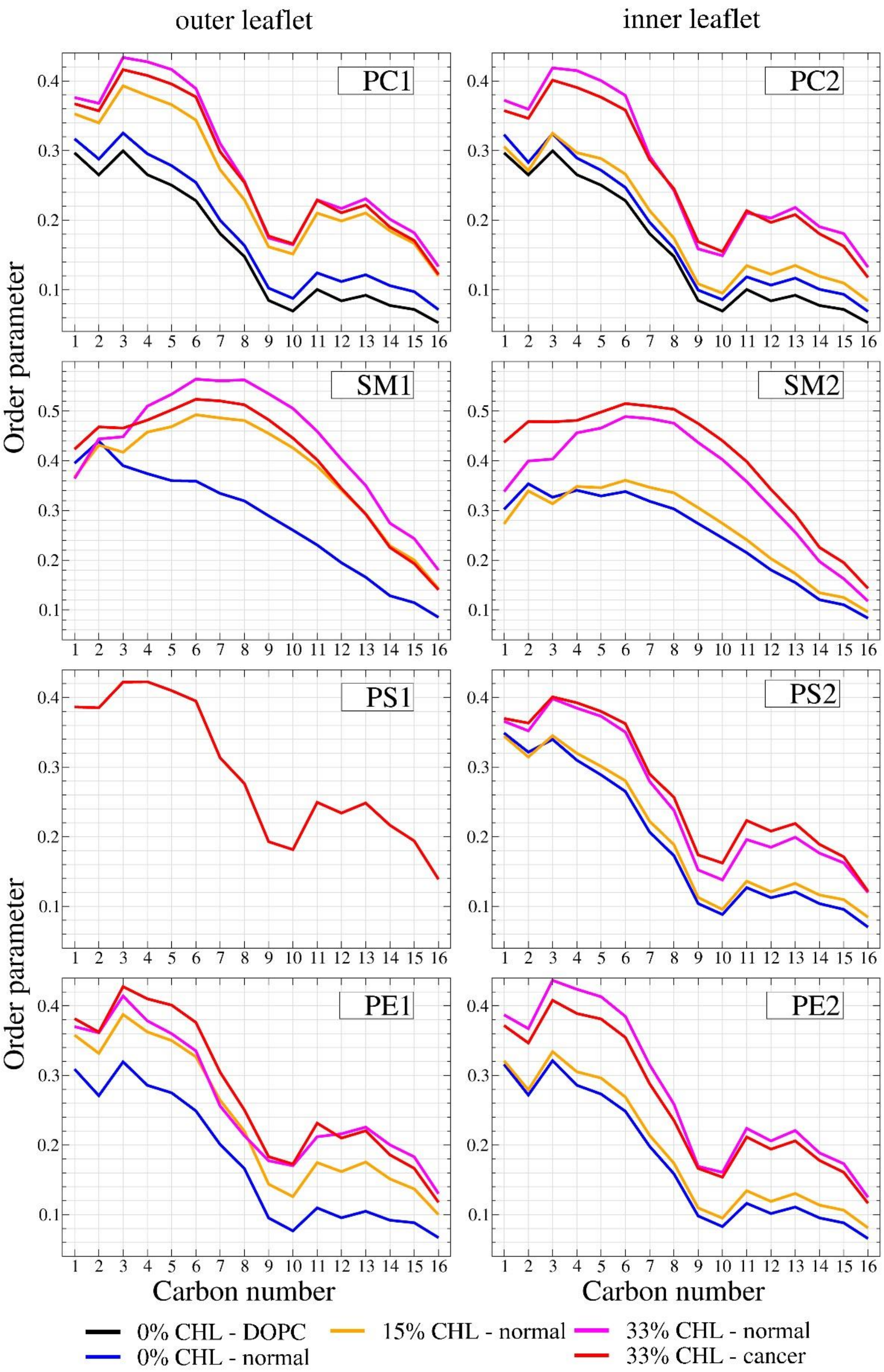

Figure IV-17. Order parameter of the lipid tails for all studied phospholipid species in the inner and outer monolayers for the different membrane models.

The order parameters of the lipid tails also show remarkable dependence on cholesterol content. All phospholipids (PC, PE and PS) show very similar trends. The order parameter increases with the increase in cholesterol content in the corresponding monolayer. This general trend is logical and easily explained by the fact that rigid CHL molecules intercalate between the lipid tails and increase their ordering. Such behavior has already been observed in pure 2,3dipalmitoyl-D-glycero-1-phosphatidylcholine (DPPC) and 3-palmitoyl-2-oleyl-D-glycero-1-phosphatidylcholine (POPC) model membranes [33, 118]. Asymmetric distribution of cholesterol at 15% is also clearly visible by the different position of the corresponding curve for inner and outer monolayers (the orange curve is much higher for PC1 and PE1 than for PC2 and PE2).

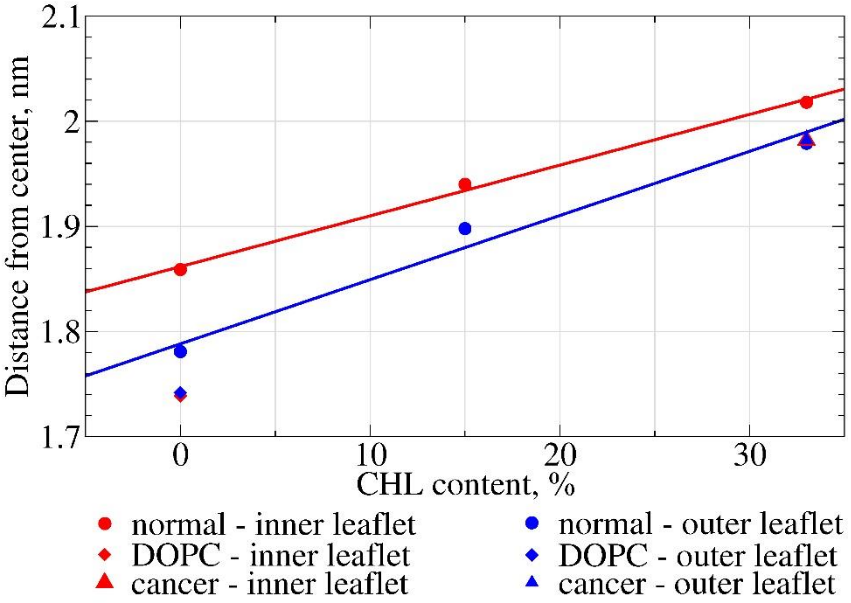

Figure IV-18. Absolute distance from the center of the membrane to the peak of head groups density for different membrane models as a function of cholesterol content. The lines show linear regression of the corresponding values for inner and outer leaflets.

The ordering of PC tails in pure DOPC membrane is lower than the ordering of PC tails in the normal membrane with 0% cholesterol. This is explained by the influence of a more ordered saturated SM tails in the normal membrane.

The ordering of the tails of SM lipids themselves follows the same pattern except there is a remarkable difference of the curves with low content of cholesterol (SM1 at 0% and SM2 at 0% and 15%). In the absence of cholesterol the order of saturated SM tails decreases monotonously towards the center of the membrane. In contrast, in the presence of cholesterol the ordering increases and reaches the maximum in the middle of the tail near carbons 7 and 8. This clearly demonstrates the formation of strong SM/CHL complexes. The similar changes of the order parameter were also reported in the case of pure DPPC membranes with an increasing cholesterol content [118] which is in line with the well-known affinity of cholesterol to saturated lipid tails [30].

It is thus possible to infer that cholesterol concentration changes the physical properties of the membrane more than the redistribution of the lipids between the leaflets.

The effect of cholesterol in our simulations is consistent with previous studies which suggest significant ordering and stiffening of the membrane upon an increase in cholesterol concentration. Such stiffening and decrease of the flexibility of the lipid tails is known to have important consequences on the membrane permeability.

However, there is one puzzling observation in our results: a pronounced asymmetry of cholesterol density distribution in the system with 15% of cholesterol. The question of cholesterol distribution in large heterogeneous and asymmetric systems has only rarely been addressed in MD simulations, but uneven distributions of cholesterol between the leaflets of two model membranes has been reported recently by Ingólfsson et al. [50, 51]. Close inspection of our system shows that the asymmetry comes from only three cholesterol molecules, which go from the inner to outer monolayer in the course of equilibration. Thus, statistical significance of observed asymmetry is questionable since it could be easily caused by the random motion of few cholesterol molecules rather than systematic reasons. At the same time there is a well-established strong affinity of cholesterol to sphingomyelin which may drive cholesterol molecules to SM-reach outer monolayer of the normal membrane. It is possible to speculate that cholesterol tends to populate the outer leaflet up to a saturation concentration first and then redistributes to the inner leaflet. 15% cholesterol content is likely to be insufficient to saturate the outer leaflet completely which may cause the observed asymmetry. In contrast, 33% cholesterol content is enough for saturation which leads to an equal distribution between the monolayers. One should consider this speculation with care because lateral diffusion and the flip-flop processes should be sampled much better to draw reliable conclusions. It is rather straightforward to test this hypothesis in a series of simulations with different cholesterol distributions but this is beyond the scope of the current work.

7. Properties of the cancer membrane

The distribution of different lipid species in the membranes of cancer cells is usually discussed in terms of PS exposure, while the distribution of other lipids is rarely considered. This limits available experimental data concerning lipid content of the cancer cell membranes. Taking into account the lack of reliable data we decided to consider the simplest model of the cancer cell membrane where distribution of all lipid species is the same in both monolayers. We are aware that this model is likely to be oversimplified and in reality the membrane is likely to remain somewhat asymmetric. However, a fully symmetric model is the ideal reference system, which could be used to compare the membranes of different cancer cells if their lipid composition and distribution become available.

The differences in order parameter between normal and cancer membrane with 33% of cholesterol are rather small. The tails of PC and PE lipids are less ordered in the cancer membrane while the tails of PS are more ordered in the inner monolayer. This is easily explained by the redistribution of SM lipids. In the cancer membrane SM is distributed evenly between the monolayers, while in the normal membrane most of SM is in the outer leaflet. This leads to a decrease in the ordering in the outer monolayer and its increase in the lower monolayer.

8. Limitations and conclusions

Our simulations have several limitations which need to be mentioned. The major limitation of our technique is that of maintaining the membrane curvature by the external walls, due to the mechanical restraints imposed by the walls. In the case of the flat membranes we have shown that it is was possible to compare the bicelle with the walls with a free lipid bilayer with periodic boundary conditions. We show that the influence of the walls is minor in this case and could be neglected. However, no such control is possible for the curved membranes. Strictly speaking it is not known if the influence of the walls remains as small for the curved bicelles as it was in the flat membrane. That is why the effects of curvature revealed in this work should be interpreted with caution. It is very unlikely that the effects themselves are artifacts produced by the simulation setup, but their absolute values could be influenced by the walls and thus should be interpreted at the semi-qualitative level.

Another limitation comes from the fact that such complex multicomponent system as a model plasma membrane is unlikely to be equilibrated completely at sub-microsecond time scales. Ideal sampling of such heterogeneous membrane may only be reached at larger times than the time of lateral diffusion of lipids through the whole bicelle (tens or even hundreds of microseconds). Unfortunately, such times are not reachable in all atom simulations providing limited access to computational resources, which is a common limitation of all MD studies in the field. Moreover, SM-rich outer monolayer is likely to exhibit spontaneous demixing of the lipid species and the formation of raft-like complexes of cholesterol and SM are at the microsecond time scales. No such events are sampled in our simulations. Despite limited sampling, our simulations revealed reliable differences in behavior of different lipid species which are likely to stand at larger time scales as well.

We provide – along with a tested setup to build realistic model membranes – an insight in the changes of various properties of the plasma membrane upon bending. This could be summarized as follows:

- The thickness of the hydrophobic core of the concave monolayer decreases by approximately 1.3 Å in comparison to that of the flat membrane, while the thickness of the convex monolayer does not change. This effect is almost symmetric in both the inner and outer monolayers.
- The area per lipid increases in the convex monolayer and decreases in the concave monolayer in comparison to that of the flat membrane. As a result the density of the head groups decreases in the convex monolayer and increases in the concave monolayer. This effect is pronounced to different extent for inner and outer monolayers

- The order parameter of the phospholipids decreases significantly in the distal parts of the tails in the concave monolayer and to a lesser extent in the proximal part of the tails of convex monolayer.
- The cholesterol inclination angle decreases when the curvature of a particular monolayer changes from concave to convex. The magnitude of this effect is larger in the outer monolayer.
- The distance of the cholesterol heads from the membrane surface is minimal in the flat membrane and increases upon bending. The magnitude of this effect is larger in the inner monolayer.
- The amount of cholesterol in the minor fraction located between the membrane leaflets is zero in the membrane with positive curvature and increases to 1.7% in the flat membrane and to 2.5% in the membrane with negative curvature.

On another hand, changes in cholesterol content in cancer cell membranes significantly influence the membrane properties, including their thickness as well as the order parameters.

Finally, the cancer model shows that the lipid redistribution also has strong influences on the membrane structure, showing important variations in the order parameters.

Chapter V - **Cisplatin – at the molecular level**

Cisplatin (c*is*-diamminedichloroplatinum(II)), later referred to as cDDP is one of the oldest and most widely used anti-tumor agents (see Figure V-1 for its chemical structure), which is adopted for the treatment of a wide range of solid neoplasms including ovarian, testicular, colorectal, bladder, head and neck, small and non-small cell lung and other carcinomas, sarcomas, lymphomas or germ cell tumors [64, 65]. In the special case of testicular cancer, chemotherapy based on cisplatin exhibits cure rates which exceed 90% [66]. Despite this large success, research studies are still conducted to improve the understanding of the action of cisplatin at the molecular level in order to circumvent the severe dose-limiting side effects such as neurotoxicity or ototoxicity and other adverse effects such as nephrotoxicity or emetogenesis [66-68] which are generally addressed by hydration and/or the use of diuretics. As another concern, a molecular insight is of great need to understand and palliate both the intrinsic and acquired resistances[5] [67, 69] which require an increase in the dose and thus in the side effects in the best cases or which can totally prevent the use of cisplatin in other cases. Finally, as the family of metal complexes used for chemotherapy is vast (see [68, 123-125] for some insights), it is of major concern, for better drug design in this field, to understand how to create drugs of this family which will not inherit the side effects nor face the chemoresistance of cDDP.

---

[5] Only 1 % of the cisplatin in the cell will finally interact with nDNA [70] which is commonly admitted to be one of the main cell target of that drug. Resistance is a major issue extensively investigated in the literature [67, 68, 119-122], which involves upregulation of some nucleophilic proteins or molecules such as thiol-containing ones like glutathiones (GSH) or metalloproteins (*e.g.* metallothionein), a potential modification and downregulation of the cisplatin uptake was hypothesized, as well as an increase of cisplatin efflux by means of the conjugated actions of the multidrug resistance protein MRP1 and the GS-X pump for instance. Also, it was hypothesized that the cell might improve the DNA-repair processes [67, 69].

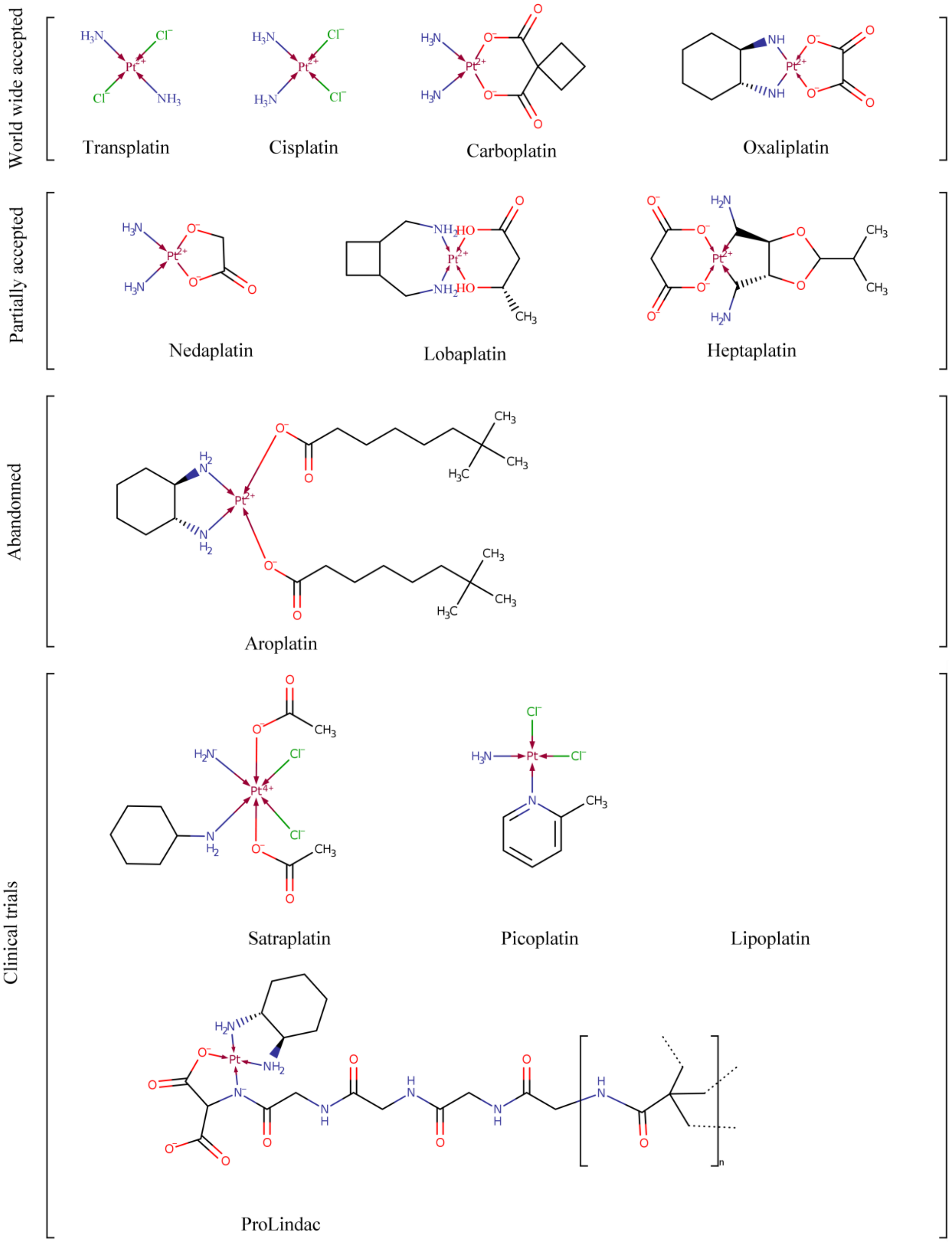

Figure V-1. Chemical structures of the platinum salts used the most in chemotherapy. The lipoplatin structure – which is under patent (Regulon®) – is not represented.

1. A question of pathways – the modes of action of cisplatin

Since it was first approved by the US food and drug administration – the FDA – back in 1978, its modes of action were actively investigated. It is known that a cell infused with cDDP will probably undergo apoptosis, necrosis or senescence.

1.1. Cisplatin interacts with the DNA

The first mechanism shown to lead to the cell death takes place in the nucleus where the active forms of cDDP covalently binds to nuclear DNA (nDNA)– as discussed by Rosenberg and coworkers, in 1971 [126], forming nDNA adducts. It was shown [127-129] that before the bonds formations, the native cisplatin experiences one or two substitutions[6] of its chloro ligands to form the active and so-called aquated species $[\mathrm{Pt(NH_3)_2Cl(OH_2)}]^{+}$ or $[\mathrm{Pt(NH_3)_2(OH_2)_2}]^{2+}$. The precise nature of these adducts has been widely discussed in the literature [65, 67, 122, 130], and it is shown that cDDP binds preferably to the N7 position of the imidazole ring (see Figure V-2 for a closer view) of the purine bases of nDNA, namely guanine (G) and – in a lesser extent – adenine (A). One may note that cisplatin may also bind to N1 atoms of adenine or N3 of atom of cytosine [131]. These adducts can be either mono- or bi-functional. The first ones, if they still present their second chloro ligand, were shown to lose it in 90 % of the cases [67] and thus become bi-functional adducts. The last ones were shown to occur mostly on the same strand of nDNA [67] and are thus referred to as intrastrand crosslinks, while other bi-functional adducts being on the both strands are called interstrand crosslinks. Experimental and theoretical studies (see [65] for a review) were dedicated to find the most biologically significant cDDP-nDNA adducts. Figure V-2 shows the most representative conformations and indicates their probability of occurrence. It is clear that most of the adducts (in between 82 and 92 %) appear to be intrastrand crosslinks [130]. Moreover, it was shown that a majority of them involve bases adjacent to one another [130]. Once cDDP is linked to nDNA, there can be a variety of protein-dependent processes – *e.g.* nDNA-repair pathways.

---

[6] More details concerning the chemistry of cDDP in solution are given in the section **Error! Reference source not found.**.

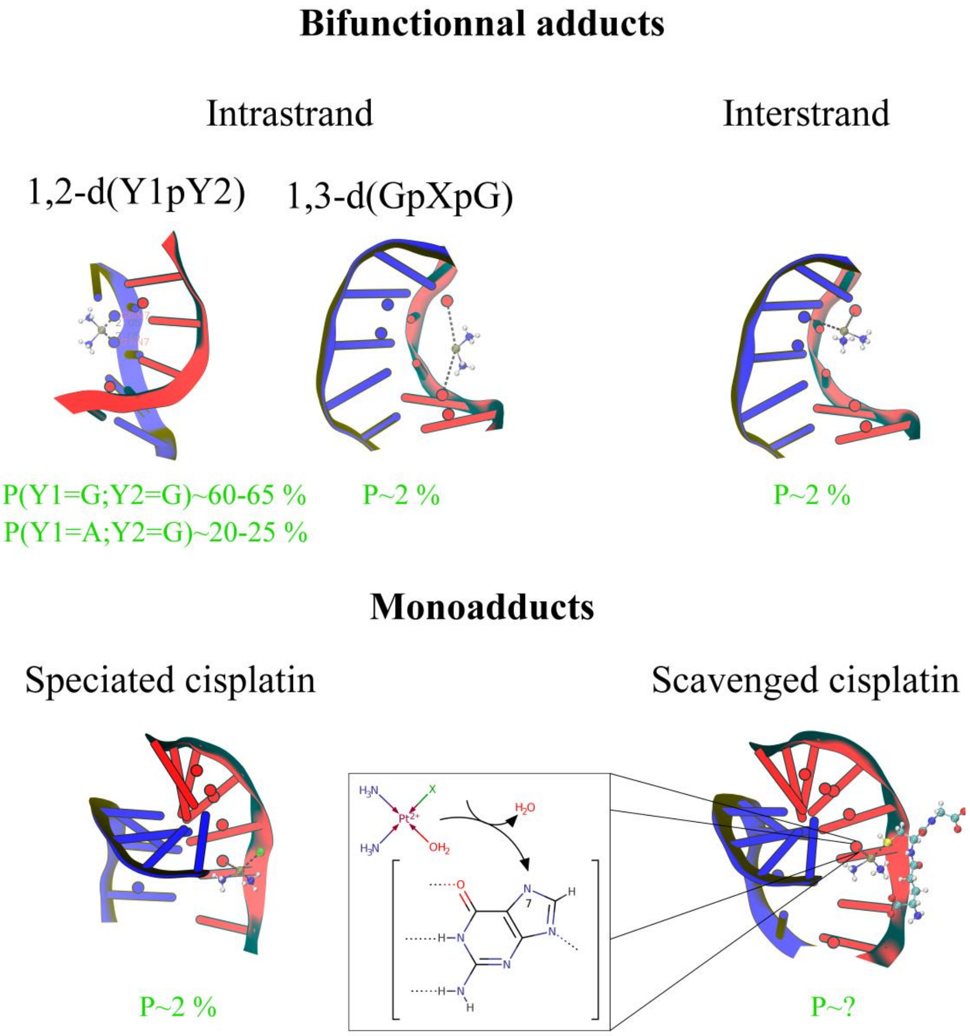

Figure V-2. cDDP-nDNA main crosslinks, their relative proportions P and a representation of the chemical structure of guanine exhibiting the atom N7 of the imidazole ring of a guanine being attacked by a monoaquacisplatin **[65, 130, 132]**. In the case of monoadducts, the distinction is present in between speciated cisplatin in the medium and cisplatin bound to any nucleophile present in the environment (on the scheme, a glutathione molecule is represented). The two strands of DNA are represented in blue and red ribbons, the N7 atoms of the guanines are represented as large blue or red spheres.

If the adducts stand still, they can impeach some cellular processes such as nDNA replication or RNA transcription. Especially, interstrand adducts forbid the strand separation required by some of these previous processes. The presence of adducts is also positively correlated to signal-transduction processes pathways. The link in between impeded cellular processes and the cell death is still not completely elucidated, but the outcome is most likely the cell apoptosis or – in some cases the cell necrosis or senescence [122] (see Figure V-3 for a schematic representation of cell-death/survival pathways in the presence of platinum-nDNA adducts). For a more complete discussion on the subject, one is invited to read one of the numerous works on this precise topic [66, 119, 120, 130].

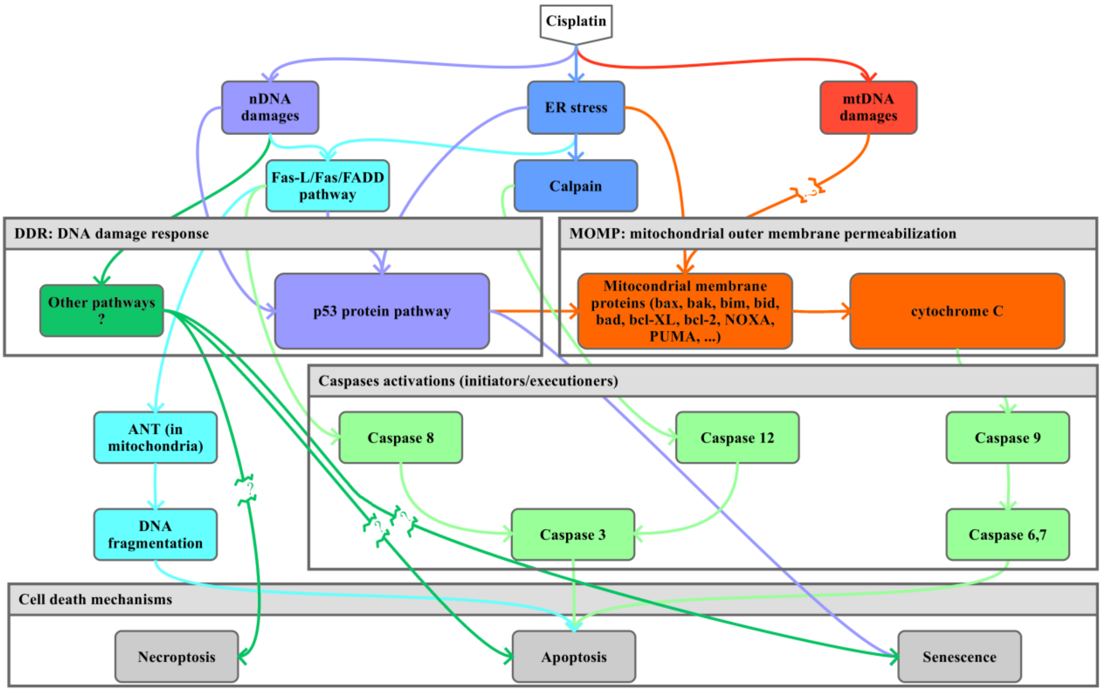

Figure V-3. Schematic representation of the principal modes of action of cisplatin inducing the cell death by apoptosis, necrosis or senescence. Cisplatin mainly induces damages to nDNA and mtDNA as well as to ER proteins which involves various cell mechanisms in cascade. The activation of the DNA damage repair pathways results in different cell mechanisms including DNA repair which may end in the cell death if the amount of death signals become statistically relevant, meaning that the damages are numerous and/or the reparation processes failed. The modes of action of cisplatin at the mitochondrial level are still not elucidated. However, it is hypothesized that mtDNA damages may involve mitochondrial outer membrane permeabilization (MOMP) and finally end in cell apoptosis. Endoplasmic reticulum (ER) stress main pathway does not lead to MOMP. It involves calpains which ultimately activate the ER stress-specific caspase 12 [66, 119, 121, 122]. Unknown processes involved along one pathway are indicated by broken lines.

1.2. Cisplatin induces endoplasmic reticulum stress leading to cell death

Another mode of action of cisplatin is shown to take place in the endoplasmic reticulum (ER) [65, 67, 120, 122] which may also end in the apoptotic death of the cell. Mandic *et al.* [133] have been using three enucleated human cancer cell lines (cytoplasts) to demonstrate that cisplatin-induced apoptosis can still occur. They show that a specific marker of the ER stress-induced apoptosis – caspase-12– is activated in cisplatin-infused cytoplasts as well as in the native cancer cell lines in similar time scales and proportions, thus proving that cisplatin induced ER stress leading to apoptosis is another valid pathway. Caspase-12 is a protease[7] involved in the unfolded protein response (UPR). This last process is the response of the cell to the ER stress. It involves a complex pathway activating notably different caspases which may end in the cell death by apoptosis. The authors of the study infer that alterations in calcium homeostatis and/or accumulation of unfolded proteins due to the intake in cisplatin may result in this ER stress. An hypothesis for the ocurrence of cDDP-induced ER stress may be an increased level

---

[7] Proteases are enzymes catalyzing hydrolysis of peptide bonds of a protein, resulting in breaking the protein down in smaller peptides: this process is called proteolysis.

of reactive oxygen species (ROS). Upregulation of ROS can induce oxidative stress and – subsequently – altering calcium homeostasis and resulting in ER stress. However, the authors used on the studied cells (but apparently not the cytoplasts) some ROS scavengers. They showed that the low ROS concentration does not inhibit ER stress. Nonetheless, it was shown that cDDP directly plays a role in the intracellular calcium concentration [120]. Three years later, the same research group published a new study [134] showing that the nuclear-dependent and the ER-stress pathways are concurrent processes which depend on the cisplatin concentration. It was shown that for high doses of cisplatin greater than ten times the IC_{50}, the prevalent death pathway is mostly independent from nuclear processes. On the other hand, at low concentrations, nDNA damages-induced apoptosis prevails. Figure V-3 includes the ER stress as one of the pathways potentially leading to the cell death.

1.3. Cisplatin strongly interacts with mitochondria

It is now shown that some anticancer drugs, including cDDP, have the propensity to penetrate mitochondria and have adverse effects on their functionning, *i.e.* damaging mitochondrial DNA (mtDNA) [135]. Mitochondria are considered as reservoirs of cationic species since their membrane exhibit an electrochemical gradient due to the difference in pH in between the inside and outside environments of this organelle and to the membrane intrisic potential. The special case of cancer cells arises some strategic interests in designing drugs effective at the mitochondrial level. Cationic species would comparably diffuse in cancer cells mitochondria better than in normal ones since the membrane potential was shown to be higher in the case of several cancer cell lines as MCF-7 when compared to that measured in normal cells. Moreover, the population of mitochondria is shown to be decreased in cancer cells which makes them easier to address. Altogether, these properties make mitochondria choice targets for the design of selective medicine if one can find any compound sufficiently effective through this pathway [120]. Nonetheless, the propensity of mtDNA damages to alter the cell survival was long believed to be negligeable, especially considering that the amount of mitochondria in a cell can be important. Furthermore, the potential direct pathways leading to cell death upon mtDNA damages are still not unraveled. However, several studies show that mtDNA might be as sensitive as 300 to 500-fold the nDNA [135, 136] which could be explained by the lack of protective proteins as histones and the limited damage repair processes involved for mtDNA as compared with nDNA. It is worth noting that, in 2004, Tacka and coworkers [137] state that the damages directly provoked by cDDP in Jurkat cells mitochondria do not lead to cell apoptosis. These results seem not to be specific to the Jurkat cells since Liang and Ullyatt [138] found an increased sensitivity to cDDP in U937 cell lines depleted from mtDNA. One of the hypothesis, recently supported by Podratz *et al.* [139], is that cDDP-induced damages of the mtDNA can be one of the sources of the side effects in normal cells – in particular its neurotoxicity. However, the past 15 years has shown more and more evidences of the mitochondrial activity of cDDP on top of its side toxicity. Yang and colleagues [136] used head and neck squamous cell carcinoma (HNSCC) enucleated cells and cells free from mtDNA. The cytoplasts – free from nDNA

– have shown the same dose-dependent sensitivity to cDDP as parental cells whereas the cells free from mtDNA have shown 4- to 5-fold more resistance. Other studies support that mitochondria are a major target of cDDP leading to cell death [140, 141]. Finally, one interesting work by Wisnovsky *et al.* [142] present a novel modification of cDDP by a mitochondria targeting peptide which actively uses mtDNA as an effective target inducing cell death.

These new and contradictory results on the action of cDDP on mitochondria which are shown either to promote cell death or cell resistance might be the signature that cDDP effects on cell life are more complex and maybe dose-, time- or line-dependent [143]. For a complete and recent review on the different subcellular targets of cDDP, the reader is invited to read the complete review by Sancho-Martínez et al [144].

2. Cisplatin: a simple molecular structure but a complex reactivity in biological media

The mechanisms of actions of cDDP inside the cell are not yet elucidated. At the same time, its transport through the membrane is also not well understood. The complexity now comes from the chemistry of cDDP and more specially, to its reactivity. One should mind that the chemistry of cisplatin in solution is complex [131] and that the question of the permeation of cDDP is intrinsically linked to that of the proportions of the different cisplatin species [128] as well as its direct environment [73].

2.1. Cisplatin speciation via aquation/hydroxylation

In various solvents, the chloro ligands of cDDP undergo nucleophilic substitution, in particular, aquation[8] or hydroxylation. These processes of nucleophilic substitutions driving to different cisplatin-derived species in equilibrium are often referred to as a chemical speciation process. Hence, due to these only reactions, five species are in a dynamic equilibrium along with the native cisplatin (see Figure V-4); the cationic mono-, di-aqua- or aqua-hydroxo-cisplatin and the neutral mono- or di-hydroxo-cisplatin. The reactions of protonation/deprotonation depend on the pH of the solution [128]. The pKa of these reactions was partially determined experimentally [76, 145-147] for pH in the range 4 to 8. The reactions of aquation or hydroxylation are highly affected by the pH as well as by the chloride concentration[9] [148]. One of the cornerstones in the studies of the speciation of cisplatin is the work by House and colleagues [76, 145-147, 149-153] who have been determining the reaction constants and, when possible, the kinetic constants, in numerous cases. These previous studies were corroborated by many works including spectroscopic analyses [154, 155] as well as mass spectroscopy potentially associated

---

[8] The term aquation is apparently preferred to hydrolysis in the case of (metal) complexes. One should note that the term hydrolysis is more precise and appropriate in the case of cisplatin since it refers only to substitution reactions whereas the aquation does not forbid reactions where the water molecule binds to the target molecule without any departure group.

[9] The chloride concentration is sometimes expressed as the pCl in the literature. In the following, chloride concentration and pCl will be used with the same meaning.

with liquid chromatography [156-160] or theoretical computations [161-165] in different media trying to reproduce different conditions found in the biological environment (urine, blood, intercellular or intracellular medium) in order to access to the relative proportions of the different species in each case in a hypothetical steady state.

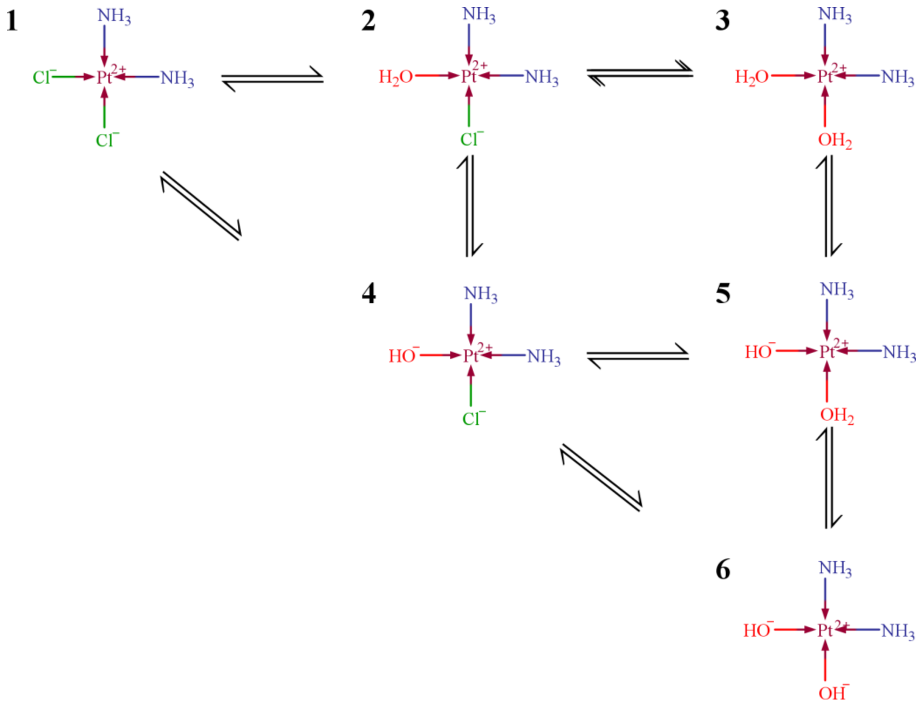

Figure V-4. Representation of the aquated and hydroxylized species of cisplatin in equilibrium in saline solution.

Different parameters influence the dynamic equilibrium in between the solvated species of cisplatin, including notably the pH and the pCl which are not the same in the extracellular medium (pH~7.4; $[Cl^-]$~104mM) as in the cytoplasm (pH~7.4 or slightly less; $[Cl^-]$~4mM) [166]. Nonetheless, the pH in the vicinity of tumoral regions and inside cancer cells may significantly drop down whereas the intracellular concentration in chloride ions might be greater than in normal cells (pH~6-7.4; $[Cl^-]$~20-55mM) [128, 155]. Other important factors in the relative proportions of the different Pt species in solution are the initial concentration in salt [148] and the effect of temperature. Many studies have addressed the main species in different environments similar to the cytoplasm or the extracellular medium (see Table V-1 for the references and the main results and Figure V-5 for a concise representation of the results). These studies give consistent results showing that above 150mM the native form of cisplatin accounts for ~90% or more of the species in presence. In the conditions of the extracellular medium – *i.e.* for $[Cl^-]$~100-110mM, pH~6.8-7.5 and a temperature of 37°C – the native cisplatin is the major species which mainly counts for more than 2/3 of the species (at the exception of the results by Miller et al. [76]). The second species to be favored is the monohydroxocisplatin which is in most of the recent studies in the 10-30% range. Monoaquacisplatin and aquahydroxocisplatin are the only two other species in such conditions which are not yet in negligible amounts, ranging from 0 to 7%. Since the pH is greater than the pKa of the protonation reaction (2⇌ 4) in between the monoaqua- and monohydroxo-cisplatin, it is quite expectable to see mostly monohydroxyspecies. Also, if the formation of monoaquaspecies is not favored in such conditions, one should remark that the formation of diaqua species is extremely unfavorable since the second hydrolysis (2⇌3) requires acidic conditions to be in real competition or any other external catalyzing contributions and that the deprotonation reaction of aquahydroxocisplatin (5 ⇌ 3) exhibits a pKa as low as 5.9. At this high chloride concentration, it is interesting to note the influence on both the pH and the temperature. Lowering the pH (which can be a good model of the human urine environment) was shown to decrease the amount of monosubstituted species and to favor the native cDDP at levels above 95% [148, 166]. On the other hand, increasing the temperature has exactly an opposite end [76].

Inside the cell, the chloride concentration drops considerably, reaching the commonly accepted value of 4 mM. However, the work by Jennerwein *et al.* [166] made measurements of different cancer cell lines and state that this last value is underestimated in such conditions. They finally advise to use values ranging 20-50mM in models and computations. At the exception from the work by Falta et al. [157], in between 10 and 30mM of chloride ions, the native cisplatin was always found to in the 40-60% range while its proportion drops to less than 30% around 4-5mM. In these conditions, and especially at low chloride concentrations, aquahydroxocisplatin becomes an important species and some studies have shown also a non-negligible presence of dihydroxocisplatin. Jennerwein *et al.* [166] found that for chloride concentration as low as 1.5mM, the three species involving hydroxide group count for more than 90% of the species. On the other hand, in acid conditions, even with such low chloride concentrations, only native cisplatin (30-50%) and monoaquacisplatin (40-60%) remain notably.

Interestingly, for water solutions with no chloride content, native cisplatin disappears for the both pH ranges stated before, while monoaquacisplatin and aquahydroxocisplatin become the main species along with diaquacisplatin which can form in sufficiently acid conditions.

These results are possibly some clues to a better understanding of both the cisplatin transport and its efficiency in the cell. First, it is possible to infer that resistance can be related to changes in the environment. Indeed, we see that an increase in the chloride concentration from 4mM to 25mM decreases drastically the amount of monoaquacisplatin – which is the form known to interact with nDNA and mtDNA – to promote its native form. Although the diaqua form is more reactive with the DNA bases than the monoaqua, in normal conditions, its concentration in the cytosol is extremely low. Furthermore, such reactive species as the diaqua form would have a much lower lifetime before being metabolized by any other nucleophilic compound. These conclusions are in line with the actual kinetic scheme of cisplatin-DNA bindings where first appears a monoadduct in between one DNA base and the aqua ligand of monoaquacisplatin [127, 129]. As a major conclusion, it is clear that the cellular environment have a drastic impact on the chemistry of cisplatin. It is visible that there is still a lack of understanding of the preponderant chemical forms of cDDP in the vicinity of tumoral regions. To our knowledge, no recent studies have already addressed the speciation of cisplatin in different cancer cell lines, in a long term experiment (>48h), at body temperature, and with a pH found in these conditions of 6-7. These parameters may influence drastically the distribution of the species in presence, especially by inducing both an important increase in the monoaquacisplatin concentration at the expense of a quasi-null concentration in hydroxo species and by inducing a more global redistribution of the species present inside and outside the cell, having potential implications on cDDP or on the plasma membrane.

Table V-1. This table summarizes the proportions of the different cisplatin species one can expect in a solution of water and chloride ions. The basic pH are shown in green, while in acid conditions, pH is shown in red.

Reference	Year	$[\mathrm{Pt}]_0$	Time	T	pH	$[\mathrm{Cl}^-]$	Cl/Cl	Cl/OH2	Cl/OH	OH/OH2	OH/OH	OH2/OH2	Other	Sum
		$\mu mol \cdot L^{-1}$	h	°C		$\mathrm{mmol} \cdot \mathrm{L}^{-1}$								
Yotsuyanagi *et al.*[10] [148]	2002	$[10^{-2}; 10^4]$	∞[11]	25	7,4	154	89.00%	3.00%	8.00%	0.00%	0.00%	0.00%	0.00%	100.00%
Yotsuyanagi *et al.* [10] [148]	2002	$[10^{-2}; 10^4]$	∞	25	5,6	154	97.00%	3.00%	0.00%	0.00%	0.00%	0.00%	0.00%	100.00%
Yotsuyanagi *et al.*[10] [148]	2002	$[10^{-2}; 10^4]$	∞	25	7,4	110	85.00%	4.00%	11.00%	0.00%	0.00%	0.00%	0.00%	100.00%
Jennerwein *et al.* [166]	1995	NA	∞	37	7,4	108,2	84.00%	NC	NC	NC	NC	NC	NC	84.00%
Martin[12] [167]	1999	"low"[13]	∞	25	7,4	104	67.00%	4.00%	26.00%	0.90%	1.20%	0.01%	0.00%	99.11%
Howe-Grant[14] [169]	1980	NA	NA[15]	NA	7,4	103	84.00%	3.50%	3.50%	3.90%	4.90%	0.06%	0.00%	99.86%
Leroy *et al.*[16] [170]	1979	1	∞	37[17]	7,5	100	83.00%	4.00%	12.00%	< 1.00%	< 1.00%	< 1.00%	0.00%	99.00%
Miller *et al.* [76]	1990	1000	∞	25	7,4	100	68.00%	7.00%	24.00%	NC	NC	NC	0.00%	99.00%
Miller *et al.* [76]	1990	2200	∞	45	7,4	100	50.00%	20.00%	30.00%	NC	NC	NC	0.00%	100.00%
Leroy *et al.*[16] [170]	1979	1	∞	37[17]	5,0	100	95.00%	4.00%	< 1.00%	< 1.00%	< 1.00%	< 1.00%	0.00%	99.00%
Jennerwein *et al.*[16] [166]	1995	50	∞	37	7,2	22,7	59.20%	4.60%	28.60%	3.80%	3.70%	0.06%	0.00%	99.96%
Falta et *al.* [157]	2011	50	13	4	7,4	15	89.60%	0.00%	10.40%	0.00%	0.00%	0.00%	0.00%	100.00%
Falta et *al.* [157]	2011	50	13	4	7,4	15	79.52%	16.64%	0.00%	0.00%	0.00%	3.85%	0.00%	100.01%

---

[10] The authors provide an analysis of the speciation as a function of the initial concentration in platinum species.

[11] Stands for results intended for the steady state from pharmokinetics computations at the opposite of uptake experiments following the concentrations of each species individually.

[12] The authors provide an analysis of the speciation as a function of the pH.

[13] “Low” values are used because such a "low" concentration induces less parasite reactions as oligomerization.

[14] Values reported by Berners-Price and Appleton [168]. The original reference was not found.

[15] Not available

[16] The authors provide an analysis of the speciation as a function of the chloride concentration in the environment.

[17] The values of the equilibrium constants were measured at different temperature ranging from 25 to 37°C.

Yotsuyanagi et *al.*[10,18] [148]	2002	10	∞	25	7,1	10	44.00%	24.00%	30.00%	2.00%	0.00%	< 1.00%	0.00%	100.00%
Leroy *et al.*[16][170]	1979	1	∞	37[17]	7,5	5	31.00%	28.00%	32.00%	7.00%	< 1.00%	< 1.00%	0.00%	98.00%
Leroy *et al.*[16][170]	1979	1	∞	37[17]	5,0	5	50.00%	45.00%	2.00%	< 1.00%	< 1.00%	2.00%	0.00%	99.00%
Howe-Grant[14][169]	1980	NA	NA	NA	7,4	4	9.20%	10.00%	10.00%	29.20%	36.60%	4.60%	0.00%	99.60%
Martin[12] [167]	1999	"low"[13]	∞	25	7,4	4	3.00%	30.00%	5.00%	28.00%	35.00%	0.30%	0.00%	101.30%
Miller *et al.* [76]	1990	NA	∞	25	7,4	4	0.00%	50.00%	50.00%	0.00%	0.00%	0.00%	0.00%	100.00%
Berners-Price *et al.* [154]	1992	9300	40	37	7,4	4	NA	5.00%	NA	15.00%	NA	0.10%	NA	20.10%
Hann *et al.* [156]	2003	6	48	25	6,0	2,9	48.85%	47.26%	0.00%	0.00%	0.00%	0.00%	3.89%	100.00%
Jennerwein *et al.* [166]	1995	50	∞	37	7,2	1,5	NA	3.10%	37.90%	18.90%	37.00%	0.60%	0.00%	97.50%
Hann *et al.* [148]	2003	6	48	25	6,0	1,5	31.56%	61.66%	0.00%	0.00%	0.00%	0.00%	6.78%	100.00%
Miller *et al.* [76]	1990	NA	∞	25	7,4	0	0.00%	60.00%	40.00%	0.00%	0.00%	0.00%	0.00%	100.00%
Hann *et al.* [148]	2003	6	48	25	6,0	0	2.59%	24.14%	0.00%	0.00%	0.00%	31.03%	42.24%	100.00%
Yotsuyanagi et *al.*[10,18] [148]	2002	10	∞	25	4,8	0	<1.00%	26.03%	<1.00%	23.56%	<1.00%	48.49%	<1.00%	98.08%

---

[18] These values are meant for computations with no initial chloride ions, but, as far as the cisplatin releases chlorides, the media, considered to be closed, is enriched and the pCl changes, which, for important concentrations of Pt species, drives at the end to lower the presence of diaqua species and favors the mono aqua. Obviously, in sufficiently acid pH, the monohydroxy species are not proned to appear (pH<pKa).

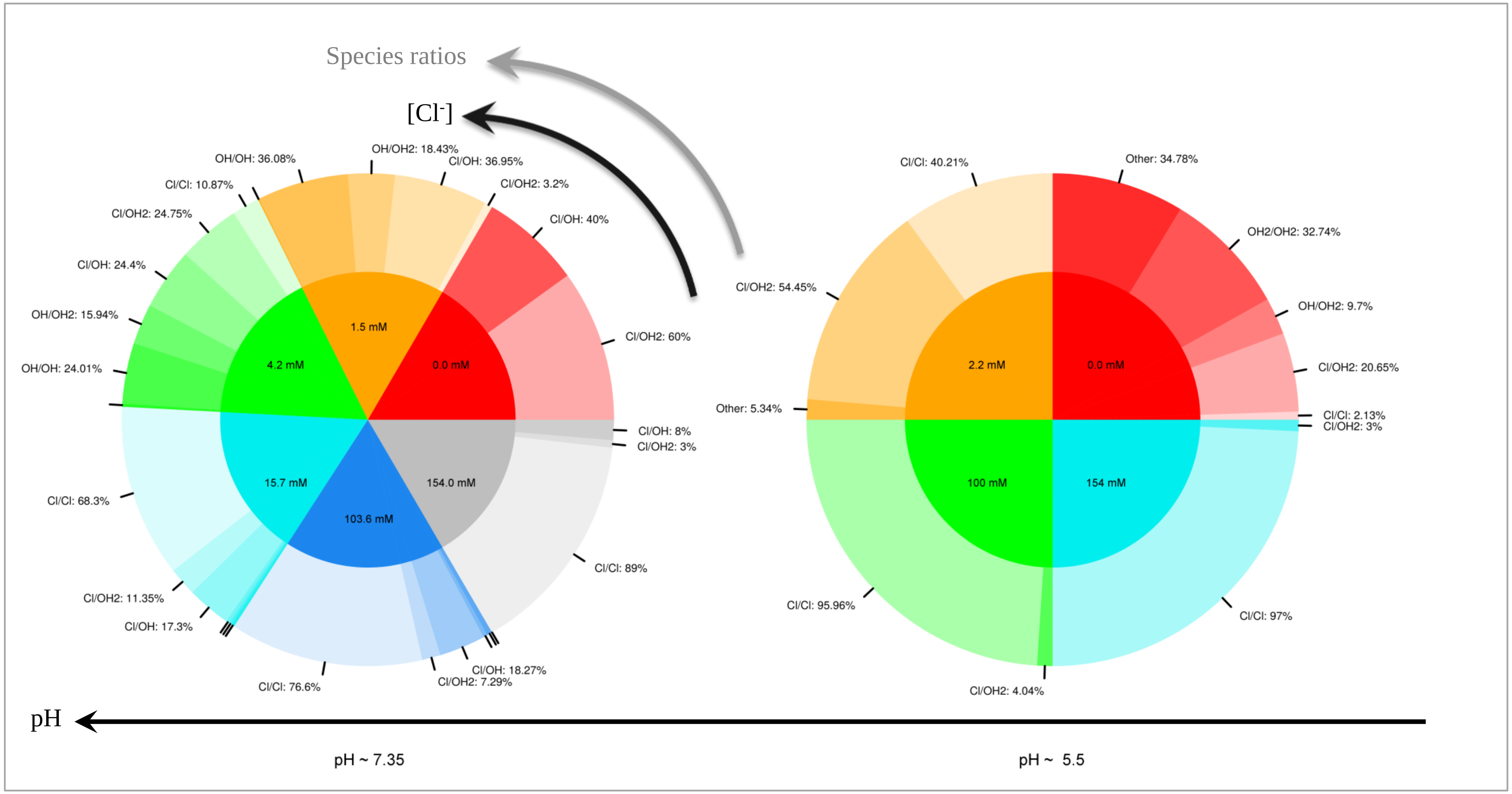

Figure V-5. Main species of cDDP derivatives in the different conditions reported in the literature. The values are averages from the data in the literature reported in Table V-1. Values smaller than 3 % are not reported on the charts. Data on the left chart correspond to a pH close to the normal physiological conditions while the data in the right chart correspond to acid conditions. One may easily see that for the both pH values, the amount of native cDDP varies greatly with the chloride content. Native cDDP becomes the preponderant species for much lower concentrations in chloride ions in acid conditions than in normal physiological conditions. Normal physiological pH drives to the creation of monohydroxo species as well as – in a lesser extent, monoaqua species. On the other hand, in acid conditions, monoaqua and eventually diaqua species might be present, but pure hydroxo species are in negligible amounts.

2.2. Other relevant interactions of cisplatin in the biological media

Thiols – or R-SH– are a group of nucleophiles from which different cysteine-containing peptides or proteins are involved in metal metabolization inside and outside the cell and have proven to bind efficiently to cDDP. The action of GSH and metallothioneins – the two most representative thiol-containing metal chelators in biological environment – was studied in order to understand their role in cisplatin resistance, either intrinsic or acquired as well as the kinetics of the reactions involved in these processes [171-173]. The concentration of these both species which is in the order of the millimolar in the cytoplasm and the strong affinity of cDDP to them make them be part of efficient intrinsic resistance mechanisms. Furthermore, this is known that these species have tendency to see their levels increased upon continuous exposure to platinum compounds. Pt-glutathione may be selectively excreted by an ATP-dependent process or form monovalent nDNA adducts which are shown not to be cytotoxic. Reactions in between thiol-containing molecules and platinum-based anticancer drugs are complex and numerous. They were the topic of a recent thesis in our team [77]. The pKa of the thiol function being of 10.4, we could easily think that the only species present in the biological environment are protonated ones. However, even with a global pH of 7.4, the dynamic equilibrium as well as local variations of the direct environment of a precise thiol group might induce a deprotonation followed by the chelation of cisplatin. It is not easy to weigh the importance of this reaction pathway with the possibility of a complexation of platinum with a free sulfur electron pair occurring before the deprotonation. If the both reactions might happen, one should note that the kinetics of the substitution is prohibitively slow for protonated species, indicating that most of the reactions should occur with deprotonated species. On top of this kinetic argument, many complex processes occur and the role of enzymes should be considered, since it is known that some enzymes are involved in the deprotonation of the GSH thiols.

Another important type of reactions of cDDP occurs with carbonates[19] which are naturally present, especially in blood (see Figure V-6 for a representation of some of these species). These reactions were shown for the first time by the groups of J. C. Dabrowiak, J. Goodisman and their collaborators [174, 175] who were studying before the speciation of cDDP and its interactions with thiols. Interestingly, is should be noted that monocarbonatocisplatin present in the extracellular media is shown to rapidly disappear in presence of Jurkat cells. This might be the sign of a rapid and selective uptake.

---

[19] In reality, in biological medium, one will most likely observe an equilibrium in between carbone dioxide (CO_2), carbonate ions (CO_3^{2-}), bicarbonate ions (HCO_3^-) and carbonic acid (H_2CO_3), but, for the sake of clarity, this dynamic equilibrium will be referred to as carbonate.

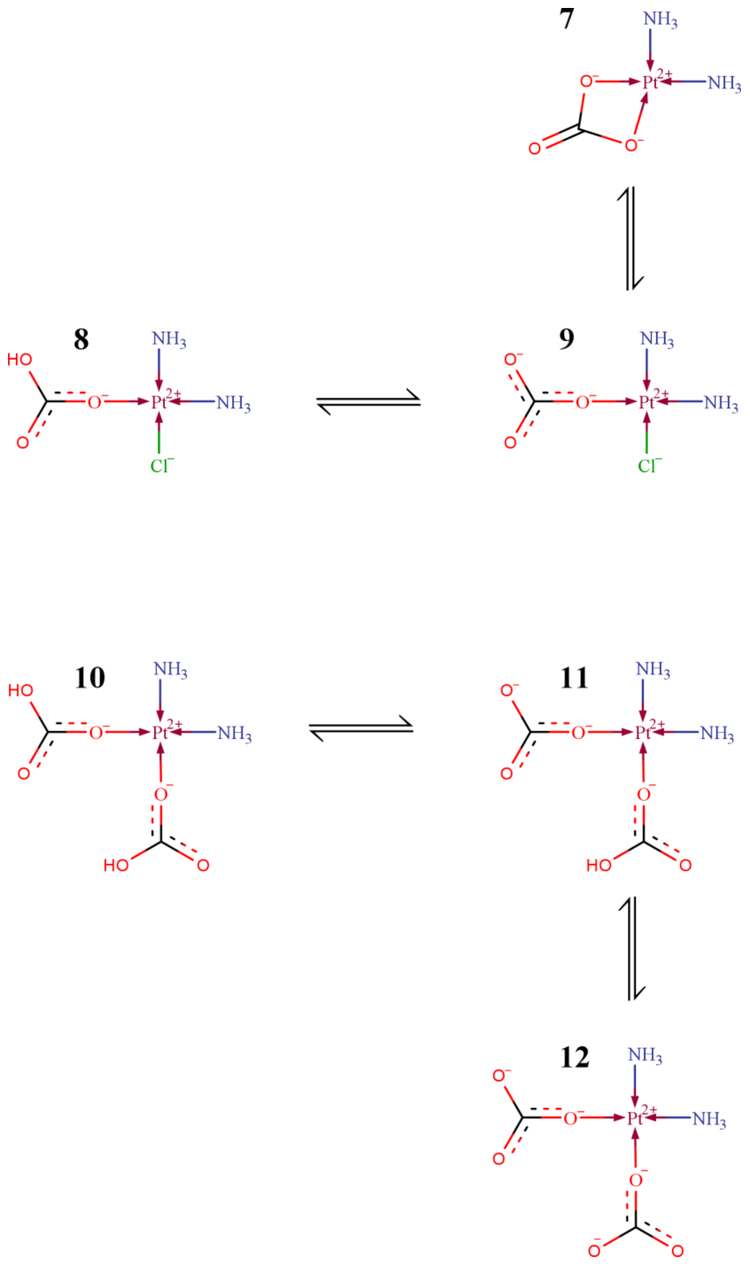

Figure V-6. Representation of some species present when cisplatin is in presence of carbonate ions.

Finally, one should know that oligomerization is another active process of cDDP (see Figure V-7). Dimers or trimers might be in majority for very high cDDP concentrations (above $20\ \text{mmol} \cdot \text{L}^{-1}$): while only 8% of the total compounds are monomers, 50% are dimers and 42% are trimers [167, 168]. Whether or not those compounds exhibit cytotoxicity is a complex issue which is not yet fully answered. Note that most of the studies dealing with cisplatin assert that oligomers are formed in negligible amounts in physiological conditions and unstable [131].

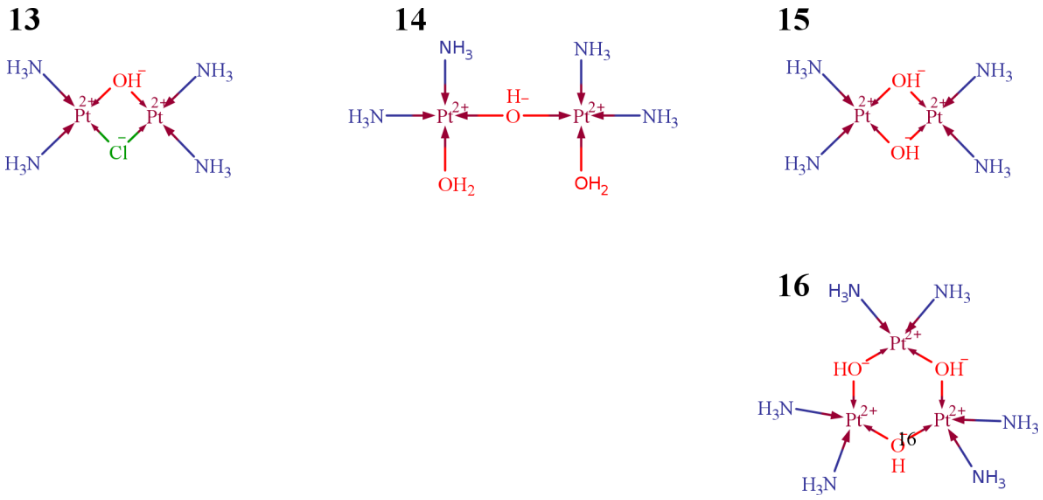

Figure V-7. Most common dimers and trimers in present in concentrated cisplatin solutions.

3. Permeation of cisplatin: the state-of-the-art

In the two previous sections, we have shown that the modes of action of cDDP are more complex than a simple binding to the DNA strands. In addition, because of a complex speciation in solvent (depending on pH, pCl and temperature), but also because of a high propensity to react with R-SH or carbonate groups, cDDP can have many derivatives with various concentrations. Only some of them can certainly reach their target (DNA, mitochondria, *etc.*) or participate to the resistance mechanism to this drug. Another complexity rises now concerning the permeation of these species through the membrane of the cells. Which species are more likely to enter the cell and by which means? Do they undergo passive diffusion or do they use any active transporters? The two major species in the extracellular environment – namely the native cisplatin and monoaquacisplatin – exhibit similar partition coefficients[20] in octanol/water systems (log(P) of -2.4 and -2.7, with P, the permeability). Obviously the both species are rather hydrophilic, however, it is known that the native cisplatin has the propensity to passively diffuse through lipid membranes [176]. Thus, the first hypothesis on the transport mechanism was still the one of passive diffusion. Meanwhile, the past 20 years has seen many publications dealing with active transport of cisplatin to the cytoplasm though ion channels. It is thus of importance to understand how these possible mechanisms of transport function to address the problems of drug resistance mechanisms which might be intrinsically linked to the entering in the cell.

3.1. Cisplatin interacts with copper transporter 1 (ctr1[21]) protein

Since 2002 and the works by Ishida et al. [177] and Lin et al. [178], the idea which was for a long time disregarded, that active transport plays a significant role in the cisplatin permeation, was explored again.

---

[20] The partition coefficient is – de facto – measured as the ration in between the concentration of the compound of interest in the organic phase *versus* its concentration in the water phase.

[21] For the sake of clarity, the convention was chosen to write in capital letters for referring to the so-called CTR1 gene and in lowercase to designate the so-called ctr1 protein.

The high affinity copper transporter 1 (ctr1) is the main transmembrane protein known to selectively carry copper ions in a wide range of organisms' cells including fungi or mammals. Uptake studies in knockout yeast (Saccharomyces cerevisiae) from their CTR1 gene as well as in mice cell lines lacking one or the both CTR1 alleles show an increased resistance to cisplatin. Hence, these authors conclude that ctr1 protein was certainly engaged in the transport of cisplatin and that its underexpression might be a cause of the observed resistance of some cancer cell lines to cDDP-based chemotherapies. In addition, Ishida et al. [177] have shown that the increase of resistance to cisplatin was related with none of the other consequences of the CTR1 gene deletion but the expression of ctr1 proteins. Consequently, not only the Pt-nDNA adducts are less present in mutated cells (by ~40 %) but this decrease correlates the decrease in Pt uptake. Furthermore, competition in between Cu^{2+} and Pt was also studied: an increase in Cu^{2+} extracellular concentration lowers the Pt uptake. One should note that this might also be related to the internalization of ctr1 proteins upon high Cu^{2+} concentrations. The authors have shown a similar effect upon Pt exposure which is another proof of the cDDP affinity for the ctr1 proteins. Finally, authors of the both studies remind that previous research was done showing the affinity of cDDP for other copper transporters, the ATP7A and ATP7B which are implied in copper efflux and were shown to be possible mediators of the cDDP efflux as well.

Thereafter, the group of Howell who led one of the two previous studies made similar measurements in human cancer cell lines to define the role of the human ctr1 (hctr1) protein in the transport of cisplatin [179] by inducing a 20-fold increase in the expression of the hCTR1 gene in A2780 ovarian carcinoma cell line[22]. If it was shown that such an increase in the hCTR1 gene expression leads to an increase in the Pt uptake, this resulted only in a little increase in the sensitivity to cisplatin (1.8%) which significance is not asserted. This last observation was further investigated by showing that the increased Pt uptake is not followed by an increase in the amounts of Pt-nDNA adducts. One should note that, although the role of the ctr1 proteins is the same in yeast, murine and human cells and that murine and human CTR1 genes have 92% of respective sequence in common, the ctr1 protein of each of those organisms have distinct amino acid sequences which may influence their interactions with cDDP in rather different manners.

Up to now, there is an important debate concerning the transport of cisplatin through the copper channels. Different studies support the hypothesis that hctr1 plays a major role in the transport of cisplatin, showing an increase in the sensitivity to cisplatin of human cancer cells where hctr1 was overexpressed in comparison with normal cancer cells [180] or indirect proofs [181]. However, more and more studies show contrasting or negative results [182-187] tending to exclude the hypothesis upon which hctr1 is a major route for cisplatin. cDDP possibly downregulates membrane-anchored hctr1 and this phenomenon happens in time-scale far shorter than the observed acquired resistance to cDDP. Also, even if some works sustain that internalized hctr1 are part of a dynamic endocytosis cycle implying their

---

[22] This line is often studied in cisplatin essays given the fact that a recognized subline exhibit strong cisplatin resistance.

regeneration [180], the studies in the team of Howell [188, 189] mention a stable decrease in the exposed hctr1 population.

Altogether, several conclusions appear to emerge:

1. **Cisplatin exhibits an undeniable affinity to hctr1**, most likely due to the presence of methionine-rich motifs in this protein to which cDDP was proven to bind [178]. Some indirect arguments for this affinity where based on the principle of homology or on correlations observation stating, for instance, that if cisplatin might be carried out by copper scavenging proteins as ATP7A or ATP7B then, it might have affinity to copper influx proteins [177], or that there is a possible correlation in between cisplatin resistant cells and cells exhibiting a deficiency in copper transport [190, 191] inferring that the cause might be in the both case related with the amount of hctr1. Nonetheless, multiple direct evidences [192, 193] as well as theoretical computations [64, 194-198] prove this affinity.
2. In the studies concerning the active transport of cisplatin, another axis of discussion than the simple hypothesis of active transport emerged: the acquired or intrinsic resistance to cisplatin and its link to hctr1 are addressed. It is now clear that cisplatin intrinsic resistance is a complex issue most likely due to a variety of line-dependent causes. As it was stated by Song *et al.* [180], a variety of cisplatin-resistant cell sublines do not exhibit any reduction of the human CTR1 gene expression. In the same way, in several publications, it was shown that cisplatin exposure impairs hctr1 and drastically reduces their presence at the plasma membrane level [188, 189]. This could be thought to be an acquired resistance phenomenon, but the very short period involved in this process (several minutes) does not correlate with the known long cisplatin uptake kinetics. Moreover, as it is stated in the review by Howell *et al.* [199] CTR1 expression was shown not to be downregulated upon cisplatin exposure in most of the case involving acquired cDDP resistance and Ivy *et al.* [185] reported several studies in which it was shown that cDDP exposure does not correlate with hctr1 internalization. Thus, it seems that **hctr1 proteins do not play a major role in cisplatin acquired or intrinsic resistance**.
3. There are contrasted conclusions concerning the mediation of cisplatin to the cytoplasm thanks to hctr1. Number of studies show that the potential increase of cisplatin uptake in cells overexpressing the CTR1 gene does not correlate with an increase in cytotoxicity, raising the question of the chemical form and the potent activity of such potentially internalized platinum molecules [179]. Furthermore, some studies show that an increase in the amount of functional hctr1 may not improve the cisplatin uptake [182]. Finally, the group of Howell recently published a study refuting the role of hctr1 as a main mediator of cisplatin, stating that the variations in sensitivity in cells with loss of CTR1 gene expression

towards normal cells does not exceed the variance in this parental population[23] [186]. Hence, it seems that, **even if hctr1 is partially involved in the transport of cisplatin to the cytoplasm, it is possibly line-dependent, most likely not the main pathway and eventually leads cisplatin into the cell in an inactivated form**.

3.2. Endocytosis plays a minor role

The endocytic routes have also been investigated and are shown to be some part of the transport of cisplatin to the cytoplasm [64, 189, 190], although, as a highly energy demanding process, these routes are mainly not considered to be the main ones. Some studies raise the idea that endocytosis-impairment is present in some cisplatin resistant cells [200]. Another study shows that pinocytosis can be progressively inhibited upon exposure to cisplatin [201]. This last observation does not allow us to conclude that cisplatin is mediated by pinocytosis, but only that cisplatin may inhibit this function, whether this process is a sign of acquired resistance or not.

3.3. Passive diffusion: the main process of cDDP influx

In order to reveal passive diffusion of chemical compounds, one usually looks at their lipophilicity through very simple experiments. Partition coefficients in different solvents are evaluated. Octanol makes a good model of any lipophilic environment. Following such observation, measurements in octanol/water systems of the partition coefficient $P_{o/w}$ of a ligand in between these two subsystems is a good indicator of the lipophilicity of a ligand. In the case of platinum salts, several measurements were reported [128, 202-205]. One of the first indirect arguments that passive diffusion plays a major role in the transport of platinum drugs is the correlation in between the drug uptake and the lipophilicity (here, $\log(P_{o/w})$) which can be fitted relevantly in many cases by a simple exponential function [75, 204, 206, 207].

One of the first and strongest arguments in favor of passive diffusion of cDDP came from that fact that its uptake was shown to be non-saturable [208-210]. In a very similar manner, some studies have shown that cisplatin intake is not impaired by competitive species – similar in their chemistry – which would be placed together in the extracellular medium [211].

Moreover, it was reported that hyperthermia induces a higher cDDP uptake which can be related to an increase in the membrane fluidity and thus in its permeability [75].

It is worth noting that cDDP permeation was shown to be inversely dependent on the plasma membrane potential [212]. A low potential was showing a better cisplatin accumulation. These results could be interpreted prematurely as a sign of active transport since mainly neutral platinum species should be

---

[23] The study also focused on other potential proteins involved in cisplatin transport such as hctr2 and has shown the same conclusions as for hctr1.

present outside the cells. cDDP accumulation in DOPC vesicles was also shown to depend on the chloride concentration [73] which was told to be a sign of the poor permeation of charged species which may be present at low chloride content in the external environment of the vesicles. One should remember that there is an important decrease in the pH of the extracellular medium of tumoral regions compared to the one of normal cells. This could lead to the formation of cationic aqua species which accumulation would be directly related to the membrane potential.

3.4. cDDP efflux; active and passive pathways involved

Study of the cisplatin efflux is important for two reasons: first, it is intrinsically related to the equilibrium of species in presence inside and outside the cell and, hence, to the distribution of species in the cytoplasm which ultimately governs the cell lifetime upon exposure with cisplatin. Thus, it is a fundamental key to understand and model the dynamics of cell life exposed to cDDP. Secondly, the efflux is not only present because of the natural dynamic equilibrium in between one and another side of the plasma membrane, but it is also a sign of the resistance mechanisms against cDDP. Indeed, there are active mechanisms devoted to the detoxification of the cell and the level of some of the molecules or proteins involved (such as the glutathiones (GSH) and some metalloproteins, such as the metallothioneins) is shown to be increased upon cisplatin exposure in order to metabolize the drugs and to excrete them.

There are active pathways of detoxification which are involving the conjugated actions of the GS-X pump and the multidrug resistance protein (MRP1) which are carrying cDDP bound to GSH [213], the role of metallothioneins (and proteins associated to their excretion). Other proteins are involved in the efflux such as ATP7A and ATP7B copper carriers [67-69, 119-122].

On the other side, passive diffusion is also present, but, due to the lower chloride concentration, more charged platinum species are in presence, which decreases drastically the efflux. Also, the gradient of potential due to the naturally high concentration of anionic species inside the cell generates the so-called Donnan effect which also lowers the efflux [73].

3.5. Conclusions

It is clear from the literature that cisplatin transport, chemistry and modes of action are still – although we are approaching the 55th birthday of the discovery of its antineoplastic properties – highly controversial topics where many questions are unanswered. Yet, it is clear that passive permeation plays a central role in cisplatin permeation through the plasma membrane. It is also true that active processes are playing an important role in the cisplatin excretion. Especially, it is known that cisplatin is mediated by the copper carriers ATP7A and ATP7B. Similarly, following their scavenging by glutathiones, it is known that GS-X pumps are another way of exit of cisplatin in this inactivated form. Nonetheless, the large amount of studies concerning the active uptake through hctr1 and – in a lesser extent – to hctr2 has shown lately mostly negative results.

However, there exist evidence in the literature that cisplatin uptake could be partially protein-mediated. The phenomenon of acquired resistance is known to be – at least – partially related to accumulation deficiencies. Although these deficiencies can be attributed to both a better efflux or a lowered intake, some studies have shown that, for some cancer cell lines, nor the level nor the level of GSH were increased while the resistance mechanisms were growing and that membrane composition did not exhibit drastic differences. It is possible that such raising resistance mechanisms are due to the impairment of an active influx transporter. Another argument in favor of the presence of active transport concerns the transport of cationic aquated species. It was shown that cisplatin accumulates more fastly at pH 6 than at pH 7.4, range for which the only two species in presence will most likely be a high proportion of native cisplatin as well as a small amount of monoaquacisplatin. However, it is known that charged species will have more difficulties to passively diffuse than neutral species, but it was also shown that these aqua species will easily accumulate. Also, it was shown that cells are more sensitive to a treatment by cisplatin with an increased ratio of aqua species to the norm.

4. Passive diffusion in a model membrane

These insights in the permeation processes lead to clear directions of investigations in the frame of molecular dynamics simulations. Since passive diffusion is a central element in the transport of cisplatin, and that the native form is the preponderant species in the extracellular media, it was of first importance to create an accurate model of the native cisplatin passive diffusion through plasma membranes. In such a concern a new force field for native cisplatin was created in our group (see section 4.1) and compared to already existing works. It was then shown that oversimplified systems such as a pure PC membrane does not give insightful results in the permeation of cisplatin of cells *in vivo*. Thus, the use of realistic membranes of normal and cancer cells (presented in Chapter IV -) was done and the results are described in the sections 4.4 and 4.5. These results are mostly based on a recent publication [103].

4.1. The development of the force field [214] and technical details

The first – and to our knowledge – only results involving molecular dynamics simulations in model membranes in order to study cisplatin permeation come from the study by Nierwzicki *et al.* [72] who computed the permeation of cisplatin and of two other platinum(II)-complexes by means MD simulations.

Consistently with the literature [215], they point that the force field they use, the CHARMM force field [97], does not consider the difference in polarities in between the lipid bilayer and the water medium. In the special concern of lipid membrane simulations, it should be noted that the two system-scale subsystems – *i.e.* the water solvent and the membrane – exhibit drastically different relative permittivity ranging from ~2 for the aliphatic chains of the lipids to ~78 in the bulk water. These changes are shown to influence the dipole moment of the species in one or another environment.

The vast majority of production-ready force fields for all-atoms (AA)MD simulations of lipid systems interacting with molecules of biological interest are using fixed point partial charges located on the related atomic position (REF) and are thus facing two distinct problems on their charge distribution; this last is 1. punctual and 2. fixed. At the date, one of the most developed force field taking into account the electronic polarization is the so-called Drude polarizable force field [216] which is actually an in-development improvement of the CHARMM27 force field.

Nierwzicky *et al.* [72] justify that – even if the membrane implies changes in the dielectric properties of cDDP environment and that this last is highly polarizable – most of the dynamics involved in the permeation relies on steric properties which remain largely unaffected by such environmental changes. We have been adopting the same hypothesis in our models.

In our simulations, the so-called QDsol topology for cisplatin was used [214]. This topology reproduces internal flexibility of the coordination bonds of platinum atom accurately by fitting them to the values obtained in *ab initio* quantum dynamics of solvated cisplatin. The ESP point charges and the Van-der-Waals parameters from previous papers in our group were used [165, 217] where geometry optimization of cisplatin at MP2(FC)/6-31G(d,p)/LanL2DZ level of theory was performed. This level of theory has been proven to be the most precise and the less time consuming for modelling cisplatin [165].

The Slipids force field [94] was used for lipids (see Chapter III -2.1). All membranes were equilibrated for at least 200 ns before computing the permeabilities.

All MD simulations were performed in Gromacs [218] versions 5.1.2 and 2016.1 in NPT ensemble at the pressure of 1 atm maintained by Berendsen barostat [219] with anisotropic pressure coupling along Y direction only (see [54, 60] for rationale of this choice). The Verlet cutoff scheme was used [220]. Long range electrostatics was computed with the PME method [221]. Velocity-rescale thermostat [222] was used. A temperature of 320K was used. An integration step of 1 fs was used in all simulations as required by the “soft” bonds of cisplatin topology [54]. No bond was converted to rigid constraints.

4.2. Model membranes

Phosphatidylcholines (PC) are the major type of lipids encountered in eukaryotes [3]. Hence, plenty of the model membranes either in experiments or in simulations use them to build simple homogeneous systems. Here are reported the results obtained with a reference single-component DOPC membrane. This system was arranged as a bicelle using the same setup as described in the previous chapter except for the fact that no repulsive potential is applied in the caps since the mixing of the monolayers is allowed in this case.

We used the model of realistic plasma membrane, referred to as “normal membrane”, developed in our previous work [54]. In this model the asymmetry of real mammalian plasma membranes is taken into account – the outer monolayer is enriched in sphingomyelin (SM) and 1,2-dioleoyl-sn-glycero-3-phosphocholine (DOPC), while the inner monolayer is enriched in 1,2-dioleoyl-sn-glycero-3-phosphoethanolamine (DOPE) and 1,2-dioleoyl-sn-glycero-3-phospho-L-serine (DOPS). The model of the plasma membrane of a cancer cell, referred as “cancer membrane” was built using the same protocol as described previously but with increased proportion of DOPS and DOPE in the extracellular leaflet (see Chapter IV -2.3 for more information on this topic).

Initial bicelle has a cholesterol molar content of 33% relative to the lipids. We also constructed the systems with cholesterol content of 15% and 0% by randomly removing half of the cholesterol molecules in the former and all of them in the later. An equal amount of cholesterol was removed from both monolayers in the case of 15% content.

4.3. Computations of permeability

4.3.1.The potential of mean force

In order to obtain an insight in the interactions of a molecule involved in a physicochemical process, it is of great interest to estimate the free energy profile along the reaction coordinates $\boldsymbol{\xi}$. The reaction coordinates $\boldsymbol{\xi} = \{ \xi_\mathrm{i}\}$ are a restriction of the whole set of coordinates the system could occupy $\mathbf{r} = \{\mathrm{r_i}\}$ which are believed to be relevant to obtain a full description of the process.

In this thesis, we were especially interested in the permeation of a ligand – generally a cancer drug – through a lipid membrane. In a nutshell, the free energy variations along the reaction coordinates are intimately related to the partition coefficient of the ligand in the binary system formed by the solvent and the membrane.

Two thermodynamic observables are the candidates of the free energy that one wants to measure; namely the Helmotz free energy F and the Gibbs free energy G. The access of one or another observable strictly depends on the macroscopic conditions of the measurement. If one samples the canonical ensemble, the measure of the Helmoltz free energy will be straightforward, but if one works in isothermal-isobaric conditions, one will access directly to the Gibbs free energy. These two observables are taking the following definitions[24]:

---

[24] The thermodynamic definitions are intended for a closed system. The statistical definition of F is related to the case of a study in the canonical ensemble.

$$\begin{gathered}\mathrm{F} = \mathrm{U} - \mathrm{TS} = -\mathrm{k_B}\ln(\mathrm{Z}) \\ \mathrm{G} = \mathrm{H} - \mathrm{TS}\end{gathered}, \tag{V-1}$$

with Z the canonical partition function, U the internal energy, S the entropy, H the enthalpy and T the temperature.

The gap in between one and another is thus only related to the variations of the term PV which is generally considered to be pretty small for liquid state systems. Hence, in the following discussion, the expression free energy will abusively make the link in between F and G.

4.3.2.PMF computation and umbrella sampling

The best estimate of the free energy variations ΔF along the reaction coordinates $\boldsymbol{\xi}$ obtained, in MD simulations is the so-called potential of mean force (PMF), first introduced by Kirkwood [223] in 1935.

The major complexity in the computation of the PMF resides in the low probability of the subsystem to sample correctly the phase space along the reaction coordinates in a limited integration time. Indeed, some of the conformations along the reaction coordinates might be drastically unfavorable, especially if there exists a potential energy barrier along the coordinates, *e.g.* a lipid membrane for a lipophobic compound. One of the most used methods developed to overcome this difficulty is the umbrella sampling (US).

To simplify the description, we can assume that the only reaction coordinate here is simply the orthogonal axis to a lipid membrane, z, and that one wants to obtain the PMF profile of a ligand through this membrane along this orthogonal axis. In the case of umbrella sampling, one will simply divide this axis into subintervals and apply a biasing potential w(z) which sums to the total potential energy V($\mathbf{r}$) – in the form of a simple harmonic potential – centered on the studied interval. To compute the interactions along the whole coordinate, the user simply has to run as many simulations as there are subintervals – generally referred to as windows.

Formally, the reduced number of coordinates simplifies greatly the computation of the free energy variations which takes the following form:

$$\mathrm{F} = -\mathrm{k_B}\ln\big(\mathrm{P(z)}\big), \tag{V-2}$$

where $\mathrm{P(z)}$ is the probability to find the ligand in a state corresponding to a given z. For any ergodic system, this probability is equal to the distribution function along z:

$$\mathrm{P(z)} = \lim_{t\to\infty}\frac{1}{t}\int_0^t \delta\big(\mathrm{z} - \mathrm{z(t)}\big)dt = \rho(z) = \frac{\int \mathrm{e}^{-\frac{\mathrm{V}(\mathbf{r})}{\mathrm{k_B T}}}\delta\big(\mathrm{z} - \mathrm{z}(\mathbf{r})\big)\mathrm{d}\mathbf{r}}{\int \mathrm{e}^{-\frac{\mathrm{V}(\mathbf{r})}{\mathrm{k_B T}}}\mathrm{d}\mathbf{r}}. \tag{V-3}$$

In the case of US, the biased probability distribution $\mathrm{P}_b\mathrm{(z)}$ will be written as follows:

$$\mathrm{P}_b(\mathrm{z}) = \frac{\int \mathrm{e}^{-\frac{\mathrm{V}(\mathbf{r})+\mathrm{w}(\mathrm{z})}{\mathrm{k_B T}}} \delta\big(\mathrm{z} - \mathrm{z}(\mathbf{r})\big)\mathrm{d}\mathbf{r}}{\int \mathrm{e}^{-\frac{\mathrm{V}(\mathbf{r})+\mathrm{w}(\mathrm{z})}{\mathrm{k_B T}}} \mathrm{d}\mathbf{r}}. \tag{V-4}$$

The link in between biased and unbiased probability distributions can be established [71] such that:

$$\mathrm{P}(\mathrm{z}) = \mathrm{P}_b(\mathrm{z})\mathrm{e}^{\frac{\mathrm{w}(\mathrm{z})}{\mathrm{k_B T}}} \left\langle \mathrm{e}^{-\frac{\mathrm{w}(\mathrm{z})}{\mathrm{k_B T}}} \right\rangle_0 , \tag{V-5}$$

where $\langle \dots \rangle_0$ is the ensemble average in the canonical ensemble over the unbiased system. Thus, the expression of the PMF is:

$$\mathrm{F}(\mathrm{z}) = -\mathrm{k_B}\ln\big(\mathrm{P}_b(\mathrm{z})\big) - \mathrm{w}(\mathrm{z}) - \mathrm{k_B}\ln\left(\left\langle \mathrm{e}^{-\frac{\mathrm{w}(\mathrm{z})}{\mathrm{k_B T}}} \right\rangle_0\right). \tag{V-6}$$

In the above expression, the last term is a constant, the second one is the analytical expression of the bias potential and the first one is determined by sampling the phase space for the accessible values of z. The constant term is there the only unknown term which subsists. When one is interested in the free energy difference, this term is generally neglected. However, with the use of different windows, one still needs to create a coherent single free energy profile. One should note that the splitting of the reaction coordinates in different windows is technically necessary for different reasons. First, it is frequently necessary that one needs to sample unfavorable conformations which are along the reaction coordinates. Thus, in order not to undersample these regions of the phase space, it is necessary to restrain the force the sampling to these precise regions so that they will be really explored. Second, it is technically much more efficient to run a bunch of short simulations which give high probability to explore, altogether, a wide range of the phase space, than to run an extremely long simulation with the hope that every region will be sampled. Finally, as far as the biasing potential is not infinite, all of these windows are not excluding each other, which means that every region is sampled many times. Obviously, the regions which are far from the center of the precise window in one run have a very small probability to be explored during the run, but, overall, the ligand might still explore places which are more favorable for runs in adjacent windows.

4.3.3.Weighted histogram analysis method (WHAM)

The most used method to bind together the results of the computations of the free energy in the different $\mathrm{N_w}$ windows is the so-called weighted histogram analysis method (WHAM). The idea is to construct the whole probability distribution function as a weighted sum, of weights $\{\alpha_i\}$, of the unbiased distribution functions from each window:

$$\mathrm{P}(\mathrm{z}) \propto \sum_{i=1}^{N_w} \alpha_i(z) P_i(z). \tag{V-7}$$

The weights are chosen in order to minimize the variance of the probability distribution function in a self-consistent procedure using generally the Lagrange multiplier method [71].

4.3.4.Technical detail on the computations of the PMF in the present work

The potentials of mean force (PMF) of translocation of cisplatin were computed using the umbrella sampling method. In order to improve the sampling of the lateral heterogeneity of the membrane several cisplatin molecules (3 in the case of plasma membrane model and 5 in the case of DOPC model) were placed in equal intervals along the x-axis at the bilayer part of the bicelle.

In order to check if the lateral heterogeneity of the membrane is sampled sufficiently we analyzed the local lipid environment of each cisplatin molecule present in the system during the simulations (Figure V-8). The lipid molecule was considered to be in the local vicinity of the ligand if any of its atoms was closer than 0.8 nm to any atom of the ligand. The data were averaged over the last 10 ns of all umbrella sampling windows used for the computation of the PMFs of cisplatin.

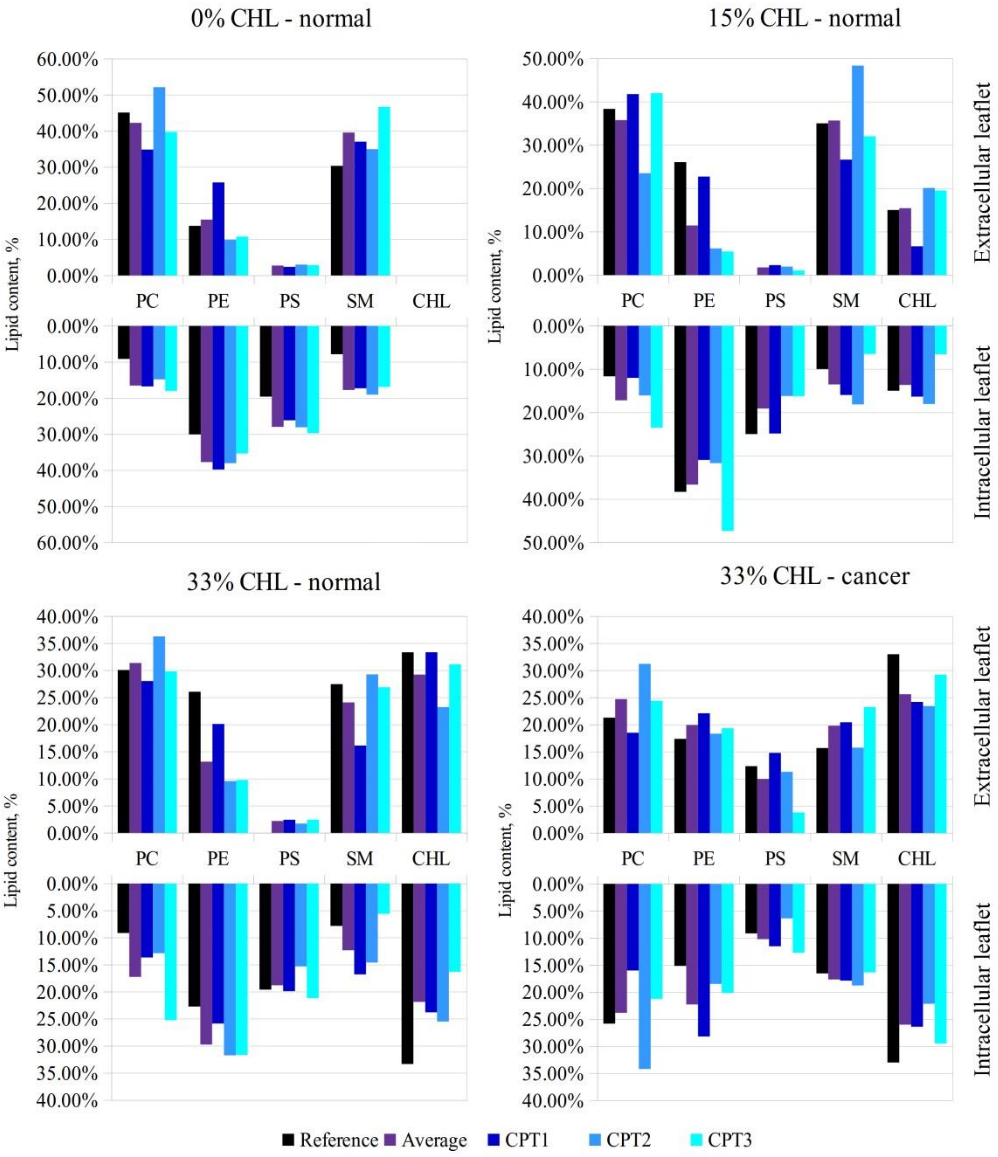

Figure V-8. Local membrane composition in the vicinity of individual ligands and their average in comparison to overall composition of the corresponding membrane leaflets (reference).

The local membrane composition felt by each individual cDDP molecule follows the overall membrane composition. However, some differences exist in between different cDDP molecules due to the lateral inhomogeneity of our model membranes.

In our bicelle setup, the lipids preferring large positive curvature could redistribute from the bilayer part of the bicelle to its caps which may change the lipid content of the areas under analysis. It is clear from Figure V-8 that the microenvironments of the ligands are somewhat different from the initial distributions of the corresponding monolayers shown in Table V-2. However, these changes are small enough, not systematic and do not lead to the loss of asymmetry in normal membranes or its appearance in cancer membrane. Thus, we conclude that the possible redistribution of the lipids between bilayer part of the bicelle and its caps is not an issue in our setup.

The harmonic biasing potential with the force constant of $1000\,\mathrm{kJ\cdot mol^{-1}\cdot nm^{-2}}$ was applied to the center of mass of each ligand in Z dimension, which is perpendicular to the membrane plane. The potentials were centered at discrete points distributed along z-axis at 0.1 nm intervals. Additional weak flat-bottom potential was applied along the x-axis for each ligand to prevent their accidental interaction due to uncontrollable lateral diffusion. This produced 50 to 57 umbrella sampling windows spanning through the whole bilayer along the z-axis. The PMFs were computed as average of all ligands using the weighted histogram technique as implemented in Gromacs. Each window was simulated for at least 16 ns with the last 5 ns being used for sampling.

Table V-2 shows the summary of performed simulations with their corresponding simulation times per window and total simulation times.

Table V-2. Summary of simulations performed

System / **Simulation time**	**DOPC**	**0% CHL - normal**	**15% CHL - normal**	**33% CHL - normal**	**33% CHL - cancer**
Time per umbrella sampling window (ns)	16	16	16	20	20
Total simulation time (µs)	0.8	0.8	0.8	1.0	1.0

Figure V-9 is a plot showing the convergence of the free energy profile for one of our systems. The umbrella sampling runs were carried out up to the moment a visual convergence was reached. In this figure, four PMF are plotted which are taking the last 5 ns of runs of different lengths. The errors of the PMFs were estimated using the bootstrapping method [224]. For each system 400 bootstraps were computed by considering complete histograms as independent data points using the Gromacs WHAM tool.

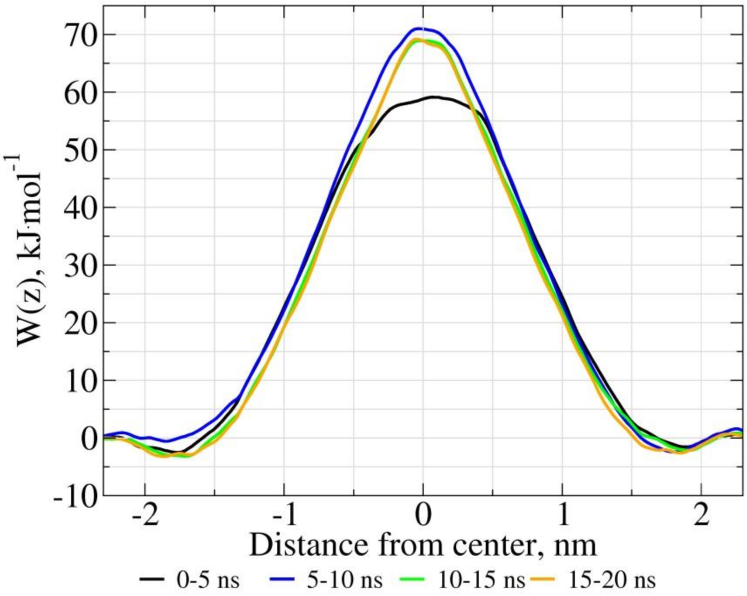

Figure V-9. PMFs convergence in the case of the cisplatin through the cancer model membrane.

4.3.5.Computation of the permeability

MD simulations provide a unique opportunity for studying the diffusion of drugs and small molecules through realistic model membranes in atomic details, although the methodology of computing permeabilities from MD simulations is still subject to debate. The most widespread method of computing permeabilities is the inhomogeneous solubility-diffusion (ISD) model [225, 226], which accounts for transversal heterogeneity of the membrane by means of non-uniform diffusion coefficient of the ligand. The ISD model was used successfully in many studies [227, 228] (see [229] for extensive review). However, a number of publications report consistent difficulties in computing free energy profiles and diffusion coefficients and discuss possible improvements in ISD methodology [227, 230-234]. One of the major concerns comes from the difficulty of determining equilibrium state of the ligand in the membrane related to extremely slow transitions in bilayer structure, which occur on the time scale well beyond the capabilities of routine all-atom MD simulations [235]. Another concern is related to computations of diffusion coefficients of the ligands. Anomalous diffusion regimes were recently reported for small molecules in lipid bilayers [236], which questions the validity of ISD approximation on typical MD time scales. The influence of the long-lived correlations of the restrained solute on diffusion coefficients in the membrane was also suggested as a possible source of errors in ISD [237].

There is a consensus that obtaining precise quantitative values of permeabilities from MD simulations is an extremely complex task. Particularly, comparing permeabilities of different ligands in MD simulations is notoriously difficult and currently hampers wide usage of membrane simulations in evaluation of drug candidates. However, MD simulations could still be used to compare the permeabilities of the same ligand in different environments on the semi-quantitative level. In this case the very similar systematic errors apply to all MD simulations, which make them comparable to each other and to available experimental trends despite the fact that exact values of permeabilities are unlikely to be sufficiently accurate.

The diffusion coefficients D of the ligands were computed for each umbrella sampling window using the force correlation method [238]:

$$\mathrm{D(z) = (RT)^2 \Big/ \int_0^{\infty} \langle \Delta F_z(z,t) \Delta F_z(z,0) \rangle dt} \tag{V-8}$$

where R is the gas constant, T is an absolute temperature, $\mathrm{\Delta F_z(z,t)}$ is the difference between the instantaneous force and mean force acting on the permeant at given time t. The autocorrelation functions were fitted by single exponential decay prior to integration as implemented in Gromacs tools. Diffusion coefficients of all the ligands were averaged for each window. The trajectory was divided into four equal parts and *D* was computed independently for all of them. The standard deviation of these values is reported as the error of diffusion coefficient and their mean value is used to compute permeabilities. The permeability coefficients P of cisplatin were computed using standard ISD model[238]:

$$\mathrm{P = 1 \Big/ \int_{z_1}^{z_2} R(z) dz,} \tag{V-9}$$

where R(z) is the local permeation resistance of the membrane at depth z expressed as:

$$\mathrm{R(z) = e^{\frac{W(z)}{kT}} \Big/ D(z),} \tag{V-10}$$

where W(z) is the PMF of a given ligand. The integration limits z_1 and z_2 were chosen as ±2.3 nm from the membrane center (the points in the water phase outside the membrane). The value of P is insensitive to the choice of these limits since the resistance R in water phase is negligible. The errors of resistances and permeabilities were estimated using the error propagation formalism based on the standard deviations of W(z) and of D(z). For the resistance R, in any point z we get:

$$\mathrm{\sigma\big(R(z)\big) = R(z) \sqrt{\left(\frac{\sigma\big(W(z)\big)}{k_B T}\right)^2 + \left(\frac{\sigma\big(D(z)\big)}{D(z)}\right)^2},} \tag{V-11}$$

where σ is the standard deviation of R. In order to get the global resistance one has to integrate R(z) over z. Since the integral is approximated by a discrete sum the following expression for the standard deviation of R could be derived:

$$\mathrm{\sigma(R) = \sqrt{\sum_i (R_i dz_i)^2},} \tag{V-12}$$

where i denotes one discrete value and dz_i is the size of i-th integration step. Finally, the error of P is computed as:

$$\mathrm{\sigma(P) = P \frac{\sigma(R)}{R}.} \tag{V-13}$$

4.4. Permeation of cisplatin

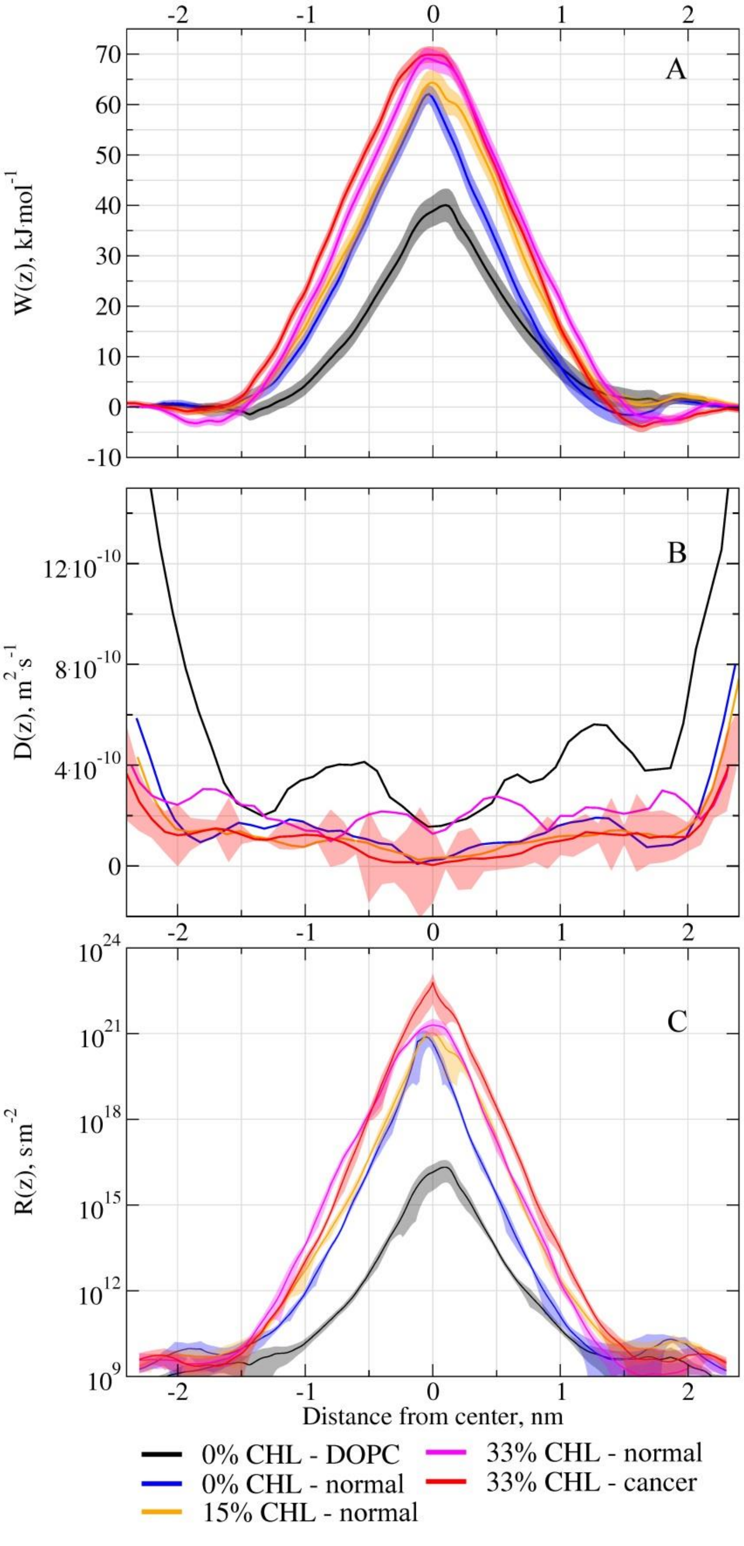

Figure V-10. (A) The PMFs of cisplatin, *W(z)*; (B) the local diffusion coefficient of cisplatin, *D(z)*; (C) the local resistance of the membrane *R(z)* (in log scale) for different membrane models. The errors are shown as ribbons for each curve. The errors for diffusion coefficients overlap a lot thus the errors of only one curve are shown in panel B to keep the figure readable. The errors of all other diffusion coefficients curves are shown separately in the Figure V-11.

Figure V-10A shows the PMFs of cisplatin permeation through the membranes under study. There is a high energy barrier in the center of the membrane, which is expected for such hydrophilic compound as cisplatin. The shape of the central energy barrier is roughly symmetric because the core region of the membrane is similar in both monolayers except some excess of saturated lipid tails in outer monolayer of asymmetric membrane.

The height of the barrier is the smallest for pure DOPC membrane (~40 kJ/mol) which is comparable to previous results obtained in a pure 1,2-dimyristoyl-sn-glycero-3-phosphocholine (DMPC) membrane (~50 kJ/mol)[72]. For normal membrane with 0% cholesterol it is much higher (~62 kJ/mol) and increases even more with the increase of CHL content (up to 70 kJ/mol). The difference in the barrier height between the systems with 0% and 15% cholesterol is minimal, but its width is much larger for the 15% system. It is remarkable that the width of the barrier increases mostly in the outer monolayer, which is enriched in cholesterol in the system with 15% CHL content. The PMFs for normal and cancer membranes at 33% CHL content are almost identical.

Figure V-10B shows diffusion coefficient of cisplatin in different systems. Again, pure DOPC membrane shows the highest values of D. There are no significant differences in D between normal membranes with 0%, 15% and 33% of CHL content, which suggests that cholesterol does not influence transversal diffusion of cisplatin. In contrast, there is a clear difference between normal and cancer membrane models. Diffusion of cisplatin in the cancer membrane is surprisingly slower especially in the center of the bilayer and in the regions of head groups. Figure V-11 shows the diffusion coefficients and their error bars.

Figure V-10C shows the resistance R of different membranes to the permeation of cisplatin. The curves follow the shape of the PMFs but their heights are modulated by the difference in diffusion coefficients. The integration of these curves gives the permeabilities presented in Table V-2.

Table V-3. Values of the permeation resistances and permeabilities of cisplatin for different model membranes together with their respective errors.

System	Cholesterol content	Resistance, R, $s \cdot m^{-1}$	Permeability, P, $m \cdot s^{-1}$
DOPC	0%	$4.5 \pm 0.1 \cdot 10^{6}$	$2.2 \pm 0.05 \cdot 10^{-7}$
Normal	0%	$1.15 \pm 0.04 \cdot 10^{11}$	$8.7 \pm 0.3 \cdot 10^{-12}$
Normal	15%	$2.08 \pm 0.04 \cdot 10^{11}$	$4.8 \pm 0.1 \cdot 10^{-12}$
Normal	33%	$5.75 \pm 0.08 \cdot 10^{11}$	$1.74 \pm 0.03 \cdot 10^{-12}$
Cancer	33%	$6.3 \pm 0.2 \cdot 10^{12}$	$1.59 \pm 0.06 \cdot 10^{-13}$

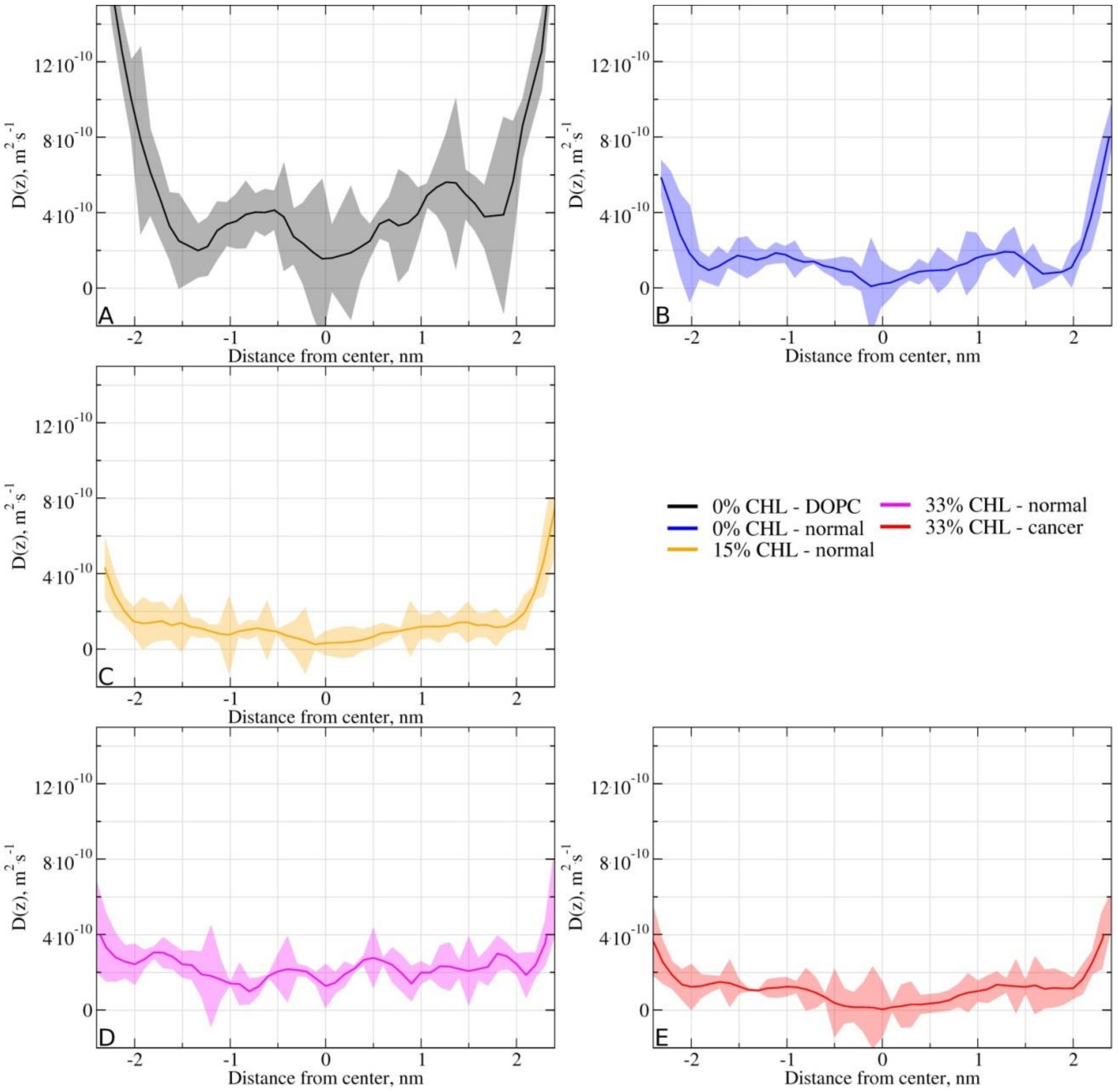

Figure V-11. Diffusion coefficients of cisplatin and their standard deviations.

It is clearly seen that the permeability is the largest for pure DOPC membrane and drops by 4-5 orders of magnitude in the model for plasma membrane with 0% cholesterol. The increase in cholesterol concentration from 0% to 33% decreases the permeability further by another order of magnitude. Finally, symmetrization of the lipid content of the monolayer in the cancer membrane leads to an even larger decrease of permeability. The cancer membrane appears ~11 times less permeable than the normal one.

4.5. Permeability in comparison to experimental results

It is very important to compare our results with the permeabilities of the membranes of model vesicles and living cells to cisplatin available in the literature. Such comparison could only be done on the semi-quantitative level due to two factors: (1) as it was already mentioned, the calculations of permeability using the ISD methodology are known to suffer from inherent limitations (the ISD methodology is likely to provide correct trends when applied to the same ligand in different membranes but it is unlikely to produce values of permeabilities which are quantitatively accurate); (2) the experimental results rarely report permeabilities which could be compared directly to MD data. The majority of the experimental work reports the kinetics of cisplatin permeation through the lipid membranes of cells and artificial liposomes as a single-step first order process [239]. Thus, an effective kinetic constant of permeation, *k* is usually measured in such studies. A relation between permeability and effective kinetic constant is non-trivial in general case and depends on the membrane area, volume of the cell or liposome and membrane heterogeneity [240-242]. Unfortunately there is no experimental research where the area to volume ratio of the cells is determined at the same time as the kinetic constant of cisplatin permeation. That is why in order to estimate the permeability from the available kinetic data we have to use an oversimplified model of spherical cell with radius *r*, which was initially proposed for the liposomes [240-242]:

$$\mathrm{P} = \frac{\mathrm{k} \cdot \mathrm{r}}{3}. \qquad \text{(V-14)}$$

We considered three experimental data, which allowed the determination of the permeabilities of cisplatin in either cells or artificial membranes (Table V-4).

In the work of Eljack et al. [73] the permeation of cisplatin in pure DOPC vesicles was studied depending on the concentration of chloride ions in solution (the values for 10 mM and 150mM external chloride concentrations are shown in Table V-4). Our results for pure DOPC membrane are one order of magnitude higher (~$10^{-7}\mathrm{m} \cdot \mathrm{s}^{-1}$ in simulations versus ~$10^{-8}\mathrm{m} \cdot \mathrm{s}^{-1}$ in experiment). It is necessary to note that only the counterions necessary to balance the system charge are present in our simulations. We also did not consider the complex interplay of reactions between different cisplatin derivatives which are present in salt solutions and may influence an effective concentration of native cisplatin in the experiment. Furthermore, the membranes of our systems are flat while the membranes of real cells and liposomes are significantly curved. We plan to investigate the influence of the curvature on the permeation of the drugs in future studies but it is clear from multiple indirect evidences that the curvature should affect the permeability. That is why our setup is not directly comparable to experimental conditions which may partially explain observed discrepancies.

The work of Ghezzi *et al.* [75] reports a time-dependent uptake of cisplatin in breast cancer MCF-7 cell line. Considering the uptake of cisplatin as a first order kinetic process, we fitted the evolution of the intracellular concentration by an exponential function to obtain the kinetic constant. The average volume of the cells is estimated at 2 pL in this work. We assumed that the cells are spherical and computed the permeability. The obtained value of ~$10^{-11}\mathrm{m} \cdot \mathrm{s}^{-1}$ is 1-2 orders of magnitude higher than our simulation results. In order to obtain the kinetic constant from the work from Ghezzi *et al.*, we considered that the uptake is a first-order reaction:

$$\mathrm{Pt_{extra}} \underset{\mathrm{k_-}}{\overset{\mathrm{k_+}}{\rightleftharpoons}} \mathrm{Pt_{intra}}, \qquad \text{(V-15)}$$

where $\mathrm{Pt_{extra}}$ and $\mathrm{Pt_{intra}}$ are the platinum species outside and inside the cell respectively, and k_+ and k_-, the rate constant of the reaction in the direct and indirect directions respectively. To model the kinetics of the permeation, two paradigms can be undertaken: 1. the chemical reaction is an equilibrium in between the both directions, or 2. the reaction goes mainly in one or another direction.

- *Hypothesis of a direct reaction*

Based on the literature, we first used the second paradigm, rewriting the previous chemical reaction as follows:

$$\mathrm{Pt_{extra}} \xrightarrow{k_+} \mathrm{Pt_{intra}} \qquad \text{(V-16)}$$

One can write the following kinetic equation:

$$-\frac{\mathrm{d[Pt_{extra}]}}{\mathrm{dt}} = \mathrm{k_+[Pt_{extra}]}. \qquad \text{(V-17)}$$

The straightforward solution of such first order differential equation is:

$$\mathrm{[Pt_{extra}](t) = [Pt_{extra}]_0\ e^{-k_+t}}, \qquad \text{(V-18)}$$

where $\mathrm{[Pt_{extra}]_0}$ is initial extracellular concentration at time $t = 0$.

If one is in a closed system with N, the number of molecules, kept constant, the following conservation law emerges:

$$\mathrm{n_{Pt_{tot}}(t) = n_{Pt_{extra}} + n_{Pt_{intra}} = n^0_{Pt_{extra}} + n^0_{Pt_{intra}} = n^0_{Pt_{extra}}} \qquad \text{(V-19)}$$

where $\mathrm{n_{Pt_{tot}}(t)}$ is the total amount of substance in the both subsystems which is a constant equal to the initial extracellular amount of substance at time $\mathrm{t = 0}$, $\mathrm{n^0_{Pt_{extra}}}$, assuming that the initial amount of intracellular cisplatin $\mathrm{n^0_{Pt_{intra}}}$ is null. The amount of substance of extracellular and intracellular cisplatin are written $\mathrm{n_{Pt_{extra}}}$ and $\mathrm{n_{Pt_{intra}}}$ respectively. Thus, we can introduce the concentrations as follows:

$$\mathrm{[Pt_{intra}](t) \cdot \frac{V_{intra}}{V_{extra}} = [Pt_{extra}]_0 - [Pt_{intra}](t)}. \qquad \text{(V-20)}$$

Thus, reminding the expression of the solution of the kinetic equation of the reaction, one as:

$$\mathrm{[Pt_{intra}](t) \cdot \frac{V_{intra}}{V_{extra}} = [Pt_{extra}]_0 \cdot \left(1 - e^{-k_+t}\right)}. \qquad \text{(V-21)}$$

Ghezzi et al. reported the evolution of the accumulation ratio R of the intracellular concentration and the extracellular concentration as a function of time which gives:

$$\mathrm{R(t) = \frac{[Pt_{intra}](t)}{[Pt_{extra}](t)} = \frac{V_{extra}}{V_{intra}} \cdot \left(\frac{1 - e^{-k_+t}}{e^{-k_+t}}\right) = \frac{V_{extra}}{V_{intra}} \cdot \left(e^{-k_+t} - 1\right)}. \qquad \text{(V-22)}$$

It is clear that this last expression of R(t) does not fit the experimental values.

- *Reversible reaction*

We thus have to go back to the initial form of the reversible reaction, considering both k_+ and k_-. For the sake of clarity, we will write $[\mathrm{Pt_{extra}}](t) = x$, $[\mathrm{Pt_{intra}}](t) = y$, $[\mathrm{Pt_{extra}}]_0 = x^0$ and $[\mathrm{Pt_{intra}}]_0 = y^0$. We can write the coupled system of differential equations governing the kinetics as follows:

$$\begin{cases} \frac{dx}{dt} = \dot{x} = -k_+ x + k_- y \cdot \frac{V_{intra}}{V_{extra}} \\ \frac{dy}{dt} = \dot{y} = k_+ x \cdot \frac{V_{extra}}{V_{intra}} - k_- y \end{cases}. \tag{V-23}$$

Taking the first equation of this last system, we can isolate y and find $\dot{y}$:

$$y = \frac{1}{k_-} \cdot \frac{V_{intra}}{V_{extra}} \cdot (\dot{x} + k_+ x), \tag{V-24}$$

and:

$$\dot{y} = \frac{1}{k_-} \cdot \frac{V_{intra}}{V_{extra}} \cdot (\ddot{x} + k_+ \dot{x}). \tag{V-25}$$

We can then inject these expressions in the second differential of the system in order to obtain a simple homogeneous second order differential equation:

$$\ddot{x} + (k_+ + k_-) \cdot \dot{x} = 0 \tag{V-26}$$

which admits, at the exception of the trivial solution, a solution of the form:

$$x = C + D \cdot e^{-(k_+ + k_-)t}, \tag{V-27}$$

where C and D are integration constants. Hence, the form of y can be expressed as:

$$y = \frac{V_{extra}}{V_{intra}} \cdot \left[\frac{k_+}{k_-} \cdot C - D \cdot e^{-(k_+ + k_-)t}\right]. \tag{V-28}$$

To determine the constant C and D, we refer to the initial conditions for t=0:

$$\begin{cases} C + D = x^0 \\ \frac{V_{extra}}{V_{intra}} \cdot \left[\frac{k_+}{k_-} \cdot C - D\right] = y^0 \end{cases}, \tag{V-29}$$

which gives us:

$$\begin{cases} C = \frac{k_-}{k_+ + k_-} \cdot \left(x^0 + \frac{V_{intra}}{V_{extra}} \cdot y^0\right) \\ D = \frac{1}{k_+ + k_-} \cdot \left(k_+ x^0 - \frac{V_{intra}}{V_{extra}} \cdot k_- y^0\right) \end{cases}. \tag{V-30}$$

Noting that $y^0 = 0\ \mathrm{mol \cdot L^{-1}}$, one can write the expression of the solutions of the system of differential equations:

$$\begin{cases} [\mathrm{Pt_{extra}}](\mathrm{t}) = \dfrac{1}{\mathrm{k_+ + k_-}} \cdot [\mathrm{Pt_{extra}}]_0 \cdot \left(\mathrm{k_- + k_+ \cdot e^{-(k_+ + k_-)t}}\right) \\ [\mathrm{Pt_{intra}}](\mathrm{t}) = \dfrac{\mathrm{k_+}}{\mathrm{k_+ + k_-}} \cdot \dfrac{\mathrm{V_{extra}}}{\mathrm{V_{intra}}} \cdot [\mathrm{Pt_{extra}}]_0 \cdot \left(1 - \mathrm{e^{-(k_+ + k_-)t}}\right) \end{cases}. \tag{V-31}$$

Thus, the expression of the accumulation ratio R becomes:

$$\mathrm{R(t)} = \frac{[\mathrm{Pt_{intra}}](\mathrm{t})}{[\mathrm{Pt_{extra}}](\mathrm{t})} = \frac{\mathrm{V_{extra}}}{\mathrm{V_{intra}}} \cdot \frac{\mathrm{k_+} \cdot \left(1 - \mathrm{e^{-(k_+ + k_-)t}}\right)}{\mathrm{k_- + k_+ \cdot e^{-(k_+ + k_-)t}}}. \tag{V-32}$$

- *Limit cases*

  - $k_+ \gg k_-$

This limit case permits us to verify that the expression found in the first hypothesis is valid. Indeed, we can show that in such conditions, the accumulation ratio is expressed as:

$$\begin{gathered}\mathrm{R(t)} = \frac{\mathrm{V_{extra}}}{\mathrm{V_{intra}}} \cdot \frac{\mathrm{k_+} \cdot \left(1 - \mathrm{e^{-(k_+ + k_-)t}}\right)}{\mathrm{k_- + k_+ \cdot e^{-(k_+ + k_-)t}}} \sim \frac{\mathrm{V_{extra}}}{\mathrm{V_{intra}}} \cdot \frac{\mathrm{k_+} \cdot \left(1 - \mathrm{e^{-k_+ t}}\right)}{\mathrm{k_+ \cdot e^{-k_+ t}}} \sim \frac{\mathrm{V_{extra}}}{\mathrm{V_{intra}}} \\ \cdot \frac{1 - \mathrm{e^{-k_+ t}}}{\mathrm{e^{-k_+ t}}} = \frac{\mathrm{V_{extra}}}{\mathrm{V_{intra}}} \cdot \left(\mathrm{e^{-k_+ t}} - 1\right). \end{gathered} \tag{V-33}$$

This expression will not give a valid fit from the experimental data.

  - $k_+ \ll k_-$

This case represents a counterintuitive situation for which the efflux would have a higher rate constant than the uptake:

$$\mathrm{R(t)} = \frac{\mathrm{V_{extra}}}{\mathrm{V_{intra}}} \cdot \frac{\mathrm{k_+} \cdot \left(1 - \mathrm{e^{-(k_+ + k_-)t}}\right)}{\mathrm{k_- + k_+ \cdot e^{-(k_+ + k_-)t}}} \sim \frac{\mathrm{V_{extra}}}{\mathrm{V_{intra}}} \cdot \frac{\mathrm{k_+} \cdot \left(1 - \mathrm{e^{-k_- t}}\right)}{\mathrm{k_-}}. \tag{V-34}$$

The form of this expression might be a valid form to fit the experimental data. However, such an explanation that no uptake is present drives to a complete nonsense, since intracellular platinum species are shown to exist in non-negligible amount.

  - $\frac{d[\mathrm{Pt_{extra}}]}{dt} \sim 0$

The last assumption is equivalent considering that the concentration in the extracellular medium is big enough so that the internalized platinum species do not drive to a significant variation. In such conditions, the solutions of the system of differential equations are written again as follow:

$$\begin{cases} [\mathrm{Pt_{extra}}](\mathrm{t}) = [\mathrm{Pt_{extra}}]_0 \\ [\mathrm{Pt_{intra}}](\mathrm{t}) = \dfrac{\mathrm{k_+}}{\mathrm{k_+ + k_-}} \cdot \dfrac{\mathrm{V_{extra}}}{\mathrm{V_{intra}}} \cdot [\mathrm{Pt_{extra}}]_0 \cdot \left(1 - \mathrm{e^{-(k_+ + k_-)t}}\right) \end{cases}. \tag{V-35}$$

This drives to another expression of R:

$$\mathrm{R(t)} = \frac{[\mathrm{Pt_{intra}}](\mathrm{t})}{[\mathrm{Pt_{extra}}](\mathrm{t})} = \frac{\mathrm{k_+}}{\mathrm{k_+ + k_-}} \cdot \frac{\mathrm{V_{extra}}}{\mathrm{V_{intra}}} \cdot \left(1 - \mathrm{e^{-(k_+ + k_-)t}}\right). \tag{V-36}$$

The decision was made to use this last equation to compute an effective rate constant $k_{eff}=k_{+}+k_{-}$. The best fit on the experimental data of Ghezzi et al. (Figure V-12) gives a rate constant of 0.091 h^{-1} (fitting R^2 value of 0.97).

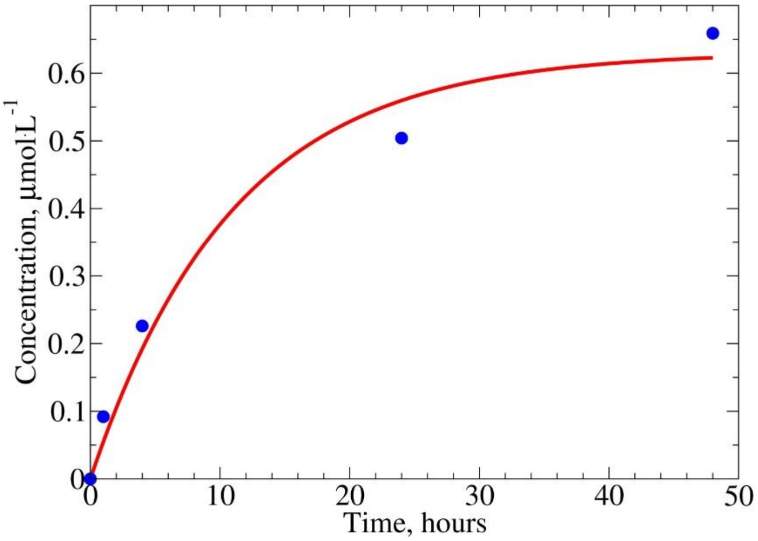

Figure V-12. Fitting of the experimental values obtained by Ghezzi *et al.* [93] by analytical formula assuming first-order cisplatin uptake reaction.

Finally, the work of El-Kareh *et al.* [74] reports the kinetic constant of cisplatin in different cell lines, which were computed in order to build a pharmacokinetic model for several platinum(II) species. Since the volumes and the area to volume ratios of the studied cells are not reported in this paper, we assumed again that the cells were spherical and that their volume was the same (2 pL) as in the work of Ghezzi *et al.*[75] mentioned above. This allowed us to obtain a rough estimate of permeabilities. However, the obtained values are likely to be underestimated since the cells are not spherical and their real area to volume ratio will tend to be higher since real system exhibits complex shape with high membrane curvature.

The only computational work which is directly comparable with the present study is the paper by Nierwzicki *et al.*[72] where the permeability of cisplatin in a pure DMPC bilayer was reported as $6.67\ 10^{-7} m \cdot s^{-1}$. This value is of the same order of magnitude as our result for pure DOPC bilayer.

Table V-4. Values of permeabilities for cisplatin estimated from the literature.

Author	**System**	**Permeability**
---	---	$\mathrm{P\ m \cdot s^{-1}}$
Nierwzicki *et al.*[72]	DMPC bilayer (MD simulations)	$6.67\ 10^{-7}$
Eljack *et al.[73]*	DOPC vesicles ($[Cl^{-}] = 150\ mM$	$1.06\ 10^{-8}$
	DOPC vesicles ($[Cl^{-}] = 10\ mM$	$8.93\ 10^{-10}$

El-Kareh *et al.[74]*	A2780/CP3 human ovarian resistant cancer	$1.87\ 10^{-9}$
	COLO 205 colon carcinoma	$1.24\ 10^{-9}$
	A2780 human ovarian wild type cells	$1.21\ 10^{-9}$
	CAL 27 head and neck cancer	$1.19\ 10^{-10}$
	MKN45 gastric cancer	$1.01\ 10^{-10}$
	MKN74 gastric cancer	$4.90\ 10^{-11}$
	C32 human melanoma	$4.79\ 10^{-11}$
	G361 human melanoma	$2.21\ 10^{-11}$
Ghezzi *et al.[75]*	MCF-7 breast cancer	$6.57\ 10^{-11}$

It is possible to conclude that direct quantitative comparison between MD simulations of permeability and the data obtained experimentally on real cell lines remains challenging. The largest uncertainty comes from the fact that the area to volume ratio of the studied cells is not estimated in the experimental studies. Without these data one is restricted to the primitive and inaccurate model of the cell as spherical homogeneous vesicle, which can easily lead to severe underestimation of the permeability by several orders of magnitude. Taking this into account our results look reasonable and consistent.

Although our simulation setup is not directly comparable to experimental conditions and is subject to inherent limitations of the ISD methodology, it is much closer to real membranes than the vast majority of membrane models routinely used in MD studies today. We demonstrated that taking into account realistic lipid composition and cholesterol content brings estimated permeabilities much closer to the experimental values in comparison to simplified membrane models. We expect that accounting for membrane curvature in future works will reproduce experimental results even better. It is possible to speculate that MD simulations of realistic curved and asymmetric membranes with variable cholesterol content allow for reliable semi-quantitative estimation of permeabilities for cisplatin and other platinum drugs.

4.6. Conclusions

In this work we studied the influence of lipid composition and cholesterol content on the permeation of cisplatin through the model membranes of normal and cancer cells.

- It is shown that the loss of lipid asymmetry in the cancer membranes leads to decrease their permeability to cisplatin by one order of magnitude in comparison to the asymmetric membranes of normal cells. This effect is caused by slower diffusion of cisplatin in the cancer membrane while the energy barrier of permeation remains the same. It is possible to speculate that this effect may contribute to cisplatin resistance in the cancer cells, which exhibit pronounced loss of lipid asymmetry.

- The change of cholesterol molar ratio from 0% to 33% also decreases the permeability of the membrane by approximately one order of magnitude. Thus, changes of cholesterol content in cancer cell membranes may significantly influence their permeability to cisplatin.
- It is also shown that the single-component DOPC membrane is a very poor model for cisplatin permeation in real cells since its permeability is 5-6 orders of magnitude higher than one of the membranes with a more realistic lipid composition.
- We also conclude that direct quantitative comparison between MD simulations of permeability and the data obtained experimentally on real cell lines remains challenging due to the lack of models, which take into account complex shape of the cells, and uncertainty related to chemical modifications of cisplatin in solution.

5. Ongoing work

Permeability coefficients give probing results on the kinetics of cisplatin passive diffusion. To build a better picture of the distribution of the cisplatin species inside and outside the cell, it is worth including also the complex chemistry displayed by cisplatin (see section 2) and though studying more particularly the influence of the saline medium on the speciated cisplatin. Some preliminary results are presented in section 5.1. This study would permit to build a picture of the pharmacokinetics of cisplatin at the cell level giving a precise description of the diffusion phenomenon of the different species. Especially, this would permit to have an insight in the relative importance of influx or efflux mechanisms which are present. This would ultimately permit a better understanding of the transport of the charged aqua species. Finally, it is of great interest to broaden the study to other platinum salts such as carboplatin and oxaliplatin (see section 5.2). Comparing the results obtained with these three platinum salts to the numerous uptake experiments would help in understanding how the passive routes are important for the cell accumulation of these species.

5.1. Simulation of the permeation of speciated species

In the course of the analysis of cisplatin permeation during this thesis, it appears that the complex chemistry of solvated cisplatin plays a fundamental role. It is clear that the study of the permeation of native cisplatin only through the membrane in a system containing only the counterions necessary to make it be neutral is not enough to understand completely the complex process of passive diffusion of cisplatin. We thus started to create naïve topologies of the speciated species of cisplatin. In this scope, we designed the topology of the monoaquacisplatin and the monohydroxocisplatin. The ESP point charges and the Lennard-Jones parameters of the aqua and of the hydroxo ligands were computed in our group. The parameters of the ammine groups and of the remaining chloride were not modified from the existing force field. The models of the di-substituted species are under development.

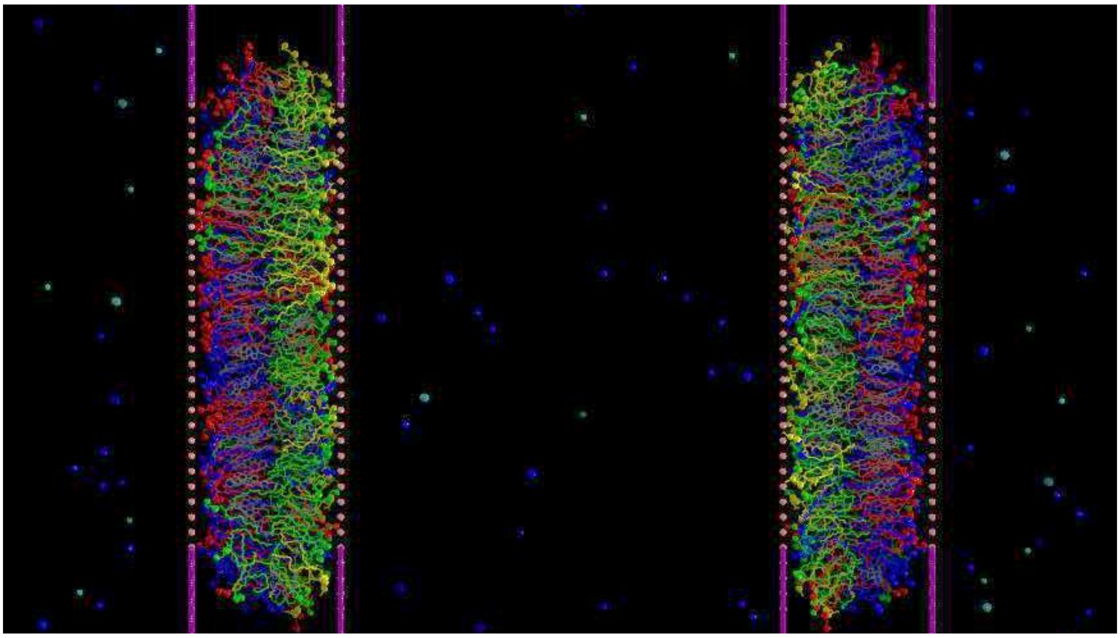

Figure V-13. Graphical representation of the system built to test the speciated cisplatin compounds and the influence of the chloride ions. The lipid membranes are presented in the same manner as in the previous chapter. The spheres around the membrane represent the dummy particles which maintain the bicelle curvature (pink) and the ones which forbid the ions to go from one compartment to another (purple) by other means than passive diffusion through the membrane. For the sake of clarity, water is not represented, but the ions (chloride in green and sodium in dark blue spheres) are depicted.

The first step of this work was to check both the feasibility of this time-consuming study and the presence of a visible influence on the permeation process of the aquation. At the same time, the model for this study takes into account the chloride concentration of the extra- and intra-cellular compartments. As shown in Figure V-13, the system consists in two normal model membranes. The inner part of the system represents the cytoplasm and consists in a region mainly depleted from chloride. This region has to be big enough due to the very low concentration in chloride (which was taken around 4 mM) not to make the assumption that no chloride ions will be present. The choice was to create a region big enough so that 4 chloride ions (as well as 4 sodium ions) will be present in this area. The extracellular compartment was designed with a chloride concentration equivalent to 110 mM.

The second step consists in the computation of the PMF of the different aquated species through the whole system. In order to obtain a first insight and to avoid a waste in computational resources, we limited the feasibility check to the computation of the free energy profile for only one of the two membranes.

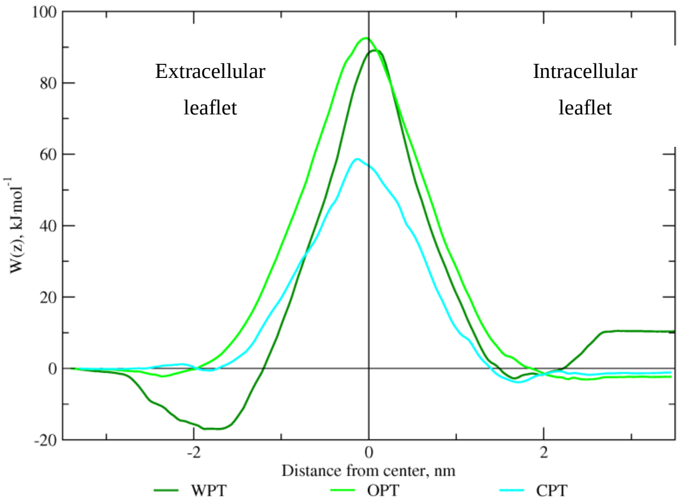

Figure V-14. PMF profile of native cisplatin (CPT), monoaquacisplatin (WPT) and monohydroxocisplatin (OPT) in the "normal" membrane model. The negative distances to the center are towards the extracellular compartment, with a chloride concentration of 110 mM and the positive values are towards the intracellular compartment with a chloride concentration of 4 mM.

The first results are valuable to understand in a non-quantitative manner, whether or not there is any measurable influence on the permeation due to the presence of chloride ions and to the speciation. Figure V-14 shows the PMFs for native cisplatin as well as for the both monosubstituted species. The profile shows the variations of the free energy profile towards the distance of the center of the bicelle; negative values are towards the extracellular compartment and positive values towards the cytoplasmic compartment. It is clearly visible that native cisplatin is most likely to permeate the membrane from the extracellular medium as compared with the two other species. Interestingly, there exists a real asymmetry which must result – at least partly – from the asymmetric concentration in chloride in the two compartments. The both neutral species – monohydroxocisplatin and native cisplatin – do not exhibit a strong influence from the asymmetric concentration in chloride ions. The potential barrier for the efflux process is slightly higher for these both species, but in a non-significant amount. There exists thus a strong difference in between the charged species monoaquacisplatin and the neutral ones. The free energy value inside the cell is about 10 kJ·mol^{-1} higher than for the native cisplatin and the monohydroxocisplatin.

So, the permeation of cisplatin strongly depends on its precise chemical state. Moreover, the difference in chloride concentration in between the extracellular medium and the intracellular medium also plays an important role on the permeation of the different species. It is thus of great interest to continue these computations.

Further computations should be led to increase the accuracy in this issue. It is necessary to draw a profile through the whole system. Indeed, the accuracy of the PMF would be increased if we can assume that our system is periodic. We showed in the present calculation that the variation in concentration in chloride ions could result in a *skewed* free energy profile where the portion of the profile for which the ligand is inside the extracellular medium is shifted from the one where the ligand is in the intracellular medium. However, it is possible to obtain a skewed profile for periodic systems where no difference exists in between the solvent present at the beginning and at the end of the profile. This kind of signature may happen in the case of undersampled systems. This is why it would be important, in the future, to compute the whole profile over the two membranes present in the simulation box.

5.2. Carboplatin and oxaliplatin

Cis-diammine(cyclobutane-1,1-dicarboxylato)platinum(II) and [SP-4-2-(1R-trans)]-(1,2-cyclohexanediaminecyclohexane) also known as carboplatin and oxaliplatin respectively (see Figure V-1) are two platinum salts which were developed in order to circumvent the nephrotoxicity of cDDP and the mechanisms of resistance driving to its potentially poor distribution.

Carboplatin – the second generation of platinating anticancer agents – was originally designed by replacing the very labile chloro ligands by a bidentate dicarboxylate ligand, namely cyclobutane-1,1-dicarboxylate (CBDCA) which shows a better stability thanks to the six-membered ring formed with the platinum atom [66, 124]. This assumption was confirmed by means of quantum chemistry simulations [243, 244]. Carboplatin exhibit lower nephro- and neuro-toxicity as compared as with cisplatin with, as a counterpart, a dose-limiting myelo suppressive effect. Its modes of actions have great similarities with the ones of cDDP, and it was shown to act in the very same manner at the nDNA level [67] at the difference that 20-40-fold higher concentrations of carboplatin are required to form as many adducts as with cisplatin and that the kinetics is around 10-fold slower [130]. This slower kinetics, which is mostly the sign of a slower aquation – with kinetic constant $k \sim 10^{-8}$ s^{-1} as compared to $k \sim 10^{-5}$ s^{-1} for cDDP [124, 128] is the key to the lower toxicity of carboplatin. Although there are some dynamic differences in between these both species, it was shown that most of cells exhibiting intrinsic or acquired resistance to cisplatin are also resistant to carboplatin [67, 119]. This last observation implies that the two species should have a very similar chemistry in solution, including a high affinity to sulfur-containing species such as GSH or metallothioneins [69, 130] and that they potentially use the same modes of uptake and efflux. It is believed that the differences observed in the kinetics of the transport might come to the fact that carboplatin keeps its native form in the extracellular media in greater proportions than cDDP. Once in the cell, the precise chemistry of carboplatin leads to active aquated forms which can be analog to cisplatin species [121, 175]. Once again, the slower kinetics of carboplatin leads to a lower excretion rate which is most likely the sign of less efficient cell scavenging mechanisms that are told to be linked to the stable CBDCA ligand. This allows carboplatin to exhibit a retention half-life of 30 hours which should be compared with the 1.5 to 3.6 hours in the case of cisplatin [65].

Oxaliplatin – the 3rd generation of platinum-based anticancer drugs – was then developed in order to address the problem of distribution found with cisplatin and carboplatin which is intrinsically related to the resistance phenomena of some cell lines [245]. Not only the chloride moieties are replaced by an oxalate leaving group, but the ammines have also been substituted by the 1,2-diaminocyclohexane (DACH) bidentate carrier ligand. Importantly, it was shown that the loss of DNA repair pathways does not enhance the action of oxaliplatin as it was shown for cisplatin or carboplatin, inferring that its modes of action are different [130]. However, it was shown that oxaliplatin readily forms intra- or inter-strand adducts with the guanines of the nDNA [120, 123]. It is worth noting that, on the top of the interactions at the nuclear level, oxaliplatin also shows cytotoxic effects in cytoplasts [122]. Not only the modes of action are different for oxaliplatin but it also exhibits a lower affinity to hctr1 [130]. Oxaliplatin is efficient against several cisplatin or carboplatin resistant cell lines which is believed to be related with the presence of the DACH ligand [66, 121, 122, 124]. At the nuclear level, the DACH ligand could lead to a poor recognition of the oxaliplatin-nDNA adducts as compared as with cisplatin or carboplatin, which can explain the differences in cytotoxicity in between these drugs. The DACH ligand is also believed to play a role in the lower nephrotoxicity of oxaliplatin relatively to cisplatin, although oxaliplatin neurotoxicity remains dose-limiting.

Computing the permeability coefficient as well as the partition coefficient for different platinum species would be another insight in the understanding of the link in between lipophilicity and the propensity of the species to permeate a plasma membrane. We thus started to make these computations in the cases of cisplatin, carboplatin and oxaliplatin.

Computations of the PMFs, diffusion coefficients, resistance and permeability coefficients where done in the same way as reported in section 4.

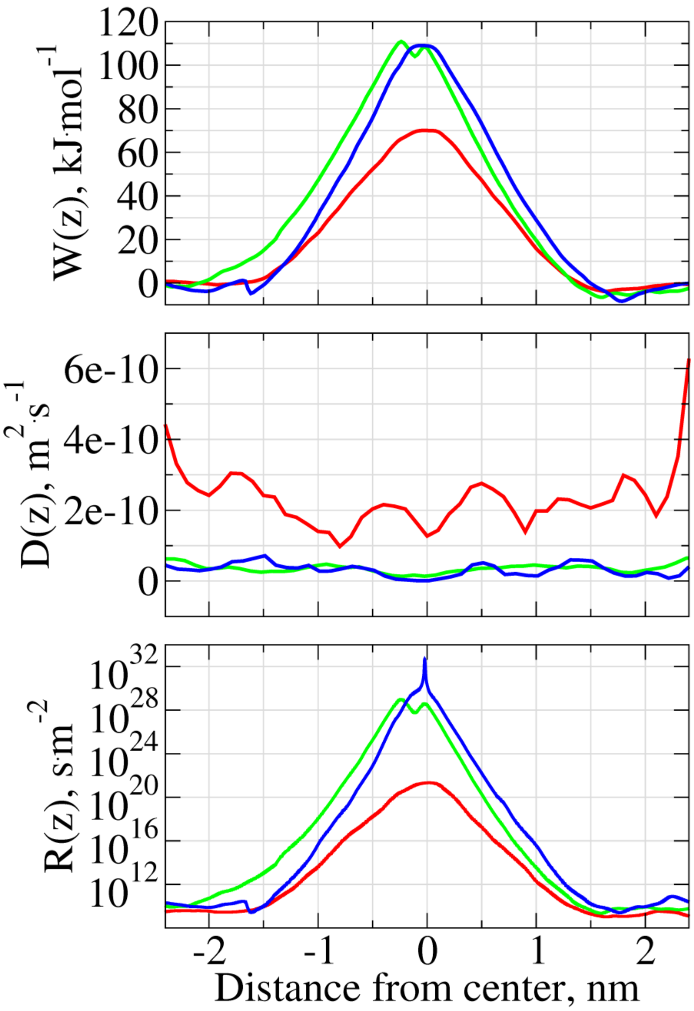

Figure V-15. The upper panel represents the PMFs of the three species, the middle panel shows the diffusion coefficients and the lower panel the resistance. Cisplatin is represented in red, carboplatin in green and oxaliplatin in blue.

It is clear, from Figure V-15, that our present results suggest a drastically higher thermodynamic barrier for both carboplatin and oxaliplatin. Also, the diffusion coefficient of these species is visibly ~4-fold lower. It results in extremely high resistance coefficients and low permeability coefficients (see Table V-5). Permeability coefficients obtained in this work differ significantly from experimental data by 8-10 order of magnitudes. A major problem is revealed here concerning carboplatin and oxaliplatin modeling. The results of the partition coefficients computed from the PMFs are far from the experimental values due, most likely, to the discrepancy in the partial charges of carboplatin and oxaliplatin. They are thus not included in the discussion. Such discrepancies cannot be due to the ISD model but certainly originate in the parameterization of these two molecules.

Table V-5. Permeability coefficients obtained in this work compared with the ones computed from experimental data.

Author	**System**	**Permeability**		
		Cisplatin	**Carboplatin**	**Oxaliplatin**

---	---	$\mathrm{P\ m \cdot s^{-1}}$	$\mathrm{P\ m \cdot s^{-1}}$	$\mathrm{P\ m \cdot s^{-1}}$
This work	Normal membrane	$1.74\ 10^{-12}$	$7.91\ 10^{-20}$	$2.62\ 10^{-22}$
Ghezzi *et al.[75]*	MCF-7 breast cancer (Effective)	$6.60\ 10^{-11}$	$4.50\ 10^{-10}$	$4.74\ 10^{-11}$
	MCF-7 breast cancer (Influx)	$3.26\ 10^{-13}$	$1.46\ 10^{-12}$	$3.08\ 10^{-13}$
	MCF-7 breast cancer (Efflux)	$6.56\ 10^{-11}$	$4.48\ 10^{-10}$	$4.74\ 10^{-10}$
El-Kareh *et al.[74]*	A2780/CP3 human ovarian resistant cancer	$1.87\ 10^{-9}$		
	COLO 205 colon carcinoma	$1.24\ 10^{-9}$		
	A2780 human ovarian wild type cells	$1.21\ 10^{-9}$		
	CAL 27 head and neck cancer	$1.19\ 10^{-10}$		
	MKN45 gastric cancer	$1.01\ 10^{-10}$		
	MKN74 gastric cancer	$4.90\ 10^{-11}$		
	C32 human melanoma	$4.79\ 10^{-11}$		$3.22\ 10^{-10}$
	G361 human melanoma	$2.21\ 10^{-11}$		$1.97\ 10^{-10}$
	MIAPaCa2 human pancreatic cancer			$8.52\ 10^{-10}$
	Colo357 human pancreatic cancer			$3.11\ 10^{-10}$
	NMG64/84 human colon cancer			$1.39\ 10^{-10}$
	HT29 human colon cancer			$5.76\ 10^{-11}$
	PMH/89 human pancreatic cancer			$2.75\ 10^{-12}$

It should be noted that the force fields of carboplatin and oxaliplatin were developed in our group. Partial charges were probably extracted a too crude way. LJ parameters were mostly assigned according to those of similar molecules displaying similar groups. However, in the frame of a present international collaboration, new computations of the partial charges and of the Lennard-Jones parameters indicate a potential discrepancy with the values present in the initial force field. These computations are ongoing, and a new force field for both carboplatin and oxaliplatin will be developed in order to obtain a realistic model of these drugs.

Chapter VI - **The influence of the local curvature of the membrane on the permeation**

In the second chapter, we described the influence of the local curvature on the inner properties of the membrane. We have shown that curvature has impacts on cholesterol distribution and orientation as well as on the lipid distribution resulting in variations in the lipid order parameter and on the leaflet dimensions. Nowadays imagery techniques are often used to have an insight in the properties of the cells observed and have a sufficient resolution which permits to characterize the membrane roughness [45]. Roughness could be viewed as a mesoscopic image of the distribution of local curvatures of a cell membrane. Recent studies [45] show that membrane roughness could permit to discriminate cancer from normal cells. These observations imply at the same time that a cancer membrane has a distribution of curvatures shifted to higher curvatures and possibly a widened distribution of curvatures. Knowing that curvature has important consequences on the membrane structure, we wondered if these changes have an impact on the membrane permeability. Keeping in mind that cancer cells present a rougher surface, the possible changes in permeation in between curved and flat membrane could help to explain the differences in permeation in cancer and normal cells. In addition, up to now, regions of the plasma membrane which are preferred for passive diffusion remain unknown and, to our knowledge, no study has already addressed the impact of curvature on the permeation of small molecules and drugs. In this work, we tried to fill this gap. The present work is in the process for publication.

1. Curved membranes are more likely to allow passive diffusion

It is known that membrane lipidomics and cholesterol content are linked to both the permeation and the membrane properties. In order to understand the interconnections in between these membrane properties and permeation, we performed AAMD computations of the permeation for water, chloride, sodium and two anticancer drugs; cisplatin and gemcitabine.

To discriminate the sources of the changes in permeation, we decided to address the question thoroughly for the three common species that are water and chloride and sodium ions. We studied their permeation in four model membranes and for 2 or 3 values of the curvature (see Figure VI-1). In order to exacerbate the effects induced by the curvature, we selected an extreme value of ±0.2 nm^{-1} which could be found on the surface of the membrane in some reshaping processes, during the creation of vesicles [246] or at the junction with specific proteins such as BAR domains [247]. The use of such high values allows detecting curvature-related changes of permeability reliably and in a reasonable computational time, however, further computations will have to address intermediate values.

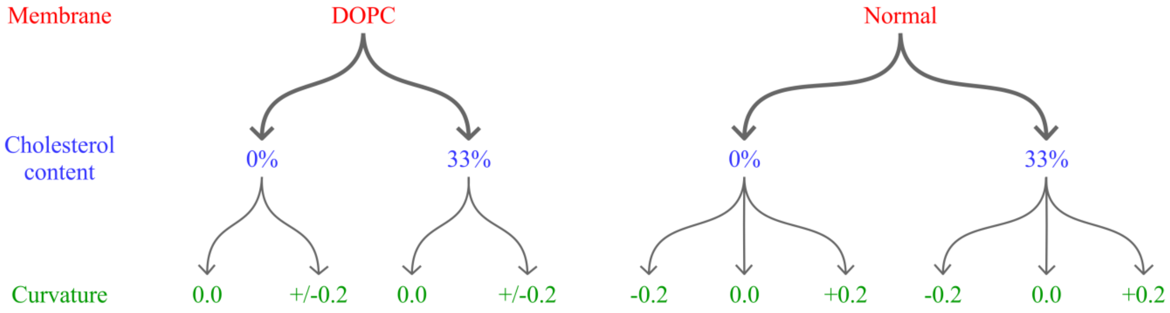

Figure VI-1. Diagram representing the different systems for which the permeation was studied for water, sodium and chloride. The cholesterol content is intended as a molar value and the curvature is expressed in nm^{-1}.

The PMFs, the coefficient diffusion and the resistance coefficient were computed for the three species in the same way as in the previous chapter. They are presented in Figure VI-2 for the water, Figure VI-3 for the chloride ion and Figure VI-4 for the sodium ion.

2. Technical details

The analysis of the permeation for the five species that are water, chloride, sodium, cisplatin and gemcitabine implied 36 computations of the free energy profile. The simulation time per window ranging in between 15 ns and 45 ns, for a total of 50 to 61 windows per system; these simulations result in a total of more than 40 μs of simulations in AAMD. These simulations represent a total of 3 million of hours of CPU time spent on three different resources: the Mésocentre de Franche-Comté, for building the systems, and pre-equilibration processes, the Centre de calcul régional Romeo and GENCI-CINES, on the Occigen machine for production runs.

The general setup for these computations was the same as in the previous chapters. Some of the systems were shown to induce a bias during the production run demanding some more computations to improve the accuracy of the data. The model membrane used in these simulations is restrained on the x axis by constraining its center of mass. In Gromacs packages the constraint is applied on one selected atom from the selected group. However, up to v. 2018, no monitoring on the selected atom was made. It happens that for some of our systems, the precise atom may diffuse along the membrane shifting rapidly the membrane on the x axis. In some cases these changes can be very fast so that the ligand inside the membrane cannot follow these translations smoothly. This may result in bias in the estimation of the free energy.

3. Analysis of the results

3.1. Curvature lowers the free energy peak

The main result which should be noted from the different computations for water, chloride and sodium is that the energy barriers of all the permeating ligands are lower in the curved systems in comparison to the flat ones. Magnitude of this effect varies depending on the precise ligand. It is worth mentioning that this effect does not depend on the membrane composition.

The signature of this effect is also present in the resistance profile and consequently in the computed permeation coefficients. The values of the permeation coefficients are reported in Table VI-1 for the three studied ligands. There is no obvious dependence of the absolute change of permeability on the size or the chemical nature of the ligand. It is noticeable that – in the case of water – these variations are under one order of magnitude. In the case of Na^+ or Cl^-, otherwise, these changes are of 1-2 orders of magnitude.

Table VI-1. Values of the permeability coefficient for water, sodium and chloride in different systems. The errors are not indicated. They were computed in the same manner as in the previous chapters and are systematically 1-2 orders of magnitude smaller than the values.

	0 % CHL					**33 % CHL**				
	DOPC		**Normal**			**DOPC**		**Normal**		
C, nm^{-1}	**0**	**±0.2**	**-0.2**	**0**	**+0.2**	**0**	**±0.2**	**-0.2**	**0**	**+0.2**
H_2O	$2.87\ 10^{-5}$	$3.39\ 10^{-5}$	$2.66\ 10^{-5}$	$2.04\ 10^{-5}$	$5.65\ 10^{-5}$	$2.12\ 10^{-5}$	$3.80\ 10^{-5}$	$3.74\ 10^{-6}$	$2.54\ 10^{-6}$	$5.49\ 10^{-6}$
Na^+	$6.16\ 10^{-13}$	$2.77\ 10^{-12}$	$5.29\ 10^{-14}$	$1.81\ 10^{-15}$	$1.35\ 10^{-14}$	$4.54\ 10^{-15}$	$5.27\ 10^{-14}$	$1.71\ 10^{-15}$	$1.59\ 10^{-17}$	$8.38\ 10^{-17}$
Cl^-	$3.11\ 10^{-15}$	$8.64\ 10^{-15}$	$1.24\ 10^{-14}$	$8.28\ 10^{-17}$	$7.72\ 10^{-15}$	$2.67\ 10^{-17}$	$1.56\ 10^{-15}$	$6.40\ 10^{-16}$	$1.51\ 10^{-17}$	$1.51\ 10^{-16}$

3.2. Curvature shifts the position of the potential energy barrier

It is also visible on the results that for all the free energy profiles as well as for the local resistance coefficients, a shift of the maximum value is present when curvature is present. This shift of the peaks is systematically towards the concave monolayer.

To quantify this phenomenon, we plotted the position of the peak as a function of the curvature for all the studied species, including the anticancer drugs gemcitabine and cisplatin for the normal model membrane (Figure VI-5). The estimate of the peak position was made by the computation of the first moment m_1 of the PMF profiles such that:

$$m_1 = \frac{\int_{z_2}^{z_1} zW(z)dz}{\int_{z_2}^{z_1} W(z)\,dz}. \tag{VI-1}$$

These shifts are the signature of the changes in the area per lipid shown in Chapter IV -. The concave membrane is more densely packed involving a higher barrier to any permeant.

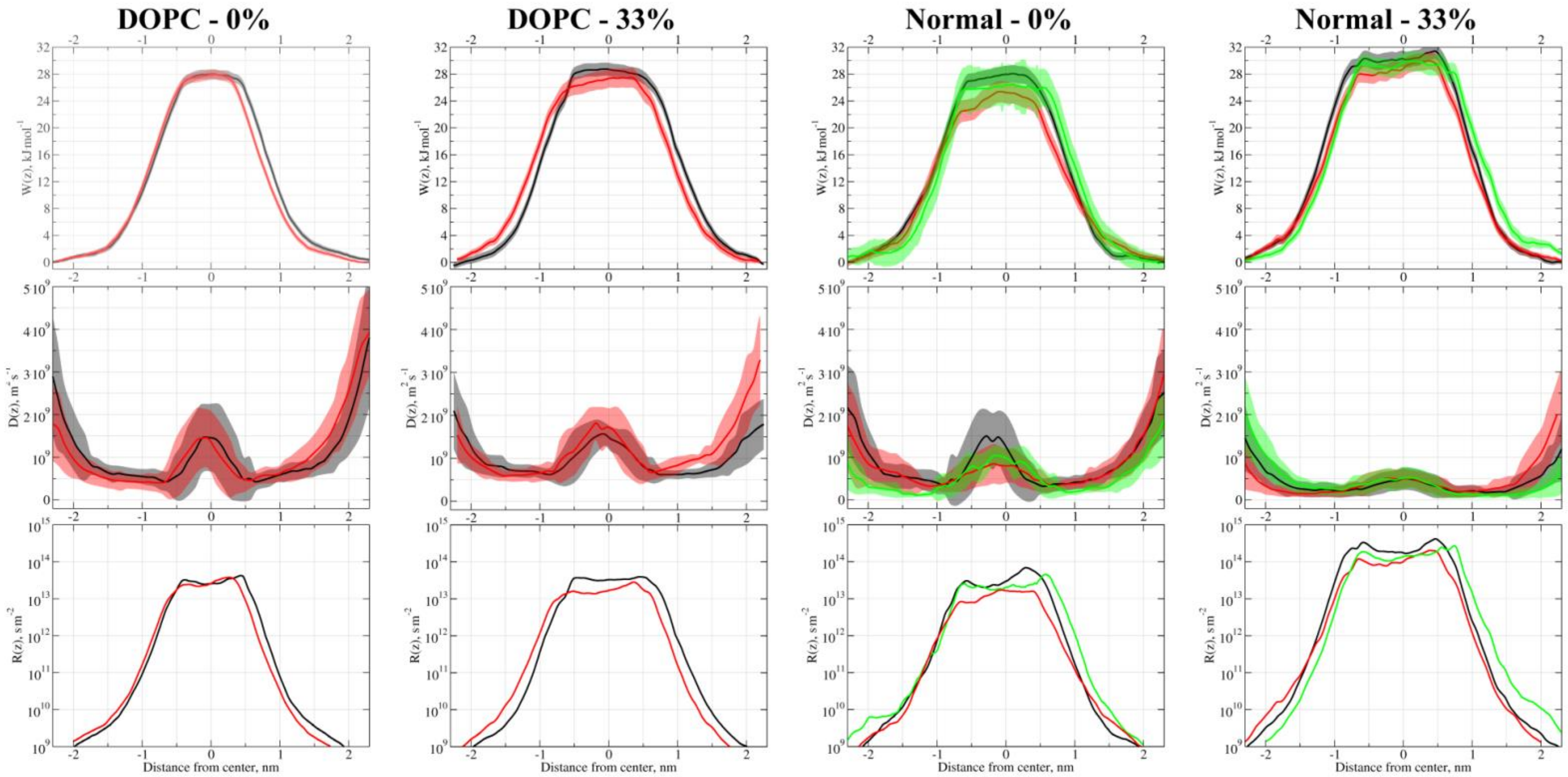

Figure VI-2. Free energy profile, diffusion coefficient and resistance coefficient for water in four different model membranes: pure DOPC, DOPC with 33% CHL, normal model membrane and this last model depleted from its cholesterol content. For the pure DOPC membrane, only one curvature was sampled given the symmetry of the membrane. For the asymmetric systems (normal model membranes), positive and negative curvatures were explored. For all the systems, the flat membrane is in black. For DOPC, the curved membrane is in red. For the normal model membranes, negative curvature is in green and positive curvature is in red.

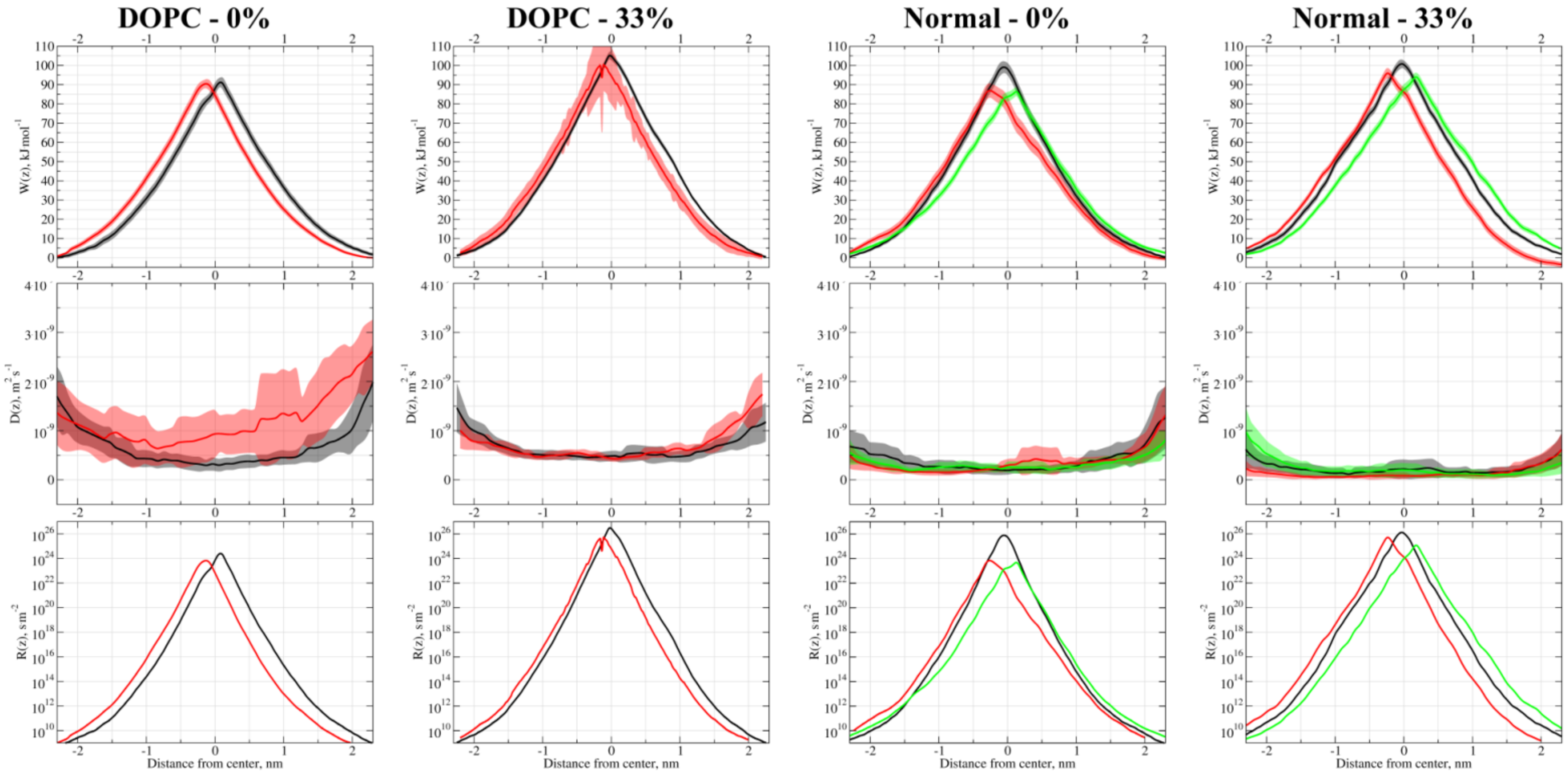

Figure VI-3. Free energy profile, diffusion coefficient and resistance coefficient for chloride in four different model membranes: pure DOPC, DOPC with 33% CHL, normal model membrane and this last model depleted from its cholesterol content. For the pure DOPC membrane, only one curvature was sampled given the symmetry of the membrane. For the asymmetric systems (normal model membranes), positive and negative curvatures were explored. For all the systems, the flat membrane is in black. For DOPC, the curved membrane is in red. For the normal model membranes, negative curvature is in green and positive curvature is in red.

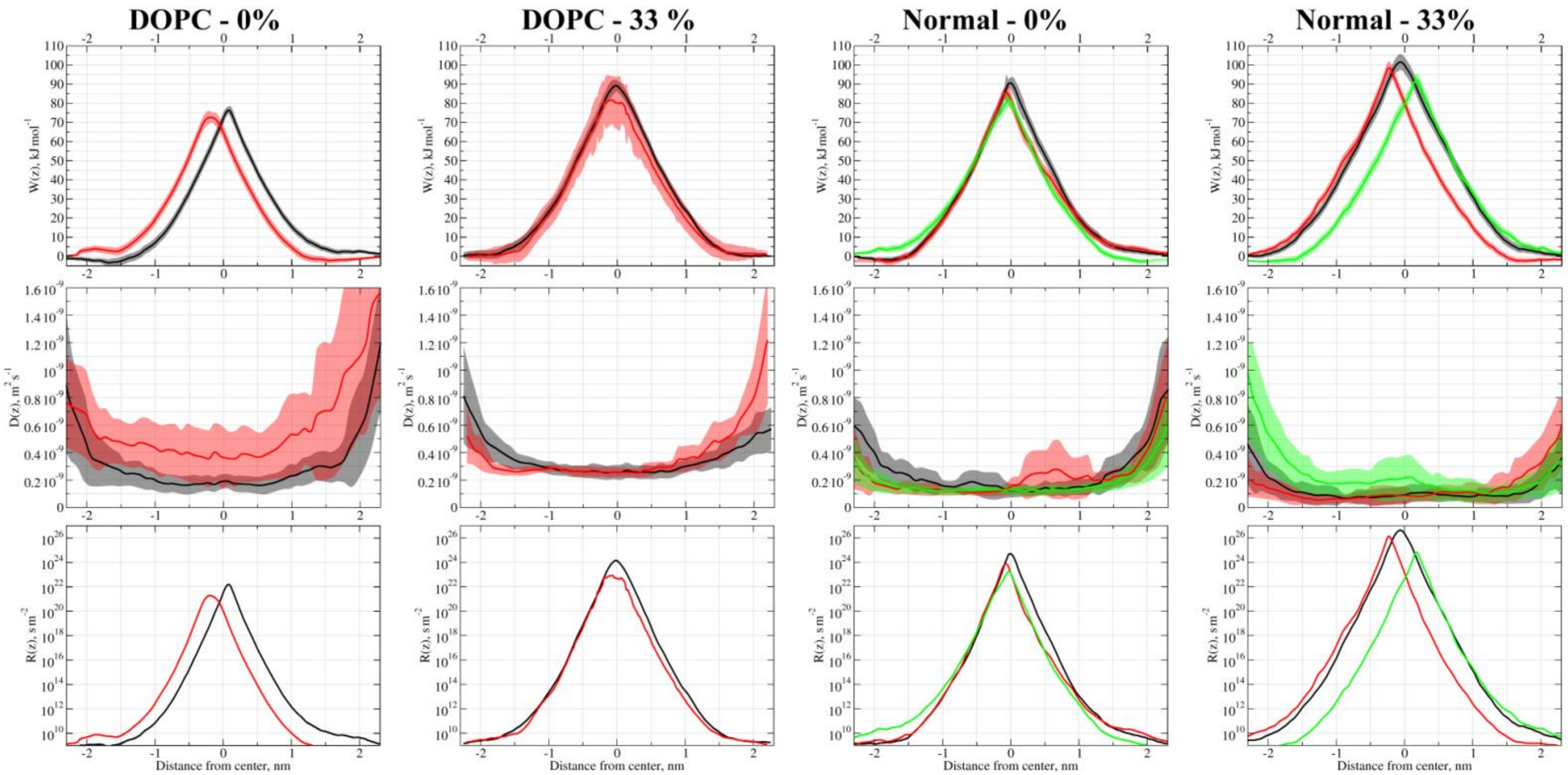

Figure VI-4. Free energy profile, diffusion coefficient and resistance coefficient for sodium in four different model membranes: pure DOPC, DOPC with 33% CHL, normal model membrane and this last model depleted from its cholesterol content. For the pure DOPC membrane, only one curvature was sampled given the symmetry of the membrane. For the asymmetric systems (normal model membranes), positive and negative curvatures were explored. For all the systems, the flat membrane is in black. For DOPC, the curved membrane is in red. For the normal model membranes, negative curvature is in green and positive curvature is in red.

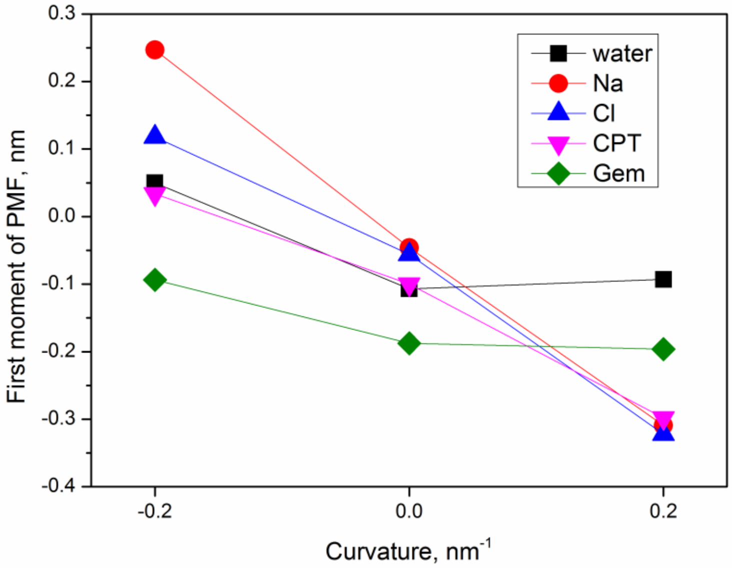

Figure VI-5. Positions of the peaks of PMFs, computed as the first moments of the corresponding curves, as a function of curvature.

3.3. The influence of bending on the diffusion coefficient

The first observation is that D is mainly unaffected by bending in the core of the bicelle – up to 1 nm to the center. The maximal changes in this region are about 1.5-fold the values of the planar model membrane. The difficulties inherent to diffusion coefficient computation do not allow us to make a strong assumption based on these observations. Nonetheless, it should be noted that bending creates a slight asymmetry in the diffusion coefficient profile where one can observe lower values of D for the concave monolayer in most of the cases. However, the membrane resistance profiles show that these relative changes of D have a little or no influence on the permeation process which is mainly affected by the value of the free energy.

4. Effect on two anticancer drugs

Figure VI-6 shows the effects of curvature for the anticancer drugs cisplatin and gemcitabine for the normal model membrane only. Although the size of these molecules is much bigger than those of water or ions, the effects are the same as observed and described before.

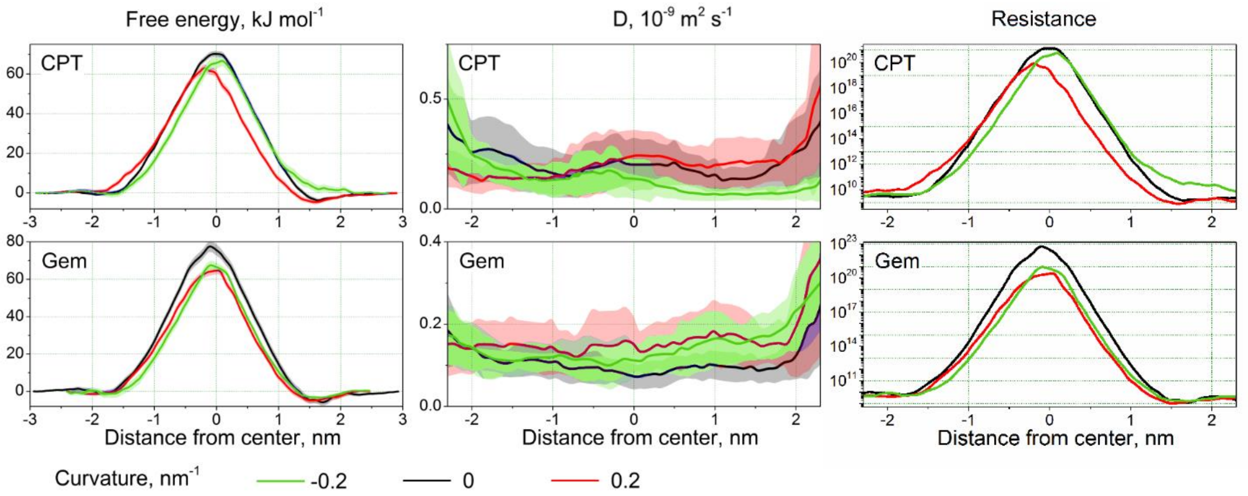

Figure VI-6. Free energy profile, diffusion coefficient and resistance coefficient for cisplatin (CPT) and gemcitabine (Gem) in the normal model membrane.

In the precise case of these anticancer drugs, these differences of energy and resistance peaks are of real interest. First, we can hypothesize that, on the cell membranes, highly curved areas are most likely to allow permeation. Table VI-2 shows the different values of permeability for these drugs in the normal model membrane. This effect is especially remarkable in the case of gemcitabine which shows difference of two orders of magnitude in between curved and flat model membranes.

Table VI-2. Permeability coefficients for cisplatin (CPT) and gemcitabine (Gem) for the normal model membrane.

Curvature, nm^{-1}	**CPT**	**Gem**
-0.2	$7.0 \cdot 10^{-12} \pm 3.1 \cdot 10^{-13}$	$4.5 \cdot 10^{-12} \pm 1.5 \cdot 10^{-13}$
0.0	$2.3 \cdot 10^{-12} \pm 6.2 \cdot 10^{-14}$	$8.3 \cdot 10^{-14} \pm 3.6 \cdot 10^{-15}$
+0.2	$5.0 \cdot 10^{-11} \pm 1.6 \cdot 10^{-12}$	$1.4 \cdot 10^{-11} \pm 4.2 \cdot 10^{-13}$

Chapter VII - **Conclusions and perspectives**

In this work we have shown that modeling finely the plasma membrane and especially its lipid matrix is a very important issue for studies devoted to drug permeation. The complexity of the models grows constantly with the available numerical resources and with the precise data given by the lipidomics. This work was, in its first part, dealing with the creation of realistic models of the lipid matrix of the plasma membrane. The structure of these models and their properties show that mono-component lipid bilayers as it was and still is customary to see in the literature are a very crude model. The study of the permeation of cisplatin in the normal model membrane and in the pure DOPC bicelle show a difference of 5-6 orders of magnitude in the permeability coefficient. This comes from two main factors: the **lipid heterogeneity** and the **cholesterol content**. Cholesterol is known to play an important role in the membrane fluidity and is believed to be one of the cornerstones of the formation of lipid rafts. In the present work, it was shown that the increase in cholesterol content from 0% to 33% decreases the permeability of the membrane to cisplatin by 1 order of magnitude. The remaining difference in between the mono-component reference model made from DOPC and the normal model membrane depleted from cholesterol is due to the composition made of different lipids. This heterogeneity, in the case of the plasma membrane drives it to be less permeable than the simple DOPC model.

On top of that, the **asymmetry** of the membrane leaflet also plays a major role in the drugs permeation. It is known that plasma membranes in their normal functioning state exhibit an actively maintained asymmetry in between their leaflets. Meanwhile, it was shown that apoptotic cells as well as some non-apoptotic cancer cell lines exhibit a *symmetrization* process which results in the overexposition of PS – and possibly of PE. In order to address this issue and to understand if this phenomenon has an impact on the permeation of anticancer drugs, we made a model of a cancer plasma membrane. Cisplatin permeation is slightly affected by these changes in an unfavorable manner. This observation could be a contribution of the observed acquired and/or intrinsic resistance to cisplatin of some cancer cell lines.

Finally, the local **curvature** of the plasma membrane was shown to induce important modification of the membrane structure and permeation. The mechanical stress induced by the membrane curvature induces changes in the thickness of the convex monolayer and modifies the area per lipid of the both leaflets. The core of the membrane – the distal parts of the lipids fatty acids – is reorganized and the order parameter is decreased in this region. Curvature also drives cholesterol to reside more in the core of the membrane which could explain partly the variations of the order parameter. These structural properties have a visible effect on the permeation of various ligands. The permeation of water, chloride, chloride ion, sodium ion, gemcitabine and cisplatin was shown to be increased in curved model membranes whether they are simple DOPC bicelles or asymmetric ones. Hence, even if the intensity of this effect is depending on the chemical nature of the ligand, it appears to be systematic.

At the end, four interlinked parameters appear to drive the membrane permeability: 1. the lipid heterogeneity, 2. the cholesterol content, 3. the membrane asymmetry and 4. the membrane curvature. Of course, the model membranes which were developed do not present a perfect picture of the lipid matrix of the plasma membrane. First, their complexity is limited to four types of headgroups, and, no phosphatidic acid (PA), phosphatidylglycerol (PG) or other more *exotic* types of lipids is embedded. One of the reasons of this first simplification is the will to obtain systems from which the size is not prohibitive in terms of computational resources. Yet, if one increases the number of constituents, their presence in the membrane should remain statistically relevant which means to increase the size of the system accordingly. Not only the size of a complex system increases, but also the complexity to sample correctly all the lateral heterogeneity which rapidly results in situations which are on the edge of the computational possibilities. It is for the very same reason that only one type of fatty acid was studied here. The cutting-edge simulations [50, 51, 81, 82] which involve both a large heterogeneity in the lipid types and in their fatty acids are actually investigated in coarse grained MD. Unfortunately, such simulations do not permit to obtain the expected refinement in the analysis of ligand permeation.

1. Drawing a better picture of the platinum salts permeation

In this work, we have computed the permeation of cisplatin and we have also started to investigate some other salts (carboplatin, oxaliplatin) and some derivatives of the native form of cisplatin. This work could ultimately results in a new pharmacokinetics model (see Figure VII-1 for a schematic representation) of the cisplatin including speciation and transport. This model basically consists in two compartments; the extracellular and the intracellular media, linked together by the plasma membrane. The computation of the permeability coefficient of the different speciated species allows us to associate a kinetic constant to the transport reaction modeled as a simple first-order process for every species. The chemistry of cisplatin in solution is already given in the literature (especially by Miller *et al.* [76]). The links in between each *reservoir* has to be done. This could be made in a self-consistent way, by computing for different conditions of pH and chloride content the concentrations of the different species and by modifying the sensitive kinetic constants[25] iteratively. The constraints on the result are given by the values found in the literature for these different conditions. Finally, on top of these reactions, metabolization reactions with GSH and metallothionein could be added. The kinetic constants can be

---

[25] In the set of speciation equations, the kinetic constants related to the hydroxylation processes do not have accurate values.

taken from a former work made in our group [77]. Altogether, this model may give help to understand 1. if passive diffusion is the main process of influx and efflux, 2. which species play the main role inside the cell and which conditions are more favorable to the cisplatin attack. This work could help to understand some of the resistance processes which are possibly related to a change in the physiological conditions in the vicinity of the tumor area.

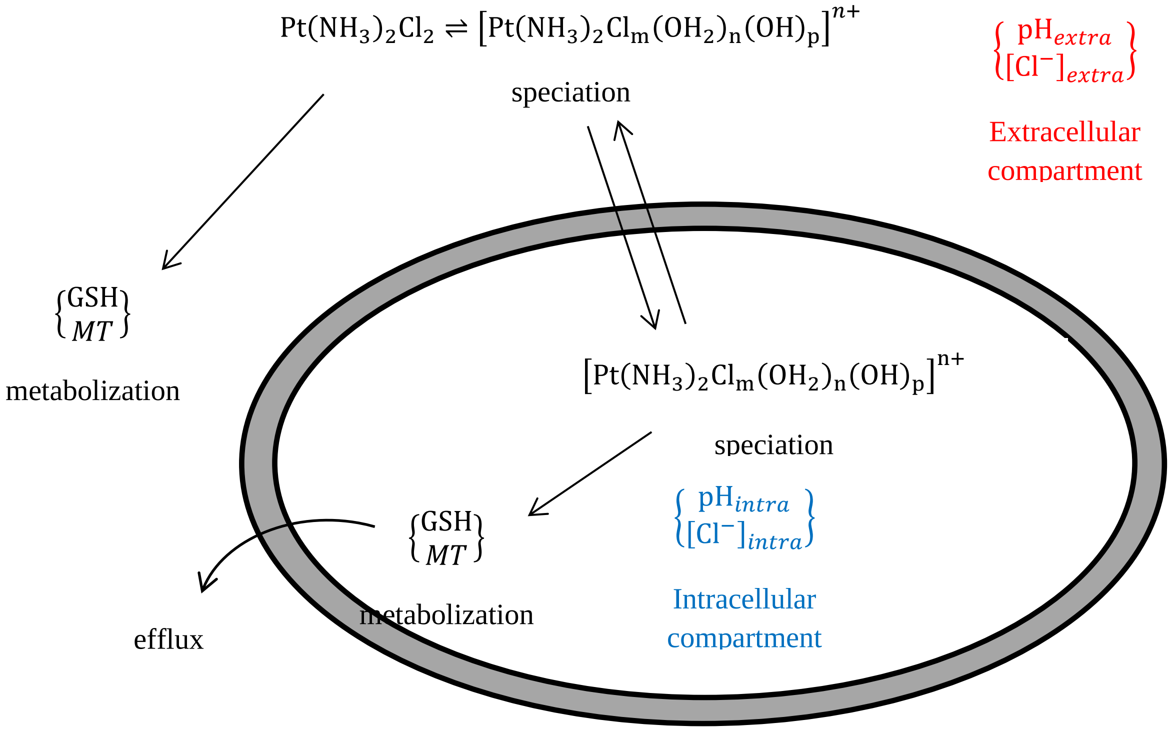

Figure VII-1. Representation of the pharmacokinetics model for cisplatin. Two compartments are present; the extracellular and the intracellular one. These compartments are assigned realistic values of pH and chloride concentration. The speciation of cisplatin is taken into account by means of first order reactions. The processes of metabolization could be taken into account through the interactions with glutathiones and metallothioneins. The diffusion process is encoded as a first order reaction based on the computations of permeation of the different species through the normal lipid membrane model.

In order to have a wider picture of the cisplatin permeation, it would help to understand a better way the transport of new generation of platinated anticancer drugs. In this purpose, it is of great importance to finish the development of accurate force fields for both carboplatin and oxaliplatin. It is assumed that the modes of transport and action of carboplatin are very similar to the ones of cisplatin and the study of its permeation would be an important confirmation from a numerical point-of-view. At the same time, uptake experiments of oxaliplatin show a different behavior to many cisplatin resistant cells. In the will to unravel the origins of the drug resistance, it is of first interest to understand if the chemistry of these drugs in solution, in the specific physiological conditions around cancer cells could influence their propensity to permeate the plasma membrane. This could add or discriminate a possibly important factor to the present hypotheses related to active drug scavenging.

2. On the way to selectivity: finding relevant marker of the cancer cells

In this work, we have shown that cisplatin permeates slightly more in the normal lipid membrane model than in the cancer one. Up to now, drug selectivity remains challenging. Since the cancer and normal cells membranes exhibit differences, it is worth questioning if one can achieve selectivity on the basis of these differences. In order to investigate lipids as new targets for drugs, we recently developed collaboration with the team of P. Couvreur (Institut Galien, France). They use squalene, a natural precursor of cholesterol, to functionalize drugs. Squalene interacts with a large variety of cells and, as a lipid, has a strong lipophilicity. The so-called *squalenoylation* technology [78] is based on the conjugation of squalenic acid with a variety of drugs. The resulting conjugated molecules spontaneously self-assemble into nanoparticles, which deliver efficiently the drugs into the target cells. Currently, anticancer (gemcitabine [79], doxorubicin [80]), antiviral (dideoxycytidine [78]) and neuroprotective (adenosine [248]) drugs were used in this technology with great success.

In the frame of our collaboration, we started to analyze the permeation of squalene-gemcitabine (SQGem) in both normal and cancer lipid model membranes.

By means of AAMD, we are actually computing the free energy profiles of gemcitabine, squalene and SQGem in the normal and cancer model membranes. One should note that this project is ongoing and that the results presented here are preliminary.

Figure VII-2 shows a partial free energy profile for gemcitabine in the normal membrane. One can notice the symmetry in this profile which indicates that gemcitabine is mainly not influenced by the type of the headgroups of the asymmetric membrane. On top of that, it is clear that, with a potential barrier of 24 kT (for T=310K), the permeation process is not favorable at all. Indeed, cisplatin barrier is in the order of 16 kT in the same conditions.

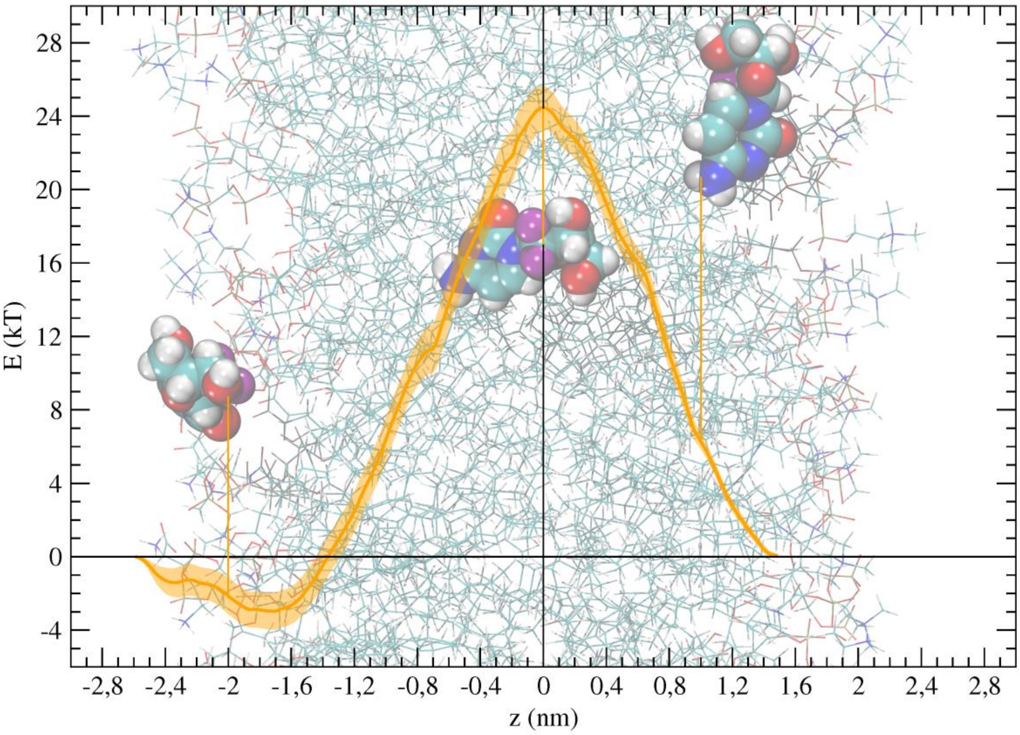

Figure VII-2. PMF profile of the gemcitabine in the normal model membrane. Statistical errors are estimated by means of a bootstrapping method as described in previous chapter and are plotted in the same color as the free energy profile in a lighter tone. A representation of the membrane is drawn to give a better understanding of the profile. Three gemcitabine molecules are also represented at the positions of three windows of computation.

Figure VII-3 depicts the free energy profile of the strongly lipophilic squalene through the normal membrane. For squalene, as well as for SQGem, the computation of the PMF is not straightforward given the size of the molecule. The computations were done, in this case for a subpart of the squalene composed of 6 carbons and their hydrogen atoms from an extremity of the aliphatic chain. In order to obtain a relevant free energy profile, the squalene (and later SQGem) was put inside the membrane. A 50 ns long equilibration simulation in the membrane was made with a pulling on the extremal part of the squalene to keep it in the headroups area of the membrane. The pulling was applied by means of a harmonic potential with a force constant of $1000\ \mathrm{kJ} \cdot \mathrm{mol}^{-1} \cdot \mathrm{nm}^{-2}$. Hereafter, the sampling was made by US method, following the extraction of the squalene. To extract the squalene, the last frame from the previous window was used as a starting point of the next window. The center of the biasing potential was moved accordingly to the studied window and a pre-equilibration simulation of 20 ns was made. The proper sampling was then obtained after another 20 ns of simulation. Windows are separated by 0.1 nm. The obtained profile seems thus to be shifted from the membrane, but represents the free energy variations of the selected group of 6 atoms from the extremal part of squalene. The profile really shows an estimate of the free energy of the whole squalene (or of the SQGem) since the influence of the membrane on the other parts of the molecules will exert their influence on the motion of the only selected atoms.

At the time, another setup designed to compute the free energy profile of long and complex molecules is under development in our group. It takes into account in a refined way the complex process of permeation of long molecules as squalene or SQGem for which a unique reaction coordinate might not be sufficient to describe accurately the complete diffusion process.

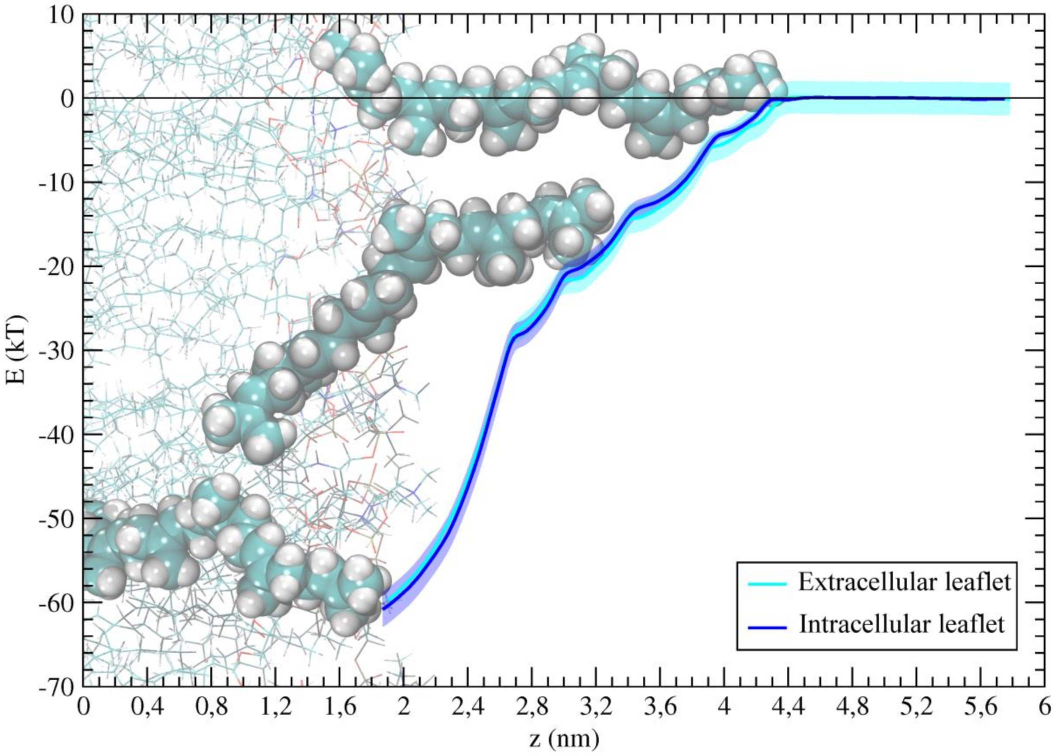

Figure VII-3. PMF profile of the squalene in the normal model membrane. Statistical errors are estimated by means of a bootstrapping method as described in previous chapter and are plotted in the same color as the free energy profile in a lighter tone. A representation of the membrane is drawn to give a better understanding of the profile. Three squalene molecules are also represented at the positions of three windows of computation. One should note that the profile represents the free energy variations of a subselection of the whole molecule.

Figure VII-3 shows that squalene has a strong affinity to the membrane. A visible and large well of ~60 kT is present with its minimum when the squalene is totally inside the membrane. Another interesting point is that no significant differences seem to exist in between the both leaflets.

The setup for the study of SQGem was the same as the one used for the squalene. The subpart of the SQGem for which the PMF profile was computed is the gemcitabine. Figure VII-4 shows the PMF of SQGem in the normal membrane. It is first clear that the ligand has a high affinity with the membrane. Secondly, it is interesting to note that the transversal lipid asymmetry of the membrane seems to play here a role since a difference in the depth of the well of 6-8 kT exists in the middle of the bicelle. It could be hypothesized that this difference of interaction in between the two layers could act as a reservoir for the SQGem in asymmetric membranes and have a certain impact on the kinetics of its uptake.

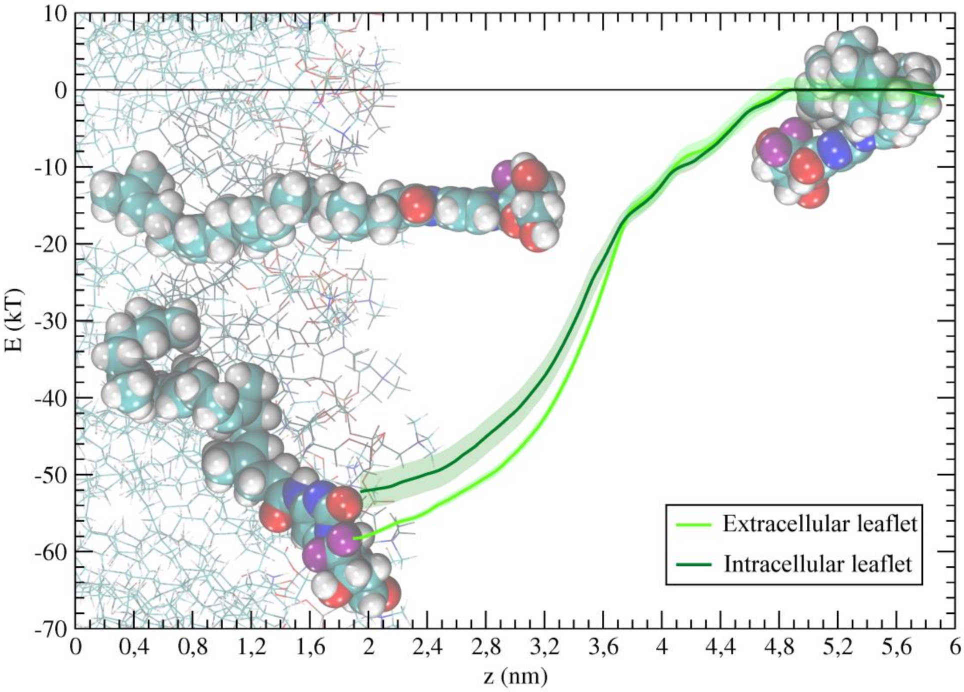

Figure VII-4. PMF profile of the squalene-gemcitabine in the normal model membrane. Statistical errors are estimated by means of a bootstrapping method as described in previous chapter and are plotted in the same color as the free energy profile in a lighter tone. A representation of the membrane is drawn to give a better understanding of the profile. Three squalene molecules are also represented at the positions of three windows of computation. One should note that the profile represents the free energy variations of a subselection of the whole molecule.

These first numerical analyses are being completed by a more thorough numerical analysis including the computation of the free energy profiles of the both squalene and SQGem in the normal and cancer membrane with a more refined setup.

Overall, the first results obtained in the frame of this project support the idea that PS/PE exposure could be an efficient marker of cancer cells and that carrier such as squalene could efficiently create selective drugs.

Chapter VIII - **Bibliography**

1. Kiessling V, Wan C & Tamm LK (2009) Domain coupling in asymmetric lipid bilayers. *Biochim Biophys Acta* **1788**, 64-71, doi: 10.1016/j.bbamem.2008.09.003.
2. Meer Gv (2011) Dynamic Transbilayer Lipid Asymmetry. *Cold Spring Harb Perspect Biol* **3**, a004671, doi: 10.1101/cshperspect.a004671.
3. Meer Gv, Voelker DR & Feigenson GW (2008) Membrane lipids: where they are and how they behave. *Nature Reviews Molecular Cell Biology* **9**, 112-124, doi: 10.1038/nrm2330.
4. Connor J, Bucana C, Fidler IJ & Schroit AJ (1989) Differentiation-dependent expression of phosphatidylserine in mammalian plasma membranes: quantitative assessment of outer-leaflet lipid by prothrombinase complex formation. *PNAS* **86**, 3184-3188, doi: 10.1073/pnas.86.9.3184.
5. Utsugi T, Schroit AJ, Connor J, Bucana CD & Fidler IJ (1991) Elevated Expression of Phosphatidylserine in the Outer Membrane Leaflet of Human Tumor Cells and Recognition by Activated Human Blood Monocytes. *Cancer Res* **51**, 3062-3066.
6. Kirszberg C, Lima LG, Da Silva de Oliveira A, Pickering W, Gray E, Barrowcliffe TW, Rumjanek VM & Monteiro RQ (2009) Simultaneous tissue factor expression and phosphatidylserine exposure account for the highly procoagulant pattern of melanoma cell lines. *Melanoma Research* **19**, 301-308, doi: 10.1097/CMR.0b013e32832e40fe.
7. Rao LVM, Tait JF & Hoang AD (1992) Binding of annexin V to a human ovarian carcinoma cell line (OC-2008). Contrasting effects on cell surface factor VIIa/tissue factor activity and prothrombinase activity. *Thrombosis Research* **67**, 517-531, doi: 10.1016/0049-3848(92)90013-z.
8. Schröder-Borm H, Bakalova R & Andrä J (2005) The NK-lysin derived peptide NK-2 preferentially kills cancer cells with increased surface levels of negatively charged phosphatidylserine. *FEBS Letters* **579**, 6128-6134, doi: 10.1016/j.febslet.2005.09.084.
9. Riedl S, Rinner B, Asslaber M, Schaider H, Walzer S, Novak A, Lohner K & Zweytick D (2011) In search of a novel target — Phosphatidylserine exposed by non-apoptotic tumor cells and metastases of malignancies with poor treatment efficacy. *Biochimica et Biophysica Acta (BBA) - Biomembranes* **1808**, 2638-2645, doi: 10.1016/j.bbamem.2011.07.026.
10. Ran S, Downes A & Thorpe PE (2002) Increased Exposure of Anionic Phospholipids on the Surface of Tumor Blood Vessels. *Cancer Res* **62**, 6132-6140.
11. Stafford JH & Thorpe PE (2011) Increased Exposure of Phosphatidylethanolamine on the Surface of Tumor Vascular Endothelium. *Neoplasia* **13**, 299-IN292, doi: 10.1593/neo.101366.
12. Sugimura M, Donato R, Kakkar VV & Scully MF (1994) Annexin V as a probe of the contribution of anionic phospholipids to the procoagulant activity of tumour cell surfaces. *Blood Coagul Fibrinolysis* **5**, 365-373.
13. Cichorek M, Kozłowska K, Witkowski JM & Zarzeczna M (2000) Flow cytometric estimation of the plasma membrane diversity of transplantable melanomas, using annexin V. *Folia Histochem Cytobiol* **38**, 41-43.
14. Cabrera MPdS, Costa STB, Souza BMd, Palma MS, Ruggiero JR & Neto JR (2008) Selectivity in the mechanism of action of antimicrobial mastoparan peptide Polybia-MP1. *Eur Biophys J* **37**, 879, doi: 10.1007/s00249-008-0299-7.
15. Riedl S, Zweytick D & Lohner K (2011) Membrane-active host defense peptides – Challenges and perspectives for the development of novel anticancer drugs. *Chemistry and Physics of Lipids* **164**, 766-781, doi: 10.1016/j.chemphyslip.2011.09.004.
16. dos Santos Cabrera MP, Arcisio-Miranda M, Gorjão R, Leite NB, de Souza BM, Curi R, Procopio J, Ruggiero Neto J & Palma MS (2012) Influence of the Bilayer Composition on the Binding and Membrane Disrupting Effect of Polybia-MP1, an Antimicrobial Mastoparan Peptide with Leukemic T-Lymphocyte Cell Selectivity. *Biochemistry* **51**, 4898-4908, doi: 10.1021/bi201608d.

17. Yesylevskyy S, Marrink S-J & Mark AE (2009) Alternative Mechanisms for the Interaction of the Cell-Penetrating Peptides Penetratin and the TAT Peptide with Lipid Bilayers. *Biophysical Journal* **97**, 40-49, doi: 10.1016/j.bpj.2009.03.059.
18. Tan LT-H, Chan K-G, Pusparajah P, Lee W-L, Chuah L-H, Khan TM, Lee L-H & Goh B-H (2017) Targeting Membrane Lipid a Potential Cancer Cure? *Front Pharmacol* **8**, doi: 10.3389/fphar.2017.00012.
19. Klähn M & Zacharias M (2013) Transformations in plasma membranes of cancerous cells and resulting consequences for cation insertion studied with molecular dynamics. *Phys Chem Chem Phys* **15**, 14427-14441, doi: 10.1039/c3cp52085d.
20. Ali MR, Cheng KH & Huang J (2007) Assess the nature of cholesterol-lipid interactions through the chemical potential of cholesterol in phosphatidylcholine bilayers. *Proc Natl Acad Sci U S A* **104**, 5372-5377, doi: 0611450104 [pii]

10.1073/pnas.0611450104.
21. Radhakrishnan A & McConnell H (2005) Condensed complexes in vesicles containing cholesterol and phospholipids. *Proc Natl Acad Sci U S A* **102**, 12662-12666, doi: 0506043102 [pii]

10.1073/pnas.0506043102.
22. Ohvo-Rekila H, Ramstedt B, Leppimaki P & Slotte JP (2002) Cholesterol interactions with phospholipids in membranes. *Prog Lipid Res* **41**, 66-97, doi: S0163782701000200 [pii].
23. Giang H & Schick M (2014) How Cholesterol Could Be Drawn to the Cytoplasmic Leaf of the Plasma Membrane by Phosphatidylethanolamine. *Biophysical Journal* **107**, 2337-2344, doi: 10.1016/j.bpj.2014.10.012.
24. Marquardt D, Geier B & Pabst G (2015) Asymmetric Lipid Membranes: Towards More Realistic Model Systems. *Membranes* **5**, 180-196, doi: 10.3390/membranes5020180.
25. Wood WG, Igbavboa U, Müller WE & Eckert GP (2011) Cholesterol asymmetry in synaptic plasma membranes. *Journal of Neurochemistry* **116**, 684-689, doi: 10.1111/j.1471-4159.2010.07017.x.
26. Nicolson GL (2014) The Fluid—Mosaic Model of Membrane Structure: Still relevant to understanding the structure, function and dynamics of biological membranes after more than 40years. *Biochimica et Biophysica Acta (BBA) - Biomembranes* **1838**, 1451-1466, doi: 10.1016/j.bbamem.2013.10.019.
27. Choubey A, Kalia RK, Malmstadt N, Nakano A & Vashishta P (2013) Cholesterol Translocation in a Phospholipid Membrane. *Biophysical Journal* **104**, 2429-2436, doi: 10.1016/j.bpj.2013.04.036.
28. Marquardt D, Kučerka N, Wassall SR, Harroun TA & Katsaras J (2016) Cholesterol's location in lipid bilayers. *Chemistry and Physics of Lipids* **199**, 17-25, doi: 10.1016/j.chemphyslip.2016.04.001.
29. Yesylevskyy SO & Demchenko AP (2012) How cholesterol is distributed between monolayers in asymmetric lipid membranes. *Eur Biophys J* **41**, 1043-1054, doi: 10.1007/s00249-012-0863-z.
30. Berkowitz ML (2009) Detailed molecular dynamics simulations of model biological membranes containing cholesterol. *Biochim Biophys Acta* **1788**, 86-96, doi: 10.1016/j.bbamem.2008.09.009.
31. Feigenson GW (2009) Phase diagrams and lipid domains in multicomponent lipid bilayer mixtures. *Biochimica et Biophysica Acta (BBA) - Biomembranes* **1788**, 47-52, doi: 10.1016/j.bbamem.2008.08.014.
32. Baoukina S, Rozmanov D & Tieleman DP (2017) Composition Fluctuations in Lipid Bilayers. *Biophysical Journal* **113**, 2750-2761, doi: 10.1016/j.bpj.2017.10.009.
33. MacDermaid CM, Kashyap HK, DeVane RH, Shinoda W, Klauda JB, Klein ML & Fiorin G (2015) Molecular dynamics simulations of cholesterol-rich membranes using a coarse-grained force field for cyclic alkanes. *The Journal of Chemical Physics* **143**, 243144, doi: 10.1063/1.4937153.
34. Rosetti C & Pastorino C (2012) Comparison of Ternary Bilayer Mixtures with Asymmetric or Symmetric Unsaturated Phosphatidylcholine Lipids by Coarse Grained Molecular Dynamics Simulations. *J Phys Chem B* **116**, 3525-3537, doi: 10.1021/jp212406u.
35. Feigenson GW (2006) Phase behavior of lipid mixtures. *Nature Chemical Biology* **2**, 560-563, doi: 10.1038/nchembiol1106-560.

36. Issack BB & Peslherbe GH (2015) Effects of Cholesterol on the Thermodynamics and Kinetics of Passive Transport of Water through Lipid Membranes. *J Phys Chem B* **119**, 9391-9400, doi: 10.1021/jp510497r.

37. Jedlovszky P & Mezei M (2003) Effect of Cholesterol on the Properties of Phospholipid Membranes. 2. Free Energy Profile of Small Molecules. *J Phys Chem B* **107**, 5322-5332, doi: 10.1021/jp021951x.

38. Saito H & Shinoda W (2011) Cholesterol Effect on Water Permeability through DPPC and PSM Lipid Bilayers: A Molecular Dynamics Study. *J Phys Chem B* **115**, 15241-15250, doi: 10.1021/jp201611p.

39. Wennberg CL, van der Spoel D & Hub JS (2012) Large Influence of Cholesterol on Solute Partitioning into Lipid Membranes. *J Am Chem Soc* **134**, 5351-5361, doi: 10.1021/ja211929h.

40. McMahon HT & Boucrot E (2015) Membrane curvature at a glance. *J Cell Sci* **128**, 1065-1070, doi: 10.1242/jcs.114454.

41. Mim C & Unger VM Membrane curvature and its generation by BAR proteins. *Trends in Biochemical Sciences* **37**, 526-533, doi: 10.1016/j.tibs.2012.09.001.

42. Baenke F, Peck B, Miess H & Schulze A (2013) Hooked on fat: the role of lipid synthesis in cancer metabolism and tumour development. *Disease Models & Mechanisms* **6**, 1353-1363, doi: 10.1242/dmm.011338.

43. Di Paolo G & Kim T-W (2011) Linking lipids to Alzheimer's disease: cholesterol and beyond. *Nat Rev Neurosci* **12**, 284-296, doi: http://www.nature.com/nrn/journal/v12/n5/suppinfo/nrn3012_S1.html.

44. Schwingshackl L & Hoffmann G (2013) Comparison of Effects of Long-Term Low-Fat vs High-Fat Diets on Blood Lipid Levels in Overweight or Obese Patients: A Systematic Review and Meta-Analysis. *Journal of the Academy of Nutrition and Dietetics* **113**, 1640-1661, doi: https://doi.org/10.1016/j.jand.2013.07.010.

45. Wang Y, Xu C, Jiang N, Zheng L, Zeng J, Qiu C, Yang H & Xie S (2016) Quantitative analysis of the cell-surface roughness and viscoelasticity for breast cancer cells discrimination using atomic force microscopy. *Scanning* **38**, 558-563, doi: 10.1002/sca.21300.

46. Li QS, Lee GYH, Ong CN & Lim CT (2008) AFM indentation study of breast cancer cells. *Biochemical and Biophysical Research Communications* **374**, 609-613, doi: 10.1016/j.bbrc.2008.07.078.

47. Lekka M, Gil D, Pogoda K, Dulińska-Litewka J, Jach R, Gostek J, Klymenko O, Prauzner-Bechcicki S, Stachura Z, Wiltowska-Zuber J, et al. (2012) Cancer cell detection in tissue sections using AFM. *Archives of Biochemistry and Biophysics* **518**, 151-156, doi: 10.1016/j.abb.2011.12.013.

48. Adams M, Wang E, Zhuang X & Klauda JB (2017) Simulations of simple Bovine and Homo sapiens outer cortex ocular lens membrane models with a majority concentration of cholesterol. *Biochimica et Biophysica Acta (BBA) - Biomembranes*, doi: 10.1016/j.bbamem.2017.11.010.

49. Andoh Y, Okazaki S & Ueoka R (2013) Molecular dynamics study of lipid bilayers modeling the plasma membranes of normal murine thymocytes and leukemic GRSL cells. *Biochimica et Biophysica Acta (BBA) - Biomembranes* **1828**, 1259-1270, doi: 10.1016/j.bbamem.2013.01.005.

50. Ingólfsson HI, Carpenter TS, Bhatia H, Bremer P-T, Marrink SJ & Lightstone FC (2017) Computational Lipidomics of the Neuronal Plasma Membrane. *Biophysical Journal* **113**, 2271-2280, doi: 10.1016/j.bpj.2017.10.017.

51. Ingólfsson HI, Melo MN, van Eerden FJ, Arnarez C, Lopez CA, Wassenaar TA, Periole X, de Vries AH, Tieleman DP & Marrink SJ (2014) Lipid Organization of the Plasma Membrane. *J Am Chem Soc* **136**, 14554-14559, doi: 10.1021/ja507832e.

52. Sharma S, Kim BN, Stansfeld PJ, Sansom MSP & Lindau M (2015) A Coarse Grained Model for a Lipid Membrane with Physiological Composition and Leaflet Asymmetry. *PLOS ONE* **10**, e0144814, doi: 10.1371/journal.pone.0144814.

53. Vácha R, Berkowitz ML & Jungwirth P (2009) Molecular model of a cell plasma membrane with an asymmetric multicomponent composition: Water permeation and ion effects. *Biophysical Journal* **96**, 4493-4501, doi: 10.1016/j.bpj.2009.03.010.

54. Yesylevskyy SO, Rivel T & Ramseyer C (2017) The influence of curvature on the properties of the plasma membrane. Insights from atomistic molecular dynamics simulations. *Scientific Reports* **7**, 16078, doi: 10.1038/s41598-017-16450-x.

55. Marrink SJ, Risselada HJ, Yefimov S, Tieleman DP & de Vries AH (2007) The MARTINI Force Field: Coarse Grained Model for Biomolecular Simulations. *J Phys Chem B* **111**, 7812-7824, doi: 10.1021/jp071097f.

56. Marrink SJ, de Vries AH & Mark AE (2004) Coarse grained model for semiquantitative lipid simulations. *J Chem Phys* **108**, 750-760.

57. Monticelli L, Kandasamy SK, Periole X, Larson RG, Tieleman DP & Marrink SJ (2008) The MARTINI Coarse-Grained Force Field: Extension to Proteins. *J Chem Theory and Comput* **4**, 819-834.

58. Lopez CA, Rzepiela AJ, de Vries AH, Dijkhuizen L, Hunenberger PH & Marrink SJ (2009) Martini Coarse-Grained Force Field: Extension to Carbohydrates. *J Chem Theory Comput* **5**, 3195–3210.

59. Daleke DL (2008) Regulation of phospholipid asymmetry in the erythrocyte membrane. *Current Opinion in Hematology* **15**, 191-195, doi: 10.1097/MOH.0b013e3282f97af7.

60. Cherniavskyi YK, Ramseyer C & Yesylevskyy SO (2016) Interaction of C60 fullerenes with asymmetric and curved lipid membranes: a molecular dynamics study. *Physical Chemistry Chemical Physics* **18**, 278-284, doi: 10.1039/c5cp05838d.

61. Yesylevskyy S & Ramseyer C (2014) Determination of mean and Gaussian curvatures of highly curved asymmetric lipid bilayers: the case study of the influence of cholesterol on the membrane shape *PCCP* **16**, 17052-17061.

62. Yesylevskyy S & Demchenko A (2012) How cholesterol is distributed between monolayers in asymmetric lipid membranes. *Eur Biophys J* **41**, 1043-1054, doi: 10.1007/s00249-012-0863-z.

63. Yesylevskyy SO & Ramseyer C (2014) Determination of mean and Gaussian curvatures of highly curved asymmetric lipid bilayers: the case study of the influence of cholesterol on the membrane shape. *Physical Chemistry Chemical Physics* **16**, 17052-17061, doi: 10.1039/c4cp01544d.

64. Arnesano F, Losacco M & Natile G (2013) An Updated View of Cisplatin Transport. *European Journal of Inorganic Chemistry* **2013**, 2701-2711, doi: 10.1002/ejic.201300001.

65. Dasari S & Bernard Tchounwou P (2014) Cisplatin in cancer therapy: Molecular mechanisms of action. *European Journal of Pharmacology* **740**, 364-378, doi: 10.1016/j.ejphar.2014.07.025.

66. Wang D & Lippard SJ (2005) Cellular processing of platinum anticancer drugs. *Nature Reviews Drug Discovery* **4**, 307-320, doi: 10.1038/nrd1691.

67. Rabik CA & Dolan ME (2007) Molecular mechanisms of resistance and toxicity associated with platinating agents. *Cancer Treat Rev* **33**, 9-23, doi: 10.1016/j.ctrv.2006.09.006.

68. Medici S, Peana M, Nurchi VM, Lachowicz JI, Crisponi G & Zoroddu MA (2015) Noble metals in medicine: Latest advances. *Coordination Chemistry Reviews* **284**, 329-350, doi: 10.1016/j.ccr.2014.08.002.

69. Stewart DJ (2007) Mechanisms of resistance to cisplatin and carboplatin. *Critical Reviews in Oncology/Hematology* **63**, 12-31, doi: 10.1016/j.critrevonc.2007.02.001.

70. Gonzalez VM, Fuertes MA, Alonso C & Perez JM (2001) Is Cisplatin-Induced Cell Death Always Produced by Apoptosis? *Mol Pharmacol* **59**, 657-663, doi: 10.1124/mol.59.4.657.

71. Vargiu AV (2008) *Molecular recognition of ligands targeting DNA: a computational approach*. PhD, Scuola Internazionale Superiore di Studi Avanzati (SISSA) di Trieste, Trieste.

72. Nierzwicki L, Wieczor M, Censi V, Baginski M, Calucci L, Samaritani S, Czub J & Forte C (2014) Interaction of cisplatin and two potential antitumoral platinum(II) complexes with a model lipid membrane: a combined NMR and MD study. *Physical Chemistry Chemical Physics* **17**, 1458-1468, doi: 10.1039/c4cp04360j.

73. Eljack ND, Ma H-YM, Drucker J, Shen C, Hambley TW, New EJ, Friedrich T & Clarke RJ (2014) Mechanisms of cell uptake and toxicity of the anticancer drug cisplatin. *Metallomics* **6**, 2126-2133, doi: 10.1039/c4mt00238e.

74. El-Kareh AW, Labes RE & Secomb TW (2008) Cell Cycle Checkpoint Models for Cellular Pharmacology of Paclitaxel and Platinum Drugs. *AAPS J* **10**, 15-34, doi: 10.1208/s12248-007-9003-6.

75. Ghezzi A, Aceto M, Cassino C, Gabano E & Osella D (2004) Uptake of antitumor platinum(II)-complexes by cancer cells, assayed by inductively coupled plasma mass spectrometry (ICP-MS). *J Inorg Biochem* **98**, 73-78, doi: 10.1016/j.jinorgbio.2003.08.014.

76. Miller SE & House DA (1990) The hydrolysis products of cis-dichlorodiammineplatinum(II) 3. Hydrolysis kinetics at physiological pH. *Inorganica Chimica Acta* **173**, 53-60, doi: 10.1016/s0020-1693(00)91054-5.

77. Minervini T (2019) *Etude théorique des interactions entre dérivés du cisplatine et composés soufrés d'intérêt biologique*. Université de Bourgogne Franche-Comté, Besançon.

78. Lepeltier E, Bourgaux C, Rosilio V, Poupaert JH, Meneau F, Zouhiri F, Lepêtre-Mouelhi S, Desmaële D & Couvreur P (2013) Self-assembly of squalene-based nucleolipids: relating the chemical structure of the bioconjugates to the architecture of the nanoparticles. *Langmuir* **29**, 14795-14803, doi: 10.1021/la403338y.

79. Lepeltier E, Bourgaux C, Maksimenko A, Meneau F, Rosilio V, Sliwinski E, Zouhiri F, Desmaële D & Couvreur P (2014) Self-assembly of polyisoprenoyl gemcitabine conjugates: influence of supramolecular organization on their biological activity. *Langmuir* **30**, 6348-6357, doi: 10.1021/la5007132.

80. Maksimenko A, Dosio F, Mougin J, Ferrero A, Wack S, Reddy LH, Weyn A-A, Lepeltier E, Bourgaux C, Stella B, et al. (2014) A unique squalenoylated and nonpegylated doxorubicin nanomedicine with systemic long-circulating properties and anticancer activity. *PNAS* **111**, E217-E226, doi: 10.1073/pnas.1313459110.

81. Marrink SJ, Corradi V, Souza PCT, Ingólfsson HI, Tieleman DP & Sansom MSP (2019) Computational Modeling of Realistic Cell Membranes. *Chem Rev* **119**, 6184-6226, doi: 10.1021/acs.chemrev.8b00460.

82. Koldsø H, Shorthouse D, Hélie J & Sansom MSP (2014) Lipid Clustering Correlates with Membrane Curvature as Revealed by Molecular Simulations of Complex Lipid Bilayers. *PLOS Computational Biology* **10**, e1003911, doi: 10.1371/journal.pcbi.1003911.

83. Mozafari MR, Pardakhty A, Azarmi S, Jazayeri JA, Nokhodchi A & Omri A (2009) Role of nanocarrier systems in cancer nanotherapy. *Journal of Liposome Research* **19**, 310-321, doi: 10.3109/08982100902913204.

84. Qiao W, Wang B, Wang Y, Yang L, Zhang Y & Shao P (2010) Cancer Therapy Based on Nanomaterials and Nanocarrier Systems. In *Journal of Nanomaterials*.

85. Pérez-Herrero E & Fernández-Medarde A (2015) Advanced targeted therapies in cancer: Drug nanocarriers, the future of chemotherapy. *European Journal of Pharmaceutics and Biopharmaceutics* **93**, 52-79, doi: 10.1016/j.ejpb.2015.03.018.

86. Rapaport DC (2004) *The Art of Molecular Dynamics Simulation*. 2 edn. Cambridge University Press, Cambridge.

87. Marx D & Hutter J (2009) *Ab Initio Molecular Dynamics: Basic Theory and Advanced Methods*. Cambridge University Press, Cambridge.

88. Kutzelnigg W (1997) The adiabatic approximation I. The physical background of the Born-Handy ansatz. *Molecular Physics* **90**, 909-916, doi: 10.1080/002689797171904.

89. Makri N & Miller WH (1987) Time-dependent self-consistent field (TDSCF) approximation for a reaction coordinate coupled to a harmonic bath: Single and multiple configuration treatments. *The Journal of Chemical Physics* **87**, 5781-5787, doi: 10.1063/1.453501.

90. Dirac PAM (1993) *The Principles of Quantum Mechanics*. 4th Edition edition edn. Oxford University Press, Oxford.

91. Messiah A (2003) *Mécanique quantique, tome 1.* Dunod, Paris.

92. Bornemann FA, Nettesheim P & Schütte C (1996) Quantum-classical molecular dynamics as an approximation to full quantum dynamics. *The Journal of Chemical Physics* **105**, 1074-1083, doi: 10.1063/1.471952.

93. Jämbeck JPM & Lyubartsev AP (2012) Derivation and Systematic Validation of a Refined All-Atom Force Field for Phosphatidylcholine Lipids. *The Journal of Physical Chemistry B* **116**, 3164-3179, doi: 10.1021/jp212503e.

94. Jämbeck JPM & Lyubartsev AP (2012) An Extension and Further Validation of an All-Atomistic Force Field for Biological Membranes. *Journal of Chemical Theory and Computation* **8**, 2938-2948, doi: 10.1021/ct300342n.

95. Jämbeck JPM & Lyubartsev AP (2013) Another Piece of the Membrane Puzzle: Extending Slipids Further. *Journal of Chemical Theory and Computation* **9**, 774-784, doi: 10.1021/ct300777p.

96. Ermilova I & Lyubartsev AP (2016) Extension of the Slipids Force Field to Polyunsaturated Lipids. *The Journal of Physical Chemistry B* **120**, 12826-12842, doi: 10.1021/acs.jpcb.6b05422.

97. Klauda JB, Venable RM, Freites JA, O'Connor JW, Tobias DJ, Mondragon-Ramirez C, Vorobyov I, MacKerell AD & Pastor RW (2010) Update of the CHARMM all-atom additive force field for lipids: validation on six lipid types. *J Phys Chem B* **114**, 7830-7843, doi: 10.1021/jp101759q.

98. Wang J, Wolf RM, Caldwell JW, Kollman PA & Case DA (2004) Development and testing of a general amber force field. *Journal of Computational Chemistry* **25**, 1157-1174, doi: 10.1002/jcc.20035.

99. Abraham MJ, van der Spoel D, Lindahl E & Hess B (2018) *GROMACS User Manual version 2016*.

100. Toukmaji AY & Board JA (1996) Ewald summation techniques in perspective: a survey. *Computer Physics Communications* **95**, 73-92, doi: 10.1016/0010-4655(96)00016-1.

101. Darden T, York D & Pedersen L (1993) Particle mesh Ewald: An N·log(N) method for Ewald sums in large systems. *The Journal of Chemical Physics* **98**, 10089-10092, doi: 10.1063/1.464397.

102. Singer SJ & Nicolson GL (1972) The fluid mosaic model of the structure of cell membranes. *Science* **175**, 720-731.

103. Rivel T, Ramseyer C & Yesylevskyy S (2019) The asymmetry of plasma membranes and their cholesterol content influence the uptake of cisplatin. *Scientific Reports* **9**, 1-14, doi: 10.1038/s41598-019-41903-w.

104. McMahon HT & Gallop JL (2005) Membrane curvature and mechanisms of dynamic cell membrane remodelling. *Nature* **438**, 590-596.

105. McMahon HT, Kozlov MM & Martens S (2010) Membrane Curvature in Synaptic Vesicle Fusion and Beyond. *Cell* **140**, 601-605.

106. Gores GJ, Herman B & Lemasters JJ (2005) Plasma membrane bleb formation and rupture: a common feature of hepatocellular injury. *Hepatology* **11**, 690-698.

107. Taylor RC, Cullen SP & Martin SJ (2008) Apoptosis: controlled demolition at the cellular level. *Nature Reviews Molecular Cell Biology* **9**, 231-241.

108. Jahn R, Lang T & Südhof TC (2003) Membrane fusion. *Cell* **112**, 519-533.

109. Churchward MA, Rogasevskaia T, Höfgen J, Bau J & Coorssen JR (2005) Cholesterol facilitates the native mechanism of Ca2+-triggered membrane fusion. *Journal of cell science* **118**, 4833-4848.

110. Cadd TL, Skoging U & Liljeström P (2005) Budding of enveloped viruses from the plasma membrane. *Bioessays* **19**, 993-1000.

111. Lorizate M & Kräusslich H-G (2011) Role of Lipids in Virus Replication. *Cold Spring Harb Perspect Biol* **3**, a004820.

112. Griffiths RE, Kupzig S, Cogan N, Mankelow TJ, Betin VMS, Trakarnsanga K, Massey EJ, Lane JD, Parsons SF & Anstee DJ (2012) Maturing reticulocytes internalize plasma membrane in glycophorin A–containing vesicles that fuse with autophagosomes before exocytosis *Blood* **119**, 6296-6306.

113. Roubinet C, Decelle B, Chicanne G, Dorn JF, Payrastre B, Payre F & Carreno S (2011) Molecular networks linked by Moesin drive remodeling of the cell cortex during mitosis. *JCB* **195**, 99-112.

114. Huttner WB & Zimmerberg J (2001) Implications of lipid microdomains for membrane curvature, budding and fission: Commentary. *Current opinion in cell biology* **13**, 478-484.

115. Yesylevskyy SO, Demchenko AP, Kraszewski S & Ramseyer C (2013) Cholesterol Induces Uneven Curvature of Asymmetric Lipid Bilayers. *The Scientific World Journal* **2013**, 10, doi: 10.1155/2013/965230.

116. Yesylevskyy SO, Kraszewski S & Ramseyer C (2014) Determination of the shape and curvature of nonplanar lipid bilayers that are bent in a single plane in molecular dynamics simulations. . *Journal of Molecular Modeling* **20**, 2176.

117. Hornak V, Abel R, Okur A, Strockbine B, Roitberg A & Simmerling C (2006) Comparison of multiple Amber force fields and development of improved protein backbone parameters. *Proteins: Structure, Function, and Bioinformatics* **65**, 712-725, doi: 10.1002/prot.21123.

118. Hofsäß C, Lindahl E & Edholm O (2003) Molecular Dynamics Simulations of Phospholipid Bilayers with Cholesterol. *Biophysical Journal* **84**, 2192-2206.

119. Siddik ZH (2003) Cisplatin: mode of cytotoxic action and molecular basis of resistance. *Oncogene* **22**, 7265-7279, doi: 10.1038/sj.onc.1206933.

120. Florea A-M & Büsselberg D (2011) Cisplatin as an Anti-Tumor Drug: Cellular Mechanisms of Activity, Drug Resistance and Induced Side Effects. *Cancers* **3**, 1351-1371, doi: 10.3390/cancers3011351.

121. Galluzzi L, Senovilla L, Vitale I, Michels J, Martins I, Kepp O, Castedo M & Kroemer G (2012) Molecular mechanisms of cisplatin resistance. *Oncogene* **31**, 1869-1883, doi: 10.1038/onc.2011.384.

122. Galluzzi L, Vitale I, Michels J, Brenner C, Szabadkai G, Harel-Bellan A, Castedo M & Kroemer G (2014) Systems biology of cisplatin resistance: past, present and future. *Cell Death & Disease* **5**, e1257, doi: 10.1038/cddis.2013.428.

123. Boulikas T & Vougiouka M (2003) Cisplatin and platinum drugs at the molecular level. (Review). *Oncol Rep* **10**, 1663-1682.

124. Wheate NJ, Walker S, Craig GE & Oun R (2010) The status of platinum anticancer drugs in the clinic and in clinical trials. *Dalton Trans* **39**, 8113-8127, doi: 10.1039/c0dt00292e.

125. Ndagi U, Mhlongo N & Soliman ME (2017) Metal complexes in cancer therapy - an update from drug design perspective. *Drug Des Devel Ther* **11**, 599-616, doi: 10.2147/dddt.s119488.

126. Mansy S, Rosenberg B & Thomson AJ (1973) Binding of cis- and trans-dichlorodiammineplatinum(II) to nucleosides.i. Location of the binding sites. *J Am Chem Soc* **95**, 1633-1640, doi: 10.1021/ja00786a045.

127. Raber J, Zhu C & Eriksson * LA (2004) Activation of anti-cancer drug cisplatin — is the activated complex fully aquated? *Molecular Physics* **102**, 2537-2544, doi: 10.1080/0026897042000275053.

128. Hall MD, Okabe M, Shen D-W, Liang X-J & Gottesman MM (2008) The Role of Cellular Accumulation in Determining Sensitivity to Platinum-Based Chemotherapy. *Annu Rev Pharmacol Toxicol* **48**, 495-535, doi: 10.1146/annurev.pharmtox.48.080907.180426.

129. Kozelka J (2009) Molecular origin of the sequence-dependent kinetics of reactions between cisplatin derivatives and DNA. *Inorganica Chimica Acta* **362**, 651-668, doi: 10.1016/j.ica.2008.04.024.

130. Kelland L (2007) The resurgence of platinum-based cancer chemotherapy. *Nature Reviews Cancer* **7**, 573-584, doi: 10.1038/nrc2167.

131. Ahmad S (2017) Kinetic aspects of platinum anticancer agents. *Polyhedron* **138**, 109-124, doi: 10.1016/j.poly.2017.09.016.

132. Fuertes MA, Castilla J, Alonso C & Pérez JM (2003) Cisplatin biochemical mechanism of action: from cytotoxicity to induction of cell death through interconnections between apoptotic and necrotic pathways. *Curr Med Chem* **10**, 257-266.

133. Mandic A, Hansson J, Linder S & Shoshan MC (2003) Cisplatin Induces Endoplasmic Reticulum Stress and Nucleus-independent Apoptotic Signaling. *J Biol Chem* **278**, 9100-9106, doi: 10.1074/jbc.M210284200.

134. Berndtsson M, Hägg M, Panaretakis T, Havelka AM, Shoshan MC & Linder S (2007) Acute apoptosis by cisplatin requires induction of reactive oxygen species but is not associated with damage to nuclear DNA. *International Journal of Cancer* **120**, 175-180, doi: 10.1002/ijc.22132.

135. Singh G, Sharkey SM & Moorehead R (1992) Mitochondrial DNA damage by anticancer agents. *Pharmacol Ther* **54**, 217-230.

136. Yang Z, Schumaker LM, Egorin MJ, Zuhowski EG, Guo Z & Cullen KJ (2006) Cisplatin Preferentially Binds Mitochondrial DNA and Voltage-Dependent Anion Channel Protein in the Mitochondrial Membrane of Head and Neck Squamous Cell Carcinoma: Possible Role in Apoptosis. *Clin Cancer Res* **12**, 5817-5825, doi: 10.1158/1078-0432.ccr-06-1037.

137. Tacka KA, Dabrowiak JC, Goodisman J, Penefsky HS & Souid A-K (2004) Effects of Cisplatin on Mitochondrial Function in Jurkat Cells. *Chem Res Toxicol* **17**, 1102-1111, doi: 10.1021/tx0499564.

138. Liang BC & Ullyatt E (1998) Increased sensitivity to cis-diamminedichloroplatinum induced apoptosis with mitochondrial DNA depletion. *Cell Death Differ* **5**, 694-701, doi: 10.1038/sj.cdd.4400401.

139. Podratz JL, Knight AM, Ta LE, Staff NP, Gass JM, Genelin K, Schlattau A, Lathroum L & Windebank AJ (2011) Cisplatin induced Mitochondrial DNA damage in dorsal root ganglion neurons. *Neurobiology of Disease* **41**, 661-668, doi: 10.1016/j.nbd.2010.11.017.

140. Park SY, Chang I, Kim J-Y, Kang SW, Park S-H, Singh K & Lee M-S (2004) Resistance of mitochondrial DNA-depleted cells against cell death: role of mitochondrial superoxide dismutase. *The Journal of Biological Chemistry* **279**, 7512-7520, doi: 10.1074/jbc.M307677200.

141. Qian W, Nishikawa M, Haque AM, Hirose M, Mashimo M, Sato E & Inoue M (2005) Mitochondrial density determines the cellular sensitivity to cisplatin-induced cell death. *Am J Physiol, Cell Physiol* **289**, C1466-1475, doi: 10.1152/ajpcell.00265.2005.

142. Wisnovsky Simon P, Wilson Justin J, Radford Robert J, Pereira Mark P, Chan Maria R, Laposa Rebecca R, Lippard Stephen J & Kelley Shana O (2013) Targeting Mitochondrial DNA with a Platinum-Based Anticancer Agent. *Chemistry & Biology* **20**, 1323-1328, doi: 10.1016/j.chembiol.2013.08.010.

143. Garrido N, Pérez-Martos A, Faro M, Lou-Bonafonte JM, Fernández-Silva P, López-Pérez MJ, Montoya J & Enríquez JA (2008) Cisplatin-mediated impairment of mitochondrial DNA metabolism inversely correlates with glutathione levels. *Biochemical Journal* **414**, 93-102, doi: 10.1042/bj20071615.

144. Sancho-Martínez SM, Prieto-García L, Prieto M, López-Novoa JM & López-Hernández FJ (2012) Subcellular targets of cisplatin cytotoxicity: An integrated view. *Pharmacol Ther* **136**, 35-55, doi: 10.1016/j.pharmthera.2012.07.003.

145. Miller SE & House DA (1989) The hydrolysis products of cis-diamminedichloroplatinum(II). I. The kinetics of formation and anation of the cis-diammine(aqua)chloroplatinum(II) cation in acidic aqueous solution. *Inorganica Chimica Acta* **161**, 131-137, doi: 10.1016/s0020-1693(00)90125-7.

146. Miller SE & House DA (1989) The hydrolysis products of cis-dichlorodiammineplatinum(II) 2. The kinetics of formation and anation of the cis-diamminedi(aqua)platinum(II) cation. *Inorganica Chimica Acta* **166**, 189-197, doi: 10.1016/s0020-1693(00)80810-5.

147. Miller SE, Gerard KJ & House DA (1991) The hydrolysis products of cis-diamminedichloroplatinum(II) 6. A kinetic comparison of the cis- and trans-isomers and other cis-di(amine)di(chloro)platinum(II) compounds. *Inorganica Chimica Acta* **190**, 135-144, doi: 10.1016/s0020-1693(00)80242-x.

148. Yotsuyanagi T, Usami M, Noda Y & Nagata M (2002) Computational consideration of cisplatin hydrolysis and acid dissociation in aqueous media: effect of total drug concentrations. *International Journal of Pharmaceutics* **246**, 95-104, doi: 10.1016/s0378-5173(02)00382-4.

149. E. Miller S, Wen H, A. House D & T. Robinson W (1991) The hydrolysis products of cis-diamminedichloroplatinum(II) 4. Metal ion assisted aquation of cis-PtCl2(NH3)2 and the structure of [cis-PtCl2(NH3)2·(HgCl2)3]n. *Inorganica Chimica Acta* **184**, 111-118, doi: 10.1016/s0020-1693(00)83052-2.

150. Miller SE & House DA (1991) The hydrolysis products of cis-diamminedichloroplatinum(II) 5. The anation kinetics of cis-Pt(X)(NH3)2(OH2)+ (X ・ Cl, OH) with glycine, monohydrogen malonate and chloride. *Inorganica Chimica Acta* **187**, 125-132, doi: 10.1016/s0020-1693(00)90384-0.

151. Koubek E & House DA (1992) The hydrolysis products of cis-diamminedichloroplatinum(II) 7. The rate of the hydrogen isotope exchange reaction. *Inorganica Chimica Acta* **191**, 103-107, doi: 10.1016/s0020-1693(00)80335-7.

152. Abraham CJ, Gerard KJ & House DA (1993) The hydrolysis products of cis-diamminedichloroplatinum(II) 8. Kinetics of the base hydrolysis of PtCl2(AA) (AA=en, chxn, Tn, Me2tn) and trans-PtCl2(NH3)2. *Inorganica Chimica Acta* **209**, 119-122, doi: 10.1016/s0020-1693(00)85131-2.

153. Hindmarsch K, House DA & Turnbull MM (1997) The hydrolysis products of cis-diamminedichloroplatinum(II) 9. Chloride and bromide anation kinetics for some [PtII(N)2(OH2)2]2+ complexes and the structures of [PtIVBr4(N)2] ((N)2 = en, tn)1. *Inorganica Chimica Acta* **257**, 11-18, doi: 10.1016/s0020-1693(96)05403-5.

154. Berners-Price S, Frenkiel T, Frey U, Ranford J & Sadler P (1992) Hydrolysis Products of Cisplatin - Pka Determinations Via [h-1, N-15] Nmr-Spectroscopy. *J Chem Soc-Chem Commun*, 789-791, doi: 10.1039/c39920000789.

155. Tacka KA, Szalda D, Souid A-K, Goodisman J & Dabrowiak JC (2004) Experimental and Theoretical Studies on the Pharmacodynamics of Cisplatin in Jurkat Cells. *Chem Res Toxicol* **17**, 1434-1444, doi: 10.1021/tx0498760.

156. Hann S, Koellensperger G, Stefánka Z, Stingeder G, Fürhacker M, Buchberger W & Mader RM (2003) Application of HPLC-ICP-MS to speciation of cisplatin and its degradation products in water

containing different chloride concentrations and in human urine. *J Anal At Spectrom* **18**, 1391-1395, doi: 10.1039/b309028k.

157. Falta T, Heffeter P, Mohamed A, Berger W, Hann S & Koellensperger G (2010) Quantitative determination of intact free cisplatin in cell models by LC-ICP-MS. *J Anal At Spectrom* **26**, 109-115, doi: 10.1039/c0ja00047g.

158. Curtis L, Turner A, Vyas N & Sewell G (2010) Speciation and Reactivity of Cisplatin in River Water and Seawater. *Environmental Science & Technology* **44**, 3345-3350, doi: 10.1021/es903620z.

159. Hermann G, Heffeter P, Falta T, Berger W, Hann S & Koellensperger G (2013) In vitro studies on cisplatin focusing on kinetic aspects of intracellular chemistry by LC-ICP-MS. *Metallomics* **5**, 636-647, doi: 10.1039/c3mt20251h.

160. Vidmar J, Martinčič A, Milačič R & Ščančar J (2015) Speciation of cisplatin in environmental water samples by hydrophilic interaction liquid chromatography coupled to inductively coupled plasma mass spectrometry. *Talanta* **138**, 1-7, doi: 10.1016/j.talanta.2015.02.008.

161. Zhang Y, Guo Z & You X-Z (2001) Hydrolysis Theory for Cisplatin and Its Analogues Based on Density Functional Studies. *J Am Chem Soc* **123**, 9378-9387, doi: 10.1021/ja0023938.

162. Burda JV, Zeizinger M & Leszczynski J (2004) Activation barriers and rate constants for hydration of platinum and palladium square-planar complexes: An <i>ab initio</i> study. *The Journal of Chemical Physics* **120**, 1253-1262, doi: 10.1063/1.1633757.

163. Lau JK-C & Ensing B (2010) Hydrolysis of cisplatin—a first-principles metadynamics study. *Physical Chemistry Chemical Physics* **12**, 10348, doi: 10.1039/b918301a.

164. Melchior A, Sánchez Marcos E, R. Pappalardo R & Martínez JM (2011) Comparative study of the hydrolysis of a third- and a first-generation platinum anticancer complexes. *Theoretical Chemistry Accounts* **128**, 627-638, doi: 10.1007/s00214-010-0825-4.

165. Paschoal D, Marcial BL, Lopes JF, De Almeida WB & Dos Santos HF (2012) The role of the basis set and the level of quantum mechanical theory in the prediction of the structure and reactivity of cisplatin. *Journal of Computational Chemistry* **33**, 2292-2302, doi: 10.1002/jcc.23061.

166. Jennerwein M & Andrews PA (1995) Effect of intracellular chloride on the cellular pharmacodynamics of cis-diamminedichloroplatinum(II). *Drug Metab Dispos* **23**, 178-184.

167. Martin RB (2006) Platinum Complexes: Hydrolysis and Binding to N(7) and N(1) of Purines. In *Cisplatin*, pp. 181-205. John Wiley & Sons, Ltd.

168. Berners-Price SJ & Appleton TG (2000) The Chemistry of Cisplatin in Aqueous Solution. In *Platinum-Based Drugs in Cancer Therapy* (Kelland LR & Farrell NP, eds), pp. 3-35. Humana Press, Totowa, NJ.

169. Howe-Grant ME (1980) Aqueous platinum (II) chemistry. *Metal Complexes as Anticancer Agents* **2**, 63-125.

170. F LeRoy A, Lutz R, L Dedrick R, L Litterst C & M Guarino A (1979) Pharmacokinetic study of cis-dichlorodiammineplatinum(II) (DDP) in the beagle dog: thermodynamic and kinetic behavior of DDP in a biologic milieu. *Cancer treatment reports* **63**, 59-71.

171. Dabrowiak JC, Goodisman J & Souid A-K (2002) Kinetic Study of the Reaction of Cisplatin with Thiols. *Drug Metab Dispos* **30**, 1378-1384, doi: 10.1124/dmd.30.12.1378.

172. Hagrman D, Goodisman J, Dabrowiak JC & Souid A-K (2003) Kinetic Study on the Reaction of Cisplatin with Metallothionein. *Drug Metab Dispos* **31**, 916-923, doi: 10.1124/dmd.31.7.916.

173. Hagrman D, Goodisman J & Souid A-K (2004) Kinetic Study on the Reactions of Platinum Drugs with Glutathione. *J Pharmacol Exp Ther* **308**, 658-666, doi: 10.1124/jpet.103.059410.

174. Centerwall CR, Goodisman J, Kerwood DJ & Dabrowiak JC (2005) Cisplatin carbonato complexes. Implications for uptake, antitumor properties, and toxicity. *J Am Chem Soc* **127**, 12768-12769, doi: 10.1021/ja053353c.

175. Di Pasqua AJ, Centerwall CR, Kerwood DJ & Dabrowiak JC (2009) Formation of Carbonato and Hydroxo Complexes in the Reaction of Platinum Anticancer Drugs with Carbonate. *Inorg Chem* **48**, 1192-1197, doi: 10.1021/ic801579h.

176. Martinho N, Santos TCB, Florindo HF & Silva LC (2019) Cisplatin-Membrane Interactions and Their Influence on Platinum Complexes Activity and Toxicity. *Frontiers in Physiology* **9**, doi: 10.3389/fphys.2018.01898.

177. Ishida S, Lee J, Thiele DJ & Herskowitz I (2002) Uptake of the anticancer drug cisplatin mediated by the copper transporter Ctr1 in yeast and mammals. *PNAS* **99**, 14298-14302, doi: 10.1073/pnas.162491399.

178. Lin X, Okuda T, Holzer A & Howell SB (2002) The copper transporter CTR1 regulates cisplatin uptake in Saccharomyces cerevisiae. *Mol Pharmacol* **62**, 1154-1159.

179. Holzer AK, Samimi G, Katano K, Naerdemann W, Lin X, Safaei R & Howell SB (2004) The copper influx transporter human copper transport protein 1 regulates the uptake of cisplatin in human ovarian carcinoma cells. *Mol Pharmacol* **66**, 817-823, doi: 10.1124/mol.104.001198.

180. Song I-S, Savaraj N, Siddik ZH, Liu P, Wei Y, Wu CJ & Kuo MT (2004) Role of human copper transporter Ctr1 in the transport of platinum-based antitumor agents in cisplatin-sensitive and cisplatin-resistant cells. *Mol Cancer Ther* **3**, 1543-1549.

181. Kalayda GV, Wagner CH & Jaehde U (2012) Relevance of copper transporter 1 for cisplatin resistance in human ovarian carcinoma cells. *J Inorg Biochem* **116**, 1-10, doi: 10.1016/j.jinorgbio.2012.07.010.

182. Beretta GL, Gatti L, Tinelli S, Corna E, Colangelo D, Zunino F & Perego P (2004) Cellular pharmacology of cisplatin in relation to the expression of human copper transporter CTR1 in different pairs of cisplatin-sensitive and -resistant cells. *Biochem Pharmacol* **68**, 283-291, doi: 10.1016/j.bcp.2004.03.022.

183. Helleman J, Burger H, Hamelers IHL, Boersma AWM, de Kroon AIPM, Stoter G & Nooter K (2006) Impaired cisplatin influx in an A2780 mutant cell line: evidence for a putative, cis-configuration-specific, platinum influx transporter. *Cancer Biol Ther* **5**, 943-949.

184. Rabik CA, Maryon EB, Kasza K, Shafer JT, Bartnik CM & Dolan ME (2009) Role of copper transporters in resistance to platinating agents. *Cancer Chemother Pharmacol* **64**, 133-142, doi: 10.1007/s00280-008-0860-1.

185. Ivy KD & Kaplan JH (2013) A Re-Evaluation of the Role of hCTR1, the Human High-Affinity Copper Transporter, in Platinum-Drug Entry into Human Cells. *Mol Pharmacol* **83**, 1237-1246, doi: 10.1124/mol.113.085068.

186. Bompiani KM, Tsai C-Y, Achatz FP, Liebig JK & Howell SB (2016) Copper transporters and chaperones CTR1, CTR2, ATOX1, and CCS as determinants of cisplatin sensitivity. *Metallomics: Integrated Biometal Science* **8**, 951-962, doi: 10.1039/c6mt00076b.

187. Akerfeldt MC, Tran CMN, Shen C, Hambley TW & New EJ (2017) Interactions of cisplatin and the copper transporter CTR1 in human colon cancer cells. *J Biol Inorg Chem* **22**, 765-774, doi: 10.1007/s00775-017-1467-y.

188. Holzer AK, Katano K, Klomp LWJ & Howell SB (2004) Cisplatin rapidly down-regulates its own influx transporter hCTR1 in cultured human ovarian carcinoma cells. *Clin Cancer Res* **10**, 6744-6749, doi: 10.1158/1078-0432.ccr-04-0748.

189. Holzer AK & Howell SB (2006) The internalization and degradation of human copper transporter 1 following cisplatin exposure. *Cancer Res* **66**, 10944-10952, doi: 10.1158/0008-5472.can-06-1710.

190. Safaei R, Katano K, Samimi G, Naerdemann W, Stevenson JL, Rochdi M & Howell SB (2004) Cross-resistance to cisplatin in cells with acquired resistance to copper. *Cancer Chemother Pharmacol* **53**, 239-246, doi: 10.1007/s00280-003-0736-3.

191. Safaei R & Howell SB (2005) Copper transporters regulate the cellular pharmacology and sensitivity to Pt drugs. *Crit Rev Oncol/Hematol* **53**, 13-23, doi: 10.1016/j.critrevonc.2004.09.007.

192. Arnesano F, Scintilla S & Natile G (2007) Interaction between platinum complexes and a methionine motif found in copper transport proteins. *Angew Chem Int Ed Engl* **46**, 9062-9064, doi: 10.1002/anie.200703271.

193. Lasorsa A, Natile G, Rosato A, Tadini-Buoninsegni F & Arnesano F (2018) Monitoring Interactions Inside Cells by Advanced Spectroscopies: Overview of Copper Transporters and Cisplatin. *Curr Med Chem* **25**, 462-477, doi: 10.2174/0929867324666171110141311.

194. Arnesano F & Natile G (2008) "Platinum on the road": Interactions of antitumoral cisplatin with proteins. *Pure and Applied Chemistry* **80**, 2715-2725, doi: 10.1351/pac200880122715.

195. Nguyen TH, Arnesano F, Scintilla S, Rossetti G, Ippoliti E, Carloni P & Natile G (2012) Structural Determinants of Cisplatin and Transplatin Binding to the Met-Rich Motif of Ctr1: A

Computational Spectroscopy Approach. *Journal of Chemical Theory and Computation* **8**, 2912-2920, doi: 10.1021/ct300167m.

196. Tsigelny IF, Sharikov Y, Greenberg JP, Miller MA, Kouznetsova VL, Larson CA & Howell SB (2012) An All-Atom Model of the Structure of Human Copper Transporter 1. *Cell Biochem Biophys* **63**, 223-234, doi: 10.1007/s12013-012-9358-x.

197. Arnesano F, Nardella MI & Natile G (2018) Platinum drugs, copper transporters and copper chelators. *Coordination Chemistry Reviews* **374**, 254-260, doi: 10.1016/j.ccr.2018.07.003.

198. Calandrini V, Rossetti G, Arnesano F, Natile G & Carloni P (2015) Computational metallomics of the anticancer drug cisplatin. *J Inorg Biochem* **153**, 231-238, doi: 10.1016/j.jinorgbio.2015.10.001.

199. Howell SB, Safaei R, Larson CA & Sailor MJ (2010) Copper Transporters and the Cellular Pharmacology of the Platinum-Containing Cancer Drugs. *Mol Pharmacol* **77**, 887-894, doi: 10.1124/mol.109.063172.

200. Liang XJ, Mukherjee S, Shen DW, Maxfield FR & Gottesman MM (2006) Endocytic recycling compartments altered in cisplatin-resistant cancer cells. *Cancer Res* **66**, 2346-2353, doi: 10.1158/0008-5472.can-05-3436.

201. Reddy TBK & Chatterjee S (1997) Cisplatin inhibits pinocytosis in Dictyostelium discoideum. *Cell Biol Int* **21**, 237-241, doi: 10.1006/cbir.1997.0132.

202. Souchard J, Ha T, Cros S & Johnson N (1991) Hydrophobicity Parameters for Platinum Complexes. *J Med Chem* **34**, 863-864, doi: 10.1021/jm00106a056.

203. Gately DP & Howell SB (1993) Cellular accumulation of the anticancer agent cisplatin: a review. *Br J Cancer* **67**, 1171-1176.

204. Platts JA, Hibbs DE, Hambley TW & Hall MD (2001) Calculation of the Hydrophobicity of Platinum Drugs. *J Med Chem* **44**, 472-474, doi: 10.1021/jm001080k.

205. Oldfield SP, Hall MD & Platts JA (2007) Calculation of Lipophilicity of a Large, Diverse Dataset of Anticancer Platinum Complexes and the Relation to Cellular Uptake. *J Med Chem* **50**, 5227-5237, doi: 10.1021/jm0708275.

206. Loh SY, Mistry P, Kelland LR, Abel G & Harrap KR (1992) Reduced drug accumulation as a major mechanism of acquired resistance to cisplatin in a human ovarian carcinoma cell line: circumvention studies using novel platinum (II) and (IV) ammine/amine complexes. *Br J Cancer* **66**, 1109-1115.

207. Hall MD, Amjadi S, Zhang M, Beale PJ & Hambley TW (2004) The mechanism of action of platinum(IV) complexes in ovarian cancer cell lines. *J Inorg Biochem* **98**, 1614-1624, doi: 10.1016/j.jinorgbio.2004.05.017.

208. Gale GR, Morris CR, Atkins LM & Smith AB (1973) Binding of an antitumor platinum compound to cells as influenced by physical factors and pharmacologically active agents. *Cancer Res* **33**, 813-818.

209. Hromas RA, North JA & Burns CP (1987) Decreased cisplatin uptake by resistant L1210 leukemia cells. *Cancer Lett* **36**, 197-201.

210. Mann SC, Andrews PA & Howell SB (1990) Short-termcis-diamminedichloroplatinum(II) accumulation in sensitive and resistant human ovarian carcinoma cells. *Cancer Chemother Pharmacol* **25**, 236-240, doi: 10.1007/bf00684878.

211. Andrews PA, Mann SC, Velury S & Howell SB (1988) Cisplatin Uptake Mediated Cisplatin-Resistance in Human Ovarian Carcinoma Cells. In *Platinum and Other Metal Coordination Compounds in Cancer Chemotherapy: Proceedings of the Fifth International Symposium on Platinum and Other Metal Coordination Compounds in Cancer Chemotherapy Abano, Padua, ITALY - June 29–July 2, 1987* (Nicolini M, ed, pp. 248-254. Springer US, Boston, MA.

212. Andrews PA & Albright KD (1991) Role of Membrane Ion Transport in Cisplatin Accumulation. In *Platinum and Other Metal Coordination Compounds in Cancer Chemotherapy* (Howell SB, ed, pp. 151-159. Springer US, Boston, MA.

213. Ishikawa T & Ali-Osman F (1993) Glutathione-associated cis-diamminedichloroplatinum(II) metabolism and ATP-dependent efflux from leukemia cells. Molecular characterization of glutathione-platinum complex and its biological significance. *The Journal of Biological Chemistry* **268**, 20116-20125.

214. Yesylevskyy S, Cardey B, Kraszewski S, Foley S, Enescu M, da Silva AM, Santos HFD & Ramseyer C (2015) Empirical force field for cisplatin based on quantum dynamics data: case study of

new parameterization scheme for coordination compounds. *Journal of Molecular Modeling* **21**, 268, doi: 10.1007/s00894-015-2812-0.

215. Vorobyov I, Bennett WFD, Tieleman DP, Allen TW & Noskov S (2012) The Role of Atomic Polarization in the Thermodynamics of Chloroform Partitioning to Lipid Bilayers. *Journal of Chemical Theory and Computation* **8**, 618-628, doi: 10.1021/ct200417p.

216. Anisimov VM, Lamoureux G, Vorobyov IV, Huang N, Roux B & MacKerell AD (2005) Determination of Electrostatic Parameters for a Polarizable Force Field Based on the Classical Drude Oscillator. *Journal of Chemical Theory and Computation* **1**, 153-168, doi: 10.1021/ct049930p.

217. Lopes JF, de A. Menezes VS, Duarte HA, Rocha WR, De Almeida WB & Dos Santos HF (2006) Monte Carlo Simulation of Cisplatin Molecule in Aqueous Solution. *The Journal of Physical Chemistry B* **110**, 12047-12054, doi: 10.1021/jp057448c.

218. Hess B, Kutzner C, van der Spoel D & Lindahl E (2008) GROMACS 4: Algorithms for Highly Efficient, Load-Balanced, and Scalable Molecular Simulation. *Journal of Chemical Theory and Computation* **4**, 435-447, doi: 10.1021/ct700301q.

219. Berendsen HJC, Postma JPM, van Gunsteren WF, DiNola A & Haak JR (1984) Molecular dynamics with coupling to an external bath. *The Journal of Chemical Physics* **81**, 3684-3690, doi: doi:http://dx.doi.org/10.1063/1.448118.

220. Páll S & Hess B (2013) A flexible algorithm for calculating pair interactions on SIMD architectures. *Computer Physics Communications* **184**, 2641-2650, doi: http://dx.doi.org/10.1016/j.cpc.2013.06.003.

221. Van der Spoel D, Lindahl E, Hess B, Groenhof G, Mark AE & Berendsen HJC (2005) GROMACS: Fast, Flexible and Free. *J Comp Chem* **26**, 1701–1718.

222. Bussi G, Donadio D & Parrinello M (2007) Canonical sampling through velocity rescaling. *The Journal of Chemical Physics* **126**, 014101, doi: doi:http://dx.doi.org/10.1063/1.2408420.

223. Kirkwood JG (1935) Statistical Mechanics of Fluid Mixtures. *The Journal of Chemical Physics* **3**, 300-313, doi: 10.1063/1.1749657.

224. Hub J, De Groot B & der Spoel D (2010) g_wham-A free Weighted Histogram Analysis Implementation Including Robust Error and Autocorrelation Estimates. *Journal of Chemical Theory and Computation* **6**, 3713-3720, doi: 10.1021/ct100494z.

225. Berendsen HJC & Marrink SJ (1993) Molecular dynamics of water transport through membranes: Water from solvent to solute. *Pure and Applied Chemistry* **65**, 2513-2520, doi: 10.1351/pac199365122513.

226. Marrink S-J & Berendsen HJC (1994) Simulation of water transport through a lipid membrane. *J Phys Chem* **98**, 4155-4168, doi: 10.1021/j100066a040.

227. Lee CT, Comer J, Herndon C, Leung N, Pavlova A, Swift RV, Tung C, Rowley CN, Amaro RE, Chipot C, et al. (2016) Simulation-Based Approaches for Determining Membrane Permeability of Small Compounds. *J Chem Inf Model* **56**, 721-733, doi: 10.1021/acs.jcim.6b00022.

228. Ribeiro RP, Coimbra JTS, Ramos MJ & Fernandes PA (2017) Diffusion of the small, very polar, drug piracetam through a lipid bilayer: an MD simulation study. *Theoretical Chemistry Accounts* **136**, 46, doi: 10.1007/s00214-017-2073-3.

229. Awoonor-Williams E & Rowley CN (2016) Molecular simulation of nonfacilitated membrane permeation. *Biochimica et Biophysica Acta (BBA) - Biomembranes* **1858**, 1672-1687, doi: 10.1016/j.bbamem.2015.12.014.

230. Shinoda W (2016) Permeability across lipid membranes. *Biochim Biophys Acta* **1858**, 2254-2265, doi: 10.1016/j.bbamem.2016.03.032.

231. Dickson CJ, Hornak V, Pearlstein RA & Duca JS (2017) Structure–Kinetic Relationships of Passive Membrane Permeation from Multiscale Modeling. *J Am Chem Soc* **139**, 442-452, doi: 10.1021/jacs.6b11215.

232. Swift RV & Amaro RE (2013) Back to the Future: Can Physical Models of Passive Membrane Permeability Help Reduce Drug Candidate Attrition and Move Us Beyond QSPR? *Chemical Biology & Drug Design* **81**, 61-71, doi: 10.1111/cbdd.12074.

233. Votapka LW, Lee CT & Amaro RE (2016) Two Relations to Estimate Membrane Permeability Using Milestoning. *The Journal of Physical Chemistry B* **120**, 8606-8616, doi: 10.1021/acs.jpcb.6b02814.

234. Coimbra JTS, Fernandes PA & Ramos MJ (2017) Revisiting Partition in Hydrated Bilayer Systems. *Journal of Chemical Theory and Computation* **13**, 2290-2299, doi: 10.1021/acs.jctc.6b01258.

235. Neale C, Bennett WFD, Tieleman DP & Pomès R (2011) Statistical Convergence of Equilibrium Properties in Simulations of Molecular Solutes Embedded in Lipid Bilayers. *Journal of Chemical Theory and Computation* **7**, 4175-4188, doi: 10.1021/ct200316w.

236. Chipot C & Comer J (2016) Subdiffusion in Membrane Permeation of Small Molecules. *Scientific Reports* **6**, 35913, doi: 10.1038/srep35913

https://www.nature.com/articles/srep35913#supplementary-information.

237. Gaalswyk K, Awoonor-Williams E & Rowley CN (2016) Generalized Langevin Methods for Calculating Transmembrane Diffusivity. *Journal of Chemical Theory and Computation* **12**, 5609-5619, doi: 10.1021/acs.jctc.6b00747.

238. Marrink SJ & Berendsen HJC (1996) Permeation Process of Small Molecules across Lipid Membranes Studied by Molecular Dynamics Simulations. *J Phys Chem* **100**, 16729-16738, doi: 10.1021/jp952956f.

239. Zou J, Yang XD, An F & Wang K (1998) Relationship between cellular uptake rate and chemical behavior of diammine/diaminocyclohexane platinum (II) complexes with oxygen-ligating anionic groups. *J Inorg Biochem* **70**, 227-232.

240. Verkman AS & Solomon AK (1982) A stepwise mechanism for the permeation of phloretin through a lipid bilayer. *J Gen Physiol* **80**, 557-581.

241. Paula S, Volkov AG, Van Hoek AN, Haines TH & Deamer DW (1996) Permeation of protons, potassium ions, and small polar molecules through phospholipid bilayers as a function of membrane thickness. *Biophys J* **70**, 339-348.

242. Males RG & Herring FG (1999) A 1H-NMR study of the permeation of glycolic acid through phospholipid membranes. *Biochimica et Biophysica Acta (BBA) - Biomembranes* **1416**, 333-338, doi: 10.1016/s0005-2736(98)00236-3.

243. Carloni P & Andreoni W (1996) Platinum-Modified Nucleobase Pairs in the Solid State: A Theoretical Study. *J Phys Chem* **100**, 17797-17800, doi: 10.1021/jp961738z.

244. Pavankumar PNV, Seetharamulu P, Yao S, Saxe JD, Reddy DG & Hausheer FH (1999) Comprehensive ab initio quantum mechanical and Molecular Orbital (MO) analysis of cisplatin: Structure, bonding, charge density, and vibrational frequencies. *Journal of Computational Chemistry* **20**, 365-382.

245. Raymond E, Faivre S, Chaney S, Woynarowski J & Cvitkovic E (2002) Cellular and molecular pharmacology of oxaliplatin. *Mol Cancer Ther* **1**, 227-235.

246. Cooke IR & Deserno M (2006) Coupling between Lipid Shape and Membrane Curvature. *Biophys J* **91**, 487-495, doi: 10.1529/biophysj.105.078683.

247. Zimmerberg J & McLaughlin S (2004) Membrane Curvature: How BAR Domains Bend Bilayers. *Current Biology* **14**, R250-R252, doi: 10.1016/j.cub.2004.02.060.

248. Gaudin A, Yemisci M, Eroglu H, Lepêtre-Mouelhi S, Turkoglu OF, Dönmez-Demir B, Caban S, Fevzi Sargon M, Garcia-Argote S, Pieters G, et al. (2014) Squalenoyl Adenosine Nanoparticles provide Neuroprotection after Stroke and Spinal Cord Injury. *Nat Nanotechnol* **9**, 1054-1062, doi: 10.1038/nnano.2014.274.

ABSTRACT

Membranes in cells are usually considered to act as physical barriers that allow compartmentalization and specialization of the intracellular medium. They are also highly dynamic assemblies, changing their shape, composition and properties on a variety of spatial and temporal scales. This dynamical reshaping of membranes occurs during different cell processes such as motion, division, differentiation and vesicle trafficking. Membranes must thus be sufficiently rigid and robust to maintain the integrity of the cell compartments and flexible enough to allow continuous changes of their shapes. Many of their properties like thermodynamic and mechanical properties have been elucidated on the basis of lipid self-organization arguments. However, many open questions remain concerning the links between membranes composition and their permeability to drugs. Determination of permeability of such membranes to drugs is indeed of great importance for toxicology reason, for addressing cell resistance issues to chemodrugs, but also for finding new strategies for targeting cells, especially cancer ones. In this thesis, we searched for chemical and physical features connected to membrane lipids that could help to differentiate cancer and normal cells and though be potential markers for selective targeting. We investigated three "main ingredients" that may play an important role on the membrane permeation to drugs, namely composition (lipids and cholesterol contents), curvature and asymmetry between leaflets of the lipid membranes. Two realistic models of "cancer" and "normal" lipid matrix of the plasma membranes were built to study the permeation of small molecules – especially cancer drugs. The modes of action and transport of cisplatin – one of the main anticancer drugs – were reviewed. Cisplatin permeation was addressed to understand thoroughly the interplay in between the membrane properties and the passive diffusion process.

Keywords: molecular dynamics, plasma membrane, anticancer drug, selectivity, lipid, permeation, passive diffusion

RESUME

Les membranes cellulaires sont généralement considérées comme des barrières physiques permettant la compartimentation et la spécialisation du milieu intracellulaire. Ce sont des systèmes dynamiques, dont la forme, la composition et les propriétés changent sur une large gamme des échelles de temps et d'espace. Ce remodelage des membranes a lieu au sein de différents processus cellulaires comme leur déplacement, leur différenciation ou encore le transport de vésicules. Les membranes doivent être suffisamment robustes et rigides pour maintenir l'intégrité de la cellule et dans le même temps, suffisamment flexibles pour permettre un continuel changement de forme. Plusieurs de leurs propriétés, telles que leurs propriétés thermodynamiques ou mécaniques ont été étudiées et associées à l'auto-organisation des lipides. Cependant, plusieurs questions restent ouvertes, en particulier en ce qui concerne le lien entre la composition des membranes et leur perméabilité face à des médicaments. La détermination de leur perméabilité est d'une grande importance pour des raisons toxicologiques, pour remédier à la problématique de résistance aux médicaments de chimiothérapie exprimée par certaines lignées cancéreuses, mais aussi dans le but de développer de nouvelles stratégies pour le ciblage cellulaire. Au cours de ce travail de thèse, nous avons recherché les propriétés chimiques et physiques connectées à la matrice lipidique des membranes plasmiques qui pourraient permettre de différencier les cellules cancéreuses des cellules saines et qui pourraient ainsi devenir de potentiels marqueurs pour un ciblage sélectif. Nous avons sélectionné trois principaux « ingrédients » qui sont susceptibles de jouer un rôle important sur la perméation : la composition de la membrane (en lipides et en cholestérol), la courbure de la membrane et l'asymétrie entre les monocouches de la membrane. Deux modèles réalistes de la matrice lipidique de la membrane plasmique de cellules cancéreuses et saines ont été construits pour étudier la perméation de petites molécules et particulièrement d'anticancéreux. Les modes d'action et de transport du cisplatine – l'un des médicaments anticancéreux les plus utilisés à ce jour – ont été étudié. Une analyse de la perméation du cisplatine a été menée pour comprendre la relation entre les différentes propriétés de la matrice lipidique de la membrane plasmique et sa diffusion passive.

Mots-clés : dynamique moléculaire, simulations, membrane plasmique, anticancéreux, sélectivité, lipide, diffusion passive

Université Bourgogne Franche-Comté
32, avenue de l'Observatoire
25000 Besançon